Chem Soc Rev

REVIEW ARTICLE

View Article Online
View Journal | View Issue

Cite this: *Chem. Soc. Rev.*, 2022, **51**, 9759

Development of nanotechnology-mediated precision radiotherapy for anti-metastasis and radioprotection

Yuanbo Pan, [abcf] Wei Tang,[e] Wenpei Fan,*[d] Jianmin Zhang*[abc] and Xiaoyuan Chen *[fghi]

Radiotherapy (RT), including external beam RT and internal radiation therapy, uses high-energy ionizing radiation to kill tumor cells. However, ionizing radiation inevitably damages the surrounding normal tissues. Therefore, it is imperative to develop precision RT for improving the treatment outcome and reducing the adverse effects. Recent breakthroughs in nanotechnology have provided a variety of strategies by which RT can precisely and efficiently eradicate local tumors. In this review, we would like to summarize a series of nanotechnology-mediated strategies to achieve precision RT, including tumor-targeted delivery, image-guided precision radiotherapy, and exo/endogenous stimuli-responsive nanomedicines for enhanced tumor accumulation/penetration. In addition, this review will also discuss two representative featured applications of precision RT: RT-induced immunotherapy against cancer metastasis and radioprotection of the surrounding healthy tissues. Since RT is usually thought to be only effective for treating local tumors, this review will interpret the unusual mechanisms of RT-mediated systemic antitumor immunity for eliminating distant cancer metastasis as well as the abscopal effects of RT in combination with other treatments (*e.g.*, photodynamic therapy (PDT), chemodynamic therapy (CDT), *etc.*). Furthermore, this review will discuss nanotechnology-mediated radioprotection strategies for shielding healthy tissues from radiation damage. Finally, the current challenges and future prospects of precision RT are also elucidated with the intention to accelerate its clinical translation.

Received 13th July 2022

DOI: 10.1039/d1cs01145f

rsc.li/chem-soc-rev

[a] *Department of Neurosurgery, Second Affiliated Hospital, School of Medicine, Zhejiang University, Hangzhou, 310009, China. E-mail: zjm135@zju.edu.cn*
[b] *Key Laboratory of Precise Treatment and Clinical Translational Research of Neurological Diseases, Hangzhou, 310009, Zhejiang, China*
[c] *Clinical Research Center for Neurological Diseases of Zhejiang Province, Hangzhou, 310009, China*
[d] *State Key Laboratory of Natural Medicines and Jiangsu Key Laboratory of Drug Discovery for Metabolic Diseases, Center of Advanced Pharmaceuticals and Biomaterials, China Pharmaceutical University, Nanjing, 210009, China. E-mail: wenpei.fan@cpu.edu.cn*
[e] *Departments of Pharmacy and Diagnostic Radiology, Nanomedicine Translational Research Program, Faculty of Science and Yong Loo Lin School of Medicine, National University of Singapore, Singapore, 117544, Singapore*
[f] *Departments of Diagnostic Radiology, Surgery, Chemical and Biomolecular Engineering, and Biomedical Engineering, Yong Loo Lin School of Medicine and College of Design and Engineering, National University of Singapore, Singapore 119074, Singapore. E-mail: chen.shawn@nus.edu.sg*
[g] *Clinical Imaging Research Centre, Centre for Translational Medicine, Yong Loo Lin School of Medicine, National University of Singapore, Singapore 117599, Singapore*
[h] *Nanomedicine Translational Research Program, NUS Center for Nanomedicine, Yong Loo Lin School of Medicine, National University of Singapore, Singapore 117597, Singapore*
[i] *Institute of Molecular and Cell Biology, Agency for Science, Technology, and Research (A*STAR), 61 Biopolis Drive, Proteos, Singapore, 138673, Singapore*

1. Introduction

1.1 Radiotherapy

Cancer remains one of the leading causes of death worldwide, accounting for nearly 10 million deaths every year.[1] As an important anticancer treatment, radiotherapy (RT) is delivered to more than 50% of all patients with cancer for both curative and palliative purposes.[2,3] There are two main types of RT: external beam RT (EBRT) and internal radiation therapy. ERBT is the most common type of RT that uses high-energy ionizing radiation *via* a linear accelerator.[4] By contrast, internal radiation therapy, including brachytherapy and radioisotope therapy (RIT), makes use of radioactive materials to kill tumor cells.[4–6] Generally, RT takes effect by ionizing radiation (*e.g.*, X-ray, γ-ray, *etc.*) and particle radiation (*e.g.*, carbon ions, electrons, neutrons, α particles, β particles, *etc.*).[7,8] All of these types of radiation are utilized to achieve therapeutic effects to meet various clinical demands. In general, RT damages tumor tissues through direct and indirect actions. Direct action refers to biomolecule damage, especially double-strand breaks in DNA, leading to necrosis or apoptosis. In indirect action, radiolysis of water molecules produces reactive oxygen species (ROS) to

destroy biological molecules, such as DNA, proteins, and lipids, to trigger cell apoptosis.[8–13] Furthermore, RT is usually used in combination with other treatments, including surgery, chemotherapy, and immunotherapy, to treat tumors. Therefore, RT has always been a mainstay part of cancer treatment.

1.2 Precision RT

Precision medicine is an emerging field that considers individual variations in genetics, the environment and lifestyle factors for targeted therapy.[14] The precision medicine of cancer patients relies heavily on the development of next generation sequencing and high-throughput data processing technologies.[15] However, current RT cannot accurately distinguish tumor tissues from healthy ones, so patients usually suffer from severe radiation damage, such as gastrointestinal syndrome (GIS) and radiation-induced lung injury (RILI), which lowers the long-term life quality of patients and limits the follow-up treatment.[16–19] Therefore, precision RT is highly desirable to maximize tumor control and minimize the toxic effects on healthy tissues at the individual patient level.[20]

1.3 Emerging nanotechnologies for precision RT

For tumors, only a small proportion of X-ray photon energy can be absorbed. Therefore, high dose radiation is usually required to kill tumor cells, imposing a radiation-related side effect on the surrounding normal tissues.[21] Recently, the rapid development of nanotechnology has shown its great value in achieving precision RT. For example, owing to a high photoelectric absorption cross-section, the Au nanoparticles (AuNPs) can enhance local dose deposition in the kilovoltage range (500–300 kVp), which causes the energy of X-ray photons absorbed by AuNPs to be transferred to the surrounding water, resulting in

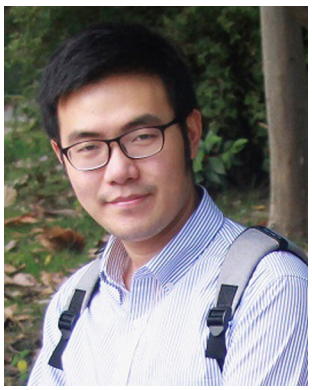

Yuanbo Pan

Yuanbo Pan received his MMed degree from Shanghai Jiao Tong University School of Medicine in 2019. Since then, he has been pursuing his PhD degree at the School of Medicine, Zhejiang University, under the supervision of Prof. Jianmin Zhang. He is currently a joint PhD student at the Yong Loo Lin School of Medicine, National University of Singapore, under the supervision of Prof. Xiaoyuan (Shawn) Chen. His research interests focus on the design and synthesis of multifunctional nanomedicines for brain disease (brain tumors, stroke, traumatic brain injury, etc.) theranostics.

Wei Tang

Dr Wei Tang received her BS degree in Chemistry from the University of Science and Technology of China in 2011 and PhD degree in Chemistry from the University of Georgia in 2016. After a postdoctoral training in the Laboratory of Molecular Imaging and Nanomedicine at the National Institutes of Health, she joined National University of Singapore as an Assistant Professor in the Department of Pharmacy and Department of Diagnostic Radiology in 2021. Her research interests focus on the development of safe and effective drug delivery technologies to empower early detection, precise stratification, and personalized therapy for cancer.

Wenpei Fan

Prof. Wenpei Fan received his PhD in 2015 from Shanghai Institute of Ceramics, Chinese Academy of Sciences. During 2015–2019, he worked at National Institutes of Health (USA) as a postdoctoral fellow. Since November 2019, he has been a full professor at the Center of Advanced Pharmaceuticals and Biomaterials, China Pharmaceutical University. He has published over 80 papers in reputed journals. His research interest focuses on the design and synthesis of multifunctional theranostic nanomedicines for drug delivery, multimodal imaging, and precision synergistic therapy.

Jianmin Zhang

Prof. Jianmin Zhang received his MD degree and PhD degree, in 1983 and 2005, respectively, both from Zhejiang University. He is now a professor and chief physician of the Department of Neurosurgery, Second Affiliated Hospital, School of Medicine, Zhejiang University. He has published over 200 papers and numerous books. His current research interests focus on basic and clinical research studies of cerebrovascular diseases and brain tumors as well as the clinical translational application of brain–computer interfaces.

ROS generation.[22] In addition, the organic materials, such as protoporphyrin IX (PpIX), were also reported to generate ROS under X-ray irradiation instead of light.[23–25] Nowadays, a wide range of multifunctional nanomaterials have been designed for tumor-targeted delivery and radiosensitization through a high-*Z* element-induced Compton effect or regulation of radioresistant tumor microenvironment (TME).[21,26] These nanoradiosensitizers accumulate in tumors *via* either passive targeting (known as enhanced permeability and retention (EPR) effect) or active targeting mechanisms, including ligand modification-based targeting, biomimetic targeting, magnetic targeting, and even subcellular organelle targeting, allowing for tumor-specific precision RT.[27–32] Based on nanoradiosensitizers, low-dose radiation is able to kill tumor cells effectively, lowering side effect on normal tissues. In addition, these nanoradiosensitizers can be endowed with multiple imaging functionalities for image-guided precision RT, including magnetic resonance imaging (MRI), computed tomography (CT) imaging, photoacoustic imaging (PAI), fluorescence imaging (FLI), positron-emission tomography (PET) imaging, single-photon-emission computed tomography (SPECT) imaging, or combination of these imaging modalities. These advanced imaging techniques can provide accurate information of tumor location and track/monitor the pharmacokinetics of nanoradiosensitizers.[33–35] Moreover, specific imaging techniques can be used to monitor the TME and tumor responses to therapy, thus beneficial in guiding precision RT.[36–38] Furthermore, the exo/endogenous stimuli responsive-nanotechnologies also play an important role in realizing precision RT. For instance, pH-responsive nanoradiosensitizers are able to self-regulate their particle sizes at different pH values for enhanced tumor penetration.[39,40]

Xiaoyuan Chen

Prof. Xiaoyuan (Shawn) Chen received his PhD in Chemistry from the University of Idaho (1999). After being a faculty at the University of Southern California and Stanford University and then Senior Investigator/Lab Chief at the National Institutes of Health, he is now a Nasrat Muzayyin Professor in Medicine and Technology, Yong Loo Lin School of Medicine and College of Design and Engineering, National University of Singapore. His current research interests are mainly theranostics (radiotheranostics, nanotheranostics, immunotheranostics, magnetotheranostics, phototheranostics, etc.) that can be clinically translatable. He has published over 900 papers and numerous books (H index 173 as of September 2022).

Besides destroying the local tumors, precision RT can also suppress distant tumor metastasis. Generally, RT is thought to be only effective in local tumor therapy; however, the nanotechnology-mediated RT is able to elicit systemic antitumor immunity against distant cancer metastasis.[41] Moreover, the abscopal effect of RT can be further enhanced by combination with checkpoint blockade therapy or other treatment protocols.[42,43] In addition, minimizing the side effects of ionizing radiation on normal healthy tissues is also an important part of precision RT. Several types of ROS-scavenging nanomaterials, including CeO_2, fullerenes, graphdiyne, and Bi_2Se_3, have been synthesized for radioprotection of normal tissues.[44–49] Moreover, various nanocarriers have been utilized to deliver molecular radioprotectors to improve their blood circulation and biodistribution. Overall, rapidly advancing nanotechnology enables precision RT to be extended to anti-metastasis and radioprotection.

In this review, the current state-of-the-art strategies for nanotechnology-mediated precision RT are summarized, including tumor-targeted delivery, image-guided positioning, and exo/endogenous stimuli-responsive tumor accumulation/penetration. Besides, this review will also discuss two representative featured applications of precision RT: RT-induced systemic antitumor immunity against distant metastasis and radioprotection of healthy tissues.

2. Tumor-targeted delivery strategies for precision radiotherapy

Tumor-targeted delivery strategies enable nanoradiosensitizers to precisely accumulate in tumor tissues for precision RT. This section will discuss various advanced tumor-targeted nanomedicine delivery strategies for achieving precision RT (Fig. 1), including EPR effect-mediated passive targeting, biological or bioorthogonal ligand-mediated targeting, cell or cell membrane-mediated homing targeting, magnetic targeting, and subcellular organelle targeting (*e.g.*, mitochondrial targeting, nucleus targeting, *etc.*) strategies.

2.1 Enhanced permeability and retention (EPR) effect-mediated passive targeting strategy

When administered intravenously, drugs are usually too small thus are easily excreted by the kidneys or too large thus are easily recognized and cleared by the reticuloendothelial system (RES), but nano-sized drugs can achieve long blood circulation for enhanced tumor accumulation.[57] Different from healthy vasculatures in normal tissues, tumors have leaky vessels, so nano-sized drugs featured with long blood circulation tend to leak into tumor tissues *via* the leaky vessels and then stay within the tumors.[58,59] This phenomenon, known as the EPR effect, is the primary pathway by which most radiosensitizers accumulate in the tumors.[40,60–65]

For example, Gao *et al.* used nitrosylated maytansinoid DM1 with the NO releasing group, *tert*-butyl nitrite $(CH_3)_3CONO$, to prepare a prodrug DM1-NO. Considering

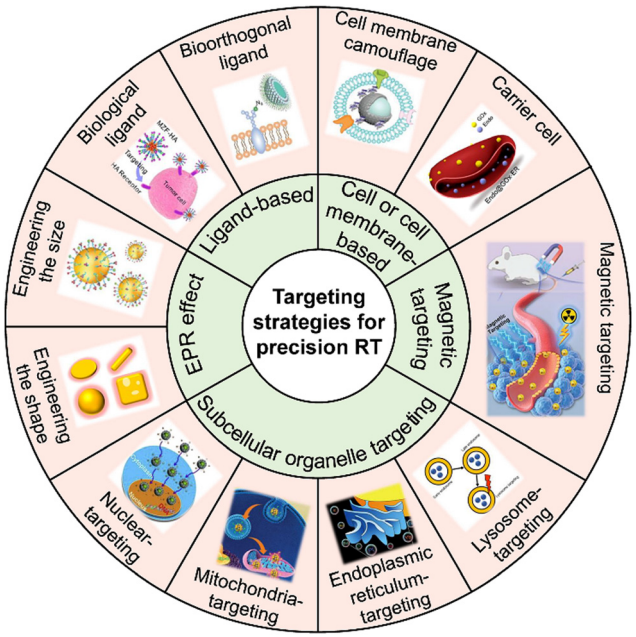

Fig. 1 Scheme of the various targeting strategies for precision RT. Adapted with permission from ref. 31, 37 and 50–56 Copyright, American Chemical Society, Wiley, Elsevier, Royal Society of Chemistry, American Scientific Publishers.

that DM1-NO could not efficiently accumulate in tumors,[66] it was loaded into the poly(lactide-*co*-glycolic)-*block*-ploy(ethylene glycol) (PLGA-*b*-PEG) nanocarrier (DM1-NO-NPs) for efficient delivery to tumors through the EPR effect. The elevated ROS induced by X-ray irradiation led to the cleavage of the S–N bond for release of DM1 and NO. DM1 could arrest the cell cycle at the G2/M phase, sensitizing cancer cells to RT. Moreover, NO could react with radiation-induced ROS to generate more harmful radicals, such as ONOO-, leading to lipid peroxidation and DNA damage. As a result, DM1–NO–NPs plus X-ray irradiation could significantly suppress tumor growth.

Furthermore, the EPR effect is quite heterogeneous within and across tumors and is highly related with cancer type, tumor volume, blood supply, and location.[67–72] For instance, Davis and Lewis's group synthesized star polymers (denoted as nanostars). Then, the nanostars were modified with Gd^{3+} for MR imaging and labeled with ^{89}Zr or ^{177}Lu for *in vivo* PET imaging or internal RIT.[63] *In vivo* PET imaging was performed in two types of tumors with different EPR characteristics by intravenous injection of ^{89}Zr-functionalized nanostars. The result revealed that the nanostars effectively accumulated in CT26 xenografts (high EPR) at 3 days post-injection (14.8 ± 4.0% ID per g). However, the nanostars were observed only at the periphery of BxPC3 xenografts (low EPR) with poor penetration. BxPC3 pancreatic cancer is characterized by a dense extracellular matrix, which might result in a low EPR effect and poor penetration of nanodrugs.[73] Finally, the ^{177}Lu-labeled nanostars were utilized for the RT of CT26 tumor-bearing mice. The result showed that the CT26 tumor growth was significantly inhibited when the imposed dose was increased to 3.7 or 7.4 MBq.

2.1.1 Engineering the shapes of nanoradiosensitizers for better EPR effect. It is well known that the EPR effect is dependent on the physicochemical characteristics of NPs such as shape and size. Both shape and size of radiosensitizers can affect their biological processes, including cell uptake, vasculature crossing, and tumor penetration/diffusion, thus further influencing their blood circulation half-life, biodistribution, and tumor accumulation.[74,75] For the shape of NPs, non-spherical NPs differ from the corresponding spherical NPs in many biophysical processes, such as flow processes in blood, processes of being recognized by RES, the ways of interaction with cell membranes, the process of penetrating and diffusing into tumor tissue, *etc.*[76] It has been reported that spherical NPs with an optimal size in the range of 50–100 nm could achieve the best tumor accumulation owing to their good EPR effect.[50,77] However, other studies showed that non-spherical NPs, especially rod-shape ones, exhibited some advantages over spherical NPs in cancer cell phagocytosis.[78,79] This is because the tumor accumulation of particles is affected by many factors, such as tumor type, tumor location, and particle size.

For example, Xia and Liu's group doped radioactive ^{198}Au into the crystal lattices of PEGylated Au nanostructures with four different shapes but similar size (~50 nm), including nanospheres, nanodisks, nanorods, and cubic nanocages (Fig. 2a–d).[50] They investigated the biodistribution, tumor accumulation, and intratumoral distribution of the four shapes of ^{198}Au-doped nanostructures in EMT6 breast tumor-bearing mice. The γ radiation of radioactive ^{198}Au was adopted to quantify the biodistribution of these Au nanostructures. However, *in vivo* tumor uptake was observed by the Cerenkov luminescence derived from the β-emission of ^{198}Au. The autoradiography imaging of tumor slices was utilized to measure the intratumoral distribution of these Au nanostructures. It was observed that Au nanospheres exhibited the longest blood circulation time and highest tumor accumulation of 23.2% ID per g at 24 h post-injection (Fig. 2e). It is worth mentioning that Au nanodisks could accumulate in the lung even at 24 h post-injection (4.9% ID per g) due to their distinct shape, indicating their potential application in lung theranostics. The *in vivo* luminescence and X-ray imaging further confirmed the highest tumor uptake of Au nanospheres (Fig. 2f). Interestingly, autoradiography imaging of tumor slices at 24 h post-injection revealed that the Au nanocages and nanorods were able to reach the tumor cores while Au nanospheres and nanodisks only stayed at the periphery of tumors. In another similar study, Ma *et al.* designed three types of PEG-modified Au nanostructures with similar size (about 50 nm) but various shapes, such as Au NPs (GNPs), Au nanorods (GNRs), and Au nanospikes (GNSs).[80] *In vitro* cell uptake experiments showed that GNPs presented higher phagocytic efficiency than GNRs and GNSs at 24 h post-incubation. Owing to higher cellular uptake efficiency, GNPs showed better RT enhancement with a sensitization enhancement ratio (SER) of 1.62, much higher than that of GNSs (1.37) and GNRs (1.21). These results suggested that the

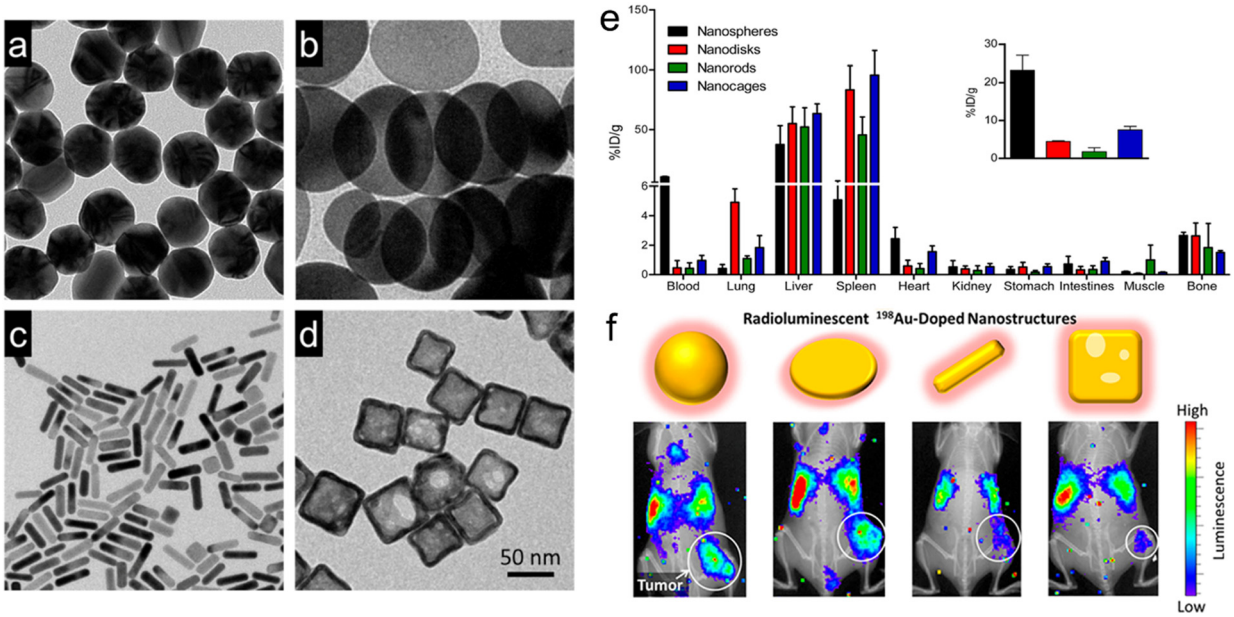

Fig. 2 Engineering the shapes of nanoradiosensitizers for better EPR effect. (a–d) TEM images of Au nanospheres (a), Au nanodisks (b), AuNRs (c), and Au cubic nanocages. (e) Biodistribution of various types of ^{198}Au-doped Au nanostructures at 1 day after intravenous administration. Inset: the amount of Au in tumor sites. (f) *In vivo* radioluminescence images of tumor-bearing mice at 1 day after administration of various types of ^{198}Au-doped Au nanostructures. Reproduced with permission from ref. 50. Copyright 2014, American Chemical Society.

shape was able to influence the cell uptake efficiency of Au nanostructures and further affect their RT efficacy.

As another example, Wang *et al.* constructed three types of PEGylated Au nanomaterials (*i.e.*, Au nanohexapods, Au nanorods, and Au nanocages) with similar sizes to investigate their *in vitro* and *in vivo* cellular uptake efficiencies.[79] The result revealed that Au nanohexapods exhibited higher cellular uptake than Au nanorods and Au nanocages. Moreover, Au nanohexapods and Au nanorods exhibited relatively high tumor accumulation of 7.2 ± 1.2 and 8.4 ± 2.2% ID per g at 24 h post-injection, respectively. However, Au nanocages showed relatively poor accumulation in tumors (2.6 ± 0.8% ID per g at 24 h post-injection).

A previous study reported that the targeting ability of AuNRs could be better than that of Au nanospheres when modified with active targeting ligands. Zhang *et al.* fabricated two shapes (rod and sphere) of RGD-modified, radioisotope ^{125}I-labeled and cisplatin-loaded Au nanostructures (RGD–^{125}IPt–AuNRs and RGD–^{125}IPt–AuNPs) with similar sizes to evaluate their *in vivo* biodistribution and chemotherapy/RT efficacy.[81] The tumor accumulation of these Au nanostructures was attributed to both the targeting peptides and the EPR effect. The scramble peptide c(RADyC) was used to modify Au nanostructures (RAD–^{125}IPt–AuNRs and RAD–^{125}IPt–AuNPs) as the non-targeting negative control. There was no significant difference in tumor accumulation between RAD–^{125}IPt–AuNRs and RAD–^{125}IPt–AuNPs. Nevertheless, RGD–^{125}IPt–AuNRs exhibited much richer tumor accumulation than RGD–^{125}IPt–AuNPs, suggesting that the shape of Au nanostructures modified with active targeting ligands played a crucial role in their tumor accumulation. The relative tumor volume in the RGD–^{125}IPt–AuNRs plus X-ray group at 21 day post-treatment was only 4.73 compared to 9.8 in the RGD–^{125}IPt–AuNPs plus X-ray group.

2.1.2 Engineering the size of nanoradiosensitizers for better EPR effect. Generally, large-sized (>100 nm) NPs are easily recognized and cleared by the RES while small-sized (<5 nm) NPs are directly excreted by the kidneys, both of which result in their short circulation half-time and poor tumor accumulation.[74,82] For the particle sizes within the range of 5 and 100 nm, smaller-sized NPs are able to rapidly enter and penetrate deeply into tumors, but are more readily metabolically cleared from tumors. However, larger-sized NPs are able to gradually enter into tumor and lead to higher accumulation owing to better retention. Thus, an appropriate NP size requires a balance between rich tumor accumulation and deep tumor penetration.

The radiosensitizers with the most appropriate size can achieve the richest tumor accumulation for precise RT with very few adverse effects on the adjacent normal tissues.[51,83] Zhang *et al.* synthesized four different sizes (4.8, 12.1, 27.3, and 46.6 nm) of PEG-modified AuNPs to evaluate the size-dependent radiosensitization *in vitro* and *in vivo*.[84] They investigated the *in vitro* radiosensitization of AuNPs by measuring the apoptosis and necrosis of HeLa cells after X-ray irradiation (2 Gy) plus AuNPs with different sizes. The apoptosis ratios induced by 4.8, 12.1, 27.3, and 46.6 nm AuNPs plus X-ray irradiation were measured to be 7.65%, 21.86%, 11.19%, and 3.77%, respectively. Meanwhile, necrosis ratios of 6.13%, 15.59%, 6.93%, and 1.09% were induced by 4.8, 12.1, 27.3, and 46.6 nm AuNPs plus X-ray irradiation, respectively. Next, the biodistribution of PEG-modified AuNPs at 24 days after

intraperitoneal injection revealed that 12.1 nm and 27.3 nm AuNPs mainly stayed in the liver and spleen, respectively, and that 12.1 nm AuNPs exhibited the richest tumor concentration. However, 4.8 nm or 46.6 nm AuNPs hardly remained in the tumor. The tumor volumes at 24 days post-treatment of 12.1 nm AuNPs + RT and 27.3 nm AuNPs + RT were significantly reduced to 37.1 and 130.3 mm^3, respectively, compared to RT alone (394.4 mm^3), 4.8 nm AuNPs + RT (349.6 mm^3), or 46.6 nm AuNPs + RT (290.4 mm^3).

In summary, the tumor accumulation of nanoradiosensitizers through the EPR effect is influenced by various factors, such as particle shape, size, surface modification, tumor type, and location, *etc.* Therefore, to achieve precise RT, it is necessary to comprehensively consider the above-mentioned factors to design nanoradiosensitizers with optimized EPR effect and maximized tumor accumulation.

2.2 Ligand-mediated active targeting

2.2.1 Biological ligand-mediated targeting. Although nanoradiosensitizers can passively target tumor tissues *via* the EPR effect, internalization of such nanoradiosensitizers can be further enhanced through surface modification of high-affinity biological ligands to bind with the specific receptors on cancer cell membranes.

Folic acid (FA) is one of the most widely used targeting ligands since the corresponding folate receptors are highly expressed in various types of tumors, such as brain, lung, breast, colon, and ovary tumors.[85] As such, FA has been commonly employed to engineer radiosensitizers with active tumor targeting for precision RT.[86–90] For example, Zhang *et al.* loaded sorafenib (SOR, a multi-targeted drug for hepatocellular carcinoma (HCC)) into bismuth-based mesoporous nanomaterials (NBOF) with surface modification of PEG–FA (P-FA) to prepare the NBOF@SOR-P-FA NPs for actively targeted chemoradiotherapy of HCC (Fig. 3a).[91] Owing to the P-FA coating, NBOF@SOR-P-FA NPs were able to bind with folate receptors overexpressed on cancer cell membranes. Thus, NBOF@SOR-P-FA plus X-ray irradiation could effectively suppress *in vitro* HCC cell viability to 16.2% (77.2% for NBOF@SOR-P-FA alone group) and increase the cell apoptosis proportion to 51.7% (31.6% for NBOF@SOR-P-FA alone group). Moreover, *in vivo* treatment with NBOF@SOR-P-FA and X-ray irradiation (6 Gy) could completely inhibit tumor growth, whereas the average tumor volume in the X-ray alone group reached over 500 mm^3 at 15 days after treatment.

Hyaluronic acid (HA), a natural high molecular weight polysaccharide in the extracellular matrix and synovial fluid, has been explored as a targeting ligand for nanomedicines.[92–94] The surface decoration of HA not only improves the dispersed nature of radiosensitizers but also endows the radiosensitizers with active targeting ability to bind with CD44 (a HA receptor) overexpressed on cancer cells.[52,95,96] For example, Du *et al.* loaded D-arginine (D-Arg) into MIL-100 (Fe) metal–organic frameworks (MOFs) with surface modification of HA to prepare HA@MOF/D-Arg NPs for radiosensitization of osteosarcoma (Fig. 3b).[97] After entering cancer cell *via* receptor-mediated endocytosis, the released D-Arg could generate nitric oxide (NO) and then decrease the expression level of hypoxia-inducible factor-1 alpha (HIF-1α) for attenuating tumor hypoxia. Moreover, the ferric ions were able to convert hydrogen peroxide into hydroxyl radicals (•OH) which could further react with NO to produce peroxynitrite anions ($ONOO^-$). Both types of ROS could effectively kill cancer cells. The decreased tumor hypoxia and increased ROS yield could sensitize cancer cells to RT. As a result, the HA@MOF/D-Arg NPs plus X-ray irradiation could significantly decrease the survival fraction of K7M2 cells to about 10% under hypoxic conditions compared to over 25% in the D-Arg + X-ray group. In addition, with the

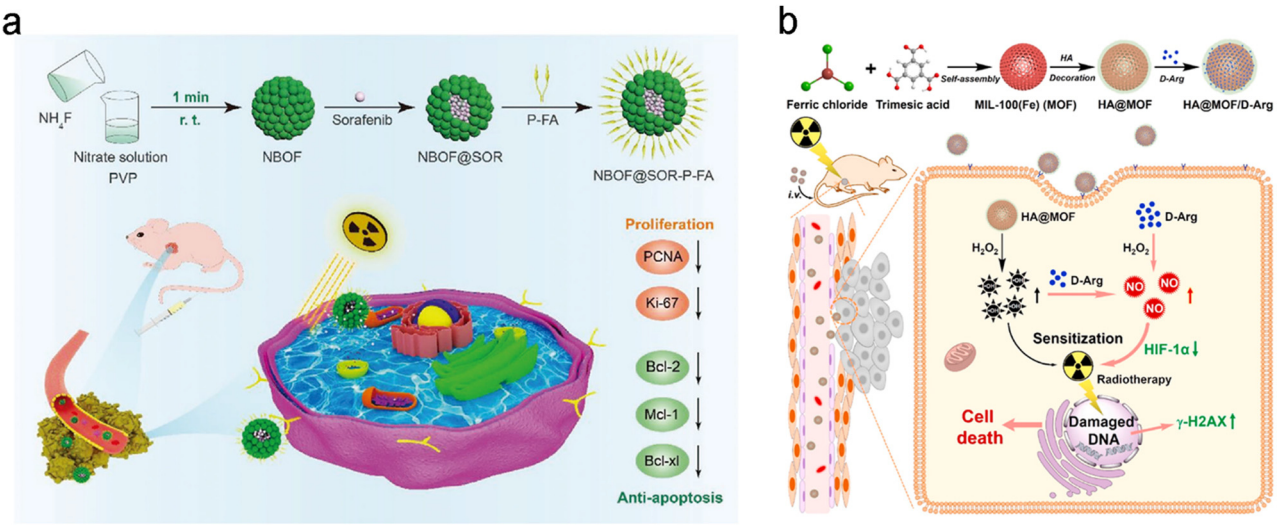

Fig. 3 Biological ligand (HA/FA)-based targeting strategies for precision RT. (a) A scheme showing the synthesis process of NBOF@SOR-P-FA and its application for targeted RT/chemotherapy of HCC. Reproduced with permission from ref. 91. Copyright 2020, Wiley. (b) A scheme showing the synthesis process of HA@MOF/D-Arg NPs and their application for targeted RT of osteosarcoma. Reproduced with permission from ref. 97. Copyright 2020, Elsevier.

modification of HA, HA@MOF/D-Arg plus 8 Gy of X-ray irradiation could efficiently target tumors and completely eradicate the tumor compared to the tumor volume of about 400 mm^3 in the D-Arg + X-ray group 20 days after treatment. Furthermore, the co-modification of two targeting ligands can further improve the receptor-mediated endocytosis efficiency. For instance, Askar *et al.* prepared a HA and FA dual ligand-modified radiosensitizer (2DG@DCA@MgO, DDM) that contained a magnesium oxide (MgO) core and a 2-deoxyglucose (2DG) shell linked to a dichloroacetate (DCA) layer.[98] The HA and FA dual-ligand modified DDM could bind with both CD44 and folate receptors overexpressed in breast cancer, allowing for selective tumor targeting/accumulation and effective RT/chemotherapy of breast cancer.

Tripeptide arginine–glycine–aspartic acid (RGD) is a structural recognition motif for $\alpha_v\beta_3$ and $\alpha_v\beta_5$ integrins overexpressed on cancer cells.[99] The radiosensitizers or radionuclides conjugated with the RGD peptide can specifically recognize the cancer cells that express integrins and then efficiently accumulate in the tumors for precision RT.[81,100–103] For example, Chen's group coordinated iridium (Ir) complex on the surface of black phosphorus (BP) nanosheets to construct a powerful nanosystem (Ir@BP) for RT of nasopharyngeal carcinoma.[104] In this design, Ir complex was able to improve the photoelectric properties, such as photoinduced carrier dynamic and photocurrent responses, allowing BP to produce more $^1O_2$ upon X-ray excitation. Then, the targeting RGD peptide was successfully decorated onto the Ir complex in the Ir@BP nanosystem, which was confirmed by the ^{1}HNMR spectrum. The western blot result showed that integrins were highly expressed on CNE-2 cancer cells, one type of human nasopharyngeal carcinoma cells. After RGD decoration, the *in vitro* endocytosis of RGD-Ir@BP in CNE-2 cells was increased from 4.92 μg/10^6 cells to 12.76 μg/10^6 cells. Due to high cell uptake, RGD-Ir@BP could significantly inhibit tumor growth and result in the tumor volume of 50 mm^3 30 days after treatment compared to 450 mm^3 in the untargeted group (BP + X-ray). In addition to the above-mentioned commonly used biological ligands, other ligands, such as prostate specific membrane antigen,[105] transferrin,[27] chimeric L6 monoclonal antibody,[106] epidermal growth factor,[107] and low-density lipoprotein receptor-related protein-1-targeting peptide,[108] have been also used to modify radiosensitizers and radionuclides for tumor-targeted precision RT.

2.2.2 Bioorthogonal ligand-based targeting. Although biological ligand-mediated active targeting strategy can improve tumor accumulation of nanomedicines, the targeting efficiency is often limited by the heterogenous distribution of targeted receptors on cancer cell membranes, which may lead to poor therapeutic efficacy.[109–111] Bertozzi and colleagues proposed the concept of bioorthogonal chemistry in 2003,[112] and since then many researchers have been exploring the potential applications of bioorthogonal chemistry in the field of cancer theranostics.[113–119] For example, the bioorthogonal chemistry can be combined with metabolic glycoengineering for tumor targeting in a two-step strategy. First, some functional group-modified sugars, such as azide-sugar, were labeled onto the cell membranes as artificial receptors *via* metabolic glycoengineering, and then followed by a bioorthogonal click reaction between the artificial receptors and complementary groups as the corresponding ligands labeled onto the theranostic agents.[120–122]

The bioorthogonal click reaction has also been applied to engineer radiosensitizers for precision RT. For example, Liu *et al.* designed a coordination polymer NP (Hf–AIE–PEG) composed of hafnium tetrachloride ($HfCl_4$) and 2,2′-(((2-(4′-(2,2-dicyano-1-phenylvinyl)-[1,1′-biphenyl]-4-yl)-2-phenylethene-1,1-diyl)bis(4,1-phenylene))bis(oxy)) diacetic acid (TPEDC-DAC, a photosensitizer with aggregation-induced emission (AIE)) for radio- and radiodynamic therapy (RT-RDT) (Fig. 4a).[53] Hf^{4+} could not only deposit X-ray energy as a high-*Z* element to increase $^{\bullet}$OH generation but also convert X-ray radiation into light for activating TPEDC-DAC to produce $^1O_2$ for RDT. Moreover, bioorthogonal click reaction was applied for improving tumor targeting and accumulation of NPs. Briefly, *N*-azidoacetylmannosamine-tetraacylated (Ac_4ManNAz), an azido-containing metabolic glycoprotein labeling reagent, was first used to label azide groups onto the cell membranes. Next, NPs (Hf–AIE–PEG–DBCO) decorated with dibenzocyclooctyne (DBCO, a bioorthogonal ligand) were added for bioorthogonal click reaction with the azide groups on membranes (Fig. 4b). *In vitro* confocal fluorescence images revealed that the fluorescence of Hf–AIE–PEG–DBCO was obviously observed at 1 h after incubation with 4T1 cells prelabeled with Ac_4ManNAz. Moreover, the fluorescence of Hf–AIE–PEG–DBCO was co-localized with the red fluorescence of the membrane tracker, indicating that Hf–AIE–PEG–DBCO was labeled on the cancer cell membrane *via* the bioorthogonal click reaction with azide groups (Fig. 4c). However, 1 h of incubation was too short for Hf–AIE–PEG to be uptaken by cells, leading to weaker fluorescence in cells. Then, the *in vivo* targeting efficiency of Hf–AIE–PEG–DBCO was evaluated using a bilateral tumor-bearing mouse model (Fig. 4d). The bilateral tumors were intratumorally pretreated with Ac_4ManNAz and PBS for 3 days, which were denoted T2 and T1, respectively. Biodistribution analyses through measuring the concentration of Hf ions revealed that the accumulation of Hf–AIE–PEG–DBCO in T2 tumor was 1.83- and 3.17-fold higher than that in T1 tumor at 1 and 3 days post-injection, respectively (Fig. 4e). These results indicated that the tumor accumulation and retention were remarkably enhanced through bioorthogonal click reaction. Finally, with the help of bioorthogonal ligand-mediated targeting, the tumor volume in the Hf–AIE–PEG–DBCO + Ac_4ManNAz + X-ray (8 Gy) group was effectively inhibited and smaller than the initial volume (Fig. 4f). However, the Hf–AIE–PEG + X-ray (8 Gy) group without the bioorthogonal click reaction showed more than 2-fold increase in the relative tumor volume after treatment. Furthermore, the bioorthogonal click reaction has also been applied for radioimmunotherapy, a selective internal RT based on radiolabeled antibodies.[123–126] Overall, the bioorthogonal click reaction could be a promising targeting strategy for precision RT owing to its highly specific recognition.

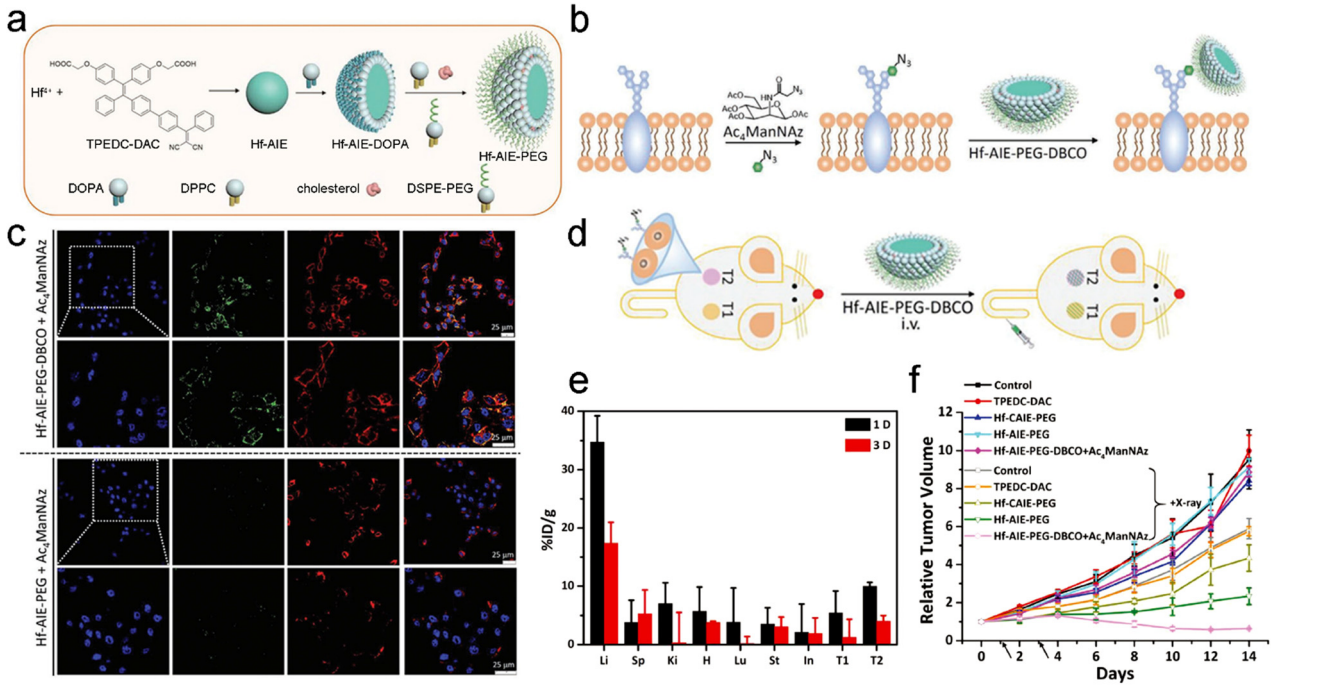

Fig. 4 Bioorthogonal ligand-based targeting strategies for precision RT. (a) A scheme of the synthesis process of Hf–AIE–PEG NPs. (b) Schematic illustration of azide expression on tumor cell membrane glycan, and bioorthogonal labeling of Hf–AIE–PEG–DBCO. (c) Fluorescence images of Ac4ManNAz pre-cultured 4T1 cells after Hf–AIE–PEG and Hf–AIE–PEG–DBCO bioorthogonal labeling for 1 h and CellMask Deep Red treatment. (d) Schematic illustration of the experimental process for bioorthogonal design on mouse. T1: tumors without Ac4ManNAz pretreatment. T2: tumors with Ac4ManNAz pretreatment. (e) Biodistribution of Hf–AIE–PEG–DBCO in tumor bearing mice at 1 and 3 days after intravenous administration. (f) Tumor growth curves of mice in different treatment groups. Black arrows indicate radiation time points. Reproduced with permission from ref. 53. Copyright 2021, Wiley.

2.3 Cell or cell membrane-mediated targeting

The synthetic nanomaterials, whether organic or inorganic, have been found to be more or less immunogenic or toxic after intravenous administration. Recent studies have explored the possibility of utilizing natural cells or cell membrane-based vesicles for the delivery of radiosensitizers, including cell membrane camouflaged NPs, exosomes, and whole cells. These vesicles with the natural membrane structure can be regarded as the "self" and exhibit excellent biocompatibility, longer blood circulation, and rich tumor accumulation. Moreover, several types of cells or cell membranes possess inherent homotypic binding ability, allowing particles or drugs to homologously target tumors. In this section, the natural cell or cell membrane-mediated targeting strategies for radiosensitizer delivery will be introduced (Table 1).

2.3.1 Cell membrane camouflage-mediated tumor targeting. Cell membrane camouflage, proposed by the Zhang's group, has attracted wide attention and has been gradually developed into a novel strategy for designing biomimetic nanomedicines.[127–129] To date, the membranes of cancer cells,[30,130–133] erythrocytes,[29,134,135] platelets,[136,137] mesenchymal stem cells,[138] and even *E. coli*[139–141] have been successfully used for the preparation of biomimetic radiosensitizing nanomedicines.

Cancer cell membrane camouflage endows biomimetic nanomedicines with homologous adhesion, immune escaping, and deep tumor penetration abilities.[142] For example, Pan *et al.* constructed glucose oxidase (GOx)-loaded TiO_2@MnO_2 core–shell nanoreactors that were further coated with B16-F10 cancer cell membrane (TiO_2@MnO_2-GOx@C) *via* a co-extrusion approach for homologous targeting and enhanced RT (Fig. 5a).[54] The GOx in these nanoreactors could catalyze the oxidization of glucose in cancer cells to produce gluconic acid and H_2O_2. Then, the MnO_2 shell could catalyze the decomposition of H_2O_2 into O_2. Moreover, the high-Z element of TiO_2 and O_2 generation could contribute to radiosensitization. The cancer cell membrane camouflage was able to improve homologous targeting abilities of TiO_2@MnO_2-GOx@C nanoreactors. *In vivo* biodistribution showed that the Mn element in tumors at 24 h post-injection of TiO_2@MnO_2-GOx@C was 4.5-fold higher than that in tumor treated with TiO_2@MnO_2-GOx, suggesting the great targeting capability of the biomimetic nanoreactors (Fig. 5b). Next, X-ray irradiation at a dose of 4 Gy was imposed at 24 h after injection. The lung metastases of melanoma (B16-F10) were completely eliminated 14 days after treatment with TiO_2@MnO_2-GOx@C plus X-ray; however, the metastatic tumors in other groups were still observed. In addition, no mice in the TiO_2@MnO_2-GOx@C plus X-ray group died even after 40 days, whereas the mice in the other groups all died within 28 days (Fig. 5c).

Membranes of erythrocytes have also been used to camouflage radiosensitizers for prolonged blood circulation.[143] For

Table 1 Biomimetic targeting strategies for precision RT

Targeting strategy	Nanoparticles	Cell/membrane type	Coating or loading method	Functions	Ref.
Cell membrane camouflage-based tumor targeting	TiO_2@MnO_2-GOx@C	B16-F10 cancer cell membrane	Co-stirring at a low temperatures	Homologous targeting	54
	GNR@Mem	Oral squamous KB cancer cell membrane	Co-extruding	Homologous targeting, improving blood circulation	131
	CQM	4T1 cancer cell membrane	NA	Homologous targeting	133
	CMC	4T1 cancer cell membrane	Co-extruding	Homologous targeting, improving blood circulation	130
	Au@MC38	MC38 cancer cell membrane	Biosynthesis	Homologous targeting	30
	TDSP-Exos	CT26 cancer cell exosome	Exocytosis	Homologous targeting, immune escaping	151
	PFC@PLGA-RBCM	Red blood cell membrane	Co-stirring at 4 °C	Improving blood circulation	29
	F-RBC bismuth NPs	Red blood cell membrane	Co-extruding	Improving blood circulation	135
	CM-EM-GNCs@DOX	Membrane from MCF-7 cancer cell and red blood cell	Co-extruding	Homologous targeting, immune escaping, improving blood circulation	134
	PLT/CANS	Platelet membrane	Co-extruding	Target anomalous vessels in tumors, immune escaping	137
	BMSNR@PM	Platelet membrane	Sonicating	Tumor targeting, immune escaping	136
	Cyp-PMAA-Fe@MSCs	Mesenchymal stem cell membrane	Sonicating	Immune escaping, improving blood circulation	138
Carrier cell-based tumor targeting	Au-Hb@PLT	Platelet carrier	Sonicating	Tumor targeting	150
	Endo@GOx-ER	Erythrocyte carrier	Hypotonic dialysis	Improving blood circulation	37

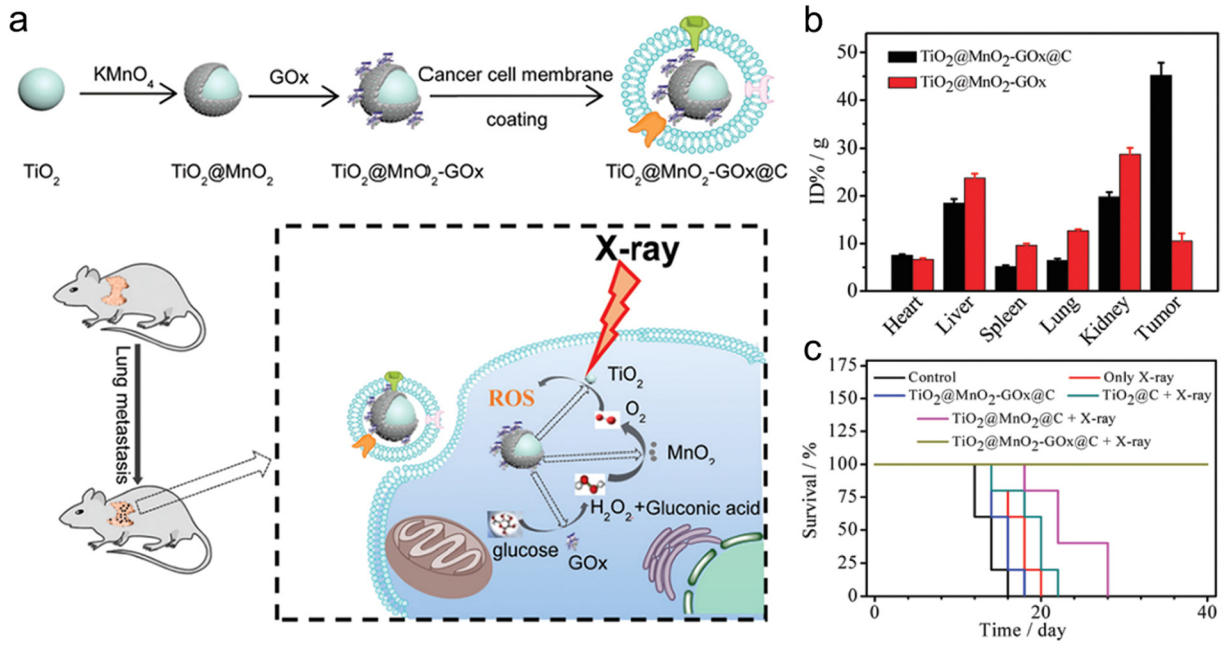

Fig. 5 Cell membrane camouflage-based tumor targeting. (a) A scheme of synthesis process of TiO_2@MnO_2-GOx@C and its application in the RT of cancer metastasis. (b) Biodistribution of Mn in major organs and tumors of mice after injection of TiO_2@MnO_2 or TiO_2@MnO_2-GOx@C NPs. (c) Survival curves of melanoma-bearing mice in different treatment groups. Reproduced with permission from ref. 54. Copyright 2020, Royal Society of Chemistry.

example, Liu's group coated red blood cell (RBC) membrane on perfluorocarbon (PFC)-loaded PLGA (PFC@PLGA-RBCM) to prepare an artificial RBC nanosystem for hypoxia relief-enhanced RT. Interestingly, PFC@PLGA-RBCM exhibited a much longer blood circulation half-life of 13.93 h compared to naked PFC@PLGA. However, the RBC membrane camouflage alone can only prolong circulation half-life while the tumor accumulation of NPs still relies on passive targeting. It is worth noting that fusion of multiple cell membrane types can integrate their respective strengths. For instance, Sun *et al.* utilized fusion membrane from both MCF-7 cancer cells and erythrocytes to coat DOX-loaded gold nanocages (CM-EM-GNCs@DOX) for PTT/RT/chemotherapy of breast cancer.[134] Due to the hybrid membrane coating, the nanocages possessed

both homologous targeting and improved immune-escape abilities. Thus, the *in vitro* cell uptake of CM-GNCs and CM-EM-GNCs in MCF-7 cells was about 3.9- and 4.1-fold higher than those in MCF 10A cells, respectively, owing to the cancer cell membrane-mediated targeting ability. Besides, due to the erythrocyte membrane-mediated immune-escape ability, the *in vitro* macrophage uptake of both EM-GNCs and CM-EM-GNCs was significantly lower than that in the CM-GNC group. Finally, effective RT-based combination treatment significantly suppressed the breast cancer growth *in vivo*. Similar to RBCs, bone marrow mesenchymal stem cells (MSCs) with low immunogenicity have also been utilized to camouflage NPs for prolonging the blood circulation time and evading immune surveillance. For example, Yin *et al.* decorated Fe(III) ions and cypate co-loaded polymethacrylic acid (PMAA) NPs with the MSC membrane to prepare Cyp-PMAA-Fe@MSCs for RT/PTT of lung cancer.[138]

Furthermore, platelet (PLT) membrane camouflage is another strategy for preparing biomimetic radiosensitizers. For example, Lyu *et al.* fabricated core–shell Au@AuPd nanospheres and then coated the nanospheres with the PLT membrane (PLT/CANS) for brachytherapy (BT) of colon cancer.[137] The PLT membrane camouflage enables these NPs to enhance immune evasion and actively target anomalous vessels in tumors, leading to rich tumor accumulation of PLT/CANS. Palladium (Pd)-based NPs could catalyze the decomposition of H_2O_2 into O_2 to alleviate hypoxic TME for radiosensitization. Moreover, high-*Z* element-based X-ray deposition could also sensitize BT. The CANS NPs coated with the RBC membrane (RBC/CANS) were regarded as the control group. The *in vivo* circulation profiles of these NPs revealed that both PLT/CANS and RBC/CANS NPs could prolong the blood circulation time compared to naked CANS. Moreover, with the PLT membrane decoration, PLT/CANS could actively target tumor and show a 1.9-fold richer tumor accumulation than that in RBC/CANS group at 24 h post-injection, which was confirmed by ICP-AES and *in vivo* FL imaging. Finally, the survival of colon tumor-bearing mice in the PLT/CANS + BT group was 100% at 30 days after treatment compared to 20% and 40% of BT and RBC/CANS + BT groups, respectively. In summary, the cell membrane camouflage as a promising tumor-targeting strategy can endow radiosensitizers with diverse excellent biological capabilities for precision RT of cancer.

2.3.2 Carrier cell-mediated tumor targeting. Recently, carrier cells, such as leukocytes, platelets and erythrocytes, have been widely used as innate carriers for drug delivery due to their large loading capacity, high biocompatibility and prolonged blood circulation.[144–149] For example, Xia *et al.* developed a specific type of platelet containing Au-hemoglobin (Hb) complex NPs (Au-Hb@PLT) for alleviating tumor hypoxia and sensitizing RT (Fig. 6a).[150] First, the Au NPs were coated with Hb to prepare Au-Hb NPs, which were then entrapped within the PLTs through intermolecular disulfide conjugations. SEM and TEM images of Au-Hb@PLT confirmed the distribution of Au-Hb NPs inside Au-Hb@PLT. Next, Au-Hb@PLT could specifically target cancer cells due to the specific binding between the P-selectin on the PLT membrane and the overexpressed CD44 receptors on the cancer cell surface. After targeting, the Au-Hb@PLT could release Au-Hb NPs that further penetrated into deep tumor tissues. *In vivo* FL imaging showed that strong FL signal of Au-Hb@PLT in tumor sites could be observed at 1 h and 2 h post-injection, whereas there was no FL signal of Au-Hb NPs in the tumor. Richer tumor accumulation led to higher RT efficacy at the same dose of X-ray radiation. Thus, the tumor inhibition rate in mice treated with Au-Hb@PLT plus RT (2 Gy) was similar to that in mice treated with RT (8 Gy) alone.

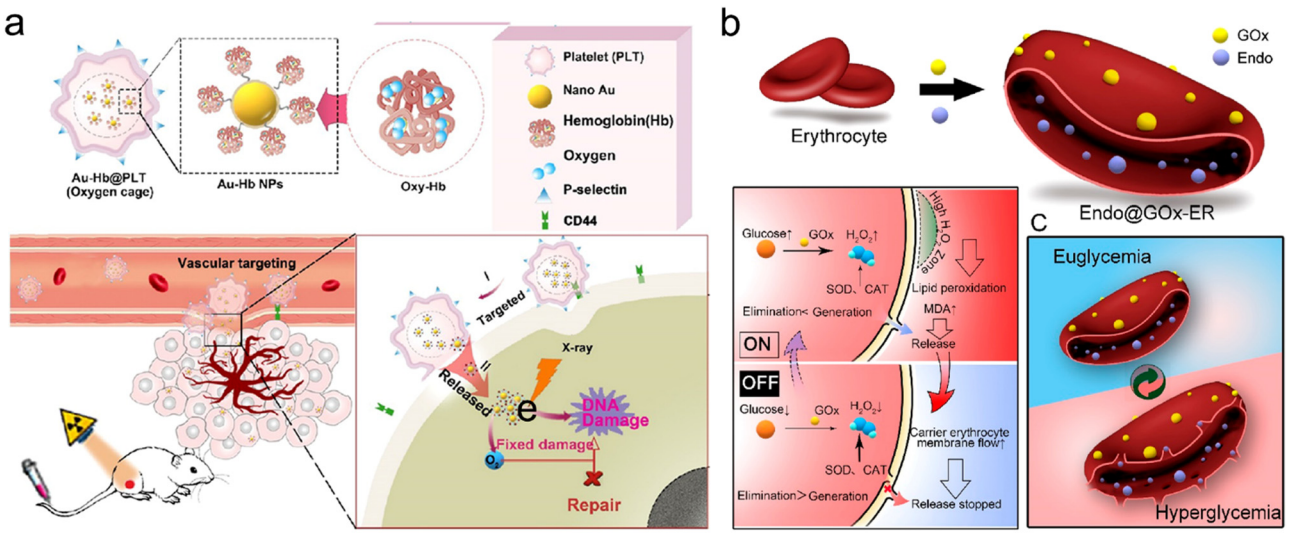

Fig. 6 Carrier cell-based tumor targeting. (a) Schematic illustration of synthetic procedures of Au-Hb@PLT and its applications in targeting tumor vessel and enhancing RT. Reproduced with permission from ref. 150. Copyright 2020, American Chemical Society. (b) Schematic illustration showing synthetic procedures of Endo@GOx-ER and closed loop glucose-regulated release of Endo from Endo@GOx-ER. Endo is stored in the ER under euglycemic conditions, whereas it is released during hyperglycemia. Reproduced with permission from ref. 37. Copyright 2020, American Chemical Society.

Furthermore, Huang *et al.* developed endostar (Endo)-loaded GOx-modified erythrocytes (Endo@GOx-ER) for glucose-regulated drug release.[37] The erythrocyte (ER) was chosen as a carrier for the delivery of Endo, an inhibitor of angiogenesis which could normalize tumor vasculature for overcoming tumor hypoxia. The TEM and confocal images showed that Endo@GOx-ER maintained normal size and shape. In this nanosystem, the release rate could be controlled by the blood glucose level (BGL). The Endo@GOx-ER could function as a physiological ER (off-state) under normoglycemia where the Endo was kept inside, reducing immune clearance. However, during hyperglycemia, GOx could effectively catalyze the decomposition of glucose to generate H_2O_2 for promoting ER membrane perforation, allowing Endo release (on-state) (Fig. 6b). In addition, naked Endo could be cleared from the body at 10 h post intravenous injection, but the Endo@GOx-ER significantly prolonged the serum circulation time of Endo to over 24 h. Overall, the Endo@GOx-ER could result in the normalization of tumor vessel and long-term alleviation of TME hypoxia, which could potentiate repeated RT. The PA imaging of 4T1 tumor-bearing mice displayed that the oxygenation levels were significantly increased even at 6 and 12 days after intravenous injection of Endo@GOx-ER, much higher than those in mice treated with free Endo. With the strategy of overcoming long-term tumor hypoxia, the survival of tumor-bearing mice in the Endo@GOx-ER + RT group was 90% at 45 days after treatment, whereas all the mice in the PBS + RT group died by day 40.

2.4 Magnetic targeting

Magnetic targeting is a promising targeting strategy based on drug-loaded magnetic materials under an external magnetic field (MF).[152,153] The magnetic field could guide the magnetic materials to the target tumors or organs where the materials could release drug, nuclear acid, or bioactive molecules for cancer therapy.[154] This strategy is able to largely avoid unwanted distribution of drugs in normal organs and thus remarkably lower side effects. For example, Lyu *et al.* prepared core–shell nanozymes, Fe_3O_4@MnO_2, for magnetic targeting and RT.[31] The Fe_3O_4@MnO_2 NPs were used in combination with GOx for enhanced RT. In this design, GOx could catalyze the oxidation of intratumoral glucose to generate H_2O_2 which then reacted with the MnO_2 shell to produce O_2 for alleviating tumor hypoxia. Meanwhile, the MnO_2 shell could also deplete the overexpressed GSH to generate Mn^{2+} for T_1-weighted MRI. Besides, the GSH depletion could greatly enhance RT efficacy by reducing ROS consumption. Importantly, the Fe_3O_4 core could be utilized for magnetic targeting and T_2-weighted MRI. As a result, the brighter or darker signals in the tumor regions of T_1- or T_2-weighted MR images were observed at 6 h after intravenous administration of Fe_3O_4@MnO_2 NPs under the assistance of MF, indicating successful tumor accumulation of Fe_3O_4@MnO_2 NPs. However, in the absence of MF, only a slight contrast change in the tumor site was observed after intravenous administration of Fe_3O_4@MnO_2 NPs. With the MF-mediated targeting, the average tumor volume in the Fe_3O_4@MnO_2 NPs + GOx + RT + MF group was remarkably suppressed and smaller than the initial volume at 18 days after treatment, whereas the average tumor volume of mice more than tripled in the Fe_3O_4@MnO_2 NPs + RT group. Besides, the magnetic targeting strategy has also been applied in radioisotope therapy.[155–159]

2.5 Subcellular organelle targeting

Subcellular organelles (*e.g.*, mitochondria, nucleus, endoplasmic reticulum, lysosome, *etc.*) play an important role in maintaining normal cellular physiological processes.[160] In recent years, a lot of radiosensitizers that specifically target various subcellular organelles have been explored. Selective delivery of radiosensitizers to subcellular organelles is able to induce cell death through different signaling pathways, reduce radioresistance of tumors and significantly enhance the RT efficacy.

2.5.1 Nucleus targeting. The nucleus contains lots of genetic materials which control the life activity of cells, including cell proliferation, differentiation, growth, and apoptosis. As we know, cancer cells are completely killed only when the DNA is seriously damaged. X-ray irradiation is able to break down the DNA of cancer cells. Nevertheless, most radiosensitizers are only delivered into the cytoplasm of cancer cells, and only a few radiosensitizers are able to passively diffuse into the nucleus, thus leading to poor RT efficacy. As such, the nucleus-targeted delivery of radiosensitizers is a promising strategy to substantially enhance the RT efficacy.

The type 1 human immunodeficiency virus (HIV-1) transactivator of transcription protein (TAT) has been evidenced to function as a nucleus-targeting molecule.[161] Shi and Bu proposed a novel ''intranuclear biophotonics'' strategy by the smart design of silicon phthalocyanine dihydroxide (SPCD) and PpIX co-loaded upconversion NPs modified with PEG and a nuclear targeting peptide TAT (UCSPs-PEG/TAT) (Fig. 7a).[55] Based on the fluorescence resonance energy transfer (FRET), the UCNP core was able to convert NIR light into visible light which further activated both two photosensitizers (SPCD and PpIX) to produce singlet oxygen ($^1O_2$). Moreover, PpIX could act as a radiosensitizer to convert water into superoxide radicals (O_2^-) and $^{\bullet}OH$ upon X-ray radiation. High-resolution and 2D/3D CLSM images revealed that UCSPs-PEG/TAT (green and red luminescence emitted by the UCNP core) could co-localize with the nucleus stained with DAPI (blue) while UCSP-PEG without the conjugation of TAT could not enter the nucleus (Fig. 7b). Due to nucleus-targeting ability, the generated ROS from PDT and RT was able to remarkably induce DNA breakage and further trigger substantial cell death. Therefore, the nuclear-targeting synergistic RT/PDT strategy (UCSPs-PEG/TAT + NIR + X-ray) decreased the relative tumor volume to around 0.5 compared to over 3.5 in the RT alone group.

Furthermore, several studies proposed a dual-targeting strategy in which cancer cell-targeting moieties and TAT were co-used to modify radiosensitizers for enhanced tumor cell nucleus-targeting RT.[162–164] For example, Pan *et al.* loaded 7-ethyl-10-hydroxy-camptothecin (SN-38) into mesoporous TiO_2 NPs ($MTiO_2$(SN-38) NPs). The NPs were then anchored with TAT

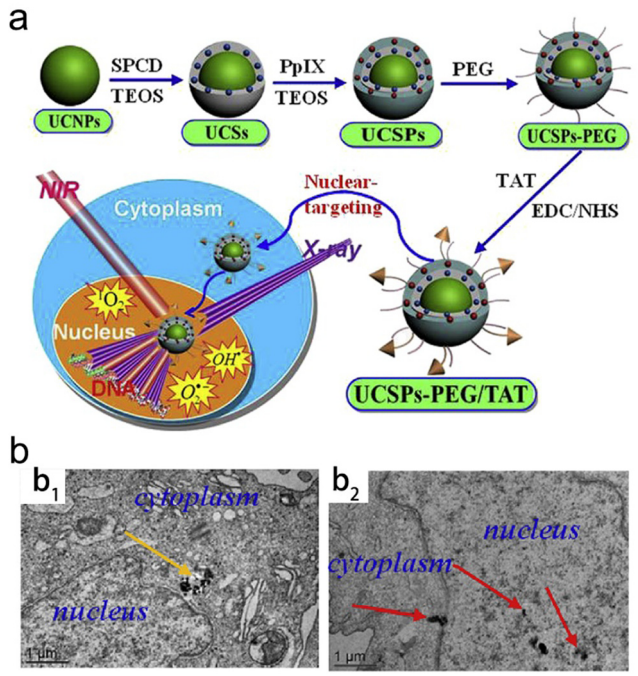

Fig. 7 Nuclear-targeting. (a) A scheme of synthetic process of UCSPs-PEG/TAT and its application in nuclear-targeted RT/PDT of tumors. (b) Bio-TEM images of HT-1080 cells at 24 h after treatment with UCSPs-PEG (b1) and UCSPs-PEG/TAT (b2). Reproduced with permission from ref. 55. Copyright 2015, Elsevier.

and RGD peptide ($MTiO_2$(SN-38)-TAT-RGD NPs) for nucleus-targeted RT.[164] The RGD peptide allowed the $MTiO_2$(SN-38)-TAT-RGD NPs to bind with the $\alpha_v\beta_3$ integrin overexpressed in several types of cancer cells. Next, the $MTiO_2$(SN-38)-TAT-RGD NPs could further target the nucleus of cancer cells thanks to the decoration of TAT. SN-38 could selectively target topoisomerase I in the nucleus and control the cell cycle of 4T1-Luc cells in the radiosensitive G2/M phase. The *in vivo* anticancer experiments revealed that the average tumor volume in the $MTiO_2$(SN-38)-TAT-RGD + X-ray group 21 days after treatment was about half of that in the $MTiO_2$(SN-38)-TAT + X-ray or $MTiO_2$(SN-38)-RGD + X-ray group. Overall, this strategy of cancer cell nucleus-targeted delivery of radiosensitizers is able to remarkably enhance the RT efficacy and reduce the side effect by lowering X-ray irradiation doses and reducing the irradiation time.

2.5.2 Mitochondria targeting. Mitochondria play a crucial role in cellular metabolism, programmed cell death, and endogenous ROS production. The imbalance of ROS potentially causes mitochondria dysfunction, leading to cell apoptosis. The ROS generated from radiosensitizers in the mitochondria can much more easily trigger cancer cell death. Therefore, mitochondria-targeting radiosensitizers show great promise in the RT of cancer.

Triphenylphosphonium (TPP), a moiety able to selectively target the inner mitochondrial membrane owing to its excellent cationic and lipophilic properties, has been widely used to engineer NPs for mitochondria-targeted delivery.[165–169] For example, Tang and colleagues modified Gd-doped titanium dioxide NPs (TiO_2(Gd) NPs) with TPP to construct a mitochondria-targeting radiosensitizer.[170] The confocal images revealed that IR806-labeled TiO_2(Gd)-TPP NPs could effectively target the mitochondria and co-localize with Mito-Tracker Green stained mitochondria of MCF-7 cells compared to TiO_2(Gd) NPs. Moreover, TiO_2(Gd)-TPP NPs were able to generate a great deal of ROS upon X-ray irradiation, resulting in mitochondrial collapse and irreversible cell apoptosis. Moreover, antitumor evaluation revealed that TiO_2(Gd)-TPP NPs plus X-ray irradiation (6 Gy) completely eliminated MCF-7 xenograft tumors at 14 days post-treatment; however, the tumor volume was still over 30 mm^3 after treatment with TiO_2(Gd) plus X-ray. Besides, other mitochondria-targeting moieties have also been used to modify radiosensitizers. For instance, Fang *et al.* fabricated peptide-templated Au nanoclusters (AuNCs) for mitochondria-targeting radiosensitization.[56] Briefly, they synthesized a new peptide (CCYKFR) containing two domains Cys–Cys–Tyr (CCY) and Dmt–D-Arg–Phe–Lys–NH2 (KFR) for peptide-templated AuNC synthesis. In the new peptide, the CCY peptide segment could reduce the Au ions into nanoclusters by the phenolic group of Tyr (Y) as well as stabilize these nanoclusters through the sulfhydryl groups of Cys (C). Moreover, the KFR peptide segment could function as a mitochondria-targeting moiety, which has been reported in other studies.[171]

Recently, cationic ruthenium (Ru)-based complexes have shown mitochondria-targeting capability without coupling exogenous targeting molecules like TPP.[172,173] On the basis of Ru, Lin's group designed a mitochondria-targeted nanoscale metal–organic framework (nMOF) for radiotherapy-radiodynamic therapy (RT-RDT).[174] They conformed $Ru(bpy)_3^{2+}$ into the nMOF to synthesize Hf-DBB-Ru [DBB-Ru = bis(2,2′-bipyridine)(5,5′-di(4-benzoato)-2,2′-bipyridine)ruthenium(II) chloride] with excellent mitochondria-targeting ability. Hf_6SBUs could effectively deposit X-ray energy to produce H_2O_2 for enhanced RT and transfer energy to $Ru(bpy)_3^{2+}$-based bridging ligands to produce $^1O_2$ for RDT. Owing to the presence of cationic $[DBB\text{-}Ru]^{2+}$, Hf-DBB-Ru displayed a strong positive potential (38.9 ± 3.1 mV). The mitochondria uptake of positively charged Hf-DBB-Ru and neutral nMOF (Hf-DBA) was evaluated. The mitochondria of MC38 cells incubated with Hf-DBB-Ru or Hf-DBA were extracted for quantitative analyses *via* ICP-MS. The result showed that Hf-DBB-Ru rapidly accumulated in the mitochondria and reached the maximum (more than 90%) at 4 h post-incubation. However, only 18% of Hf-DBA was internalized into the mitochondria at 4 h post-incubation. The *in vivo* antitumor evaluation demonstrated that the treatment/control (T/C) ratios in MC38 tumor-bearing mice treated with Hf-DBB-Ru plus X-ray (6 Gy) irradiation was 3.0% at day 22 after treatment, much lower than 42.1% of the Hf-DBA + X-ray groups.

2.5.3 Endoplasmic reticulum targeting. The endoplasmic reticulum (ER) plays a crucial role in Ca^{2+} storage, glycosylation, synthesis of lipids and several functional proteins, as well as transportation of freshly prepared membrane and secreted

proteins.[175] Many studies have reported that perturbation of these processes may result in ER stress and cell apoptosis.[176] X-ray irradiation causes the accumulation of misfolded and unfolded proteins in the ER to trigger ER stress and activate unfolded protein response (UPR), leading to cell death involving autophagy and apoptosis.[177,178]

Several studies have reported the use of increased ER stress to sensitize cancer cells to RT. For example, tunicamycin (TM) was utilized to trigger ER stress in human esophageal cancer cell line EC109.[179] The combination treatment of TM and RT effectively arrested the G2/M phase and induced cancer cell apoptosis. The *in vitro* and *in vivo* experiment results showed that TM could significantly sensitize cancer cells to RT *via* apoptosis and autophagy. Besides, ER-targeting radiosensitizers have also been designed for enhanced RT. Klein *et al.* proposed that ultrasmall aminosilanized oxidized silicon NPs (NH_2-SiNPs) with positive potential could accumulate in the membranes of ER and mitochondria of 3T3 cells.[180] Moreover, NH_2-SiNPs and SiNPs could serve as radiosensitizers. Due to ER targeting, the ROS concentrations of 3T3 and MCF-7 cells incubated with NH_2-SiNPs could increase to 120% and 180% after X-ray irradiation, whereas X-ray irradiation showed almost no impact on the ROS level of3T3 and MCF-7 cells incubated with SiNPs.

In addition, ER targeting is also a promising strategy to amplify the effects of ICD. Chen *et al.* loaded an ER-targeting photosensitizer TCPP-T^{ER} (4,4′,4″,4‴-(porphyrin-5,10,15,20-tetrayl)tetrakis(*N*-(2-(methylphenyl)sulfonamido)-ethyl) benzamide) into GSH-responsive Ds-sP (PEG-*s*-*s*-1,2-distearoyl-*sn*-glycero-3-phosphoethanolamine-*N*-[amino-(polyethylene glycol)-2000]) NPs for ER-targeting PDT which was able to effectively induce ER stress and amplify ICD, resulting in enhanced cancer immunotherapy efficacy.[181]

2.5.4 Lysosome targeting. Lysosome, known as a digestive organelle, consists of acid lumen and a lysosomal membrane constructed by the phospholipid layer, and plays an important role in degradation, nutrient sensing, and immunity.[182] Lysosome as a regulator of cellular homeostasis has been shown to be involved in several important biological processes.[183] Recently, a growing number of studies have implicated that lysosomes exhibit resistance to RT and are regarded as a potential target for radiosensitization.[184] First, the cysteine cathepsin proteases that promote the radioresistance of cancer cells are deposited in lysosomes. Second, autophagy triggered by X-ray irradiation is a lysosome-dependent degradation and cell survival process. Third, the mammalian target of rapamycin (mTOR), a crucial regulator of autophagy, has been reported to be activated by lysosomes. Hence, lysosomes play a vital role in regulating radioresistance, and lysosome targeting is a promising strategy for overcoming radioresistance and enabling precision RT.

For example, Simonet *et al.* fabricated a class of gadolinium-based NPs (GBNs), AGulX® (Activation and Guidance of Irradiation by X-ray), for the radiosensitization of head and neck squamous cell carcinoma (HNSCC).[185] Interestingly, the AGulX® preferred to accumulate into lysosomes rather than mitochondria or nucleus after the uptake by SQ20B J.L. cells. The cancer cells pre-treated with AGulX® could enhance RT efficacy, leading to severe damage of DNA and autophagic cell death. Likewise, other high-*Z* metallic NPs have also shown lysosome-targeting ability. Hullo *et al.* evaluated the radioenhancement effect of platinum NPs (PtNPs) in breast cancer cell lines.[186] They found that the PtNPs were able to accumulate in lysosomes and multivesicular bodies after internalization. The lysosome-localized PtNPs could deposit X-ray energy to effectively damage DNA and kill cancer cells. In another study, Lacombe and colleagues fabricated label-free GBNs for radiosensitization of U87 glioblastoma cells.[187] The bio-TEM and CLSM images found that GBNs were internalized into the cells and then accumulated in the lysosomes rather than nucleus or mitochondria. In addition, clonogenic assay measurements revealed that the incubation of GBNs (0.5 mM) could significantly improve irradiation-induced cell killing effects with 23% of enhancing factor. The RT enhancement based on lysosome-targeting radiosensitizers was attributed to radiation-induced lysosomal perturbations (*e.g.*, lysosomal overload, phospholipidosis, *etc.*) that further induced autophagy.

3. Exo/endogenous stimuli-responsive strategies for precision radiotherapy

Endogenous stimuli (*e.g.*, pH, GSH, H_2O_2, hypoxia, enzyme, *etc.*) and/or exogenous stimuli (*e.g.*, X-ray, NIR irradiation, ultrasound, *etc.*) can cause size or shape change, chemical degradation, surface property change, and heating up of responsive NPs, resulting in enhanced tumor accumulation/penetration and controllable drug release. This section will discuss exo/endogenous stimuli-responsive strategies for precision RT, including exogenous stimuli, endogenous stimuli in the tumor microenvironment, and a combination of these stimuli (Table 2).

3.1 Endogenous stimuli-responsive strategies

Endogenous stimuli, such as pH, GSH, H_2O_2, hypoxia, enzyme, *etc.*, have gradually become tumor-specific biotargets to trigger drug release, size/shape transformation, chemical degradation, or surface chemical/physical property change, which may contribute to enhanced tumor accumulation/penetration of radiosensitizers for precision RT.

3.1.1 pH responsiveness. Typical ranges of pH are 7.0–7.5 in normal tissues/blood and 6.5–6.9 in extracellular environment of solid tumors.[188,189] However, the pH value inside tumor cells, such as lysosome, is around 5.5.[190] The slight difference of pH values between tumor and healthy tissues has been utilized to design smart acidic pH-responsive radiosensitizers for precision RT. For example, acid-responsive radiosensitizers could degrade into smaller NPs under acidic conditions, thus enhancing tumor penetration and reducing systemic toxicity through rapid renal-clearance.[40]

Yuan's group constructed an intelligent targeting system on the basis of pH-responsive self-assembly and disassembly of

Table 2 Representative exo/endogenous stimuli-responsive strategies for precision RT

Stimuli	Nanoparticles	Responsiveness	Outcomes	Treatment	Sensitive part	Ref.
pH	Au-NNP(RTX)	Size transformation, drug release	Disassemble into ultrasmall AnNPs to enhance tumor penetration, enhance RTX delivery efficiency	Enhance RT and chemotherapy	*N*,*N*-Dibutylethylenediamine, 1-(2-aminoethyl) pyrrolidine	39
pH	Se@SiO_2@Bi NCs	Se NP release	Enhance tumor accumulation of Se NPs	Enhance RT and PTT, reduce side effect of radiation	Bi NPs	300
pH	Pt@HSA/CA NPs	Drug release	Enhance CA delivery efficiency	Enhance RT and chemotherapy	pH-responsive imine bond	193
pH	mTa_2O_5-PEG/DOX	Drug release	Enhance DOX delivery efficiency	Enhance RT and chemotherapy	Surface polymer	301
GSH	MNPs	Drug release	Enhance TPE-Pt and PPy delivery efficiency	Enhance RT and chemotherapy	RGD-POEGMA-*b*-PAZMB	201
GSH	Bi_2Se_3 HNC-s-s-HA/GA	Drug release	Enhance GA delivery efficiency	Enhance RT and PTT	S–S bond	202
GSH	GdW_{10}@CS_{siRNA} nanospheres	Gene delivery	GSH depletion, enhance gene delivery efficiency	Enhance RT and genetherapy	Polyoxometalates	302
ROS	ACF@MnO_2 NPs	O_2 generation, drug release	Hypoxia relief, enhance ACF delivery efficiency	Enhance RT and immunotherapy	MnO_2	216
ROS	Au@SA-QBA	Drug release	Enhance 8HQ delivery efficiency	Enhance RT	QBA	217
Enzyme	Au@Tat-R-EK	Tat peptide exposure	Enhance nuclear targeting of AuNPs	Enhance RT	Cathepsin B responsive peptide (CFLG)	227
Enzyme	Bac@BNP	Bi_2S_3 NPs release	Enhance tumor accumulation of Bi_2S_3 NPs	Enhance RT	MMP-2 responsive peptide (PLGVR)	228
Hypoxia	ALP-$(MIs)_n$/DOX	Drug release	Enhance DOX delivery efficiency	Enhance RT and chemotherapy	P-$(MIs)_n$	255
pH/GSH	PLGA-SS-D@BPQDs	Size expansion and surface-charge-switching (pH), BPQDs release (GSH)	Enhance tumor cell uptake, enhance tumor accumulation of BPQDs	Enhance RT	Amide linkages of DMMA (pH), S–S bond (GSH)	103
GSH/enzyme	Ce6-Leu@Mn^{2+}	Size transformation	Enhance tumor accumulation and penetration	Enhance RT and PDT	S–S bond (GSH), leucine motif (LAP)	257
GSH/hypoxia	HA-Fe-NIs-DOX	Drug and radiosensitizer release	Enhance DOX delivery efficiency, enhance radiosensitization	Enhance RT and chemotherapy	Ferrocenium ion (GSH), NIs (hypoxia)	256
X-ray	^{131}I-HSA	Upregulation of Caveolin-1	Improve the cancer cell uptake of ^{131}I-HSA NPs	Enhance RT	Cancer cells	264
X-ray	mPEG-*b*-P(LG-*co*-CELG)	Drug release	Enhance DOX delivery efficiency	Enhance RT and chemotherapy	Se–Se bond	277
Light	Ir@liposome	NIR light controllable catalases	Alleviate tumor hypoxia	Enhance RT	Ir nanocrystals	284
Light	CuS/^{131}I-PEGDA/AIPH	*In situ* gelation	Enhance tumor retention, reduce leakage to the surrounding blood or tissues	Enhance RT	AIPH	285
Light	dAuNP-FA	*In situ* crosslinking	Enhance tumor accumulation and retention	Enhance RT	DA group	303
Ultrasound	Nano-PFC	Oxygen release	Alleviate tumor hypoxia	Enhance RT	PFC	291
pH/light	Cs–Au–ICG	Size-transformation	Assemble into larger-sized aggregates (pH) for enhancing tumor accumulation, disassemble into ultrasmall AuNCs (light) for deep tumor penetration	Enhance RT and PTT	Surface charge (pH), AuNCs (light)	292
pH/ROS/light	M/H-D	Degrade to release ultrasmall HfO_2 NPs	Enhance HfO_2 delivery efficiency, enhance tumor accumulation and penetration	Enhance RT and PTT	MoS_2 nanosheets	293

AuNPs. In this system, the targeting ligands could be protected inside the assembled AuNPs at the physiological pH level (pH = 7.4), but exposed when the self-assembled AuNPs disassembled at the tumor extracellular pH level (pH = 6.8), which resulted in prolonged blood circulation, reduced RES clearance and enhanced tumor accumulation.[191,192] In another study by Yuan's group, they decorated small-sized AuNPs with PEG linked raltitrexed (RTX, chemotherapeutics and targeting ligand) and two small tertiary amine molecules (*N*,*N*-dibutylethylenediamine and 1-(2-aminoethyl) pyrrolidine denoted as NR_1 and NR_2) *via* lipoic acid (LA) to prepare self-assembled AuNPs (Au-NNP(RTX), Fig. 8a). The Au-NNP(RTX) was relatively stable with a large size of 160 nm at pH 7.4–7.0 but rapidly disassembled into ultrasmall AuNPs with a size of 6 nm under pH 6.8 conditions (Fig. 8b). After pH-responsive disassembly, the emerging ultrasmall AuNPs were able to penetrate into deeper tumor tissues. Simultaneously, the exposed RTX could target the FA receptor on the tumor cell surface and serve as a chemotherapeutic drug (Fig. 8c). Due to the excellent penetration and targeting abilities of small-sized

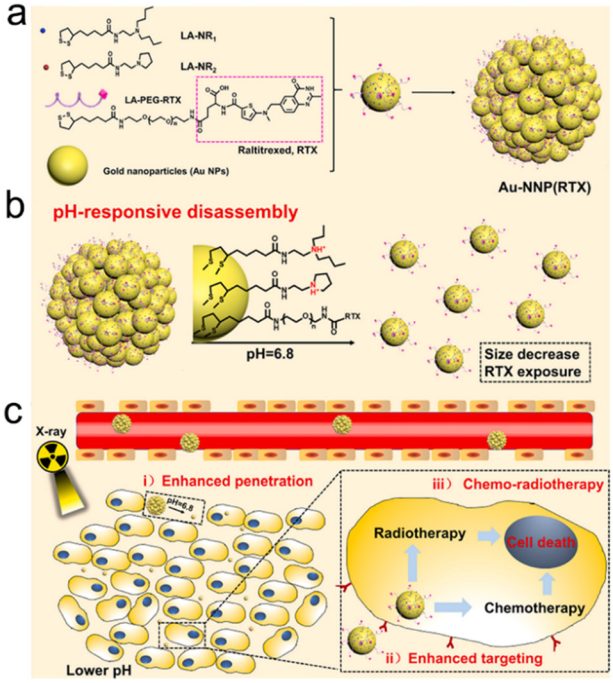

Fig. 8 pH responsiveness. (a) A scheme of Au-NNP(RTX) nanoassembly. (b) A scheme showing pH-responsive disassembly of Au-NNP(RTX). (c) A scheme showing RT/chemotherapy of tumor based on Au-NNP(RTX) nanoassembly. Reproduced with permission from ref. 39. Copyright 2021, Elsevier.

AuNPs after pH-responsive disassembly, *in vitro* penetration evaluation on CT26 tumor spheroids showed that Au-NNP(RTX) could penetrate deep into the spheroids at pH 6.8 compared to Au-NP(RTX) that could not disassemble. The *in vivo* tumor accumulation/penetration investigation *via* CLSM of tumor slices revealed that the fluorescence signals of Au-NP(RTX) stayed around blood vasculatures at 12 h after intravenous injection while the fluorescence signals of Au-P(RTX) were partly around and away from vasculatures. However, the fluorescence signals of Au-NNP(RTX) were found both around and far away from the blood vasculatures, indicating that the pH-responsive targeting strategy allowed for better penetration into tumors. As a result, the tumor-bearing mice receiving X-ray irradiation (4 Gy) at 2 h and 12 h after intravenous injection of Au-NNP(RTX) demonstrated a much higher inhibition rate of 95.4% at 14 days after treatment, which is 24% higher than that of the Au-NNP(RTX) group. Overall, the pH-responsive disassembly strategy enhanced tumor retention/penetration of radiosensitizers and targeted delivery of surviving gene, which was beneficial to achieve precision RT/gene therapy of tumors.

The low pH-responsive drug release strategy has also been used for precision RT. For example, Yu *et al.* designed a pH-responsive platinum (Pt)-based radiosensitizer by loading cinnamic aldehyde (CA) into Pt@human serum albumin NPs (Pt@HSA/CA NPs) for enhanced RT of tumors.[193] After the Pt@HSA/CA NPs entered the tumor cells, CA was released due to the break of pH-responsive imine bond at pH 5.5. The released CA could break the intracellular redox homeostasis, reduce antioxidant contents, and increase the concentration of H_2O_2. Pt could further catalyze the decomposition of H_2O_2 into O_2 for sensitizing the tumor cell to X-ray irradiation. In addition, the *in vivo* tumor inhibition rate of mice in the Pt@HSA/CA + X-ray group was 91.2%, which was much higher than 74.3% in the Pt@HSA + X-ray group. Thus, this pH-responsive precision RT strategy was able to enhance the RT efficacy against tumors with negligible side effects on healthy tissues.

In addition, Bu's group utilized 2-nitroimidazole, 1H-imidazole-4-carbonitrile and Zn^{2+} to construct pH-sensitive ZIF-82 nanocrystals for hypoxic prostate cancer therapy.[194] On entering the cancer cells, the ZIF-82 nanocrystals can be degraded into electrophilic ligands and Zn^{2+}. The low-energy electrons generated by X-ray irradiation can be captured by these electrophilic ligands to produce nitrite (NO_2^-). The NO_2^- is able to augment intratumoral nitrosative stress and inhibit autophagy to enhance X-ray therapeutic efficacy. In addition, the released Zn^{2+} can suppress migration and invasion of prostate cancer cells *via* ion interference. Overall, the promising strategy of X-ray-induced nitrosative stress showed a significant inhibitory effect on hypoxic prostate tumor.

3.1.2 GSH responsiveness. Generally, GSH plays an important role in protecting cells against external damage.[195] Nevertheless, the concentration of GSH in tumor tissues is over 4-fold higher than that in healthy tissues and is especially high in multi-drug resistant tumors.[196–198] The overexpressed GSH in tumor cells causes resistance to radiotherapy.[199,200] Fortunately, the overexpressed GSH in cancer cells can be used as a specific endogenous stimulus to design GSH-responsive radiosensitizers for precision RT. Since GSH is able to scavenge ROS generated by RT and remarkably decrease the RT efficacy, the GSH-responsive radiosensitizers can deplete GSH and enhance precision RT efficacy.

Recently, Ding *et al.* synthesized an NIR discrete metallacycle (M) using tetraphenylethylene-based di-Pt(II) organometallic precursor (TPE-Pt) and perylene bisimide fluorophore (PPy) (Fig. 9a) for the chemoradiotherapy of tumor.[201] Next, they used a GSH-responsive copolymer (RGD-POEGMA-*b*-PAZMB) to encapsulate M for the construction of M-loaded NPs (MNPs) (Fig. 9b). Due to GSH-triggered elimination of AZMB groups, the MNPs could rapidly release 51.5% and 86.4% of M at 48 h post-incubation with 1 mM and 10 mM GSH, respectively (Fig. 9c). TPE-Pt in MNPs could serve as both a chemotherapeutic drug and a radiosensitizer. Based on GSH-responsive radiosensitization, MNPs plus X-ray irradiation (6 Gy) showed the highest tumor inhibition rate (83.2%) compared to 42.3% of the X-ray alone group (Fig. 9d).

Disulfide (S–S) bond has been used to prepare GSH-responsive nanomedicines. For example, Song *et al.* decorated HA onto Bi_2Se_3 hollow nanocubes (HNCs) *via* the S–S bond, followed by loading of gambogic acid (GA, a heat shock protein inhibitor) for redox-responsive and tumor-targeted RT/PTT.[202] The Bi_2Se_3 HNC-s-s-HA/GA could actively target CD44-overexpressed cancer cells due to HA modification. Moreover, due to GSH-responsive cleavage of the S–S bond, the Bi_2Se_3 HNC-s-s-HA/GA could collapse in the presence of GSH and then

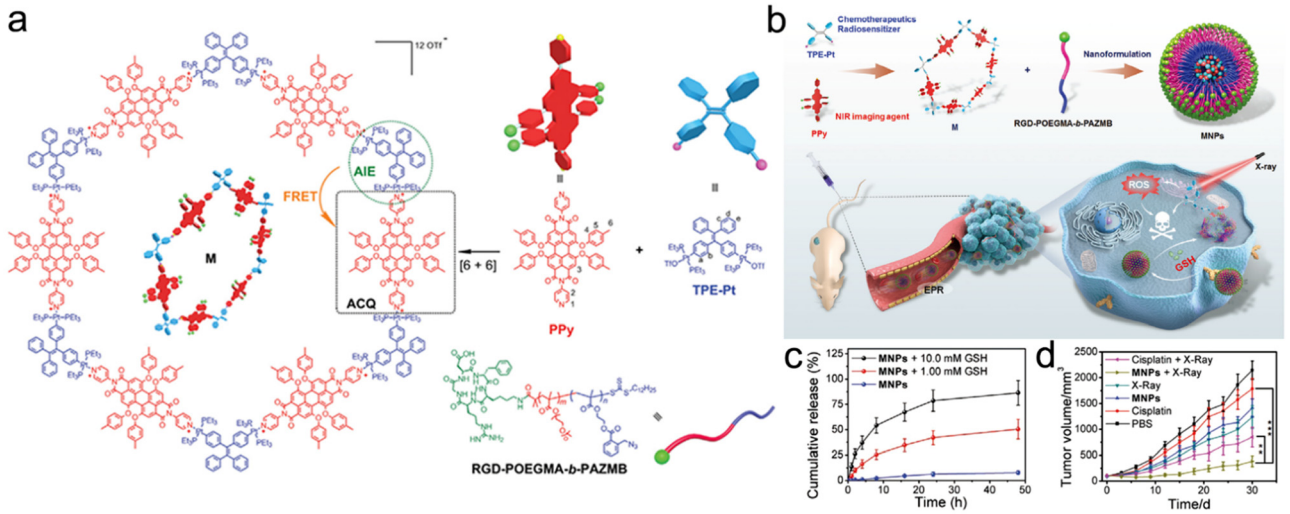

Fig. 9 GSH responsiveness. (a) Chemical structures of PPy, TPE-Pt, M, and RGD-POEGMA-*b*-PAZMB. (b) Schematic illustration of MNPs self-assembled from M and RGD-POEGMA-*b*-PAZMB, as well as their application in RT/chemotherapy. (c) Release profiles of MNPs with or without GSH at various concentrations. (d) Tumor growth curves of mice in different treatment groups. Reproduced with permission from ref. 201. Copyright 2020, Wiley.

release GA to downregulate the expression level of heat shock protein for eliminating cancer cells' resistance to PTT. Considering that the enhanced RT could kill deep tumor cells, the synergistic low-temperature PTT and RT based on the GSH-responsive Bi_2Se_3 HNC-s-s-HA/GA decreased the relative tumor volume to 0.2 at 14 days after treatment, much lower than 1.1 in the non-responsive group (Bi_2Se_3 HNC/GA + NIR +RT).

3.1.3 ROS responsiveness. ROS, including H_2O_2, $^{\bullet}OH$, $^1O_2$ and O_2^-, are able to kill tumor cells by destroying biological molecules such as DNA, proteins and lipids.[203–205] Meanwhile, the ROS level in tumor cells is higher than that in normal cells, indicating that a delicate balance of intracellular ROS content is necessary for normal functions of cancer cells.[206,207] The elevation of ROS level in tumors has been utilized to design ROS-responsive drug delivery systems for tumor-specific theranostics.[208–214]

The ROS-responsive strategy has been applied in the design of radiosensitizers for precision RT.[215–217] For example, Meng *et al.* designed a ROS-responsive nanoplatform by loading acriflavine (ACF, a cationic and hydrophilic HIF-1 inhibitor) into MnO_2 NPs (ACF@MnO_2 NPs) for enhanced RT against primary and metastatic tumors (Fig. 10a and b).[216] The ACF was loaded onto the basal template MnO_2 NPs (MnO_2-ACF intermediate) *via* electrostatic adsorption. Next, after additional MnO_2 redeposition, an external shell was constructed onto the MnO_2-ACF intermediate to obtain final ACF@MnO_2 NPs. After arriving in the lysosomes of tumor cells, ACF@MnO_2 NPs could react with acidic H_2O_2 to generate O_2 and Mn^{2+} for alleviating tumor hypoxia and increasing T_1-weighted MR imaging contrast, which could be used for radiosensitization and MR-guided RT, respectively. The UV absorption of ACF@MnO_2 NP solution ([MnO_2 = 400 μM]) at 400 nm was gradually reduced when the H_2O_2 concentration was increased from 0 to 400 μM, indicating the rapid ROS-responsiveness of ACF@MnO_2 (Fig. 10c). The H_2O_2-responsive degradation of MnO_2 enabled the rapid release of ACF (Fig. 10d), which could suppress the transcription of HIF-1 to inhibit downstream signaling molecules. They found that alleviating tumor hypoxia and inhibiting transcription of HIF-1 could downregulate the PD-L1 expression level and then relieve T-cell exhaustion. Excitingly, the infiltration of CD8+ T cells in tumors treated with ACF@MnO_2 plus RT was similar to that in tumors treated with anti-PD-L1 plus RT. The bilateral CT26 tumor-bearing mice treated with ACF@MnO_2 plus RT showed excellent tumor inhibition rates of both primary tumors (88.72%) and distant tumors (78.9%), much better than those in the anti-PD-L1 plus RT group (65.66% for primary tumors and 67.59% for distant tumors) (Fig. 10e and f). Furthermore, the ACF@MnO_2 plus RT could also inhibit the metastases of the lung and liver of 4T1 breast tumor-bearing mice. All these results suggest that ROS-responsive ACF@MnO_2 in combination with X-ray irradiation could effectively suppress the growth of primary tumors and activate immune responses against abscopal tumors through alleviation of tumor hypoxia and HIF-1 functional suppression.

3.1.4 Enzyme responsiveness. Several types of enzymes, such as lipase, protease, and glycosidase, were found to upregulate in various cancer types, such as breast, prostate, lung, and brain cancers, *etc.*[218–220] Recently, these overexpressed enzymes have been used as endogenous stimuli to design enzyme-responsive nanomaterials for specific cancer therapy.[221–225]

The radiosensitizers in response to diverse types of enzymes have been reported to specifically enhance RT and reduce adverse effects on healthy tissues for precision RT.[226–228] For example, Ding *et al.* designed multifunctional responsive peptide-modified AuNPs (Au@Tat-R-EK) for tumor-specific targeted RT (Fig. 11a).[227] The peptide was composed of three building blocks. A Tat peptide section (GRKKRRQRRRPQ) as the first unit acquired from HIV-1 transactivator of transcription, was directly decorated onto the AuNPs through the Au–S

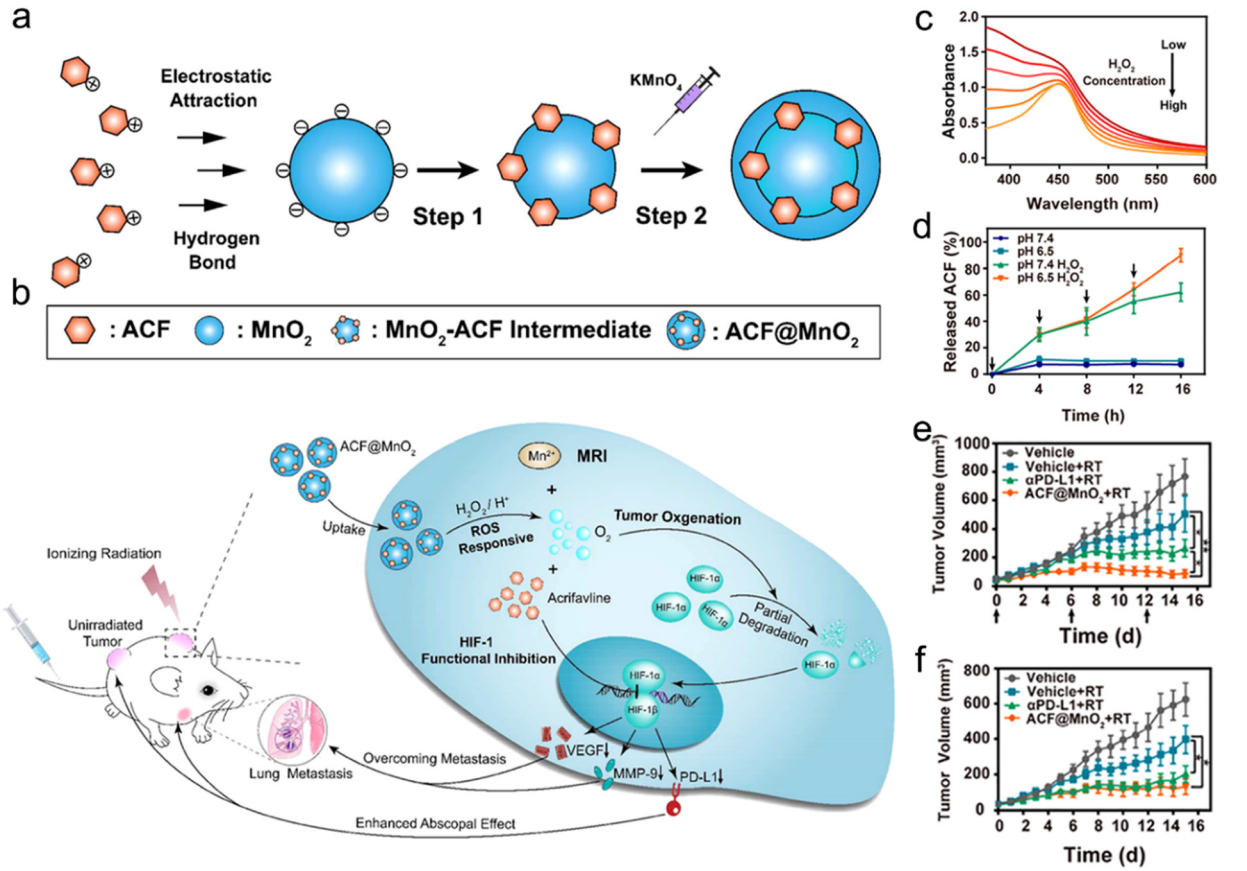

Fig. 10 ROS responsiveness. (a) A scheme of synthetic procedures of ACF@MnO_2. (b) Schematic illustration showing the mechanism of ACF@MnO_2 for RT and abscopal effect. (c) UV/vis absorption spectra of ACF@MnO_2 treated with H_2O_2 at different concentrations. (d) ACF release profiles of ACF@MnO_2 with or without H_2O_2 under pH 7.4 or pH 6.5. (e and f) Primary (e) and distant (f) tumor growth curves of mice that received different treatments. Reproduced with permission from ref. 216. Copyright 2018, American Chemical Society.

bonds for cell penetration and nucleus targeting.[229,230] The second unit was a cathepsin B-cleavable peptide (GFLG).[231–233] The outer peptide, a zwitterionic peptide (EKEKEKEKEK), endowed the NPs with outstanding biocompatibility and passive tumor targeting capability.[234,235] Cathepsin B, one of the lysosomal proteases, is significantly upregulated in the TME of various cancers, and the enzyme is secreted and bound to the cell surface.[236,237] The peptide (CFLG) of Au@Tat-R-EK could be selectively cleaved in response to cathepsin B in the TME. After specific split, the Tat peptide section was exposed, which adjusted the surface charge of AuNPs (Au@Tat) to be positive (Fig. 11b), suggesting successful enzyme responsiveness. Moreover, the Au@Tat NPs were able to enter cancer cells and target the nucleus, realizing nuclear accumulation of AuNPs. To evaluate the enzyme-responsive cell uptake, the cathepsin B-irresponsive peptide was used to prepare Au@Tat-I-EK as a counterpart of Au@Tat-R-EK. The *in vitro* cellular uptake results showed that the intracellular content of Au@Tat-I-EK was quite low even with additional cathepsin B. Addition of cathepsin B to culture medium significantly increased LM3 cell endocytosis of Au@Tat-R-EK. However, after adding GM6001, an inhibitor of cathepsin B, into the medium, the cellular uptake of Au@Tat-R-EK was remarkably inhibited. As a result, Au@Tat-R-EK exhibited great cytotoxicity *in vitro*, which could be enhanced or declined after adding cathepsin B or GM6001, respectively. In addition, the biodistribution of AuNPs by ICP-MS revealed that the tumor-bearing mice treated with Au@Tat-R-EK showed a higher tumor accumulation of 9.6% ID per g at 24 h post-injection than those in the Au@Tat-I-EK group (2.7% ID per g) (Fig. 11c). Finally, the tumor inhibition rate caused by Au@Tat-I-EK-mediated radiosensitization was 5.3 times that of the RT alone group.

Matrix metalloproteinases (MMPs), enzymes secreted by cancer cells, were reported to be extracellularly overexpressed in various malignant tumors, such as colon, breast, and brain cancers.[238–241] Accordingly, the elevated expression of MMPs has been widely used to design enzyme-responsive nanosystems for cancer theranostics.[242–244] For example, the Zhang's group developed a smart biomimetic nanosystem composed of engineered bacteria (eBac) and Bi_2S_3 NPs (BNPs) for enhanced RT of breast carcinoma (Fig. 11d).[228] Concretely, the *Escherichia coli* MG1655 was first transferred with pBAD18-ClyA plasmid for upregulation of the ClyA protein. Next, the matrix metalloproteinases-2 (MMP-2)-responsive peptide (PLGVR)-modified BNPs were chemically conjugated onto the eBac surface to construct Bac@BNP. The Bac@BNP was able to target

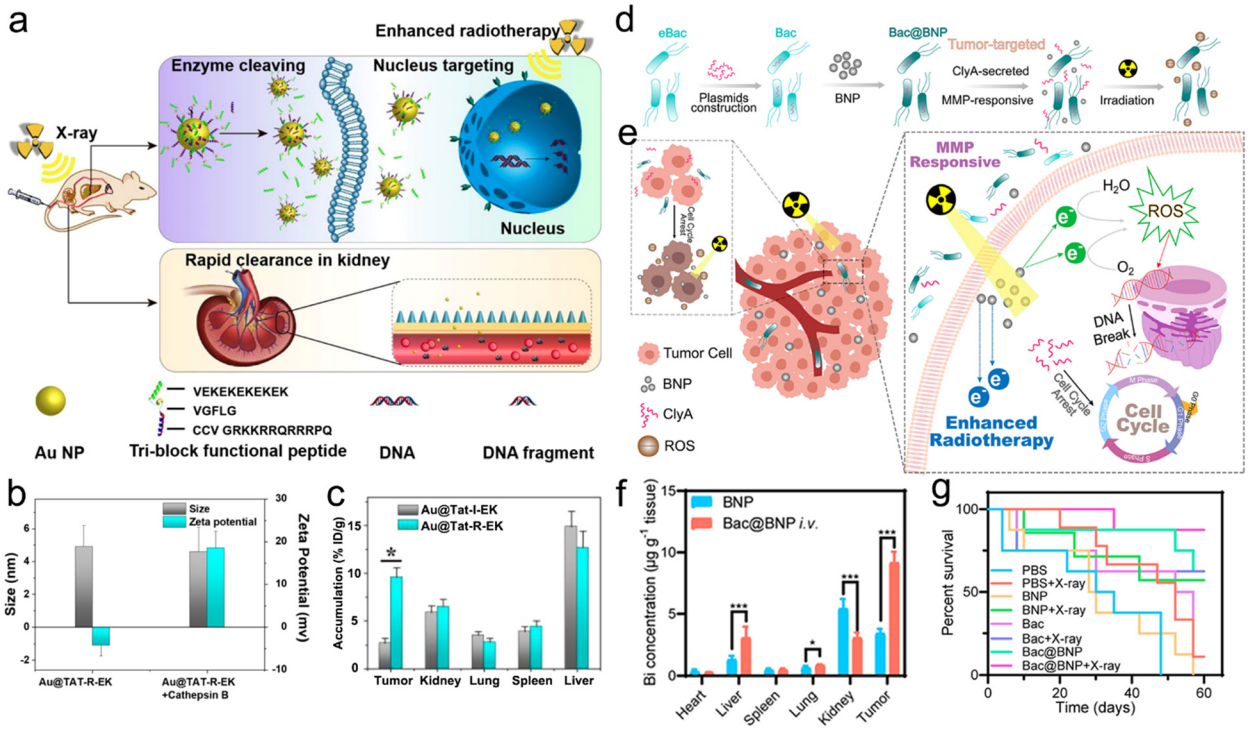

Fig. 11 Enzyme responsiveness. (a) A scheme showing the enzyme cleaving, nucleus targeting, and rapid renal clearance of Au@Tat-R-EK NPs. (b) Hydrodynamic sizes and zeta potentials of Au@Tat-R-EK NPs treated with or without cathepsin B. (c) Biodistribution of Au NPs in the major organs and tumors of mice at 24 h after intravenous administration of Au@Tat-I-EK or Au@Tat-R-EK NPs. Reproduced with permission from ref. 227. Copyright 2020, Ivyspring International Publisher. (d) A scheme of synthetic procedures and enzyme-responsive process of the Bac@BNP nanosystem. (e) Schematic illustration showing the MMP-responsive Bac@BNP nanosystem for enhanced RT. (f) Biodistribution of the Bi element in major organs and tumors of mice at 48 h after intravenous administration of BNP or Bac@BNP. (g) Survival curves of tumor-bearing mice in different treatment groups. Reproduced with permission from ref. 228. Copyright 2020, American Chemical Society.

the tumors owing to the tropism of bacteria. When Bac@BNP accumulated at the tumor sites, BNPs with a high-*Z* element were released to deposit X-ray energy, and the upregulated ClyA in Bac was secreted to arrest the cell cycle for radiosensitization (Fig. 11e). The *in vitro* cell cycle analyses *via* flow cytometry showed that the incubation of 4T1 cells with Bac and L-arabinose (an activator for ClyA expression) could significantly increase the G2/M phase from 21.06% to 45.23% and reduce the S phase from 36.89% to 3.04%. However, the cell cycles of 4T1 cells incubated with plasmid-transferred Bac (pBac) or Bac without L-arabinose showed no significant change. The *in vitro* drug release result revealed that Bac@BNP could rapidly release the BNPs in the presence of MMP-2, whereas the addition of MMP-2 inhibitor could significantly inhibit the BNP release. Moreover, the *in vivo* biodistribution evaluation *via* ICP-MS analyses of the Bi element showed that the tumor accumulation of BNPs at 48 h after intravenous injection of Bac@BNP was almost 3 times that treated with BNPs alone (Fig. 11f). Therefore, the 4T1-luc tumor-bearing mice in the Bac@BNP + X-ray group showed 87.5% of survival proportion even at 60 days after treatment, whereas the mice in the X-ray alone group all died within 30 days (Fig. 11g). Overall, the endogenous enzyme-responsive radiosensitizers can improve the RT effectiveness. However, the presence of different enzyme subtypes with a similar cleavage site should be considered during the design of enzyme-responsive radiosensitizers to prevent off-target effect or serious side effect.

3.1.5 Hypoxia responsiveness. Hypoxia is characterized by a low oxygen content due to imperfect vessel structures.[245] Additionally, hypoxia has been reported to be related to resistance to RT and chemotherapy, tumor invasiveness, and metastasis.[246] However, hypoxia is rarely present in normal tissues, making it a promising target in the design of nanomedicines for cancer theranostics.[247–254] The hypoxia-responsive strategy has been used to design radiosensitizers for precisely sensitizing cancer cells to RT.[255]

For instance, Hua *et al.* developed a hypoxia-responsive angiopep-2-lipid-poly(metronidazoles)$_n$ (ALP-(MIs)$_n$) to specifically sensitize hypoxic tumor cells to RT.[255] The ALP-(MIs)$_n$ NPs were composed of three ingredients: (1) the inner side was the hydrophobic poly(metronidazoles)$_n$ (P-(MIs)$_n$) core which could load with small molecule drugs; (2) the nitro groups in P-(MIs)$_n$ could be transformed into hydrophilic amino groups in response to hypoxia, leading to drug release; (3) the outer side was a lipid layer modified with angiopep-2 (Fig. 12a–c). They also prepared AL-PLGA and AL-PLGA/DOX as negative controls. Then, ALP-(MIs)$_n$ (n = 25, 48) NPs were loaded with DOX for hypoxia-responsive RT/chemotherapy of glioma. ALP-(MIs)25 with uniform spherical morphology under normoxic conditions was decomposed in response to hypoxic conditions, whereas

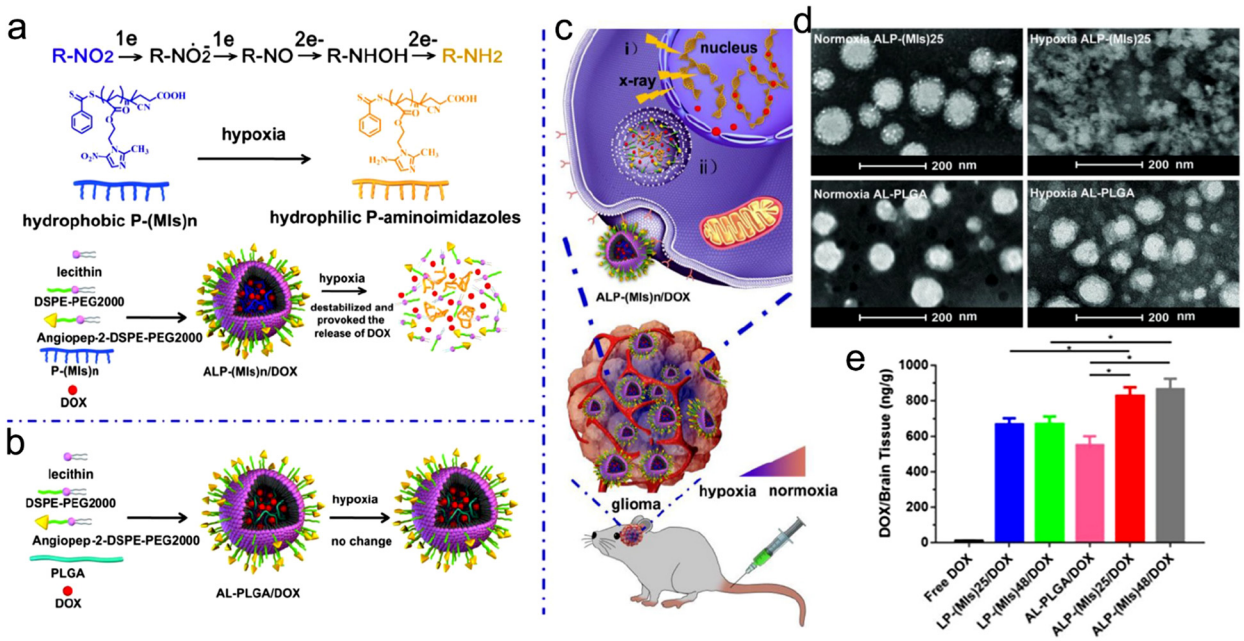

Fig. 12 Hypoxia responsiveness. (a) A scheme of ALP-$(MIs)_n$ for hypoxia-responsive DOX release and radiosensitization. (b) Construction of AL-PLGA/DOX as the negative control. (c) A scheme showing the applications of ALP-$(MIs)_n$: (i) radiosensitization in hypoxic cells; (ii) hypoxia-responsive DOX release. (d) TEM images of ALP-(MIs)25 and AL-PLGA under normoxic or hypoxic conditions. (e) DOX content in mouse brain of different treatment groups. Reproduced with permission from ref. 255. Copyright 2018, Ivyspring International Publisher.

the AL-PLGA NPs showed no change under hypoxic conditions (Fig. 12d). Moreover, ALP-(MIs)25/DOX and ALP-(MIs)48/DOX were stable under normoxic conditions but precipitated under hypoxic conditions since the nitro groups transformed into amino groups in response to hypoxia. With the hypoxia responsiveness, ALP-(MIs)25/DOX and ALP-(MIs)48/DOX could rapidly release most DOX within 4 h of incubation with hypoxic PBS. Besides, the angiopep-2, a ligand for low density lipoprotein receptor-related protein 1 (LRP-1) expressed in brain microvascular endothelial cells, enabled ALP-$(MIs)_n$ to cross the blood–brain barrier (BBB) and then accumulate in the glioma. *In vivo* DOX accumulation investigation revealed that the DOX concentrations in brain tissues of mice treated with ALP-(MIs)25/DOX and ALP-(MIs)48/DOX were significantly higher than those treated with LP-$(MIs)_n$/DOX (without angiopep-2 modification) or AL-PLGA/DOX (without hypoxia-responsiveness) (Fig. 12e). Due to higher glioma accumulation and hypoxia-responsive DOX release, the orthotopic C6-GFP-Luci glioma-bearing mice receiving 2 Gy of RT after injection of ALP-(MIs)25/DOX (57 days) or ALP-(MIs)48/DOX (59 days) exhibited a longer median survival time than those in LP-(MIs)25/DOX + RT (49 days) and LP-(MIs)48/DOX + RT groups (49.5 days). Overall, the design of endogenous stimuli-responsive radiosensitizers based on hypoxia, a distinctive feature of tumor tissues, is a promising strategy for precision RT. In further research, the stronger tumor penetration ability needs to be considered in radiosensitizer design since the degree of hypoxia in deep tumor tissues is much higher.

3.1.6 Dual endogenous stimuli responsiveness. In addition to single endogenous stimulus-responsive radiosensitization, radiosensitizers that can respond to two endogenous stimuli, such as pH/GSH,[103] GSH/hypoxia,[256] pH/enzyme,[257,258] pH/hypoxia,[259] GSH/ROS,[60,260] *etc.*, are also trending. These dual endogenous stimuli-responsive radiosensitizers can yield a better radiosensitizing effect and improve the accuracy of radiosensitizer delivery for more precise cancer RT.

For example, Chan *et al.* designed a sequentially pH/GSH-responsive delivery nanosystem (PLGA-SS-D@BPQDs) based on black phosphorus quantum dots (BPQDs) and poly(lactic-*co*-glycolic acid) (PLGA) for precise RT of tumors. The NPs were coated with several shells of polymers, including polyethylenimine (PEI), 2,3-dimethylmaleic anhydride (DMMA), and RGD polypeptide, for sequential pH/GSH-responsive delivery (Fig. 13a).[103] First, the conjugation of RGD polypeptide endowed the PLGA-SS-D@BPQD NPs with active tumor-targeting capability. Next, after reaching the TME, the NPs could gradually expand in response to acidic conditions (pH = 6.8) due to the hydrolyzation of amide linkages of DMMA, which changed the surface potential of NPs from −7.8 mV to +35.5 mV due to the exposure of the PEI layer. The positive charges potentiated tumor cell uptake of the NPs. Moreover, the average size of the NPs expanded from 157 nm to over 2500 nm in both pH 6.8 solution and tumor homogenate. Then, the disulfide bonds between the PEI layers and the PLGA were broken by intracellular GSH, which decreased the size of expanded NPs to 139 nm and released the ultrasmall BPQDs that sensitized tumor cells to X-ray irradiation. For antitumor efficacy investigation, the tumor inhibition rate of the PLGA-SS-D@BPQDs + X-ray group was 2.8 times that of the BPQDs + X-ray group.

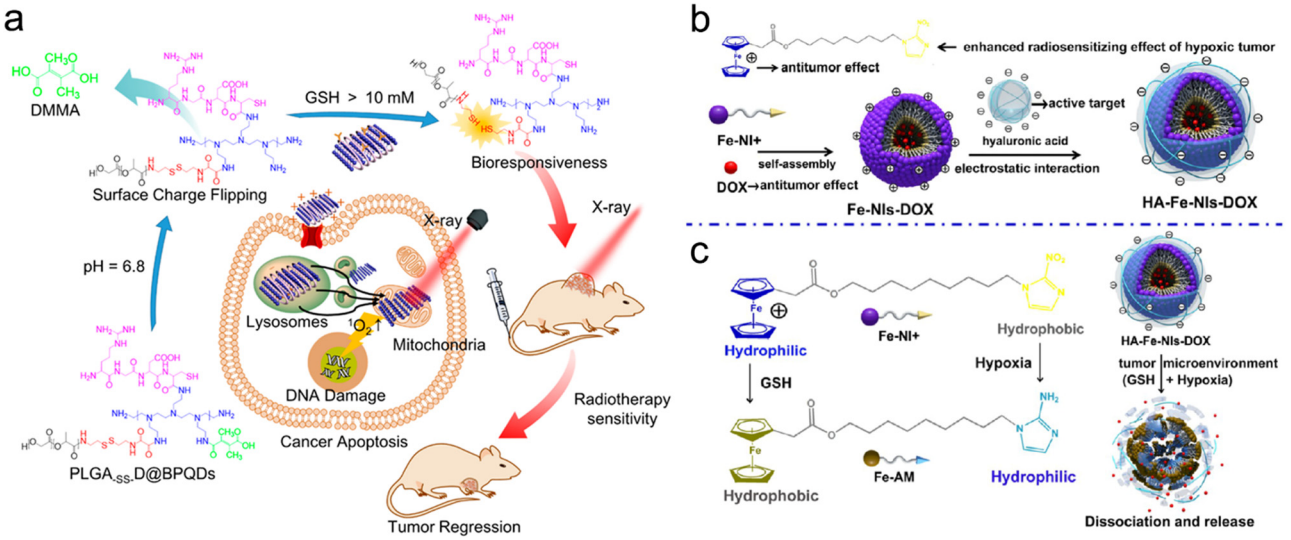

Fig. 13 Dual endogenous stimuli responsiveness. (a) Schematic illustration of synthetic procedures of PLGA-SS-D@BPQDs and their application in RT of tumors. Reproduced with permission from ref. 103. Copyright 2018, American Chemical Society. (b) A scheme of synthetic procedures of HA-Fe-NIs-DOX micelles. (c) Schematic illustration showing the mechanism of HA-Fe-NIs-DOX micelles under hypoxia and GSH. Reproduced with permission from ref. 256. Copyright 2018, American Chemical Society.

In addition to the sequential dual-responsive strategy, synergistic dual-responsive strategy has been also reported to enhance precision RT. For example, Mao *et al.* fabricated amphiphilic ferrocenium-hexane-nitroimidazoles (Fe-NIs) as a GSH/hypoxia dual-responsive nanocarrier for chemoradiotherapy (Fig. 13b).[256] The Fe-NI micelles were loaded with DOX to construct HA-Fe-NIs-DOX micelles for chemotherapy and decorated with HA *via* electrostatic interactions for active tumor targeting. It is worth mentioning that the HA-Fe-NIs-DOX micelles were able to dissociate and release DOX in response to dual endogenous GSH/hypoxia stimuli (Fig. 13c). On the one hand, the hydrophilic ferrocenium ion was converted into hydrophobic ferrocene with effective antitumor effect under GSH conditions.[261] On the other hand, NIs could function as a radiosensitizer, and the hydrophobic NIs in the micelles could be selectively reduced to hydrophilic aminoimidazoles in the presence of hypoxia.[262,263] HI-Fe-DOX micelles without radiosensitization were prepared as the negative control. The TEM images showed a well-dispersed micelle structure of HA-Fe-NIs-DOX. Then, the *in vitro* GSH/hypoxia dual-responsiveness of HA-Fe-NIs micelles was investigated by TEM imaging. The HAase was first used to degrade the HA shell to expose the Fe-NI micelles. After incubation under GSH (10 mM), HAase and hypoxic conditions, the HA-Fe-NI micelles were rapidly disassembled and the yellow precipitates were observed. The *in vitro* drug release experiments revealed that more than 80% DOX was released from the HA-Fe-NIs-DOX micelles within 6 h of incubation with hypoxia, GSH, or hypoxia plus GSH while only 37% DOX was released even after 12 h in pH 7.4 PBS buffer. Finally, due to excellent chemotherapeutic efficacy and radiosensitive effect, HA-Fe-NIs-DOX plus X-ray irradiation effectively inhibited the tumors with 0.89 of relative tumor volume at 20 days after treatment, much lower than that in the HA-Fe-DOX + X-ray group (4.03) without a hypoxic radiosensitizer.

Overall, dual endogenous stimuli-responsive strategy may indeed realize the precise delivery of radiosensitizers and lessen the side effect on healthy tissues, but it may also result in poor RT efficacy due to the complicated response process. In addition, the strength of endogenous stimuli varies spatiotemporally since it is affected by various factors in the body, including tumor type, progression, location, and individual differences between patients, resulting in unpredictable and uncontrollable antitumor effects. Furthermore, the cost of making endogenous stimuli-responsive radiosensitizers, including synthesis of specific cleavable peptide and other responsive small-molecules, also need to be considered to promote the translational use of these radiosensitizers.

3.2 Exogenous stimuli-responsive strategies

Exogenous stimuli, such as X-ray, light, ultrasound, *etc.*, have attracted extensive interest as a remote switch to spatially and temporally trigger morphology transformation of nanostructures or drug release. With exogenous stimuli, the location, timing, radiosensitizer dosage and tumor accumulation/retention can be controlled for precision RT. Moreover, these exogenous stimuli can also endow radiosensitizers with multiple functions beyond RT or radiosensitizer delivery, such as PA imaging, ultrasound imaging, CT imaging and photothermal therapy.

3.2.1 X-ray responsiveness. X-Ray, one type of ionizing radiation, has been widely used in clinical treatment and diagnosis. X-Ray can not only be used for RT to damage the DNA of cancer cells but also serve as an external stimulus with nearly unlimited tissue penetration depth to increase the cell

uptake of radiosensitizers or to trigger drug release for further enhanced RT.

X-Ray irradiation on the tumor site can significantly enhance the tumor accumulation/retention of many different types of radiosensitizers and meanwhile reduce their efflux through various mechanisms, thus leading to precision RT.[264–266] For example, Yang's group proposed an X-ray-optimized delivery strategy by enhancing tumor accumulation/retention of radionuclide-labeled human serum albumin (HSA) NPs upon X-ray irradiation (Fig. 14a).[264] First, the expression levels of Caveolin-1 in various cancer cells were upregulated at 24 h after X-ray irradiation. Previous studies reported that the upregulated expression levels of Caveolin-1 in cancer cells could increase the uptake of HSA-based NPs.[267,268] The flow cytometry of Cy5.5-labeled HSA revealed that the cell uptake of HSA NPs was remarkably increased after 6 Gy of X-ray irradiation. Next, the HSA NPs were labeled with ^{131}I (^{131}I-HSA) to evaluate their *in vivo* tumor accumulation using γ imaging. The bilateral CT26 tumor-bearing mice were intravenously injected with ^{131}I-HSA NPs, followed by γ imaging. The γ images showed that the radioactivity in the tumor pre-exposed to X-rays was still detectable at 72 h post-injection while the radioactivity in the control tumor could not be detected after 48 h, indicating enhanced tumor retention of ^{131}I-HSA under X-ray irradiation (Fig. 14b). In addition, the prolonged tumor retention time after X-ray exposure could potentiate the radionuclide therapy of ^{131}I-HSA. The *in vivo* antitumor efficacy evaluation revealed that the tumor inhibition rate of CT26 tumor-bearing mice injected with ^{131}I-HSA at 24 h after X-ray irradiation was 1.5 times that of mice receiving X-ray irradiation at 24 h post-injection of ^{131}I-HSA, further suggesting that X-ray-optimized tumor retention could improve the radiosensitizing effect.

Furthermore, X-ray-responsive drug release is another strategy to sensitize cancer cells to RT.[269–271] For example, Du *et al.* developed an X-ray-triggered peroxynitrite ($ONOO^-$) production nanoplatform for improved radiosensitizing effect (Fig. 14c).[272] First, the Ce-doped $LiLuF_4$ was chosen as scintillating NPs (SCNPs) to be conjugated with tocopheryl polyethylene glycol 1000 succinate (TPGS) through electrostatic interaction. Next, the as-prepared T-SCNPs were loaded with Roussin's black salt (RBS, a photo-responsive NO donor) *via* electrostatic attraction to produce RBS-T-SCNPs. The $LiLuF_4$:Ce^{3+} in the RBS-T-SCNPs could function as a radiosensitizer to generate ROS, such as $O_2^{\bullet-}$, upon X-ray irradiation. In addition, the SCNPs were able to convert X-ray into UV light to trigger the decomposition of RBS to generate NO. Thus, the X-ray-triggered generation of $O_2^{\bullet-}$ and NO resulted in the production of $ONOO^-$. The $ONOO^-$ could contribute to radiosensitization by effectively aggravating DNA damage and downregulating DNA-repair enzyme. The *in vitro* NO release under X-ray irradiation presented an "on/off" profile, suggesting X-ray-responsive NO release. Flow cytometry revealed that the fluorescence intensity of 3-amino-4-aminomethyl-2′,7′-difluorescein, diacetate (DAF-FM, a NO fluorescence indicator) in the A549 cells treated with RBAS-T-SCNPs plus X-ray irradiation was much higher than those treated with RBAS-T-SCNPs or X-ray alone. Therefore, RBAS-T-SCNPs exhibited almost no cytotoxicity whereas effectively decreased *in vitro* cell viability to only 5.9% compared to 52.1% in the X-ray alone group. Besides, the *in vivo* tumor inhibition rate of the RBAS-T-SCNPs + X-ray group after 20 days of treatment was more than 4 times higher than that of X-ray alone group. These results indicate that the X-ray-triggered sufficient release of $ONOO^-$ from RBS-T-SCNPs could significantly enhance RT efficacy.

Recently, various X-ray-responsive nanoplatforms based on the intrinsic weakness of certain chemical bonds have been designed for precision RT. For instance, S–S (240 kJ mol^{-1}) and diselenide (Se–Se, 172 kJ mol^{-1}) bonds have been harnessed to construct X-ray-responsive nanosystems for controllable drug release due to X-ray-induced cleavage of the S–S or Se–Se bonds.[273–276] Wang *et al.* synthesized an X-ray responsive DOX-loaded polypeptide nanogel (PNG/DOX) for on-demand controllable DOX release and synergistic RT/chemotherapy of human non-small-cell lung carcinoma (NSCLC).[277] The PNG was prepared by crosslinking poly(ethylene glycol)-*block*-poly(L-glutamic acid-*co*-γ-2-chloroethyl-L-glutamate) (mPEG-*b*-P(LG-*co*-CELG)) with an X-ray responsive Se–Se bond, which was further

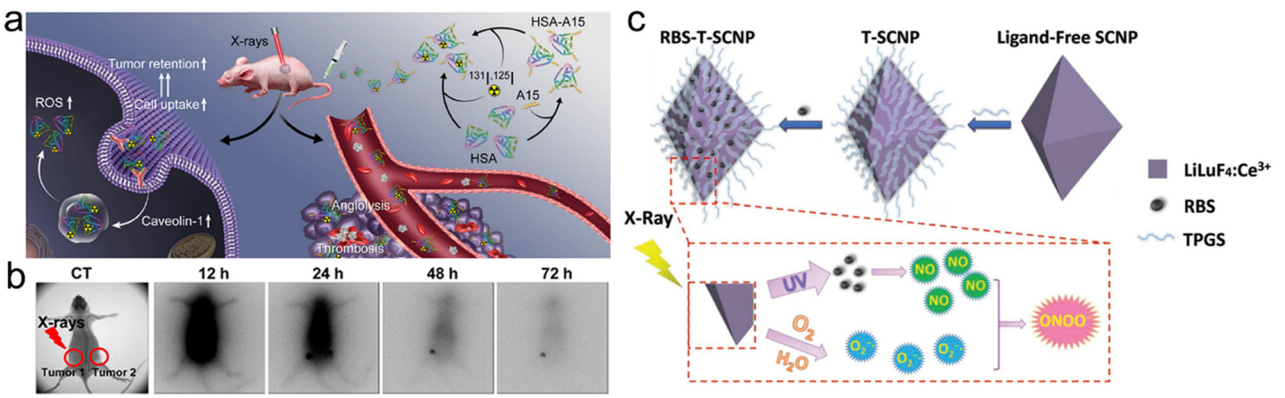

Fig. 14 X-ray stimuli responsiveness. (a) Schematic illustration showing the mechanism of HSA delivery under X-ray irradiation. (b) *In vivo* γ imaging of mice bearing bilateral CT26 tumors at various time points after intravenous administration of ^{131}I-HSA. The tumor 1 (left) was preirradiated. Reproduced with permission from ref. 264. Copyright 2020, Elsevier. (c) Schematic illustration of synthetic procedures of RBS-T-SCNPs and its application in X-ray-controlled $ONOO^-$ generation for tumor RT. Reproduced with permission from ref. 272. Copyright 2018, Wiley.

loaded with DOX as a model drug. The *in vitro* drug release result showed that DOX was rapidly released due to the Se–Se bond break upon X-ray irradiation and the released DOX amount was increased with the elevated X-ray dose. The X-ray triggered rapid release of DOX could improve the radiosensitizing effect and result in 2.4 of relative tumor volume after 24 days of treatment compared to 3.6 in the DOX + X-ray group (negative group).

3.2.2 Light responsiveness. Light as a particularly attracting external stimulus has been widely applied in controllable theranostics due to its non-invasiveness, ease of operation, adjustable exposure time and position. Ultraviolet (UV), visible (Vis), and near-infrared (NIR) light are frequently utilized to trigger drug release,[278] morphology/size transformation of nanomaterials,[279–281] catalysis,[282] and assembly/disassembly of NPs.[283]

The light stimulus has been shown to improve the radiosensitizing effect. For example, Feng *et al.* fabricated iridium nanocrystal (IrNC)-encapsulated liposomes (Ir@liposome) to regulate tumor oxygenation for radiosensitization.[284] Concretely, the Ir@liposome NPs could effectively catalyze oxygen generation from H_2O_2 to alleviate tumor hypoxia under NIR light-triggered mild hyperthermia (Fig. 15a). Next, the Ir as a high-*Z* element was able to deposit X-ray energy, which could combine with tumor hypoxia relief to improve the radiosensitizing effect. The as-prepared Ir@liposome NPs showed stronger catalytic activity with elevated temperature *in vitro*, whereas the activity of biological catalase showed almost no change after heating (Fig. 15b and c). Moreover, the NIR light at 1 W cm^{-2} could significantly improve the oxygen generation from Ir@liposome due to the photothermal heating effect, indicating the temperature-dependent catalytic activity of Ir@liposome NPs (Fig. 15d). Since GSH could effectively inhibit the catalytic activity of IrNCs, the Ir-GSH@liposome was set as the negative control. The *ex vivo* immunofluorescence staining of tumor tissues collected from mice treated with Ir@liposome plus NIR

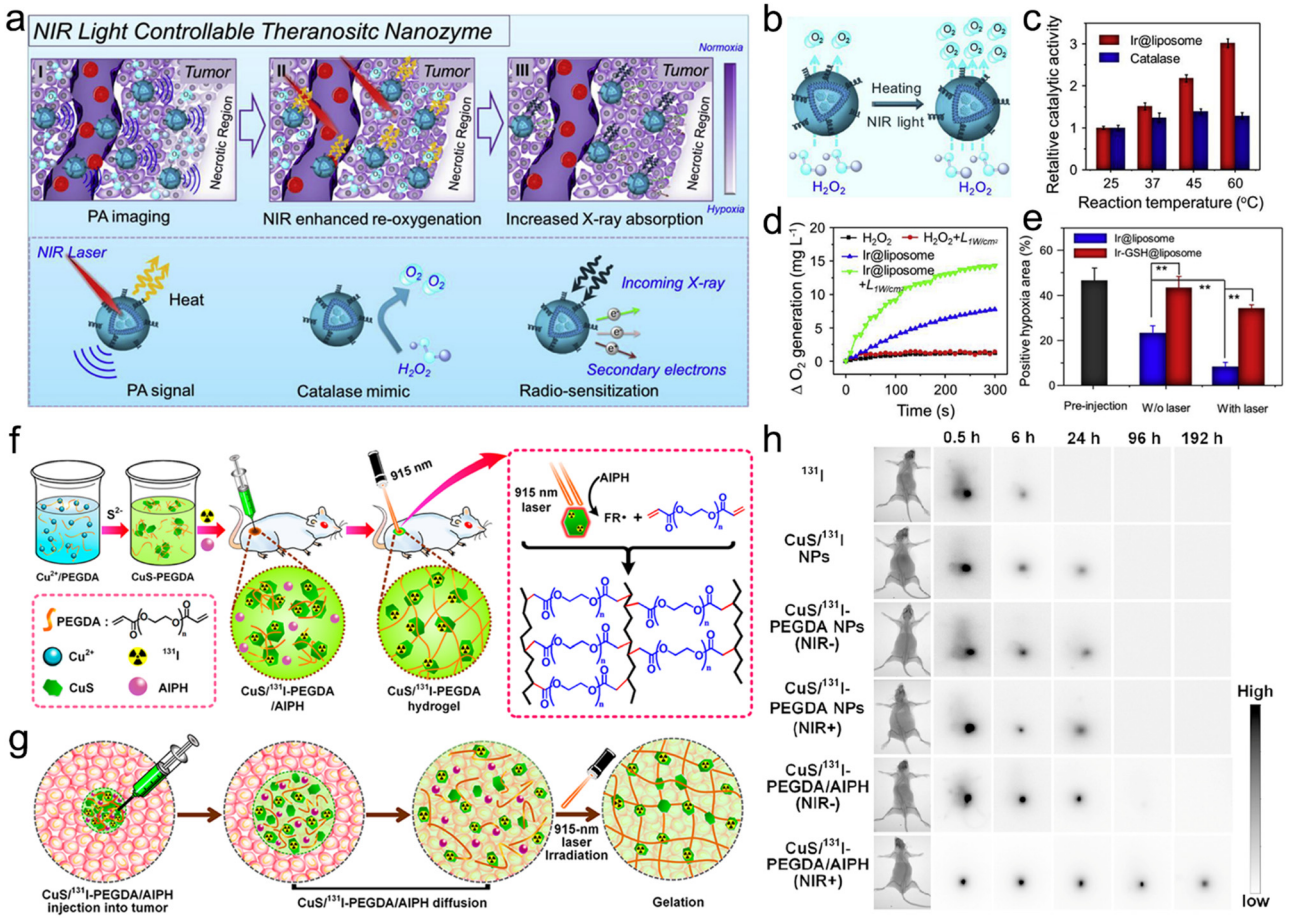

Fig. 15 Light stimuli responsiveness. (a) A scheme of NIR light controllable theranostic nanozyme (Ir@liposome) and its application in PA imaging, NIR-enhanced tumor oxygenation, and radiosensitization. (b) A scheme showing heating and NIR light controllable oxygenation through Ir@liposome mediated H_2O_2 decomposition. (c) Relative catalytic activities of catalase and Ir@liposome toward H_2O_2 decomposition at various temperatures for 1 min. (d) Oxygen generation profiles of H_2O_2 solutions with or without Ir@liposome under 785 nm laser irradiation (1 W cm^{-2}) or not. (e) Quantification analysis of tumor hypoxia regions in tumor sections with different treatments. Reproduced with permission from ref. 284. Copyright 2018, Elsevier. (f) Schematic illustration of localized synthesis of the CuS/^{131}I-PEGDA hydrogel at the tumor site. (g) Schematic illustration showing the dispersion of CuS/^{131}I-PEGDA/AIPH in the tumor region after local injection. (h) *In vivo* γ imaging of mice at different time points after local injection of various NPs with 915 nm laser preirradiation for gelation or not. Reproduced with permission from ref. 285. Copyright 2018, American Chemical Society.

light irradiation revealed that the hypoxia area in tumor slices was significantly reduced, indicating the great catalase activity of Ir@liposome (Fig. 15e). However, the hypoxia area in tumors treated with Ir-GSH@liposome did not change significantly even with laser irradiation. Based on NIR light controllable hypoxia relief and the high-*Z* element of Ir@liposome, tumors receiving NIR light and X-ray irradiation post-injection of Ir@liposome were remarkably eliminated, whereas the relative tumor volume was almost 4 in the X-ray alone group after 2 weeks of treatment.

Besides, external light can trigger morphology/size transformation of nanomaterials to enrich their tumor accumulation/retention for enhanced RT. For example, Liu's group proposed a light-triggered localized gelation strategy by making use of a hybrid hydrogel system for repeated photothermal brachytherapy (Fig. 15f).[285] The hydrogel system (CuS/^{131}I-PEGDA/AIPH) was fabricated by using ^{131}I-labeled copper sulfide (CuS/^{131}I) NPs as both a radionuclide therapeutic drug and a photothermal agent, PEG double acrylates (PEGDAs) as a polymeric matrix, and 2,2′-azobis[2-(2-imidazolin-2-yl)propane] dihydrochloride (AIPH) as a thermal activator. With great photothermal conversion performance, the gelation of CuS-PEGDA NPs could be formed *in vitro* when the temperature reached 43 °C upon 915 nm laser (2.0 W cm^{-2}) irradiation in the presence of AIPH (a thermal initiator). After local injection into the tumor sites, CuS/^{131}I-PEGDA/AIPH could gradually diffuse into the whole tumor area in 10 min, validated by *in vivo* PA imaging (Fig. 15g). Next, the subcutaneous 4T1 tumors were irradiated with 915 nm laser (1.0 W cm^{-2}, 12 min) for 10 min post-injection of CuS/^{131}I-PEGDA and AIPH. Upon laser irradiation, the tumor temperature increased to 43 °C which further triggered gelation. The gelation could fix the CuS/^{131}I-PEGDA NPs in the tumors with less leakage to the surrounding blood or tissues. The *in vivo* γ imaging of tumor-bearing mice revealed that the tumors receiving laser irradiation after local injection of CuS/^{131}I-PEGDA/AIPH exhibited significantly higher retention of radioactivity even at 192 h post-injection, while the radioactivity in tumors of other groups was almost undetectable at 96 h post-injection (Fig. 15h). The light-triggered localized gelation enabled long-term tumor retention of the CuS/^{131}I-PEGDA/AIPH hydrogel system. Moreover, mild hyperthermia has been reported to effectively improve the blood supply of tumor for relieving tumor hypoxia.[286,287] The immunofluorescence staining of tumor slices indicated that the repeated mild PTT at 10 min, 48 h, and 96 h after a single injection of CuS/^{131}I-PEGDA/AIPH remarkably reduced the

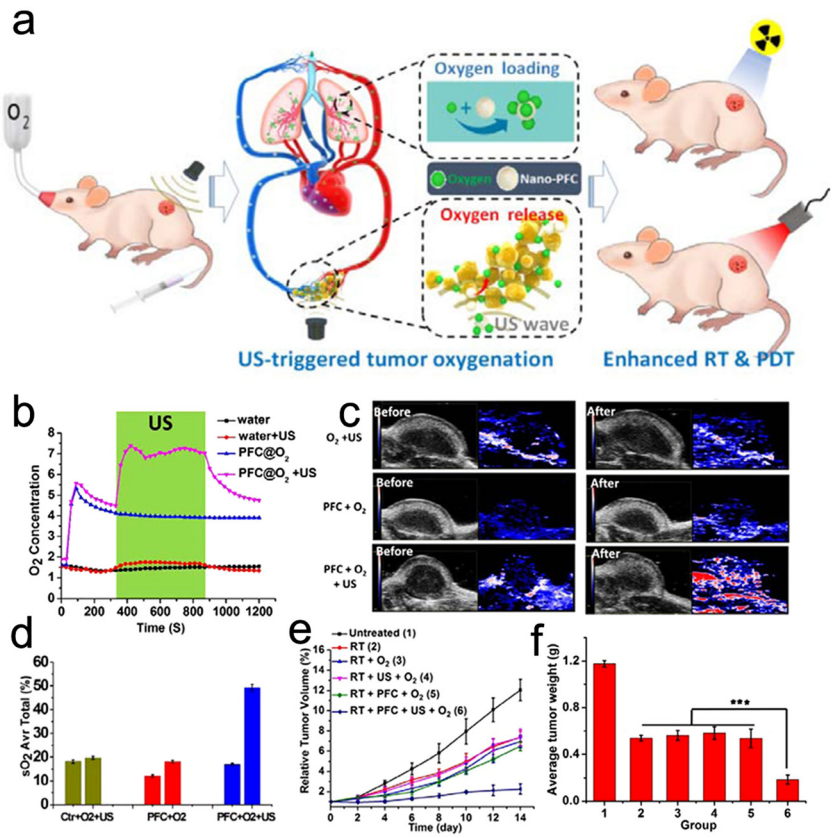

Fig. 16 Ultrasound stimuli responsiveness. (a) Schematic illustration showing the mechanism of US-triggered tumor oxygenation and enhanced RT/PDT using nano-PFC as the oxygen shuttle. (b) *In vitro* oxygen concentration in water or PFC@O_2 solution with or without US treatment. (c) *In vivo* PA imaging of Hb/HbO_2 (ex = 750/850 nm) tumors before and 30 min after various treatments. (d) Quantification analysis of oxygen concentration in the tumor before and after various treatments. (e and f) Tumor growth curves (e) and tumor weight (f) of mice in different treatment groups. Reproduced with permission from ref. 291. Copyright 2016, American Chemical Society.

tumor hypoxic area compared to single hypothermia heating at 10 min post-injection. Furthermore, the long-term tumor hypoxia relief would significantly augment the radiosensitizing effect. The 4T1 tumors receiving multiple rounds of mild PTT after *in situ* gelation of CuS/^{131}I-PEGDA/AIPH were rapidly regressed in 10 days, leading to mouse survival even at 60 days after treatment. However, all the mice in the CuS/^{131}I-PEGDA/AIPH + single round of mild PTT were dead within 26 days.

3.2.3 Ultrasound responsiveness. Ultrasound (US) has been commonly used in clinical diagnosis due to its non-invasiveness, deep tissue penetration depth, and low cost.[288,289] The micro/nanobubbles, as one type of US-responsive carriers, have been extensively applied for US-responsive delivery of gases, such as oxygen, nitrogen.[290] For example, Song *et al.* proposed a US-triggered *in situ* tumor oxygenation strategy by using HSA-stabilized PFC nanodroplets (nano-PFC) to alleviate tumor hypoxia for improving the radiosensitizing effect (Fig. 16a).[291] The prepared PFC nanoemulsion was stabilized by HSA to form a nano-PFC nanoemulsion. After adding the oxygen-saturated nano-PFC nanoemulsion into deoxygenated water, the dissolved oxygen concentration of water could rapidly increase and saturate within the first 100 s, and then exhibited a slow decrease over time. However, the nano-PFC nanoemulsion exhibited a burst release profile and rapidly increased the dissolved oxygen concentration of water upon stimulation of low power/frequency US (3.5 W, 1.0 MHz), suggesting excellent US-responsive oxygen release performance of nano-PFC (Fig. 16b). For *in vivo* oxygen delivery, the tumor-bearing mice breathing pure oxygen were intravenously administered with nano-PFC. Then, a US transducer was placed on the tumor sites to trigger burst oxygen release from nano-PFC for tumor hypoxia relief. It is worth mentioning that the nano-PFC could reach the lung through blood circulation, be reoxygenated, and then return to the tumor again. Thus, these repeated cycles of deoxygenation and reoxygenation significantly improved oxygen levels in tumors from 17% to 49% after 30 min of treatment with nano-PFC and US, validated by the *in vivo* PA imaging (Fig. 16c and d). After the 4T1 tumors were treated with US for 30 min post-injection of nano-PFC under hyperoxic inhalation, 6 Gy of X-ray irradiation outstandingly caused nearly 3 times the inhibition rate compared to that of the nano-PFC + RT + O_2 group (Fig. 16e and f). In addition, this US-triggered tumor oxygenation strategy may also be beneficial to other types of cancer therapies, such as PDT, immunotherapy, sonodynamic therapy, and chemotherapy, *etc.*

3.3 Exo/endogenous dual stimuli-responsive strategies

Beside single exogenous or endogenous stimulus-responsive strategy, exo/endogenous dual stimuli-responsive strategies are also trending. The exo/endogenous dual stimuli-responsive strategies are able to integrate the merits of auto-response to TME and remote "on-off" switchable control, thus improving the precision of responsiveness. In addition, the complementarity of endogenous and exogenous stimuli can significantly enhance the treatment efficacy and reduce the adverse effect on healthy tissues to enable precision RT.

3.3.1 pH/light responsiveness. Until now, combining pH/light as endo/exogenous stimuli to control drug release or regulate size/shape of NPs has been one of the most appealing strategies for enhanced RT. For example, Hua *et al.* proposed a pH/light-induced size-transformation strategy to enhance RT/PTT.[292] Concretely, the Au nanoclusters (AuNCs) were modified with carboxymethyl chitosan (CS) and loaded with indocyanine green (ICG) to fabricate Cs–Au–ICG NPs with an average size of about 50 nm. The Cs–Au–ICG NPs could self-assemble into larger-sized aggregates (>1000 nm) in response to the acidic TME for enhanced tumor retention. Then, NIR laser-induced photothermal heating could disassemble the aggregates into ultrasmall AuNCs for deep tumor penetration. Thus, the pH-responsive tumor accumulation/retention as well as NIR laser-triggered tumor penetration of AuNCs could significantly augment the radiosensitizing effect. The *in vivo* antitumor efficacy evaluation indicated that synergistic RT/PTT based on the pH/light-triggered size-transformation of Cs–Au–ICG NPs could effectively cause more than 2.5 times the inhibition rate compared to the ICG + RT/PTT group.

3.3.2 pH/ROS/light responsiveness. Recently, Fu *et al.* fabricated pH/ROS/light stimuli-responsive disassembled nanocomposites for enhanced tumor penetration and radiosensitization (Fig. 17a).[293] The molybdenum disulfide (MoS_2) nanosheets were loaded with hafnium dioxide (HfO_2) NPs and then modified with dextran (M/H-D). The M/H-D nanocomposites were incubated for 5 d and 10 d with physiological H_2O_2-pretreated simulated body fluid (SBF, pH = 7.4), simulated tumor microenvironment (STME, pH = 6.0), and simulated lysosomal fluid (SLF, pH = 4.5), respectively. The TEM images showed that the M/H-D nanocomposites under SLF + H_2O_2 conditions degraded more significantly compared to those treated with SBF + H_2O_2 or STME + H_2O_2. Moreover, more obvious degradation of M/H-D nanocomposites could be observed after NIR laser irradiation, indicating that the M/H-D nanocomposites could degrade and release ultrasmall HfO_2 NPs in response to both exogenous (NIR laser) and endogenous stimuli (acid pH and H_2O_2). The *in vivo* fluorescence staining of tumor slices revealed that the M/H-D nanocomposites in laser-irradiated tumors showed deeper diffusion and penetration due to the responsive release of small-sized HfO_2 NPs. The permeation area of tumor slices in the M/H-D plus laser group was over two-fold that of those treated with M/H-D alone. Thanks to the great photothermal conversion efficiency and peroxidase-like catalytic ability of MoS_2 nanosheets, the M/H-D nanocomposites could heat up the tumor upon NIR laser irradiation and catalyze intratumoral H_2O_2 to generate $^{\bullet}OH$. Simultaneously, *in situ* tumor heating was able to increase tumor oxygenation to attenuate tumor hypoxia and further sensitize RT. Therefore, these exogenous and endogenous dual stimuli-responsive nanoradiosensitizers could completely regress the SMMC-7721 tumors upon X-ray and NIR laser irradiation.

3.3.3 ROS/X-ray responsiveness. Zhang *et al.* developed a novel exogenous (X-ray) and endogenous (ROS) dual stimuli-responsive nanoradiosensitizer ($Cu_2(OH)PO_4$@PAAS NCs) by

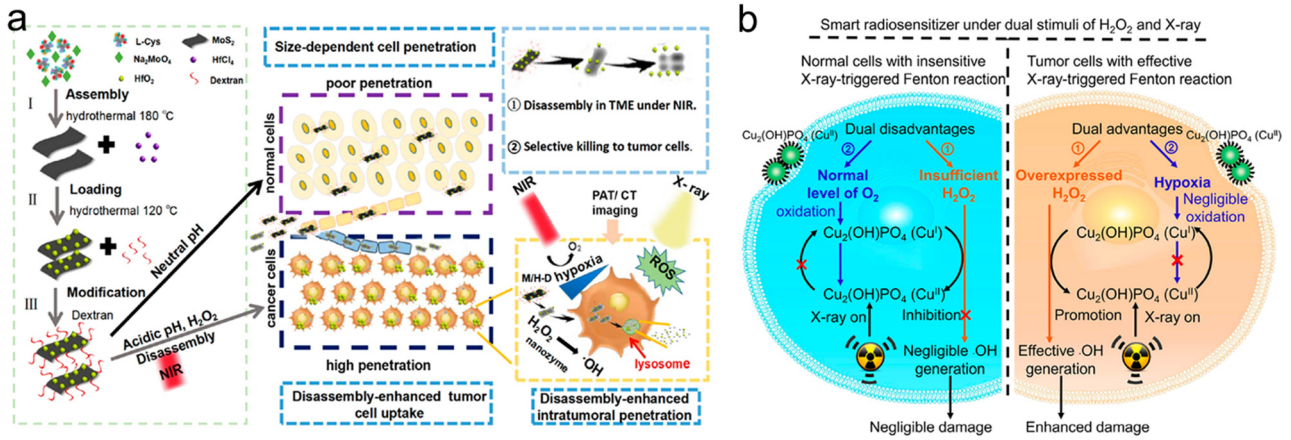

Fig. 17 Exo/endogenous dual stimuli-responsive strategies. (a) Schematic illustration of the synthetic procedures of M/H-D and its disassembly in TME under NIR laser irradiation. The disassembly of M/H-D can enhance tumor penetration. M/H-D can function as a peroxidase-like nanocatalyst to catalyze H_2O_2 to produce •OH for tumor cell killing. Reproduced with permission from ref. 293. Copyright 2020, American Chemical Society. (b) A scheme showing the mechanism of $Cu_2(OH)PO_4$@PAAS NCs for enhanced RT *via* X-ray-triggered Fenton reaction. Reproduced with permission from ref. 294. Copyright 2019, American Chemical Society.

using poly(acrylic acid) sodium (PAAS) to decorate $Cu_2(OH)PO_4$ nanocrystals (NCs) for precision RT (Fig. 17b).[294] The TEM images showed that $Cu_2(OH)PO_4$@PAAS NCs with an average diameter of 5 ± 2 nm had a spherical morphology. Conventional Fenton reaction is always spontaneous, which cannot be spatiotemporally controlled by external stimuli. However, photon-induced Fenton reaction occurs only in the presence of both photon (X-ray or light) and H_2O_2 stimuli.[295–298] The $Cu_2(OH)PO_4$@PAAS NCs could generate Cu^I active sites upon X-ray irradiation, which was detected by the selective sequestering agent neocuproine. Moreover, the rapid photocurrent responses of $Cu_2(OH)PO_4$@PAAS NCs were clearly detected upon X-ray irradiation due to production of electron–hole pairs. With the effective generation of Cu^I active sites, the $Cu_2(OH)PO_4$@PAAS NCs upon X-ray irradiation could catalyze the decomposition of H_2O_2 into •OH, which was detected by terephthalate (TA). However, there was almost no •OH generation when the $Cu_2(OH)PO_4$@PAAS NCs were treated with X-ray or H_2O_2 alone, indicating that the Fenton-like reaction could only happen in the presence of both X-ray and H_2O_2. The generated •OH was able to strengthen the DNA damage of cancer cells and further sensitize RT. The *in vitro* clonogenic assay revealed that the survival fraction of HeLa cells treated with $Cu_2(OH)PO_4$@PAAS NCs plus X-ray was 24.03% compared to 66.44% of HeLa cells treated with X-ray alone. In addition, $Cu_2(OH)PO_4$@PAAS NCs plus X-ray irradiation could almost eliminate subcutaneous HeLa tumors, whereas the relative tumor volume was still over 5–20 days after treatment.

Overall, the exo/endogenous dual stimuli-responsive radiosensitizers were able to integrate the merits of remote controllability and flexibility of auto-response to TME, thereby improving precision of responsiveness. However, the multi stimuli-responsive strategy for precision RT is currently too complicated for clinical translation.[299]

4. Image-guided techniques for precision RT

Multifunctional imaging techniques, including MRI, SPECT, CT, PET, FLI, and PAI, can provide important information on tumor location, boundaries and responses to RT. Diverse image-guided precision RT techniques, such as FL image-guided RT, MR image-guided RT, PA image-guided RT, US image-guided RT, CT image-guided RT, and nuclear image-guided RT, will be discussed in this section (Table 3). In addition, bimodal and multimodal imaging can compensate for the drawbacks of each single imaging modality and take advantage of each imaging technique.

4.1 Fluorescence (FL) image-guided precision RT

Featuring the advantages of high sensitivity, non-invasiveness, real-time detection, short imaging acquisition time, and minimal toxicity to normal tissues, FL imaging has become one of the most commonly used imaging modalities. Nevertheless, the *in vivo* application of FL imaging is restricted by strong light–tissue interaction (*e.g.*, absorption, autofluorescence, scattering, *etc.*) within the UV-vis range.[304–306] Thus, to overcome these limitations, fluorescence probes within the near-infrared (NIR) window have been developed to enhance tissue penetration and reduce background noise. Besides, FL imaging has been used to provide precise information of biodistribution and accumulation of NPs to guide precision radiotherapy.[34,61,136,307–312]

For example, Wang *et al.* doped Mn(II) ions into Ag_2Se QDs with NIR-II fluorescence to fabricate a novel nanoprobe (Mn-doped Ag_2Se QDs) for NIR-II FL imaging-guided RT (Fig. 18a).[35] The nanoprobe was then conjugated with the RGD peptide for tumor-targeted delivery. The well-prepared Mn-doped Ag_2Se–RGD–PEG nanoprobes could catalyze the decomposition of H_2O_2 into O_2 to alleviate hypoxic TME for radiosensitization.

Table 3 Representative image-guided nanotechnologies for precision RT

Imaging modality	Nanoparticles	Imaging component	Source	Tumor models	Guiding strategy	Ref.
FL imaging	CAT-SAHA@PLGA-IR775	IR775	IVIS imaging system (Ex = 745 nm, Em = 820 nm)	CT26 subcutaneous tumor-bearing mice	Determine peak concentration in tumor (24 h) for RT	34
	DiI/Au-DOX@PO-ANG NPs	DiI	IVIS imaging system	U87MG orthotopic glioblastoma-bearing mice	Determine peak concentration in tumor (24 h) for RT	312
	Mn-doped Ag_2Se–RGD–PEG	Ag_2Se QDs	NIR-II small animal imaging system (Ex = 808 nm, 980 nm long-pass filter)	4T1 subcutaneous tumor-bearing mice	Determine peak concentration in tumor (2 h) for RT	35
	CPPDA-Hf@Poloxamer	CPPDA	NIR-II small animal imaging system (Ex = 808 nm)	4T1 subcutaneous tumor-bearing mice	Determine peak concentration in tumor (24 h) for RT	317
	R-AIE-Au	Au cluster	IVIS imaging system (Ex = 570 nm, Em = 585 nm)	U87MG subcutaneous tumor-bearing mice	Determine peak concentration in tumor (24 h) for RT	38
MR imaging	CDs	Gd	MRI scanner	Heps subcutaneous tumor-bearing mice	Locate tumor (T_1 MR imaging)	322
	NSC@SiO_2-SNO	NA	3.0 T MRI scanner	4T1 subcutaneous tumor-bearing mice	Monitor oxygen level and radiosensitivity of tumor (BOLD/DWI fMRI)	36
	Hb-Lipo	NA	3.0 T MRI scanner	CT26 subcutaneous tumor-bearing mice	Monitor the tumor oxygenation (BOLD fMRI)	396
	MR-CA	Mn^{2+}	7.0 T MRI scanner	Ultrasmall subcutaneous BxPC3 pancreatic tumor-bearing mice, spontaneous BxPC3 pancreatic tumor-bearing mice	Stratify the degree of tumor hypoxia for precision RT (T_1 MR imaging)	335
US imaging	NDr(Au + PFOB + O_2)	PFOB	US machine with a sector transducer	EMT-6 subcutaneous tumor-bearing mice	Determine peak oxygen concentration in tumor (12 h) for RT	338
PA imaging	Ir-R/T NCs	Ir NCs	PA imaging system	4T1 subcutaneous tumor-bearing mice	Determine peak concentration in tumor (4 h) for RT	230
	Au-TiO_2@ZnS	Au NRs	PA imaging system	MC38 orthotopic liver cancer-bearing mice	Determine peak concentration in tumor (24 h) for RT	342
	PFC@PLGA-RBCM	HbO_2	PA imaging system	4T1 subcutaneous tumor-bearing mice	Determine peak oxygen concentration in tumor (24 h) for RT	29
	$Cu_{2-x}Se$@PtSe	HbO_2	PA imaging system	4T1 subcutaneous tumor-bearing mice	Determine peak oxygen concentration in tumor (5 h) for RT	343
CT imaging	BNTs	Bi	CT scanner	Huh-7 subcutaneous tumor-bearing mice	Determine peak concentration in tumor (9 h) for RT	40
	dAuNP-FA	AuNP	CT scanner	4T1 subcutaneous tumor-bearing mice	Determine peak concentration in tumor (8 h) for RT	352
Nuclear medicine imaging	^{64}Cu-Eu/VBBO lipo	^{64}Cu (PET)	PET scanner	FaDu subcutaneous tumor-bearing mice	Monitor biodistribution of radioisotope	370
	^{131}I-AuNFs	^{131}I (SPECT)	Infinia GE SPECT	4T1 subcutaneous tumor-bearing mice	Determine peak concentration in tumor (24 h)	364
	BSO/GA-(^{99m}Tc)Fe(II)@liposome	$^{99m}Tc^{4+}$ (SPECT)	Animal SPECT imaging system	4T1 subcutaneous tumor-bearing mice	Determine peak concentration in tumor (24 h)	370
	^{89}Zr-TiO_2-Tf NPs	^{89}Zr (PET)	Inveon small-animal PET/CT scanner	MM1.S bearing SCID mice	Monitor biodistribution of radioisotope	380
MR/CT imaging	NSC@mSiO_2-SNO/ICG NPs	Eu^{3+}-doped $NaGdF_4$ scintillating nanocrystal	3.0 T MRI scanner, CT scanner	4T1 subcutaneous tumor-bearing mice	Determine peak concentration in tumor (24 h)	64
MR/FL imaging	Cyp-PMAA-Fe@MSCs	Fe ($T_{1/2}$ MRI), Cypate (FL)	Optical and X-ray small imaging system (Ex = 780 nm, Em = 845 nm), 7.0 T MRI scanner	LLC1 subcutaneous tumor-bearing mice	Determine peak concentration in tumor (28 h)	138
MR/PA imaging	Biomimetic CMC nanoplatform	Mn^{2+}(T_1 MRI), HbO_2 (PA)	4.7 T MRI scanner, PA imaging system	4T1 subcutaneous tumor-bearing mice	Monitor tumor concentration of NPs and oxygen	130
PA/CT imaging	WS_2 QDs	WS_2 (PA/CT)	PA imaging system, CT scanner	BEL-7402 tumor-bearing mice	Determine peak concentration in tumor (2 h)	382
	Ti_2C_3@Au	Au (PA/CT)	PA imaging system, CT scanner	4T1 subcutaneous tumor-bearing mice	Determine peak concentration in tumor (24 h)	397
PA/FL imaging	Lf-Liposome-DiR	DiR (FL), HbO_2 (PA)	PA imaging system, IVIS imaging system (Ex = 748 nm, Em = 780 nm)	4T1 subcutaneous tumor-bearing mice	Determine peak concentration of NPs and oxygen in tumor (24 h)	383
	CV@CaP	*ChlorophyII* (FL/PA), HbO_2 (PA)	PA imaging system, IVIS imaging system	4T1 subcutaneous tumor-bearing mice	Determine peak concentration of NPs and oxygen in tumor (4 h)	384

Table 3 (*continued*)

Imaging modality	Nanoparticles	Imaging component	Source	Tumor models	Guiding strategy	Ref.
CT/PA/SPECT imaging	^{99m}Tc-Bi_2Se_3 nanodots	Bi_2Se_3 (CT/PA), $^{99m}Tc^{4+}$ (SPECT)	PA imaging system, SPECT imaging system, CT scanner	4T1 subcutaneous tumor-bearing mice	Determine peak concentration in tumor (12 h)	384

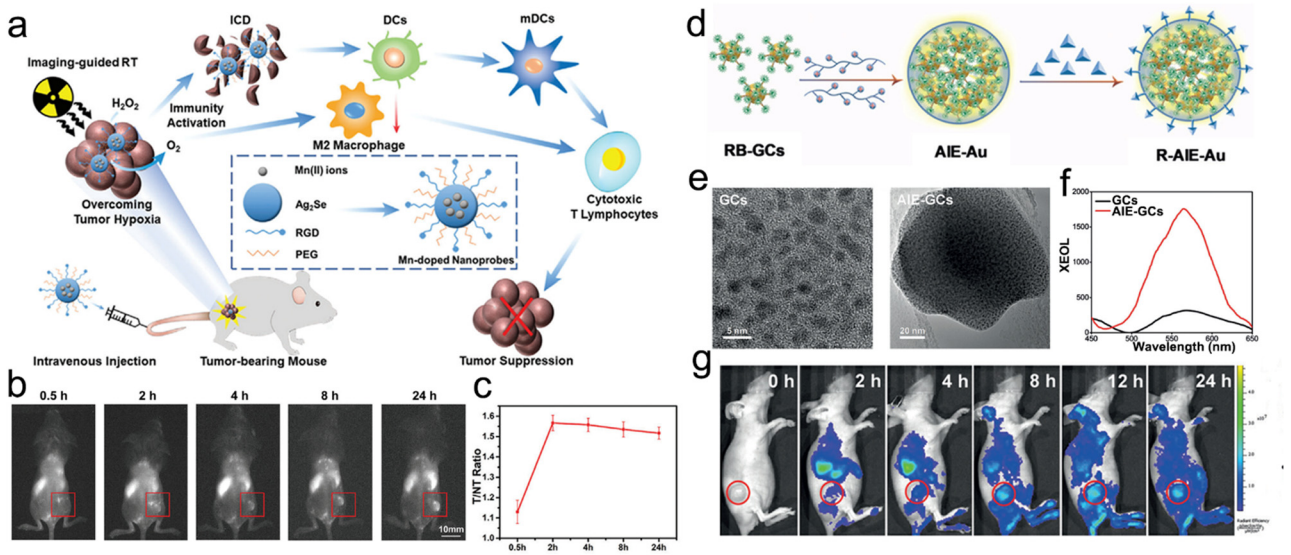

Fig. 18 FL imaging-guided precision RT. (a) A scheme showing the NIR-II FL imaging-guided RT of tumors and elicitation of antitumor immunity based on Mn-doped nanoprobes. (b) *In vivo* FL imaging of tumor-bearing mice at different time points after intravenous administration of Mn-doped nanoprobes. Scale bars = 10 mm. (c) The corresponding T/NT signal ratio curve after intravenous administration of Mn-doped nanoprobes. Reproduced with permission from ref. 35. Copyright 2021, Wiley. (d) Schematic illustration of synthetic procedures of R-AIE-Au. (e) TEM images of GCs and AIE-GCs. (f) Luminescence spectra of GCs and AIE-GCs. (g) *In vivo* FL imaging of tumor-bearing mice at different time points after intravenous administration of R-AIE-Au. Reproduced with permission from ref. 38. Copyright 2020, Wiley.

After intravenous injection of the Mn-doped Ag_2Se–RGD–PEG nanoprobes, the high-resolution NIR-II FL images revealed that the nanoprobes could selectively accumulate inside tumor boundaries (Fig. 18b). The tumor-to-normal tissue (T/NT) signal ratios gradually increased to the maximum (1.5–1.6) at 2 h post-injection (Fig. 18c). Assisted by the FL imaging guidance, 12 Gy of X-ray irradiation at 2 h post-injection of Mn-doped Ag_2Se–RGD–PEG nanoprobes completely eradicated tumors in 2 weeks. However, the tumor volume in the X-ray alone group was still above 350 mm^3 2 weeks after treatment.

Featuring unique modifiability and photoelectric properties, semiconducting polymer NPs (SPNs) have been developed as biosensors or bioimaging agents.[313,314] NIR-absorbing SPNs can even emit NIR-II fluorescence for NIR-II FL imaging.[315,316] Dai and colleagues designed a metal–polyphenolic nanosystem (CPPDA-Hf@Poloxamer) for NIR-II FL image-guided synergistic RT and photothermal therapy (PTT). Specifically, the dopamine-modified semiconducting polymer (CPPDA) was chelated with hafnium (Hf) ions and then coated with an amphiphilic polymer (Poloxamer).[317] CPPDA with broad NIR absorption could be used for FL imaging and PTT. The Hf as a high-*Z* element was able to promote X-ray deposition for radiosensitization. The CPPDA-Hf@Poloxamer presented strong NIR-II emission under both 808 nm and 1064 nm laser excitation. The *in vivo* NIR-II FL imaging under 808 nm irradiation revealed that CPPDA-Hf@Poloxamer gradually accumulated in the tumor over time and peaked at 24 h post-injection. Finally, the combined irradiation of X-ray and a 1064 nm laser at 24 h post-injection of CPPDA-Hf@Poloxamer effectively eliminated subcutaneous tumors, whereas the tumor volume in the X-ray alone group was about 400 mm^3 at 15 days post-treatment.

Unfortunately, many organic dyes suffer from the aggregation-caused quenching (ACQ) effect, which seriously attenuates the FL imaging performance. To overcome this issue, Sun *et al.* developed aggregation-induced emission (AIE) gold clustoluminogens (AIE-Au) for FL image-guided RT and PDT.[38] First, glutathione-protected gold clusters were self-assembled into AIE-GCs through a cationic polymer-mediated approach (Fig. 18e). Moreover, the X-ray-excited optical luminescence (XEOL) peak of AIE-GCs was 5.2-fold stronger than that of GCs (Fig. 18f). Next, the rose bengal (RB, a clinically used photosensitizer) conjugated GCs were self-assembled into AIE-Au and then modified with a tumor-targeting RGD peptide

(R-AIE-Au) (Fig. 18d). The *in vivo* FL imaging showed that the fluorescence signals in tumors increased over time and reached the maximum at 24 h post-injection (Fig. 18g). Guided by FL imaging, low-dose X-rays (0.5 Gy) were used to irradiate the tumor-bearing mice at 24 h post-injection and resulted in a much higher tumor inhibition rate of 97.1% compared to ~30% in the X-ray alone group.

Despite the superiority of FL imaging in guiding RT, the penetration depth and spatial resolution are still much poorer compared to other imaging techniques, such as MRI, CT, or PET.

4.2 MR image-guided precision RT

MR imaging has been extensively utilized in clinic for diagnosis due to the advantages of unlimited penetration, non-invasiveness, lack of ionizing radiation, and high spatial resolution. *In vivo* MR imaging can be used to monitor the concentration of contrast agents in various organs or tumor.[318] Furthermore, MR imaging can also show the accurate tumor location and adjacent tissues.

Wang *et al.* modified self-assembled Mn–Zn ferrite magnetic NPs with hyaluronic acid (HA) to construct a block copolymer micelle (MZF-HA) for MR image-guided RT/hyperthermia therapy (HT).[52] MZF-HA could target CD44-overexpressing tumor cells due to the selective recognition of CD44 receptors by HA. Besides, MZF-HA could heat up tumor under an alternating magnetic field (AMF) for HT. HT could also improve tumor oxygen levels and contribute to radiosensitization (Fig. 19a). Moreover, MZF-HA could be used for MRI as a T_2-weighted contrast agent with an r_2 value of 331 mM^{-1} s^{-1}. After intravenous injection, MR imaging showed gradually darkening signals in A459 xenograft tumor at 24 h and 48 h after i.v. injection, suggesting the tumor accumulation of MZF-HA (Fig. 19b). Guided by MR imaging, RT/HT remarkably reduced the relative tumor ratio to 49.6% by day 13, much lower than ~70% in the RT alone group.

Nowadays, the clinical translation of T_2-weighted contrast agents has been hampered by several limitations. For instance, the dark images based on T_2-weighted contrast agents are not preferred for observation.[75] With the bright tumor images, T_1-weighted contrast agents have attracted wide attention for guiding precision RT.[33,319–323] Gd-chelator complexes are the most commonly used T_1 contrast agents in the clinic even though they have several shortcomings, such as nephrogenic toxicity and low longitudinal relaxivity. Additionally, even small amount of Gd has been reported to remarkably improve the RT efficacy.[324] For example, Du *et al.* designed Gd-doped carbon dots (CDs) with high longitudinal relaxivity and a long circulation time for MR image-guided RT (Fig. 19c).[322] The r_1 value of Gd-doped CDs (6.45 mM^{-1} s^{-1}) was much larger than that of clinically used Magnevist (4.05 mM^{-1} s^{-1}). *In vivo* MR imaging revealed that Gd-doped CDs could significantly brighten the tumor (Fig. 19d). The values of SNR_{post}/SNR_{pre} in the tumor region reached 1.74 and 1.93 with transverse and coronal scanning, respectively (Fig. 19e). Finally, guided by T_1-weighted MR imaging, the relative tumor volume in the Gd-doped CDs + X-ray group after 7 days of treatment was about half of that in the X-ray alone group (Fig. 19f).

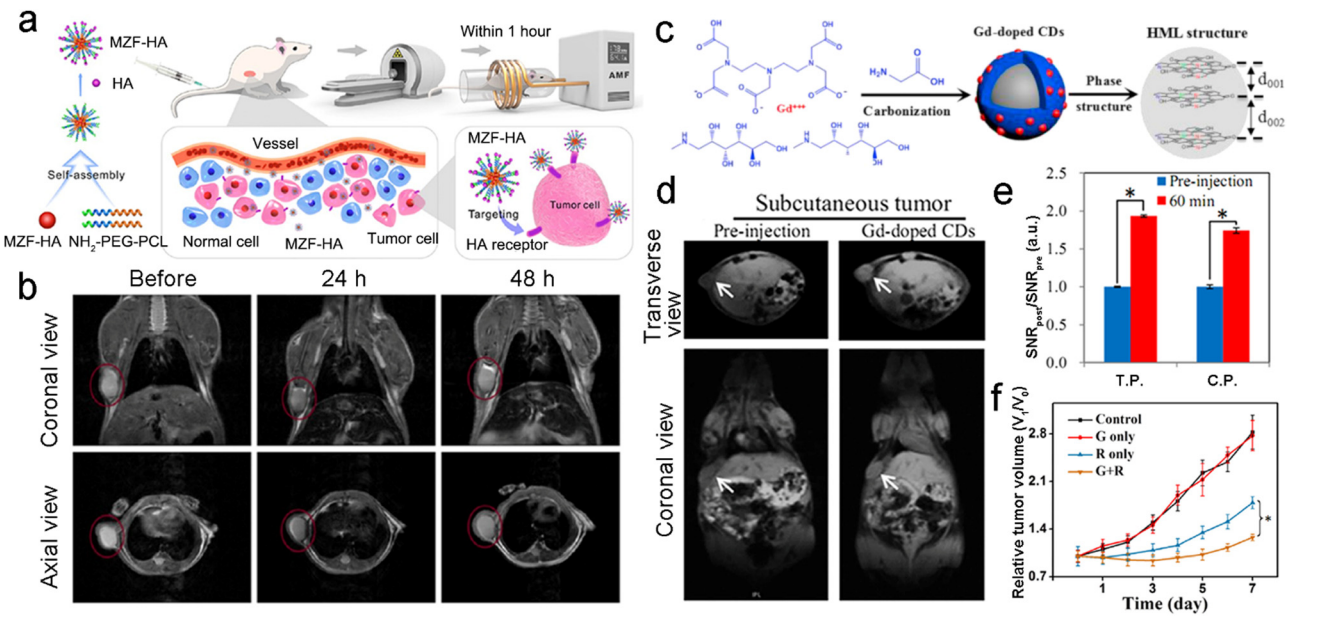

Fig. 19 MR imaging-guided precision RT. (a) Schematic illustration of the synthetic process of MZF-HA and its application in MR imaging-guided RT and hyperthermia. (b) *In vivo* T_1-weighted MR imaging of tumor-bearing mice before and after administration of MZF-HA. Reproduced with permission from ref. 52. Copyright 2020, American Chemical Society. (c) Schematic illustration of the synthetic process of Gd-doped CDs. (d) *In vivo* T_1-weighted MR imaging of subcutaneous tumor-bearing mice before and after intravenous administration of Gd-doped CDs (10 mg kg^{-1}). (e) The SNRpost/SNRpre ratio of tumor region before and after intravenous administration. (f) Tumor growth curves of tumor-bearing mice in different treatment groups. Reproduced with permission from ref. 322. Copyright 2020, Wiley.

As opposed to structural imaging, functional imaging is a medical imaging technique that detects physiological activities within a specific tissue or organ, such as blood supply, metabolism, chemical composition, *etc.*[325] The functional imaging techniques include CT perfusion imaging, functional MR imaging (fMRI), PET, magnetoencephalography (MEG), magnetic source imaging (MSI), near infrared spectroscopy (NIRS), *etc.*[326–328] fMRI can provide biological molecular information based on the anatomical structure and has attracted wide attention from basic and clinical researchers.[329] A lot of fMRI techniques have been used for *in vivo* evaluation of various biological processes in tissues, thus allowing for the presentation of spatiotemporal variations in tumor biological response to RT.[330,331] Diffusion-weighted imaging (DWI) is an fMRI technique that does not require a contrast agent. DWI can detect the random motion water protons (water diffusion). The water diffusion is closely related to tissue cellularity and cell membranes' integrity.[331] The apparent diffusion coefficient (ADC) can be used to characterize the diffusion. Compared to normal tissues with low cellularity, most tumors are hypercellular and contain lots of intact cell membranes, which restrict water diffusion and show a high signal. Since effective treatments can decrease cell density in tumor, the therapeutic effects can be monitored and evaluated in real time by DWI.[332] Blood-oxygen-level-dependent (BOLD) fMRI is a noninvasive technique for the assessment of tissue hypoxia based on endogenous paramagnetic deoxyhemoglobin levels.[333,334] An increased level of deoxyhemoglobin in hypoxic tumors leads to decreased T_2^* signal. Therefore, BOLD fMRI can be used to monitor and assess the dynamic changes of tumor oxygen levels in real time.

For example, Dou *et al.* proposed a dual fMRI (BOLD/DWI imaging) strategy for noninvasive monitoring of tumor hypoxia and radiosensitization efficacy (Fig. 20a).[36] The $NaGdF_4$:Eu^{3+} NPs were coated with a mesoporous silica layer and then loaded with S-nitrosothiol (SNO, a nitric oxide (NO) donor) (NSC@SiO_2-SNO). NSC@SiO_2-SNO could release a great deal of NO upon X-ray irradiation. The released NO was able to effectively alleviate tumor hypoxia. Next, *in vivo* BOLD/DWI imaging was used to dynamically monitor tumor oxygen levels and radiosensitivity during treatment by measuring the tumor R_2^* and ADC values. T_2-weighted MRI showed that RT plus the NSC@SiO_2-SNO could effectively inhibit tumor growth compared to the control or RT group (Fig. 20b). The tumor R_2^* value

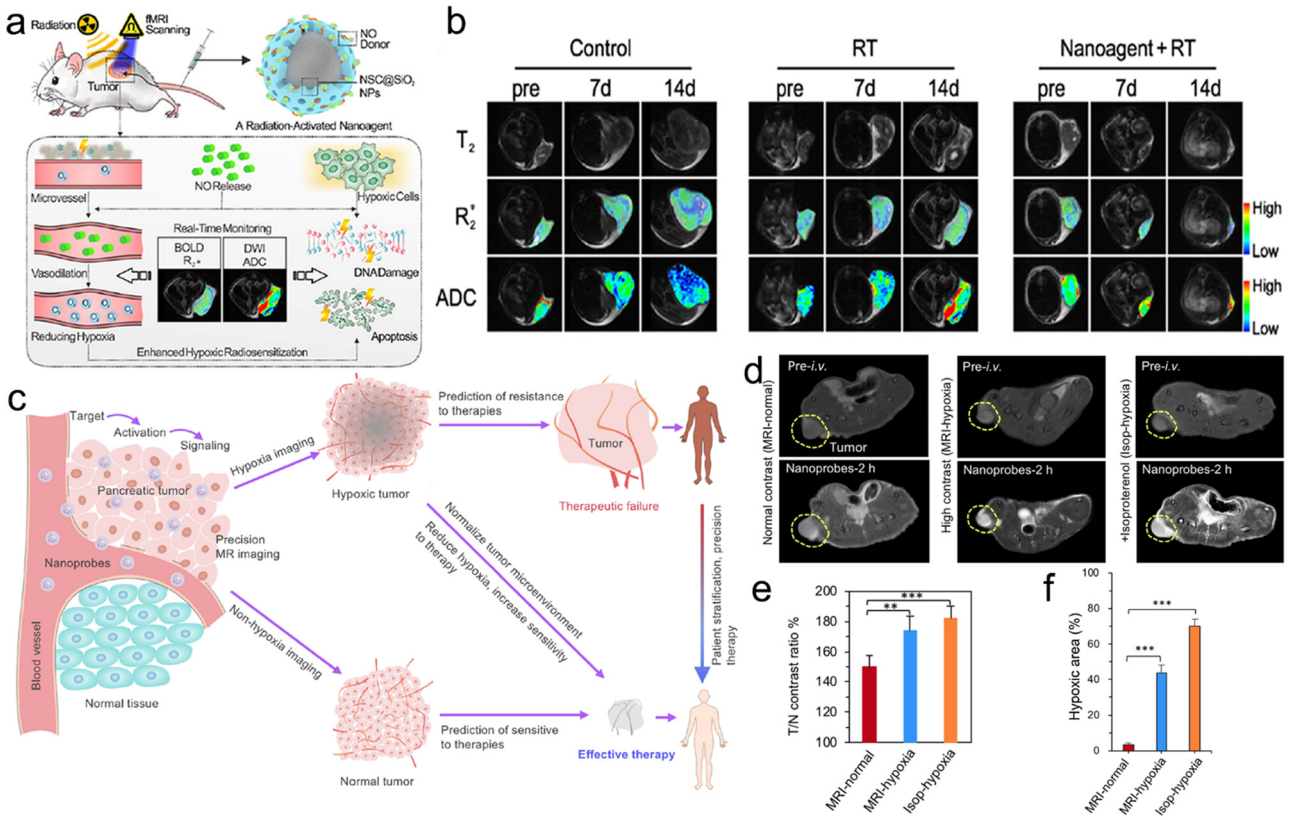

Fig. 20 Functional MR imaging-guided precision RT. (a) Schematic illustration of NO-induced tumor oxygenation and radiosensitization *via* a radiation-activated NP under real-time monitoring of BOLD/DWI imaging. (b) *In vivo* T_2-weighted, R_2^*-mapping, and ADC-mapping images before and after different treatments. Reproduced with permission from ref. 36. Copyright 2021, American Chemical Society. (c) A scheme of MR-CA nanoprobes for MR imaging of pancreatic tumors and tumor hypoxia to realize the prediction of tumor responses to RT and immunotherapy. (d) *In vivo* T_1-weighted MR imaging of subcutaneous BxPC3 pancreatic tumor-bearing mice after intravenous administration of MR-CA nanoprobes to sort tumor according to signal intensities. (e) Corresponding T/N ratios of the MR images. (f) Quantitative measurement of the hypoxia area from the immunofluorescence staining images of tumors. Reproduced with permission from ref. 335. Copyright 2021, American Chemical Society.

of both the control and RT alone groups increased slightly overtime, indicating that rapid tumor growth might lead to insufficiency of tumor blood supply and decrease of oxygen levels. However, the NSC@SiO_2-SNO-mediated RT could remarkably decrease the tumor R_2^* value from 40.25 s^{-1} at the beginning to 33.39 and 21.06 s^{-1} at day 7 and day 14, respectively, suggesting significant hypoxia relief. In addition, the tumor ADC value in the NSC@SiO_2-SNO + RT group significantly increased from the initial 0.973×10^{-3} mm^2 s^{-1} to 2.325×10^{-3} mm^2 s^{-1} at day 14, indicating that NSC@SiO_2-SNO-mediated radiosensitization could effectively kill tumor cells and decrease cell density. However, the tumor ADC value in the RT alone group only increased from 0.898×10^{-3} mm^2 s^{-1} to 1.095×10^{-3} mm^2 s^{-1}.

Besides fMRI, nanotechnology-based MR imaging can also be utilized to monitor tumor response. Mi and co-workers designed MR contrast amplification (MR-CA) nanoprobes for the early diagnosis of pancreatic tumor and prediction of tumor sensitivity to RT (Fig. 20c).[335] The MR-CA nanoprobes were fabricated based on PEGylated polyanions and self-assembly of Mn^{2+}-doped CaP NPs. The nanoprobes could degrade in response to the low pH value of TME and rapidly release Mn^{2+} to boost higher molecular relaxivity (r_1) *via* binding with surrounding proteins.[336] Owing to acid-responsive Mn^{2+} release, the MR-CA nanoprobe was able to sensitively and selectively image ultrasmall, orthotopic, and spontaneous pancreatic tumors compared to the clinically applied Gd-DOTA (Fig. 20d). Besides, the tumor-to-normal tissue (T/N) contrast ratio in the MR-CA group was much higher than that in the Gd-DOTA group (Fig. 20e). The precise MR imaging of ultrasmall pancreatic tumors allowed early detection and precision therapy of the tumors. In addition, MR-CA nanoprobe-based MR imaging could stratify the degree of tumor hypoxia so as to predict the tumor response to RT and tumor prognosis. Isoproterenol hydrochloride was injected intraperitoneally into BxPC3 tumor-bearing mice in order to establish hypoxic tumors as the positive control (denoted as isop-hypoxia). Based on T/N contrast ratios, the other BxPC3 tumors were divided into two groups: MRI-normal (normoxic tumors with the ratios lower than 160%) and MRI-hypoxia (hypoxic tumors with the ratios higher than 160%). The immunofluorescence staining of these tumors showed that MRI-hypoxic tumors exhibited around 43% hypoxic area in tumor regions compared to 3.5% and 70% in MRI-normal tumors and the positive group (isop-hypoxia), respectively (Fig. 20f). For *in vivo* anti-tumor evaluation, the MRI-hypoxic tumor showed lower sensitivity to RT and over 600 mm^3 of tumor volume after treatment, whereas the RT showed effective inhibition of tumor growth in MRI-normal tumors with nearly 200 mm^3 of tumor volume. In short, MR imaging can be used to guide RT by providing anatomical structure information, tumor accumulation of radiosensitizers, and molecular biological information of TME.[337] However, MR imaging is limited by high concentration of contrast agents and relatively long acquisition time required for imaging. Therefore, future research needs to focus on substantially improving the MR imaging sensitivity based on the contrast agents.

4.3 US image-guided precision RT

US imaging has been commonly used in clinical practice due to the advantages of low cost, real-time imaging, and noninvasiveness. US can be applied to guide precision RT by dynamically monitoring the tumor accumulation of NPs. For example, Jiang *et al.* encapsulated ultrasmall AuNPs and a liquid perfluorooctyl bromide (PFOB) core to construct a nanodroplet (NDr) for US image-guided precision RT. The NDr was then oxygenated to generate hierarchical multiplexing NDr(Au + PFOB + O_2) (Fig. 21a).[338] Next, the NDr(Au + PFOB + O_2) was doped with *N*,*N*-bis(2-hydroxyethyl)-*N*-methyl-*N*-(2-cholesteryloxycarbonyl aminoethyl)ammonium bromide (BHEM-Chol) for a slightly positive charge, thus allowing the NDrs to target the tumor vessel and accumulate in the tumor. Moreover, the AuNPs inside the NDrs could deposit X-ray energy for radiosensitization. Furthermore, under US stimulation, the NDrs could break and rapidly release a lot of O_2 for enhanced RT (Fig. 21b and c). In addition, the US imaging could real-time track the NDrs. The *in vivo* US imaging showed that echo signals in tumor regions gradually increased over time and peaked at 12 h after intravenous injection (Fig. 21d–f), indicating that the 12 h post-injection could be the optimal time point for further RT. Finally, the NDr(Au + PFOB + O_2) + US + RT group displayed the highest tumor inhibition rate of 93.04% after 20 days of treatment compared to 49.62% of the RT alone group (Fig. 21g). In this study, the US served as both an imaging modality for real-time tracking and a trigger for O_2 release, realizing precision oxygen-elevated RT.

4.4 PA image-guided precision RT

PAI as a hybrid imaging technique integrates high spatial resolution of US imaging and high contrast and sensitivity of optical imaging.[339] PA imaging contrast agents, including Au nanostars, Au nanorods, AuNPs, ICG, methylene blue, and transition-metal chalcogenides, *etc.*, have been extensively applied for tumor visualization and image-guided therapy.[340] Besides, several studies have utilized PA imaging to real-time track the tumor accumulation of radiosensitizers and monitor tumor oxygen levels for guiding precision RT.[29,37,230,341–344]

Wang *et al.* fabricated dual targeting peptide (RGD and TAT)-modified ultrasmall iridium (Ir) nanocrystals (Ir-R/T NCs) for PA imaging-guided RT (Fig. 21h).[230] Ir in the nanocrystals as a high-*Z* element could deposit X-ray energy for radiosensitization. Moreover, based on the dual targeting peptides, the Ir-R/T NCs could target 4T1 tumor cells and subsequently target the nucleus. The intrinsic NIR absorption of Ir-R/T NCs enabled PA imaging and photothermal capability. The *in vivo* PA imaging of 4T1 tumor-bearing mice displayed that the PA signals of Ir-R/T NCs in the tumor region reach the maximum at 4 h after intravenous administration (Fig. 21i). Guided by PA imaging, the X-ray and NIR irradiations were imposed on subcutaneous tumors at 4 h post-injection for synergistic RT/PTT, resulting in complete tumor eradication

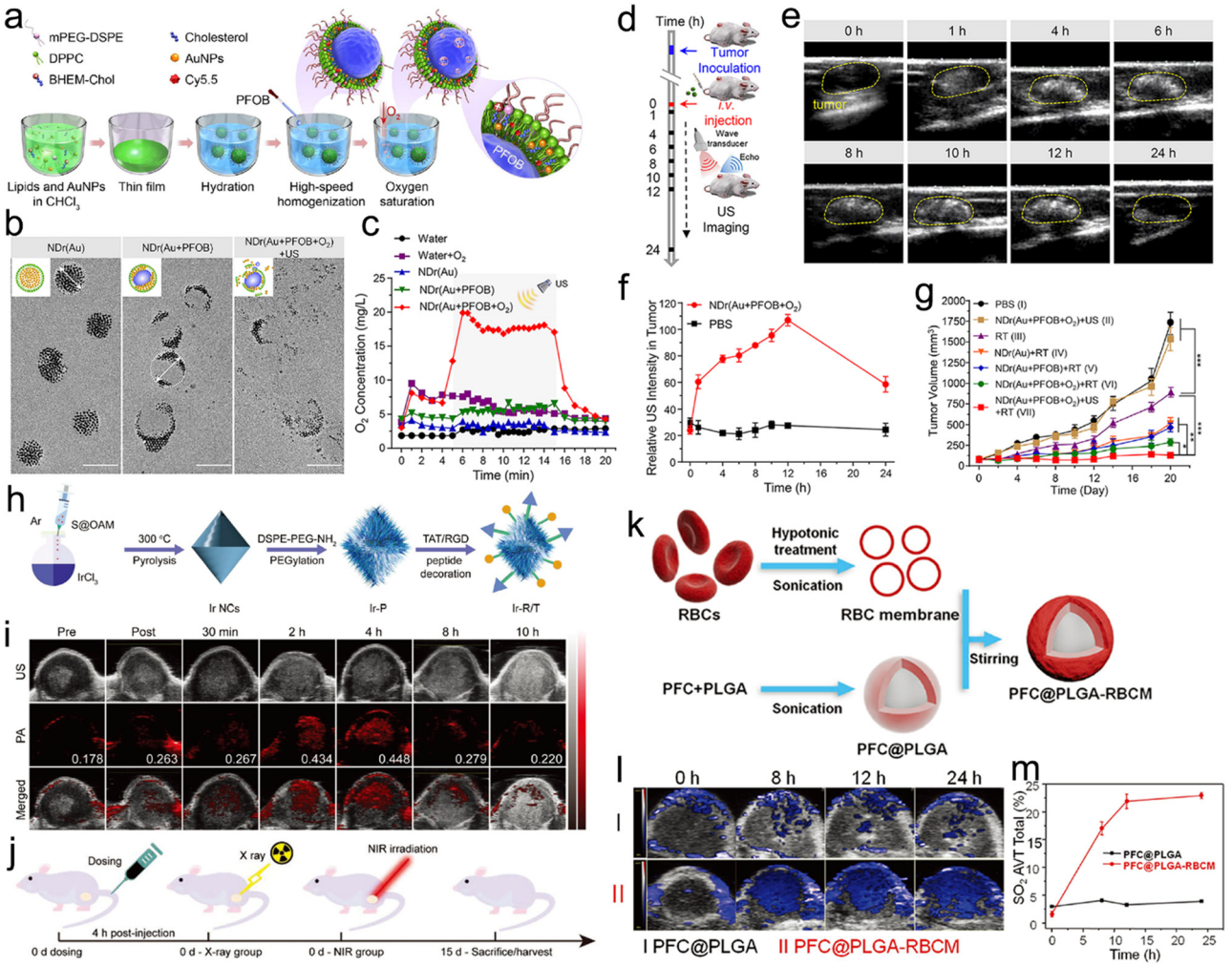

Fig. 21 US or PA imaging-guided precision RT. (a) A scheme of synthetic procedures of hierarchical multiplexing NDrs. (b) TEM images of NDr(Au), NDr(Au + PFOB), and NDr(Au + PFOB + O_2) under US (130 W, 20 kHz, 5 min). (c) *In vitro* O_2 release profiles of NDr(Au), NDr(Au + PFOB), and NDr(Au + PFOB + O2) treated with US. (d) US imaging schedule of EMT-6 tumor-bearing mice. (e) US images of tumor-bearing mice at different time points after intravenous administration of NDr(Au + PFOB + O2). Yellow dash circles: tumor regions. (f) Relative US intensities in the tumor region at different time points after intravenous administration of NDr(Au + PFOB + O2). (g) Tumor growth curves of mice in different treatment groups. Reproduced with permission from ref. 338. Copyright 2018, American Chemical Society. (h) A scheme of synthetic procedures of Ir-R/T NCs. (i) *In vivo* PA imaging of tumors at different time points after administration of Ir-R/T NCs (8 mg kg^{-1}). (j) Treatment schedule of *in vivo* RT/PTT of tumors. Reproduced with permission from ref. 230. Copyright 2019, Wiley. (k) A scheme of synthetic procedures of PFC@PLGA-RBCM NPs. (l) *In vivo* PA imaging of tumors at different time points after administration of PFC@PLGA and PFC@PLGA-RBCM NPs. (m) Quantification of oxyhemoglobin saturation concentrations based on PA images of tumors. Reproduced with permission from ref. 29. Copyright 2017, Wiley.

(Fig. 21j). However, the tumor volume in the X-ray alone group was still 520 mm^3 after 15 days of treatment.

Besides tracking tumor accumulation of radiosensitizers, the PA imaging has also been utilized to determine the tumor oxygenation status by taking advantages of the difference in the optical absorption spectrum of deoxygenated haemoglobin (λ = 750 nm) and oxygenated hemoglobin (λ = 850 nm).[345] Importantly, hypoxic TME in many types of solid tumors is closely related to radioresistance and severely hampers RT efficacy. Liu and co-workers encapsulated PFC into poly(D,L-lactide-*co*-glycolide) (PFC@PLGA) and then coated the PFC@PLGA with a red blood cell membrane (PFC@PLGA-RBCM NPs) (Fig. 21k).[29] The PFC@PLGA-RBCM NPs with excellent blood circulation could accumulate in the interior region of solid tumors. Moreover, PFC@PLGA-RBCM NPs with high oxygen carrying capability could effectively alleviate tumor hypoxia. *In vivo* PA imaging revealed that the total oxygenation levels within the whole tumor region (sO_2 Tot) increased from 1.6% of pre-injection to 24% at 24 h post-injection (Fig. 21l and m), which were further confirmed by immunofluorescence staining of tumor slices with hypoxyprobe and anti-HIF-1α. Finally, guided by PA imaging, the X-ray radiation (8 Gy) was given to the 4T1 tumor-bearing mice at 24 h post-injection of PFC@PLGA-RBCM for precision RT, resulting in tumor weight about half that of the X-ray alone group after 2 weeks of treatment.

4.5 CT image-guided precision RT

As a noninvasive medical imaging test, CT imaging has advantages of short acquisition time, deep penetration and low cost. Nevertheless, the clinically used iodinated compound-based CT contrast agents have shown limited success due to their extremely short blood circulation half-life.[346] Furthermore, patients need to be injected with a large amount of iodine-based contrast agents owing to the low X-ray attenuation effect of iodine.[347] Inorganic nanomaterials with high X-ray attenuation coefficients have been regarded as potential alternative CT contrast agents, such as bismuth (Bi), gold (Au), tantalum (Ta), and platinum (Pt).[348–351] In addition, these high-*Z* metallic nanomaterials can not only serve as CT contrast agents but also deposit X-ray energy for radiosensitization.[91,352–355]

The U.S. Food and Drug Administration (FDA) claims that renal clearance of injected metal nanomaterials is essential to avoid side effects associated with their long-term retention.[356] However, the renal-clearable nanomaterials with ultrasmall sizes cannot effectively accumulate in tumor site due to their rapid clearance *in vivo*. To address this issue, Hu *et al.* proposed a controlled assembly strategy by assembling ultrasmall $(BiO)_2CO_3$ nanoclusters (BNCs, 1.5 nm) into hollow $(BiO)_2CO_3$ nanotubes (BNTs) (Fig. 22a).[40] Due to the higher X-ray attenuation coefficient of Bi, the *in vitro* CT values (Hounsfield unit, HU) of BNTs were significantly higher than those of iohexol at equal molar concentrations. The *in vivo* reconstructed 3D CT imaging of tumor-bearing mice showed that the CT value in the tumor region increased over time and peaked at 9 h post-injection of BNT (Fig. 22b and c). However, the BNC group displayed a relatively low enhancement signal at the tumor site (Fig. 22b and c). Importantly, the BNTs could be disassembled into nanoclusters under acidic TME and then cleared *via* kidneys. In addition, the BNTs were loaded with DOX (loading efficiency of ~53%) for CT image-guided synergistic RT/chemotherapy. Guided by CT imaging, BNTs/DOX plus RT achieved a tumor suppression rate of ~83.5%, much higher than that of the BNTs plus RT group (42.4%) and BNTs/DOX alone group (32.2%) (Fig. 22d).

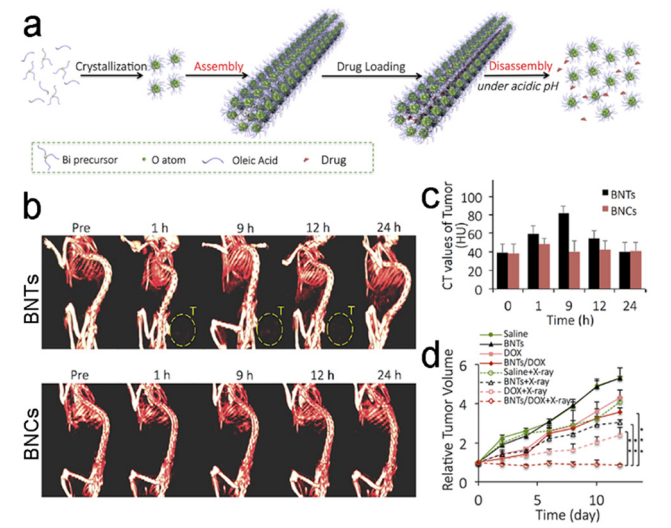

Fig. 22 CT image-guided precision RT. (a) A scheme of synthetic procedures of BNTs. (b) *In vivo* reconstructed 3D CT imaging of tumor-bearing mice at various time points after intravenous administration of BNTs and BNCs. (c) *In vivo* CT value of tumor sites at various time points after intravenous administration of BNTs and BNCs. (d) Tumor growth curves of mice received different treatments. Reproduced with permission from ref. 40. Copyright 2018, American Chemical Society.

4.6 Radionuclide image-guided precision RT

SPECT and PET, two major molecular imaging modalities in nuclear medicine, can detect radioactive signals from radioisotopes and offer functional imaging, thus allowing clinical diagnosis, delivery of targeted therapeutics, and assessment of response to treatment. For PET imaging, the positrons emitted by radionuclides interact with the nearby electrons to produce annihilation and then release energy in the form of two gamma ray photons in the opposite directions. The gamma ray photons can be detected by PET. SPECT can detect the gamma ray photons emitted by radioisotopes during radioactive decay.[357] SPECT/PET imaging can play multiple roles in cancer management, such as determining tumor volume, providing metabolic information of TME, and offering biodistribution information of radiolabeling drugs.[358–360]

A lot of studies have utilized SPECT imaging based on various radioisotopes (*e.g.*, ^{131}I, ^{99m}Tc, and ^{177}Lu) to observe pharmacokinetics and biodistribution of radioactive drugs.[361–363] For instance, Cheng *et al.* designed radioisotope ^{131}I-labeled Au nanoframeworks (^{131}I-AuNFs) for synergistic RIT/PTT of breast cancer.[364] Specifically, the AuNFs were coated with polydopamine (PDA) and further chelated with ^{131}I to construct ^{131}I-AuNFs (Fig. 23a). ^{131}I with the advantages of long half-period and suitable radiation energy was used for SPECT imaging and RIT. The as-prepared ^{131}I-AuNFs exhibited steady radioactivity and great photothermal conversion efficiency. The *in vivo* SPECT imaging was used to observe the biodistribution of ^{131}I in 4T1 tumor-bearing mice, showing that the radiosignals in the tumor regions of ^{131}I-AuNF groups gradually increased and peaked at 24 h post-injection (Fig. 23b). Guided by *in vivo* SPECT imaging, the NIR-II laser (1 W cm^{-2}, 10 min) was irradiated on subcutaneous 4T1 tumor at 24 h post-injection for PTT. The *in vivo* SPECT imaging-guided RIT/PTT strategy showed a tumor inhibition rate of 100%, much higher than 57.8% of the AuNFs plus the NIR-II laser group.

PDT as an effective antitumor treatment is hampered by limited tissue penetration depth of light and poor tumor-targeting ability of photosensitizer (PS).[365] To overcome these limitations, the scintillating materials (*e.g.*, terbium (Tb), europium (Eu), *etc.*) can convert ionizing radiation into visible light to trigger PS to generate ROS (X-ray-induced PDT).[275,366,367] Likewise, instead of X-ray irradiation, the Cerenkov luminescence emitted by RIT can also be used to induce PDT.[368,369] Lee *et al.* designed a ^{64}Cu-labeled Eu-diethylenetriaminepentaacetic acid (Eu-DTPA)/Victoria blue-BO (VBBO, a PS) co-loaded liposome (^{64}Cu-Eu/VBBO lipo) for *in vivo* PET imaging and radioisotope-mediated PDT.[370] The efficiency of luminescence resonance energy transfer between Eu-DTPA and VBBO was

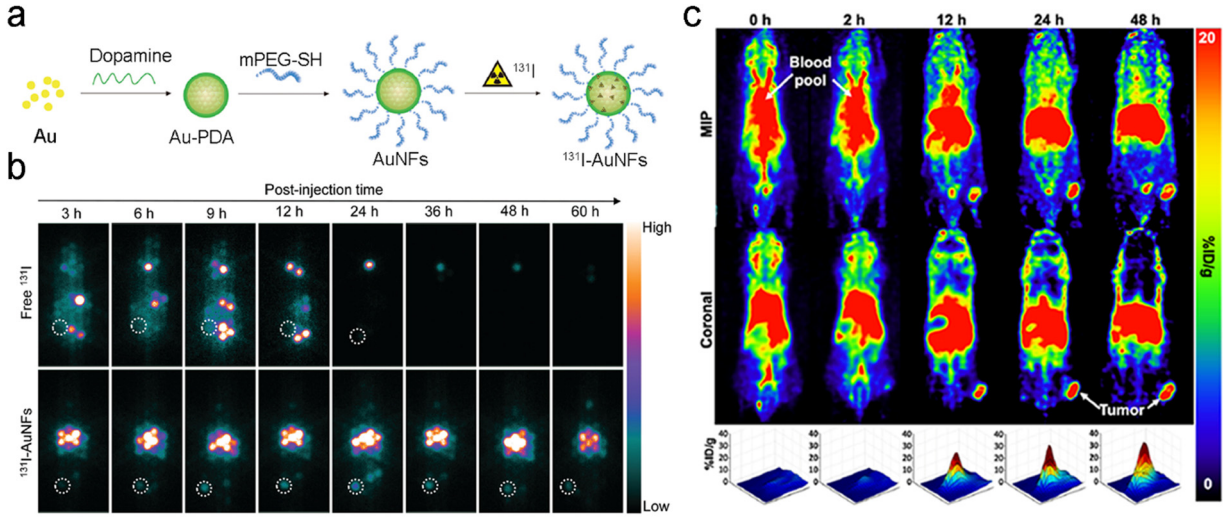

Fig. 23 PET/SPECT imaging-based RT. (a) A scheme of synthetic procedures of ^{133}I-AuNFs. (b) *In vivo* SPECT imaging of tumor-bearing mice at different time points after intravenous administration of free ^{133}I and ^{133}I-AuNFs. Reproduced with permission from ref. 364. Copyright 2021, Royal Society of Chemistry. (c) *In vivo* PET imaging of FaDu tumor-bearing mice at various time points after intravenous administration of ^{64}Cu-Eu/VBBO lipo (upper panel: maximal intensity projection (MIP); middle panel: coronal view; lower panel: surface plot for the tumor region from the coronal image). Reproduced with permission from ref. 370. Copyright 2020, American Chemical Society.

6-fold higher than that in Cerenkov luminescence energy transfer (CLET). Moreover, *in vivo* PET imaging was used to track ^{64}Cu-Eu/VBBO lipo in mice and revealed that the ^{64}Cu-Eu/VBBO lipo with 20.15 h of circulation half-life showed a high tumor uptake of up to 19.29% ID per g at 48 h post-injection (Fig. 23c). Furthermore, guided by PET imaging, ^{64}Cu-Eu/VBBO lipo could effectively eliminate the FaDu tumors. The tumor volume ratio in the ^{64}Cu-Eu/VBBO lipo group was about half of that in the ^{64}Cu-VBBO lipo group. In addition, other radioisotopes, such as ^{89}Zr, ^{86}Y, and ^{64}Cu, have also been used for PET image-guided RT.[371–374]

Although PET and SPECT can provide functional information with high sensitivity and specificity at the molecular level, PET or SPECT alone is not the most proper imaging technique for cancer diagnosis due to the lack of anatomical information. Therefore, the PET or SPECT is usually combined with a high-resolution anatomic imaging modality (CT or MRI) to provide both functional and anatomical information.[375,376] Liu and co-workers encapsulated ultrasmall gallic acid-ferrous (GA-Fe(II)) nanocomplexes and L-buthionine sulfoximine (BSO, an inhibitor of GSH) into a liposome (BSO/GA-Fe(II)@liposome).[377] Next, the BSO/GA-Fe(II)@liposome was chelated with $^{99m}Tc^{4+}$ radioisotope with a high radiolabeling efficiency and steady radioactivity for SPECT/CT image-guided RT/chemotherapy. The *in vivo* SPECT/CT imaging revealed that the BSO/GA-Fe(II)@liposome could effectively accumulate at the tumor site and reach the maximum at 24 h post-injection. Therefore, the 24 h post-injection was considered as the optimal time-point for RT of tumors. Besides, the PET/CT imaging based on various radionuclides, such as ^{86}Zr and ^{64}Cu, was also utilized to guide precision RT.[378–381] For example, Achilefu and colleagues coated titanium dioxide NPs (TiO_2 NPs) with transferrin (Tf) and further labeled the NPs with radionuclide ^{89}Zr (^{89}Zr-TiO_2-Tf NPs) for bone targeting and PET/CT imaging-guided Cerenkov radiation-induced therapy (CRIT) of multiple myeloma (MM, a type of bone-related tumor).[380]

In summary, after radiolabeling, the nuclear medicine imaging can monitor the distribution of drugs in tumors or organs and further guide precision RT. However, the PET imaging is costly while the SPECT imaging is much cheaper but the latter produces images with lower resolution. Besides, both the imaging techniques present radiation hazard, which may hamper their wide applications.

4.7 Dual-modal imaging-guided RT

Each imaging method has its own advantages and disadvantages. Nowadays, more and more nanomedicines have been designed to incorporate two or more imaging modalities, which allows for integration of merits of various imaging techniques.

4.7.1 MRI-based dual-modal imaging-guided RT. Several radiosensitizers with high-*Z* elements are able to act as CT or MR imaging contrast agents. Dou *et al.* designed radiation-responsive scintillating NPs (NSC@mSiO_2-SNO/ICG NPs) for MR/CT bimodal imaging-guided enhanced RT (Fig. 24a).[64] The Eu^{3+}-doped $NaGdF_4$ scintillating nanocrystals (NSC) were coated with mesoporous silica and then loaded with SNO and ICG. TEM images showed core–shell structure of NSC@mSiO_2-SNO/ICG NPs (Fig. 24b). The high-*Z* elements in the NSC@mSiO_2-SNO/ICG NPs could deposit X-ray radiation energy for radiosensitization. Moreover, the X-ray-induced PDT based on the NPs could generate ROS. In addition, the radiation could break the S–N bond and promote NO release. The released NO was able to kill tumor cells and dilate tumor blood vessels for alleviating tumor hypoxia. In addition, the NSC@mSiO_2-SNO/ICG NPs possessed excellent CT and MR imaging performance. The *in vivo* CT and MR imaging

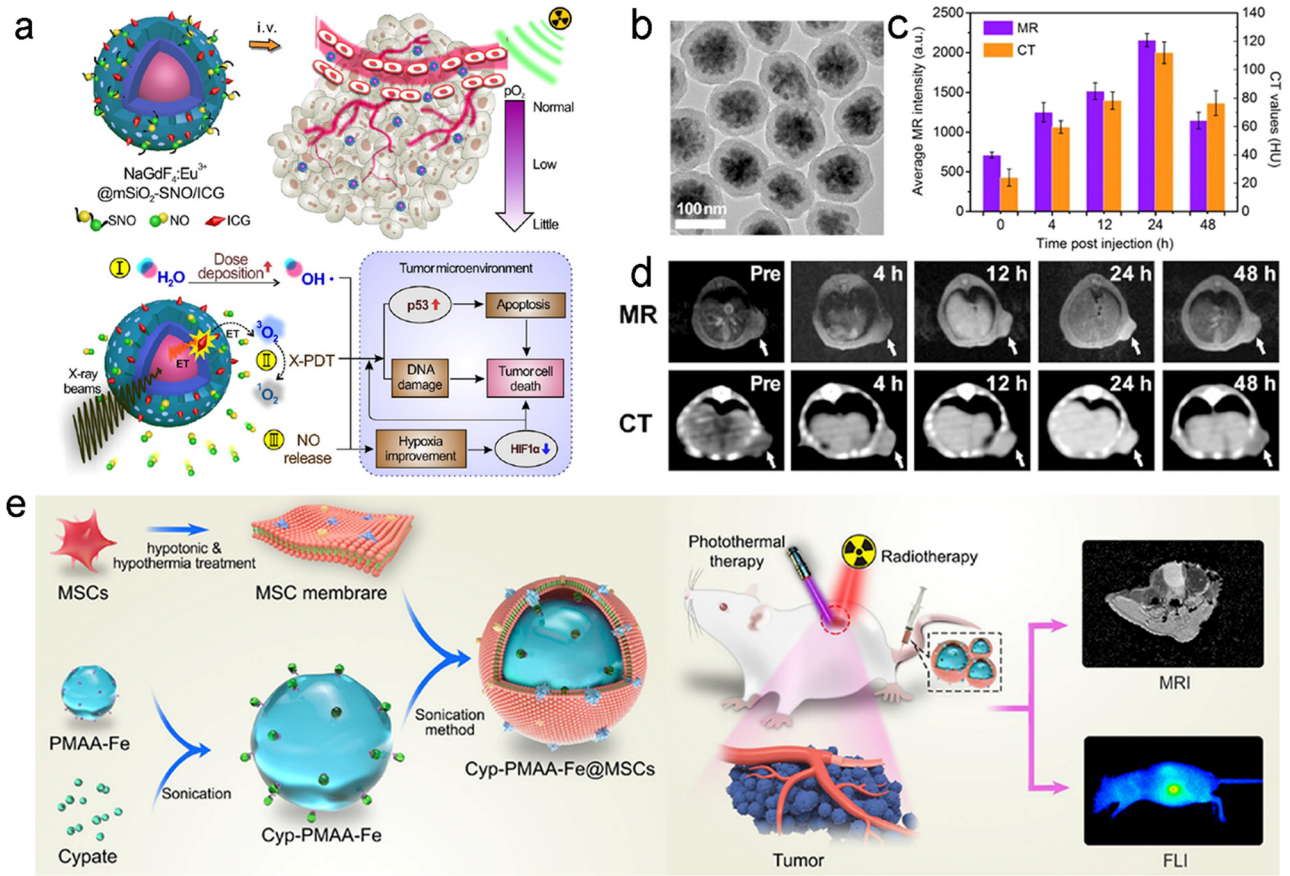

Fig. 24 MR-based bimodal imaging-guided RT. (a) Schematic illustration showing several responses induced by X-ray radiation on NSC@mSiO$_2$-SNO/ICG NPs. (b) TEM image of NSC@mSiO$_2$-SNO/ICG NPs. (c and d) *In vivo* MR/CT imaging (d) and quantification analysis (c) of tumor-bearing mice at different time points after intravenous administration of NSC@mSiO$_2$-SNO/ICG NPs. Reproduced with permission from ref. 64. Copyright 2018, Ivyspring International Publisher. (e) A scheme of synthetic procedures of Cyp-PMAA-Fe@MSCs NP and its application in MR/FL imaging-guided RT/PTT of NSCLC. Reproduced with permission from ref. 138. Copyright 2021, Springer Nature.

displayed that both CT and T_1-weighted MR signals in the tumor regions increased overtime and reached the maximum 24 h post-injection (Fig. 24c and d). For *in vivo* antitumor assessment, the 4T1 tumor-bearing mice received X-ray radiation (4 Gy) at 24 h post-injection. Guided by MR/CT imaging, the NSC@mSiO$_2$-SNO/ICG NPs plus RT completely eradicated the tumor, whereas the tumor volume in the RT alone group was more than 5 cm^3 14 days after treatment.

Furthermore, the NPs with bimodal MR and FL imaging capabilities have also been designed to guide precision RT. Yin *et al.* coordinated cypate (Cyp, a derivative of ICG with bis-carboxyl groups) with Fe(III)-loaded polymethacrylic acid (PMAA) NPs (Cyp-PMAA-Fe NPs). Then, the Cyp-PMAA-Fe NPs were coated with mesenchymal stem cell membranes (Cyp-PMAA-Fe@MSCs NPs) for MR/FL image-guided RT/PTT of non-small cell lung cancer (NSCLC) (Fig. 24e).[138] To assess the advantages of MSC cell membrane in inducing immune escape and prolonging circulation time, the Cyp-PMAA-Fe NPs were coated with red blood cell membranes (RBCs) to construct Cyp-PMAA-Fe@RBCs as negative control. The *in vivo* FL imaging of LLC1 tumor-bearing mice revealed that the FL signals of tumors at 28 h post-injection of Cyp-PMAA-Fe@MSCs were 21% higher than those in the Cyp-PMAA-Fe@RBC group, suggesting more effective tumor targeting and accumulation of Cyp-PMAA-Fe@MSCs owing to the MSC membranes. Likewise, the T_1-weighted MR imaging showed a 30.01% decrease of the T_1 signal at the tumor sites at 28 h after intravenous injection of Cyp-PMAA-Fe@MSCs. Guided by the MR/FL imaging, the mice were irradiated with NIR laser and X-rays at 28 h post-injection of Cyp-PMAA-Fe@MSCs for synergistic RT/PTT. The relative tumor volume in the Cyp-PMAA-Fe@MSCs + NIR + RT group was 0.63, much lower than 3.32 in the RT alone group.

4.7.2 PAI-based dual-modal imaging-guided RT. Dual-modal PA/CT imaging can achieve high sensitivity and spatial resolution. Yong *et al.* constructed multifunctional tungsten sulfide quantum dots (WS_2 QDs) for PA/CT imaging-guided RT/PTT of tumors.[382] The WS_2 QDs could be used as an outstanding PTT agent with relatively high photothermal conversion efficiency (η = 44.3%). Also, these QDs with high-Z elements could function as radiosensitizers. In addition, the WS_2 QDs could also be utilized as a CT and PA imaging agent. The *in vivo* PA imaging of the BEL-7402 tumor-bearing BALB/c nude mice showed that the PA signals in tumor site remarkably increased to the maximum (665 a.u.) at 2 h after intravenous

injection and gradually decreased later. Moreover, the *in vivo* CT imaging revealed that the CT value in the tumor regions also gradually increased at 2 h and peaked at 5 h post-injection. Guided by the *in vivo* PA/CT imaging, the BEL-7402 tumor-bearing mice were exposed to 808 nm laser irradiation (1 W cm^{-2}) for 10 min at 1.5 h after intravenous injection of WS_2 QDs. Next, the mice received X-ray irradiation at 30 min after laser irradiation. The dual-modal PA/CT imaging-guided synergistic PTT/RT could totally suppress tumor growth 5 days after treatment without recurrence in the following 17 days. However, the tumor growth inhibition rate in the RT alone group was only 37.64%.

4.7.3 Dual-modal optical imaging-guided RT. Several researchers have also employed dual-modal optical imaging techniques to guide precision RT.[383–385] For instance, Zhang *et al.* loaded both holo-lactoferrin (holo-Lf, a ligand of transferrin receptor (TfR)) and Dox into liposomes (Lf-Liposome-Dox nanocomposites) for dual-modal PA/FL imaging-guided radiochemotherapy.[383] First, the nanocomposites were able to target tumor cells owing to ligand (Lf)–receptor (TfR) recognition. The Lf-Liposome-Dox nanocomposites were labeled with 1,1′-dioctadecyl-3,3,3′,3′-tetramethylindotricarbocyanine iodide (DIR) for observation of their biodistribution *via in vivo* FL imaging. The *in vivo* FL images showed that FL signals in tumors gradually increased over time and strongly elevated at 24 h post-injection of Lf-Liposome-Dox. Moreover, holo-Lf could also catalyze the decomposition of H_2O_2 into O_2 for relieving tumor hypoxia. Besides, the *in vivo* PA imaging confirmed that the oxygen levels in tumor sites were rapidly increased over time and became the highest at 24 h post-injection of Lf-Liposome-Dox. Guided by the PA/FL imaging, the 4T1 tumors were exposed to 4 Gy of X-ray at 24 h post-injection of Lf-Liposome-Dox, resulting in $\sim$7 of relative tumor volume compared to $\sim$17 in the X-ray alone group. Taken together, the dual-modal PA/FL imaging technique can guide precision RT by providing images with high sensitivity, deep penetration, and high spatial resolution.

4.8 Tri- and tetra-modal imaging-guided RT

Tri-modal imaging-based techniques, such as CT/MRI/PAI,[386,387] CT/FLI/PAI,[388] MRI/PAI/PET,[389] MRI/PAI/SPECT,[390] PAI/US/PET,[391] CT/PA/SPECT,[392,393] and CT/MRI/FLI,[394] have also been reported to guide RT. For example, Li and colleagues constructed biocompatible Bi_2Se_3 nanodots for CT/PA/SPECT tri-modal imaging-guided synergistic RT/PTT of tumor.[393] These Bi_2Se_3 nanodots with relatively high photothermal conversion efficiency (η = 50.7%) could function as theranostic agents for PTT and PA imaging. Besides, these nanodots could also deposit X-ray energy and serve as a radiosensitizer. The *in vivo* PA imaging of 4T1 tumor-bearing mice revealed that the PA signals at the tumor sites were enhanced over time and reached the peak at 12 h post-injection of Bi_2Se_3 nanodots. Then the tumoral CT value increased gradually from the initial 50 HU to the peak of 94 HU at 12 h after intravenous injection of the nanodots, which was consistent with the PA imaging results. In addition, these nanodots were chelated with radioactive ^{99m}Tc for evaluation of their biodistribution *via* SPECT. The SPECT/CT images showed remarkable tumor accumulation of Bi_2Se_3 nanodots within 24 h of intravenous injection. Guided by the tri-modal imaging, the tumor-bearing mice received X-ray (6 Gy) and 808 nm laser (1 W cm^{-2}, 10 min) irradiations at 12 h post-injection of Bi_2Se_3 nanodots, resulting in a survival rate of 100% even at 36 days after treatment. However, all the mice in the RT alone group died within 32 days.

Besides, Kang *et al.* even integrated four imaging modalities (MRI/CT/PAI/FLI) into one nanoplatform for tetra-modal imaging-guided RT/chemotherapy.[395] They encapsulated rare-earth down-conversion (DC) NPs, copper bismuth sulfide (CBS) NPs, and DOX into zeolitic imidazolate framework-8 (ZIF8) to construct multifunctional nanocomposites (CBS@DC-ZIF8@DOX). After intratumoral injection of CBS@DC-ZIF8@DOX nanocomposites, the *in vivo* CT and MR images showed significant contrast enhancement. Moreover, the PA imaging at both wavelengths of 700 nm and 808 nm revealed remarkably increased PA signals in tumors after intratumoral injection. Likewise, the FL imaging of tumors after intratumoral injection of the CBS@DC-ZIF8 nanocomposites displayed a strong FL signal under 808 nm laser irradiation. For the anticancer evaluation, the 4T1 tumor-bearing mice were intratumorally administered with CBS@DC-ZIF8@DOX nanocomposites and then received X-ray radiation (6 Gy), resulting in a $\sim$1.4 of relative tumor volume at day 20. However, the relative tumor volume in the X-ray alone group was 7.5. These multi-modal imaging techniques can integrate the advantages of each imaging modality and provide a comprehensive information for guiding precision RT.

5. Feature application of precision RT for anti-metastasis

Precision treatment of tumors includes not only primary (local) tumors, but also distant tumors and metastasis. RT has been mainly utilized to treat local tumors rather than distant metastasis. Previous studies have revealed that RT is able to produce a certain level of abscopal effects; however, they are far from meeting clinical demands and only rare clinical cases have been reported over the years.[398–402] Even with the help of immune checkpoint blockades, therapeutic efficacies of RT for distant and metastatic tumors are still unsatisfactory.[403–407] The reasons why conventional RT cannot induce systemic antitumor immunity against metastasis include inefficient induction of immunogenic cell death (ICD), immunosuppressive TME, poor presentation efficiency of tumor-specific antigens, *etc.*[408] Recently, the rapidly evolving nanotechnologies enable RT to induce potent systemic immunity through various mechanisms, thereby extending the application of RT in the treatment of metastases.[409] Besides, multifunctional NPs enable RT to be combined with other therapies (*e.g.*, ICB therapy, immunoadjuvant, PTT, PDT, CDT, *etc.*) to activate systemic antitumor immune responses against distant

Table 4 Representative nanotechnologies for abscopal effect of precision RT

Nanoparticles	Local treatment	Mechanisms of RT-mediated abscopal effects	ICB/ immunoadjuvant	Cancer type	Tumor models	Ref.
DBP-Hf nMOF	RT-RDT	ICD	IDOi	Primary, distant, and re-challenged tumors	SQ20B/U87MG/PC-3/CT26/TUBO tumor-bearing mice	507
Hb@Hf-Ce6	RT-RDT	ICD, reverse the immunosuppressive TME	Anti-PD-1 antibody	Primary and distant tumors, lung metastasis	4T1 tumor-bearing mice	505
4PI-Zn@$CaCO_3$ NPs	RT	Reverse the immunosuppressive TME	IDO-1 inhibitor	Primary, distant, and re-challenged tumors	CT26 tumor-bearing mice	533
PLGA/ STING@EPBM	RT	Promote DC maturation and antigen presentation	STING agonist	Primary tumor, lung metastasis	B16-OVA/TC1/4T1 tumor-bearing mice	132
PSeR NPs	RT/ chemotherapy	Enhance the NK cell functions	NA	Primary tumor, lung metastasis	MDA-MB-231 tumor-bearing mice	270
PLGA-R837@Cat NPs	RT	ICD, reverse the immunosuppressive TME	R837, anti-CTLA4 antibody	Primary, distant, metastatic and re-challenged tumors	CT26 tumor-bearing mice, 4T1 orthotopic breast tumor metastasis	432
ALG-ATP-Aptamer/CpG-cAptamer	RT or chemotherapy	ICD	CpG, anti-PD-1 antibody	Primary, distant, and re-challenged tumors, lung metastasis	CT26 tumor-bearing mice, orthotopic 4T1 breast tumor-bearing mice	517
^{131}I-Cat/ALG	RIT	ICD	CpG, anti-CTLA4 antibody	Primary, distant, metastatic and re-challenged tumors	4T1/CT26 tumor-bearing mice, metastatic orthotopic 4T1 breast tumor-bearing mice, VX2 tumor-bearing rabbits, and patients' prostate tumor bearing mice	42
$WO_{2.9}$-WSe_2-PEG NPs	RT/PTT	ICD	Anti-PD-L1 antibody	Primary, distant, and re-challenged tumors, lung metastasis	4T1 tumor-bearing mice	528
Au@MC38	RT	ICD	Anti-PD-1 antibody	Primary and distant tumors, lung metastasis	MC38 tumor-bearing mice	30
CpG@Au NPs	RT	ICD, repolarize TAMs	CpG, anti-PD-1 antibody	Primary and distant tumors	GL261 tumor-bearing mice	458
ZGd-NRs	RT	ICD, deplete TAMs	Anti-PD-L1 antibody	Primary and distant tumors, lung metastasis	4T1/CT26 tumor-bearing mice	459
H@Gd-NCPs	RT	ICD	Anti-PD-L1 antibody	Primary and distant tumors, lung metastasis	4T1/CT26 tumor-bearing mice	41
Cu-NCPs	RT/CDT	ICD	Anti-PD-L1 antibody	Primary and distant tumors, lung metastasis	4T1/CT26 tumor-bearing mice	532
PLGA AC-NP	RT	Deliver antigen to DCs	Anti-PD-1 antibody	Primary and distant tumors	B16-F10 tumor-bearing mice	486

metastasis. The representative nanotechnologies for inducing abscopal effects of RT are summarized in Table 4.

5.1 Mechanisms of RT-mediated abscopal effect by advanced nanotechnologies

In this section, the mechanisms of RT-mediated abscopal effect by advanced nanotechnologies will be introduced, including ICD induction, repolarizing or depleting tumor-associated macrophages (TAMs), enhancing NK cell function, enhancing antigen presentation of dendritic cells, reprograming peripheral neutrophils as antigen-presenting cells, *etc.*

5.1.1 Inducing ICD. ICD is a specific death modality triggered by various physical (*e.g.*, hyperthermia, PDT, RT, *etc.*),[410–415] chemical (*e.g.*, chemotherapeutics, *etc.*),[416–419] and biological (*e.g.*, bacteria, virus *etc.*) agents.[420–423] ICD can induce the release of tumor antigens and damage-associated molecular patterns (DAMPs), including cell surface exposure of calreticulin (CRT),[424] high mobility group protein B1 (HMGB1),[425] heat shock protein 90 (HSP90),[426] HSP70,[427,428] and extracellular release of adenosine triphosphate (ATP).[429] Various antigen presenting cells (APCs), such as dendritic cells (DCs), can be activated by these antigens and then migrate to lymph nodes to elicit strong antitumor immune responses.[430,431] However, RT alone fails to induce sufficient ICD for abscopal effect due to insufficient ROS generation attributed to several reasons, such as low energy deposition in tumor tissues, immunosuppressive TME (*e.g.*, GSH, hypoxia, *etc.*), *etc.*[26,432–434]

A higher ROS yield by tumor accumulation of high-*Z* elements can induce a stronger ICD to elicit potent immune responses. For example, Qin *et al.* designed a tumor cell-reactor to produce biogenetic gold NPs (Au@MC38) for radiosensitization and abscopal effect.[30] Coated with the MC38 cell membrane, the Au@MC38 NPs could effectively target and stay in tumors for more than 72 h after injection. Moreover, Au@MC38 containing a high-*Z* element could significantly enhance radiosensitizing effect on tumors and thereby induce a high tumor inhibition rate of 87.7% under X-ray irradiation compared to 66.5% in the RT alone group. In addition, the Au@MC38-mediated radiosensitization was able to induce potent ICD of tumor cells and further elicit systematic immune responses, resulting in a higher lung metastasis inhibition rate (53.5%) compared to 34.9% in the RT alone group.

GSH depletion could also augment RT-induced ROS generation and induce more potent ICD for antitumor immunity

activation. Huang *et al.* used 5′-guanosine monophosphate (5′-GMP) and gadolinium to form nanoscale coordination polymers (NCPs) and further loaded Hemin into the NCPs (H@Gd-NCPs) for boosting RT-induced ICD.[41] The H@Gd-NCPs could effectively deposit X-ray energy to elevate the intracellular ROS level due to the high-*Z* element. Moreover, Hemin could function as peroxidase to deplete GSH in TME and thereby augment RT-induced oxidative stress. The immunofluorescence signal of CRT in CT26 cells treated with H@Gd-NCPs plus RT (8 Gy) was significantly stronger than that in Gd-NCPs + RT and RT alone groups. Western blot assay of CT26 tumor tissues indicated that *in vivo* treatment of H@Gd-NCPs + RT (6 Gy) could remarkably upregulate HMGB1 expression. Furthermore, flow cytometry analysis revealed that the tumor-draining lymph nodes (TDLNs) of mice in the H@Gd-NCPs + RT group showed a higher percentage (57.85%) of mature DCs than those in the RT alone (37.42%) and Gd-NCPs + RT groups (43.45%), suggesting that H@Gd-NCP-mediated radiosensitization was able to induce potent ICD and DC maturation. Due to high immunogenicity, the H@Gd-NCP-mediated RT would potentiate checkpoint blockade immunotherapy. The treatment of H@Gd-NCPs + RT could remarkably eliminate the primary tumors with or without αPD-L1. Moreover, the H@Gd-NCPs + RT + αPD-L1 could also eradicate the distant tumors, whereas the average tumor volume in RT + αPD-L1 was over 800 mm^3 21 days after treatment. Further mechanism study revealed that RT + αPD-L1 could enhance the ratios of $CD4^+$/$CD8^+$ T cells to 2.65%/0.91% and 2.64%/1.04% in irradiated and unirradiated tumors, respectively; however, the ratios in the H@Gd-NCPs + RT + αPD-L1 group were 5.95%/1.94% and 5.98%/2.31%. In addition, IFN-γ and infiltrating memory T cells were increased in bilateral tumors of mice treated with H@Gd-NCPs plus RT.

Furthermore, Wang *et al.* loaded FDA-approved physcion (Phy, an inhibitor of the pentose phosphate pathway (PPP)) onto PEG-decorated layered gadolinium hydroxide (PLGdH) nanosheets to prepare Phy@PLGdH nanosheets for boosting RT-mediated ICD (Fig. 25a).[435] The Phy was reported to inhibit 6-phosphogluconate dehydrogenase (6PGD) and further reduce two main products of PPP: nicotinamide adenine dinucleotide phosphate (NADPH) and ribose 5-phosphate (ribose 5-P), leading to reduced intracellular antioxidants and imbalance of nucleotide homeostasis (Fig. 25b).[436–439] As such, both Phy and high-*Z* elements could enhance the radiosensitizing effect of Phy@PLGdH nanosheets on tumors and thereby induce stronger ICD. The CT26 cancer cells treated with Phy@PLGdH + RT rapidly exposed CRT and released HMGB1/ATP compared to the RT, PLGdH + RT, or Phy@PLGdH group. To evaluate the activation of antitumor immunity, the CT26 cancer cells treated with Phy@PLGdH with or without RT were inoculated subcutaneously in the left flank of mice. Then, these mice were rechallenged with CT26 cancer cells on the right flank for observation of tumor growth. Interestingly, vaccination with CT26 cancer cells (Phy@PLGdH + RT) could significantly inhibit the growth of rechallenged tumors and led to a 70% cancer-free state over 50 days compared to 20% in the RT alone group. Nevertheless, the vaccination of CT26 cancer cells showed no significant inhibition effect on other cancer types, such as breast cancer and renal cancer, indicating that the antitumor immunity induced by Phy@PLGdH-mediated RT was tumor-specific. Besides, Phy@PLGdH + RT + αPD-L1 could significantly eliminate lung metastasis, whereas the counts of lung foci were over 40 in the RT alone group.

5.1.2 Repolarizing or depleting TAMs. Generally, TAMs, the major population of infiltrating immune cells in tumors, are classified into activated M1 (tumor-fighting) phenotype and alternatively activated M2 (tumor-promoting) phenotype with diametrically opposed effects on tumors.[440–444] During tumor progression, the TAMs are gradually converted into M2 phenotype which promotes angiogenesis, tumor growth, invasion, and metastasis.[445] Moreover, M2 phenotype TAMs are also able to enhance immunosuppressive TME by boosting the generation of regulatory T cells (Treg cells).[446,447] It is worth mentioning that TAMs, M2 phenotype in particular, have been reported to produce a large number of antioxidants during RT and lead to radioresistance of tumors.[448] Seifert *et al.* revealed that the high-dose radiation (12 Gy) was able to downregulate the expression levels of Irf5, iNOS, and H2eb1 as well as upregulate the Arg1 expression in pancreatic tumors, indicating induction of M2 phenotype TAMs.[449] In addition, several studies have reported that depletion of TAMs could reverse immunosuppressive effects and enhance the RT efficacy of tumors.[450,451]

So far, lots of nanomedicines have been designed for TAM repolarization. For example, Ma *et al.* revealed that graphene oxide (GO) promoted the polarization of M1 TAMs by interaction with toll-like receptors (TLRs) of macrophages and activation of NF-κB pathways.[452] Zanganeh *et al.* reported that FDA-approved iron oxide NPs (Ferumoxytol) were able to improve the proportion of M1 phenotype TAMs in tumor tissues after intravenous administration.[453] Kim's group developed M1 macrophage-derived exosome-mimetic nanovesicles to re-educate M2 phenotype TAM to M1 macrophages *in vitro* and *in vivo*.[454] Shi *et al.* utilized NP-based ROS photogeneration to repolarize TAMs to M1 phenotype.[455]

Recently, several nanoradiosensitizers have been designed to regulate TAMs and further elicit antitumor immunity for suppression of distant, metastatic, and recurrent tumors.[456,457] For example, Cao *et al.* modified AuNPs with CpG (an agonist of TLR9) to form CpG@Au NPs as a TAM repolarizing nanosystem for enhanced radioimmunotherapy (Fig. 26a and b).[458] Bone marrow-derived macrophages (BMDMs) treated with CpG@Au NPs showed significant upregulation of M1 type markers (iNOS and CD86) and downregulation of M2 marker CD206. The reeducating TAMs could reduce radioresistance, and AuNPs as a high-*Z* element could enhance RT efficacy. The GL261 tumor-bearing mice were intratumorally injected with CpG@Au NPs, followed by X-ray irradiation (2 Gy). Immunohistochemistry (IHC) and flow cytometry analyses showed that CpG@Au + RT treatment could significantly downregulate CD206 and upregulate CD86 expression in tumors (Fig. 26c). As a result, the relative tumor volume in the CpG@Au + RT group was over 2 compared to 6 in the RT alone group (Fig. 26d). In addition,

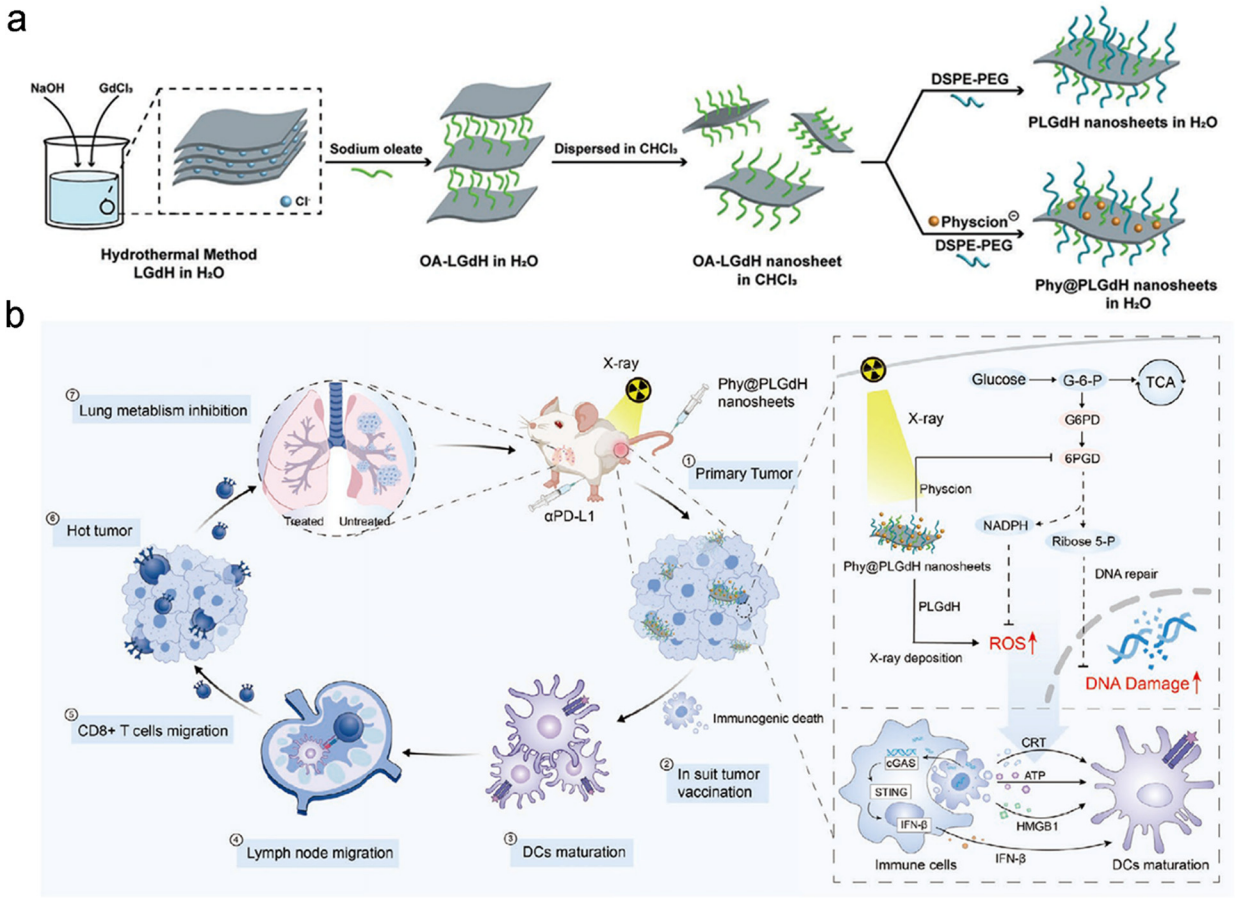

Fig. 25 Inducing ICD. (a) A scheme of synthetic procedures of Phy@PLGdH nanosheets. (b) Schematic illustration showing *in situ* tumor vaccination of Phy@PLGdH nanosheets. Reproduced with permission from ref. 435. Copyright 2022, Wiley.

the immune checkpoint blockade (ICB) was introduced into the TAM reeducation-mediated RT to investigate whether the elicited systemic immunity was able to induce the abscopal effect of RT. The bilateral GL261 tumor model was used to evaluate the abscopal effect of RT (Fig. 26e). The results displayed that the CpG@Au + RT + anti-PD-1 treatment was able to significantly suppress the growth of both primary and distant tumors (Fig. 26f and g). However, anti-PD-1+ RT treatment showed almost no inhibition effect on distant tumors. Overall, the TAM repolarization could trigger potent systemic antitumor immunity and improve the abscopal effect of RT in cooperation with ICB.

Besides, Huang *et al.* combined TAM depletion with ICD induction to boost RT-induced antitumor immunity.[459] They constructed bifunctional coordination polymer nanorods (ZGd-NRs) through self-assembly of zoledronic acid (Zol) and gadolinium. With the high-*Z* element, ZGd-NRs could improve the radiosensitizing effect and thereby induce strong ICD in CT26 tumor cells. Meanwhile, the percentage of mature DCs in TDLN of mice treated with ZGd-NR plus RT was increased to 33.6%, much higher than 14.1% of the RT alone group. In addition, Zol was able to inhibit the mevalonate pathway and thereby induce apoptosis of macrophages.[460] The treatment of ZGd-NRs + RT could reprogram immunosuppressive TME by depleting intratumoral F4/80$^+$CD11b$^+$ TAMs and decreasing secretion of IL-10, TGF-β1, and VEGFA. Therefore, the ZGd-NR-mediated RT could remarkably suppress distant tumor growth while RT alone had a negligible inhibitory effect on distant tumors. Besides, the distant tumors could be completely eradicated in the ZGd-NR + RT + αPD-L1 group. Further mechanism experiments showed that ZGd-NR-mediated RT could increase the levels of infiltrated CD4$^+$/CD8$^+$ T cells to 3.97%/1.37% and 4.14%/1.41% in primary and distant tumors, respectively, much higher than those in the RT alone group (1.46%/0.28% and 1.75%/0.29% for primary and distant tumors). These results indicated that ZGd-NR-mediated RT could activate systemic antitumor immune responses by TAM depletion and ICD induction.

5.1.3 Enhancing NK cell function. Natural killer (NK) cells, an important type in the innate immune system, serve as the first line of defense.[461,462] NK cells were known for their ability to kill cancer cells without priming or prior activation, which is distinct from adaptive immune cells, such as T cells and B cells.[463–465] The natural killer group 2A (NKG2A, an inhibitory checkpoint receptor of NK cells) can bind human leukocyte antigen-E (HLA-E). Therefore, cancer cells expressing HLA-E can avoid being killed by NKG2A-positive NK cells.[466–468] In

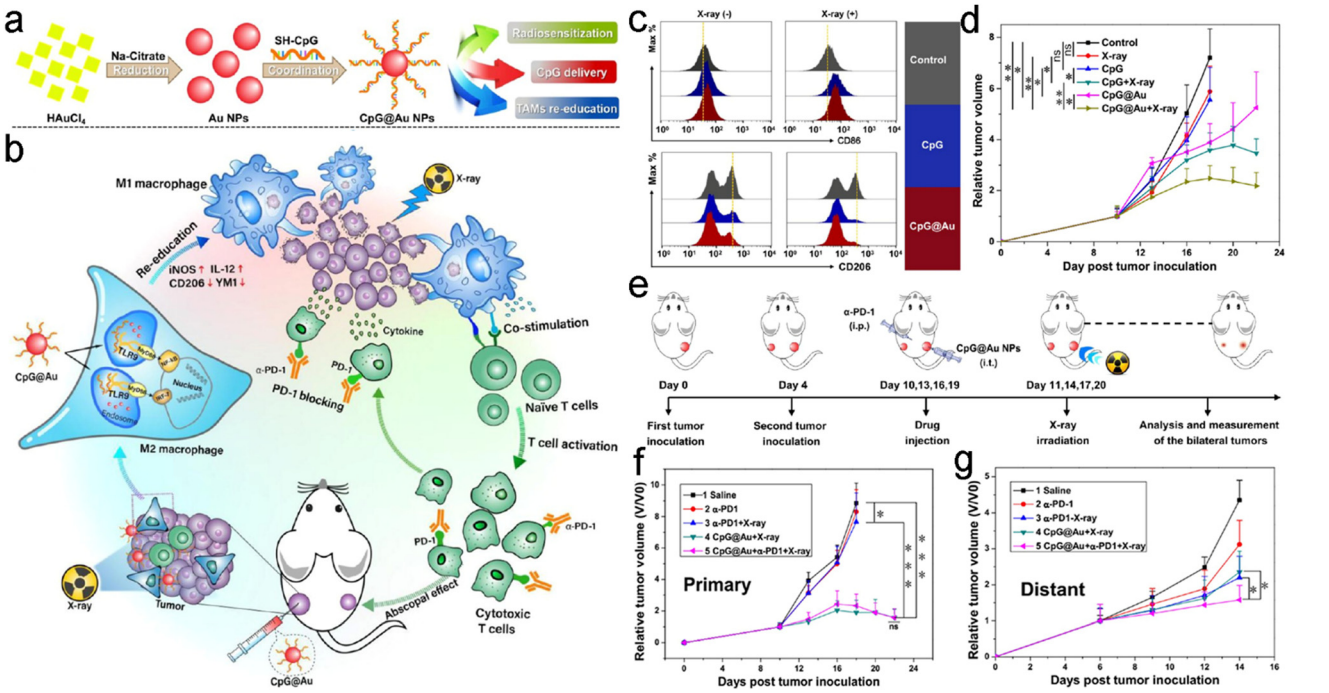

Fig. 26 Repolarizing TAMs. (a) A scheme of synthetic process of CpG@Au NPs. (b) A scheme showing mechanism of TAM reeducation and enhanced RT/ICB based on CpG@Au NPs. (c) Flow cytometry analysis showing CD206 and CD86 expression of GL261 tumors in different treatment groups. (d) Tumor growth curves of mice receiving various treatments. (e) Schematic illustration of treatment schedule. Tumors on the left and right sides were regarded as distant and primary tumors, respectively. (f and g) Primary (f) and distant (g) tumor growth curves of mice in different treatment groups. Reproduced with permission from ref. 458. Copyright 2021, American Chemical Society.

addition, ionizing radiation was reported to upregulate the expression levels of several ligands (*e.g.*, NKG2D, CD112, *etc.*) on cancer cell membrane to enhance the susceptibilities of cancer cells to NK cell attack.[464,469,470]

A previous study found that inorganic selenium compound selenite (SeO_3^{2-}) was able to block the HLA-E expression of tumors at the posttranscriptional level and thereby improve sensitization of tumor cells to CD94/NKG2A-positive NK cells, suggesting that selenite could enhance NK cell-based immunotherapy.[471] Recently, organic seleninic acid was also reported to activate NK cells for immunotherapy.[270,472] In addition, the diselenide bond can be oxidized into seleninic acid upon γ-ray irradiation.[473–475] Li *et al.* assembled cytosine-containing diselenides (Cyt–SeSe–Cyt) with pemetrexed (a clinically used chemotherapeutics) through hydrogen bonds to construct diselenide-pemetrexed (Pem/Se) assemblies for RT/chemotherapy/immunotherapy.[472] Upon γ-ray irradiation, the diselenide bonds and hydrogen bonds were cleaved, resulting in the disassembly of Pem/Se assemblies and pemetrexed release. The MDA-MB-231 cells treated with Pem/Se assemblies and γ-ray irradiation (5 Gy) showed significant downregulation of HLA-E due to the generation of seleninic acid. The tumor inhibition rate of MDA-MB-231 tumor-bearing mice in the Pem/Se + γ-ray radiation group was about 1.5 times that of the Pem + γ-ray radiation group. The immunofluorescence staining of tumor slices revealed that the Pem/Se + γ-ray radiation treatment significantly reduced HLA-E expression and upregulated the expression levels of IFN-γ and CD49b, suggesting elevated immunoactivity of NK cells in tumor tissues. In addition, the NK cells in metastases were also activated after the Pem/Se + γ-ray radiation treatment, and the induced systemic immune response could inhibit lung metastases.

In another similar study, Gao *et al.* proposed a NK cell-based immunotherapy strategy using radiation-sensitive NPs (PSeR NPs).[270] The PSeR NPs were loaded with DOX and then decorated with RGD-modified PEG (Fig. 27a). The TEM images further showed that the PSeR NPs with spherical morphology gradually collapsed into irregular structures upon elevated doses of γ-ray irradiation owing to the oxidation of diselenide bonds (Fig. 27b). Due to structural collapse, DOX could be rapidly released from PSeR NPs. Moreover, they found that seleninic acid (RSeO(OH), oxidation products of diselenides) could react with intracellular GSH to affect the redox balance in cancer cells. The GSH/GSSG ratio and expression levels of glutathione peroxidase (GPx) and GSH-transferase (GST) were remarkably decreased in MDA-MB-231 cells treated with PSeR NPs + γ-ray radiation (5 Gy). Whereas, CAT was upregulated after treatment of PSeR NPs + γ-ray radiation. These intracellular alterations could potentiate efficacy of RT and chemotherapy. Besides, the PSeR NPs + γ-ray radiation (5 Gy) treatment could induce the NK cell-mediated cytotoxicity through blocking HLA-E expression and releasing Granzyme B (GZB)/IFN-γ. Next, the MDA-MB-231 tumor-bearing nude mice with normal NK cell but defective $CD8^+$ T cells were used to evaluate the efficacy of NK cell-based immunotherapy induced by PSeR/DOX and RT. The results showed that the tumor inhibition rate in

the PSeR/Dox + RT group was almost 2-fold higher than that in the DOX + RT group (Fig. 27c). The confocal images of tumor tissues displayed upregulated HLA-E expression after combined treatment (Fig. 27d). Simultaneously, GZB and IFN-γ were significantly increased in serum and tumors (Fig. 27e and f). These results suggested that the excellent antitumor efficacy was attributed to synergistic RT/chemotherapy and NK cell-mediated immunotherapy. Furthermore, to evaluate the *in vivo* anti-metastasis efficacy of NK cell-mediated immunotherapy, the MDA-MB-231 cells treated with or without PSeR + radiation were intravenously injected into nude mice to establish the human breast cancer lung metastasis model. The mice receiving MDA-MB-231 cells treated with PSeR + radiation showed almost no metastatic foci in lung tissues compared to the control groups.

5.1.4 Enhancing antigen presentation of dendritic cells. RT can induce the release of cancer-specific antigens and generation of pro-inflammatory proteins while killing cancer cells.[476–479] These tumor-derived protein antigens (TDPAs) would be delivered to APCs, such as DCs, and elicit antitumor immune response. Therefore, with the rapid development and application of nanotechnologies, enhancing antigen presentation has been a promising strategy to improve the abscopal effect.[480–485]

Min *et al.* designed antigen-capturing NPs (AC-NPs) to enhance antigen presentation of DCs for augmenting the abscopal effect of RT.[486] They utilized PLGA to form a polymer and then decorated the polymer with various molecules to bind the TDPAs, including methoxypolyethylene glycol (mPEG AC-NPs, negative control), 1,2-dioleoyl-3-trimethylammonio-propane (DOTAP AC-NPs), amine polyethylene glycol (NH_2 AC-NPs), and maleimide polyethylene glycol (Mal AC-NPs). After incubating with irradiated B16F10 melanoma cell lysates, the unmodified PLGA AC-NPs and DOTAP AC-NPs captured most proteins compared to other types of AC-NPs. Further experiments indicated that all the AC-NPs except for mPEG AC-NPs were able to capture neoantigens and damage-associated molecular pattern proteins (DAMPs, a series of pro-inflammatory proteins). The AC-NPs could deliver these antigens toward DCs to enhance antigen presentation and thereby induce potent immune responses. Next, to evaluate the enhanced immunotherapy of AC-NPs, bilateral B16F10 melanoma-bearing mice treated with αPD-1 were utilized. Interestingly, the PLGA AC-NPs and Mal AC-NPs produced significant abscopal effects on the secondary tumors, whereas the RT alone showed negligible inhibition effect on the secondary tumors. Further mechanism study revealed that the PLGA AC-NPs and Mal AC-NPs were transported to the adjacent lymph nodes and mainly accumulated in $CD11c^+$ DCs, $F4/80^+$ macrophages, and $B220^+$ B-cells at 16 h after intratumoral injection into the irradiated tumors. Moreover, the increased $CD8^+$ T cells and decreased immunosuppressive $CD4^+FOXP3^+$ Treg cells were shown in secondary tumors treated with PLGA AC-NPs or Mal AC-NPs, indicating potent antitumor immune responses in these secondary tumors. More importantly, unlike traditional immunotherapy strategies by using several "chosen" antigens to elicit immune responses, these AC-NPs could realize personalized treatment by delivering patient-specific tumor antigens to DCs, which could facilitate the abscopal effect of RT and extend RT from local tumors to metastasis treatment.

5.1.5 Reprograming peripheral neutrophils as antigen-presenting cells. APCs are a set of immune cells that present tumor antigens for recognition by lymphocytes and further

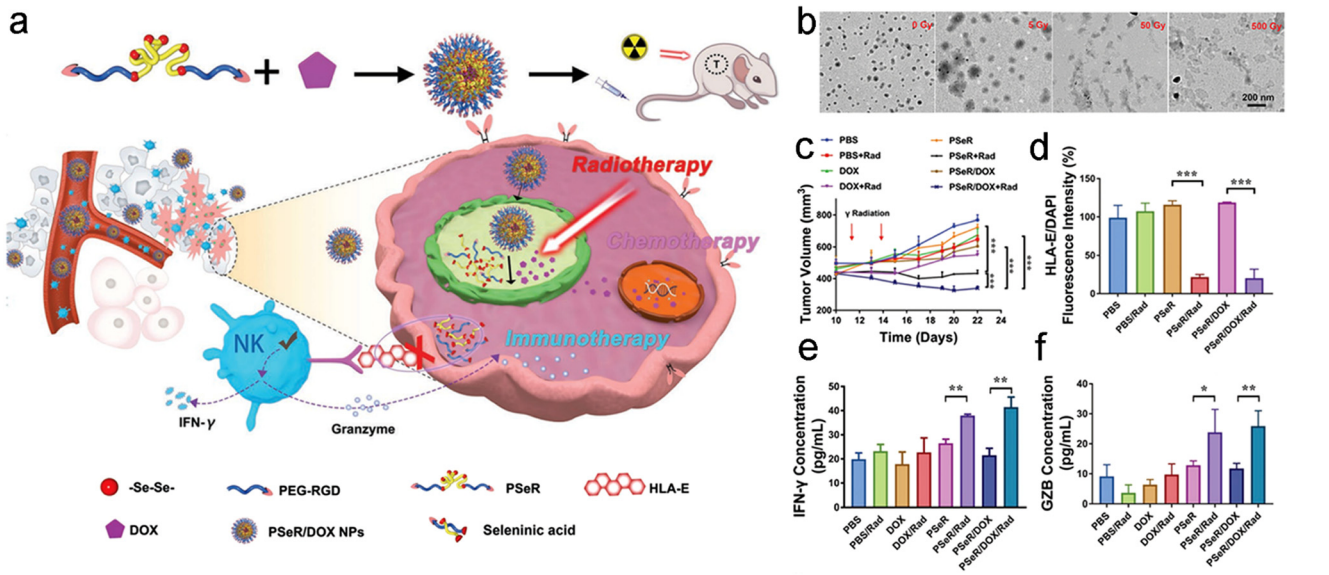

Fig. 27 Enhancing NK cell function. (a) A scheme of the synthetic process of PSeR NPs and its application in synergistic RT/chemotherapy and inducing NK cell-mediated immunotherapy. (b) TEM images of PSeR NPs under various doses of γ-ray irradiation. (c) Tumor growth curves of mice in different treatment groups. (d) Quantification analysis of HLA-E fluorescence intensities in tumors of different treatment groups. (e and f) The serum IFN-γ (e) and GZB (f) concentrations of mice in different treatment groups. Reproduced with permission from ref. 270. Copyright 2020, Wiley.

modulate cellular immune response.[487] Traditional APCs include DCs, M1 phenotype macrophages, and B cells.[488] However, the antigen presenting capability of these main types of APCs was significantly limited or disabled by the immunosuppressive TME.[489–491] Neutrophils, the most abundant peripheral leukocyte generally phenotyped as $CD11b^{+}Ly6G^{+}CD11c^{-}$, are generated in the bone marrow and differentiate into mature neutrophils as the first line of defense against foreign pathogens, such as bacteria and fungus.[492–494] Interestingly, growing evidence has shown that neutrophils are able to function as non-canonical APCs to present tumor antigen and thereby regulate antigen-specific T cell immune responses.[495–497]

For example, Guo *et al.* proposed an nMOF-mediated RT-RDT strategy to reprogram peripheral neutrophils as non-canonical APCs for enhancing antitumor immune responses.[498] They metalated the porphyrin center with Pt(II) to construct Hf-DBP-Pt (Hf-Pt-5,15-di(*p*-benzoato)porphyrin) as a nanoradiosensitizer for effective RT-RDT. The *in vitro* clonogenic assays showed that Hf-DBP-Pt exhibited stronger radiotherapeutic effects on MC38, HepG2, CT26, AsPC-1, and Panc02 cells compared to Hf-DBP, which might be attributed to stronger energy deposition and radiodynamic effect through facilitating intersystem crossing. To investigate the *in vivo* antitumor efficacy of RT-RDT, MC38 or CT26 tumor-bearing mice were intratumorally administered with Hf-DBP or Hf-DBP-Pt, followed by X-ray radiation. The results showed that both Hf-DBP and Hf-DBP-Pt could significantly inhibit tumor growth under X-ray irradiation. Further flow cytometry analysis of treated MC38 tumors indicated that Hf-DBP-Pt plus RT could recruit $CD11b^{+}Ly6G^{+}$ neutrophils into the tumors. The phenotype analysis revealed that these recruited neutrophils were reprogrammed to hybrid neu-DC characterized by upregulation of CD11c. Hf-DBP-Pt + RT elevated the proportion of neu-DC in the whole $CD11b^{+}Ly6G^{+}$ neutrophils to 36.4%, which was 10-fold higher than that in the RT alone group. In addition, the hybrid neu-DC exhibited elevated expression levels of co-stimulatory CD86, CD80, and MHC II markers, indicating that neu-DC could function as APC to present tumor antigen. In addition, the hybrid neu-DC induced by RT-RDT could remarkably augment cross-presentation of tumor antigens and enhance both innate and adaptive antitumor immune responses.

5.2 Strategies for synergistic induction of abscopal effect by RT and other therapies

This section will introduce strategies for synergistic induction of abscopal effect by RT and other therapies, including ICB therapy, immunoadjuvant, and other therapies.

5.2.1 Combination of RT and ICB therapy. Clinical studies have indicated that RT is important for ICB therapy through augmenting tumor-specific immunity.[499] In addition, RT has been shown to upregulate the PD-L1 expression of tumor cells in patients or mouse models.[499–501] Victor *et al.* initiated a phase I clinical trial of patients with melanoma metastases to examine the efficacy of RT combined with anti-CTLA4 blockade treatment.[502] The results showed that only 18% patients had partial immune response, 18% had stable disease, and 64% had progressive disease. They uncovered that overexpression of PD-L1 on the surface of tumor cells after RT and anti-CTLA4 treatment led to T-cell exhaustion and clinical failure. Therefore, addition of PD-L1/PD-1 blockade could antagonize resistance to RT + anti-CTLA4 and thereby result in long-term immunity. Interestingly, they found that RT is necessary to trigger an optimal response to checkpoint blockade since RT plus dual checkpoint blockade showed superior survival over dual checkpoint blockade. Thus, ICB therapy and RT can complement each other to elicit tumor-specific immunity.[499,500,502–504] Recently, several studies have introduced nanotechnologies to enhance the abscopal effect of the synergistic RT/ICB therapy.[42,505–507]

For example, Dai and colleagues combined RT-RDT with ICB therapy to trigger systemic antitumor immunity against primary tumors and distant metastasis (Fig. 28a).[505] First, chlorin e6 (Ce6) and catechol were conjugated onto PEG to form Ce6-PEG-polyphenols. The Ce6-PEG-polyphenols could self-assemble with Hf and were further loaded with Hb (Hb@Hf-Ce6 NPs). The Hf, a high-*Z* metal, could not only act as a radiosensitizer to enhance RT but also play a scintillator role in efficient radioluminescence. Moreover, Hb in the nanoplatform could deliver oxygen to alleviate tumor hypoxia and reverse the immunosuppressive TME (Fig. 28a). The bilateral 4T1 tumor-bearing mice were utilized to investigate the treatment efficacy of RT-RDT and immunotherapy (Fig. 28b). Hb@Hf-Ce6 NP-mediated RT-RDT could significantly inhibit the growth of both primary and distant tumors (Fig. 28c and d). Notably, the primary and distant tumor volumes in the Hb@Hf-Ce6 NP-mediated RT-RDT + αPD-1 group were about 1/6 and 1/2 of those in the RT + αPD-1 group, respectively. Next, the immune mechanism study revealed that combination of Hb@Hf-Ce6 NP-mediated RT-RDT and αPD-1 therapy could remarkably reduce M2 phenotype TAMs, regulatory T cells, and immunosuppressive IL-10 secretion as well as increase effector T cells, memory T cells, and cytokines (*e.g.*, IL-6, IL-12, IFN-γ, TNF-α, *etc.*) (Fig. 28e). In addition, Hb@Hf-Ce6 NP-mediated RT-RDT plus αPD-1 could also inhibit lung metastases with a mouse survival rate of 100%, 20 days after treatment compared to 50% in the RT + αPD-1 group (Fig. 28f).

In addition, checkpoint blockade antibody could also be encapsulated into NPs. Choi *et al.* developed snowflake-like Au nanocarriers (S-AuNC) and loaded αPD-L1 into the S-AuNC for RT/ICB therapy of tumors.[271] The S-AuNC could be decomposed under radiation to release αPD-L1. Moreover, the S-AuNC with high-*Z* elements could enhance the radiosenstizing effect and thereby induce strong ICD after intratumoral injection. This radiation-responsive *in situ* αPD-L1 release strategy enabled a controllable spatiotemporal combination of RT and ICB immunotherapy, leading to activation of potent antitumor immunity against tumor growth.

5.2.2 Combination of RT and immunoadjuvant. Cancer vaccines are generally composed of antigens (*e.g.*, tumor-specific antigens, nucleic acids encoding antigens, *etc.*) and

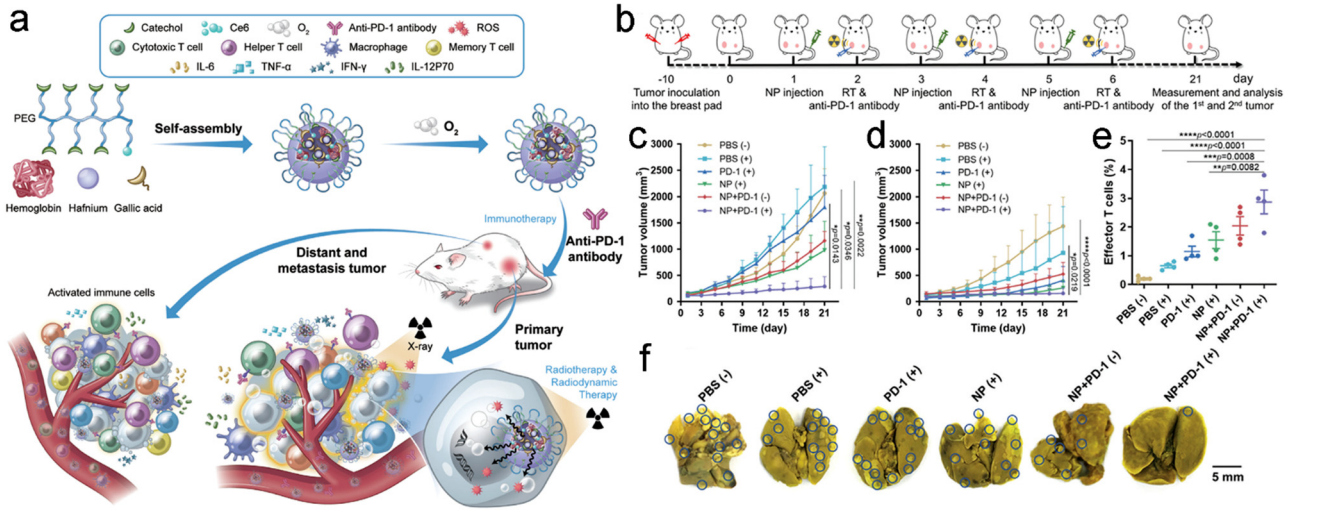

Fig. 28 Combination of RT and ICB therapy. (a) A scheme showing the synthetic process of Hb@Hf-Ce6 NP and its application in synergistic RT-RDT/αPD-1 immunotherapy against primary tumors and distant metastasis. (b) A scheme of treatment schedule for bilateral breast cancer mice. (c and d) Primary (c) and distant (d) tumor growth curves of mice in different treatment groups. (e) The percentages of effector T cells in distant tumors of mice received different treatments. (f) Representative photos of lung metastases in 4T1 tumor metastasis mice received different treatments. Reproduced with permission from ref. 505. Copyright 2020, Wiley.

adjuvants (*e.g.*, immunoadjuvants, immunologic adjuvants, *etc.*).[508,509] RT of tumors is able to produce tumor-specific antigens. Adjuvant refers to any material that improves the cellular or humoral response to antigens.[510] Thus, immunoadjuvants, such as CpG and imiquimod, can increase the immunogenicity of these tumor-specific antigens through various mechanisms, which is potential to enhance the "cancer vaccine" effect of RT.[511] However, free immunoadjuvants always exhibit lower bioavailability and poor tumor uptake.[512,513] Advances in nanotechnology enable the improvement of tumor delivery and uptake. Recently, various immunoadjuvant-loaded NPs have been developed to enhance the abscopal effect of RT.[42,432,514–517]

For example, Patel *et al.* designed bacterial membrane-coated NPs (BNPs) to promote RT to elicit systemic antitumor immunity against local tumors and metastatic relapse.[518] The BNPs were composed of four components. The inner polyplex core contained two immunological adjuvants: CpG (a TLR-9 agonist) and acid-responsive PC7A polymer for endosomal escape of antigens (Fig. 29a). The core was then coated with bacterial membranes that could activate innate immunity and DCs. Furthermore, the Mal groups were modified onto the bacterial membranes for tumor antigen capturing. The neoantigen released by irradiated tumors could be captured by BNPs (Fig. 29b and c). The neoantigen-carrying BNPs could further enhance the DC uptake owing to the bacterial membranes. After internalization by DCs, the BNPs could escape from the endosomes owing to the pH-responsive PC7A polymer. The PC7A could activate the stimulator of the interferon gene (STING) pathway to increase mature DCs, NK cells and T cells.[519,520] Furthermore, the released adjuvant CpG could activate TLR-9 on the inner membrane of endosomes and further promote DC maturation. Moreover, the intracellular neoantigens were degraded into antigen peptides for antigen presentation. Then, mature DCs could present antigens to T cells and thereby activate antitumor immunity (Fig. 29b and c). The combined treatment of RT and BNPs could completely eliminate tumors in both "cold" B78 melanoma and "hot" NXS2 neuroblastoma mouse models. In addition, the mice with complete regression of tumors were inoculated with the same cancer cells to evaluate immune memory. All the mice previously treated with RT + BNPs in the B78 tumor group eradiated the re-challenged tumors. Moreover, 75% of the NXS2 mice in the RT + BNP group eradiated the re-challenged tumor, compared to 50% in mice receiving BNPs alone and 15% in the control group. Further immune mechanism experiments indicated that the treatment of RT + BNPs could increase tumor infiltrating levels of $CD4^+/CD8^+$ T cells and secretion of IFN-γ. Therefore, the treatment of BNPs and RT could induce strong tumor-specific immune responses and long-term immune memory against primary and re-challenged tumors.

Indoleamine 2,3-dioxygenase (IDO, an immunoregulatory enzyme) is able to catalyze the conversion of Trp into Kyn and thereby cause T cell apoptosis and tumor immune escape, thus resulting in immunosuppression.[521–524] IDO inhibitors have been widely recognized as immunometabolic adjuvants to augment antitumor immunity.[525–527] Lu *et al.* designed 5,15-di(*p*-benzoato)porphyrin-Hf (DBP-Hf) based nMOFs for RT-RDT of tumor.[507] Hf clusters could absorb X-ray photons to generate •OH radicals for RT and to excite porphyrin-based photosensitizer ligands for RDT. The nMOF-mediated RT-RDT could effectively inhibit tumor growth and induce ICD upon low-dose X-ray irradiation. Then, the nMOFs were loaded with IDOi (9.4 wt%) to prepare IDOi@DBP-Hf for yielding abscopal effects. The bilateral CT26 tumor-bearing mice were utilized to evaluate antitumor efficacy. The local administration of

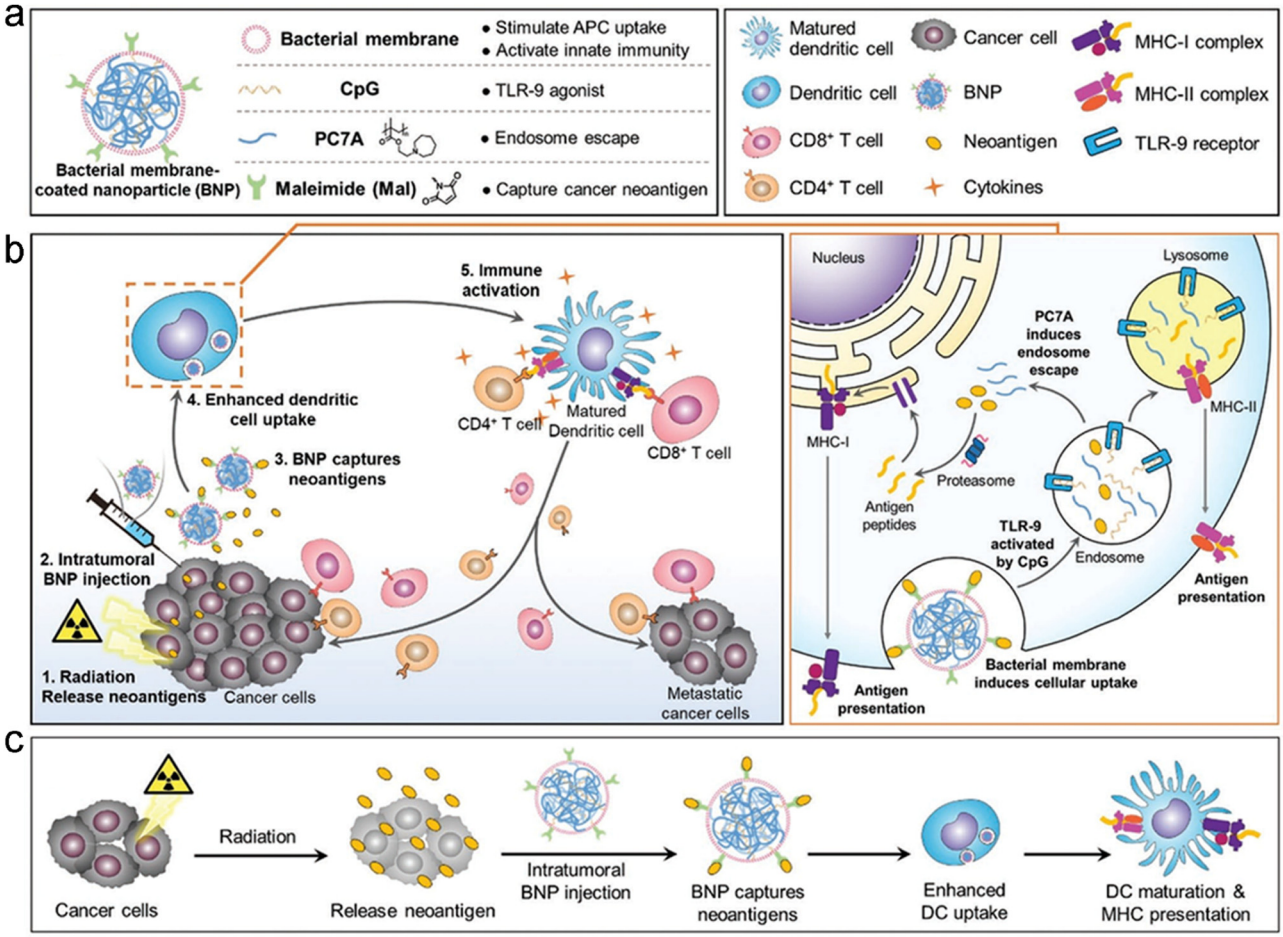

Fig. 29 Combination of RT and immunoadjuvant. (a) A scheme showing components of BNPs and the corresponding functions. (b) A scheme of antitumor immune responses induced by BNP + RT against primary and metastatic tumors. (c) Schematic illustration of the process by which BNPs interact with neoantigens to promote DC uptake and maturation. Reproduced with permission from ref. 518. Copyright 2019, Wiley.

IDOi@DBP-Hf and X-ray radiation could significantly eradicate both irradiated and unirradiated tumors. However, both IDOi@DBP-Hf alone and IDOi + RT showed negligible inhibition effect on the untreated tumors. In addition, to investigate the immune memory, the tumors on the right flanks of mice were first treated with IDOi@DBP-Hf and X-ray irradiation. Then, new TUBO tumor cells were inoculated on the left flanks of these treated mice to establish re-challenged tumors. The mice in the IDOi@DBP-Hf + X-ray irradiation group exhibited no growth of the re-challenged tumors for 2 months, suggesting a potent antitumor immune memory. In contrast, the mice in the PBS group showed no suppressive effect on the re-challenged tumors.

5.2.3 Combination of RT and other treatments. RT is able to trigger ICD and induce immune responses; however, RT-activated antitumor immunity is too weak to produce the abscopal effect.[398] Thus, several studies have adopted the synergy of RT and other treatments (*e.g.*, PTT, PDT, CDT, gas therapy, *etc.*) to elicit stronger systemic immunity for yielding stronger abscopal effect.[43,528–532]

CDT is an emerging therapy modality that converts intracellular H_2O_2 into more harmful $^{\bullet}OH$ to kill cancer cells.[129] For example, Wang *et al.* combined RT with CDT to activate systemic antitumor immunity against primary and metastatic tumors.[532] They self-assembled 5'-GMP and Cu^{2+} to prepare Cu-based NCPs (Cu-NCPs). The Cu-NCPs contained mixed valence (Cu^{+}/Cu^{2+}) since part of Cu^{2+} was reduced to Cu^{+}. Cu^{2+} in the Cu-NCPs could deplete GSH to reduce ROS scavenging, and the Cu^{+}-mediated Fenton-like reaction could convert H_2O_2 to $^{\bullet}OH$ for CDT of tumors. With these capabilities, the Cu-NCPs could potentiate RT-induced oxidative stress. Cu-NCP-mediated synergistic RT/CDT could induce strong ICD. The flow cytometry analysis revealed that the synergistic RT/CDT triggered significant DC maturation (35.1%) in TDLNs, much higher than that in the RT alone (19.7%) or Cu-NCPs alone (23.1%) group. Unsurprisingly, RT alone showed almost no inhibition effect on distant tumors of bilateral CT26 tumor-bearing mice. However, Cu-NCP-mediated synergistic RT/CDT could suppress both primary and distant tumor growth, resulting in 25% complete regression of distant tumors. After combination with PD-L1 checkpoint blockade, the rate of complete regression of distant tumors was elevated to 62.5%. The infiltrating $CD4^{+}$/$CD8^{+}$ T cell and IFN-γ secretion were significantly increased in both primary and distant tumors of the Cu-NCP-mediated RT/

CDT group. In addition, the Cu-NCP-mediated RT/CDT plus PD-L1 checkpoint blockade showed a significant inhibition effect on lung metastases of 4T1 tumors and resulted in a 90% survival rate after 100 days. However, all the mice in the RT + PD-L1 group died within 75 days. Consequently, these results indicated that synergistic RT/CDT could activate potent systemic antitumor immunity and potentiate ICB against primary tumors and distant metastases.

Phototherapy has been also used to enhance the abscopal effect of RT. Dong *et al.* constructed the semiconductor heterojunction $WO_{2.9}$-WSe_2-PEG NPs (WSP NPs) for local RT/PTT of tumor.[528] The WSP NPs could effectively deposit X-ray energy to enhance the radiosensitizing effect of tumors owing to the high-*Z* element. Moreover, the heterojunction structure could promote the separation of electrons and holes, which further increased ROS production. Furthermore, the WSP NPs could also be used for PTT under NIR laser irradiation, which would directly induce ICD and increase tumor blood supply to sensitize RT. Consequently, the WSP NP-mediated RT/PTT could trigger potent ICD and potentiate checkpoint blockade immunotherapy. WSP NPs + NIR laser + X-ray + αPD-L1 could significantly inhibit both primary and distant tumor growth, leading to 80% complete regression of distant tumors. However, RT alone showed almost no suppressive effect on distant tumors. Further flow cytometry analysis indicated that synergistic RT/PTT/αPD-L1 remarkably elevated infiltrating levels of $CD4^+/CD8^+$ T cells in distant tumors, indicating that the combined treatment was able to elicit systemic antitumor immune responses. Besides, the WSP NP-mediated synergistic RT/PTT/αPD-L1 could also induce long-term immune memory to eradicate re-challenged tumors.

6. Feature application of precision radiotherapy for radioprotection

RT based on high energy ionizing radiation can not only kill cancer cells but also simultaneously damage surrounding normal tissues, including direct damage caused by interaction between radiation and DNA as well as ROS-mediated indirect damage through interaction of radiation and water molecules.[13,534,535] Maximizing the radiosensitizing effect of tumors while minimizing side effects of ionizing radiation on healthy tissues is one aim of precision RT. Hence, a lot of radioprotectors have been designed to reduce the ionizing radiation-induced damages to healthy tissues.[536–538] Until now, most radioprotectors are organic molecular agents, such as naturally occurring compounds and chemical compounds.[536,539–542] For example, amifostine (Ethyol®), the only small-molecular chemical radioprotector approved by U.S. Food and Drug Administration (FDA) so far, shows limited clinical efficacy due to its high toxicity, short blood elimination half-time (<10 min), rapid renal clearance from the body, and narrow administration window.[543,544] With the rapid development of nanotechnology, the nanomaterial-based radioprotectors are expected to overcome these drawbacks of conventional radioprotection. This section will discuss nanotechnology-mediated radioprotection of healthy tissues, including nanoradioprotectors (*e.g.*, cerium-based nanomaterials, transition-metal dichalcogenide, *etc.*) and delivery of molecular radioprotectors.

6.1 Nanomaterials for radioprotection

Recent studies have reported that several types of nanomaterials, also known as nanoradioprotectors, possess the intrinsic radioprotective activities to scavenge excessive ROS generated from ionizing radiation. The nanoradioprotectors exhibit longer blood circulation time and poorer RES clearance compared to small-molecular radioprotectors. The nanoradioprotectors can be divided into the following six categories: (1) carbon-based nanoradioprotectors; (2) noble metal-based nanoradioprotectors; (3) metal oxide-based nanoradioprotectors; (4) transition-metal dichalcogenide (TMDC)-based nanoradioprotectors; (5) MXene-based nanoradioprotectors; and (6) organic nanoradioprotectors (Fig. 30 and Table 5).

6.1.1 Carbon-based nanoradioprotectors. Carbon-based materials composed of benzene moieties, such as fullerene, graphene, graphdiyne, and carbon NP suspension injection (CNSI), have attracted widespread attention as nanoradioprotectors owing to their great biosafety, biocompatibility, and ROS scavenging activity.

6.1.1.1 Fullerene-based nanoradioprotectors. Fullerenes are a family of cage-like molecules that contain various numbers of carbon atoms, including C_{20}, C_{40}, C_{60}, C_{70}, and C_{84}.[555–557] The fullerenes are able to react with free radicals since they have a large number of π-conjugated bonds and an unoccupied molecular orbital with the lowest energy.[558] Thus, fullerenes can act

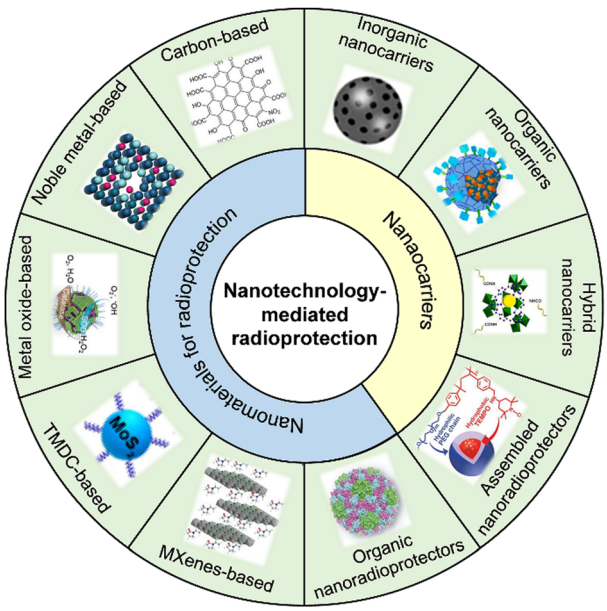

Fig. 30 Scheme of general nanotechnology-mediated radioprotection. Adapted with permission.[545–554] Copyright, Wiley, American Chemical Society, and Elsevier.

Table 5 Representative nanoradioprotectors applied to precision RT

Type	Nanoradioprotectors	Route of administration	Timing of administration	Experimental subject	Radiation type/dose	Ref.
Carbon-based	Fullerenol $C_{60}(OH)_{24}$	Intraperitoneal administration	30 min before irradiation	Adult Wister male rats	X-ray (7 and 8 Gy)	569
Carbon-based	F-NaHA	External use on the skin	1 h before irradiation	Adult BALB/c male mice	NA	571
Carbon-based	DF-1	Co-incubation	5, 15, 30 min after irradiation	Zebrafish embryos	γ-ray (0–40 Gy)	684
Carbon-based	M@Cs	Intravenous administration	30 min before irradiation	Adult C57BL/6 male mice	γ-ray (7.5 Gy)	585
Carbon-based	Graphdiyne-BSA	Intravenous administration	Before irradiation	Adult BALB/c male mice	X-ray (6.5 Gy)	594
Carbon-based	CNSI	Oral administration	Before irradiation	Adult BALB/c male mice	X-ray (4.5 Gy)	545
Noble metal-based	PtPd nanocubes	Intraperitoneal administration	Before irradiation	Adult C57BL/6 male mice	γ-ray (7.2 Gy)	609
Noble metal-based	PtPdMo nanocubes	Intraperitoneal administration	30 min before irradiation	Adult C57BL/6 male mice	γ-ray (7.2 Gy)	610
Noble metal-based	PtPdRh nanocubes	Intraperitoneal administration	30 min before irradiation	Adult C57BL/6 male mice	γ-ray (7.3 Gy)	546
Noble metal-based	Ag_{14} clusterzymes	Intravenous administration	30 min before irradiation	Adult BALB/c female mice	γ-ray (7 Gy)	685
Metal oxide-based	Ceria NPs	Intravenous administration	1 d before irradiation, weekly dose after irradiation for one month	Adult C57BL/6 male mice	X-ray (2.5, 5, and 10 Gy)	623
Metal oxide-based	CeO_2/Mn_3O_4	Intraperitoneal administration	1 h before irradiation	Adult ICR mice	γ-ray (13 Gy)	547
Metal oxide-based	Mn_{12}	Intraperitoneal administration	30 min before irradiation	Adult BALB/c mice	γ-ray (6.5 Gy)	686
TMDC-based	PVP-Bi_2Se_3@Sec	Intratumoral injection	Before irradiation	BEL-7402 tumor-bearing BALB/c nude mice	X-ray (6 Gy)	45
TMDC-based	Bi_2Se_3	Intraperitoneal administration	30 min before irradiation	Adult C57BL/6 male mice	γ-ray (7.5 Gy)	648
TMDC-based	Cys-MoS_2 dots	Intraperitoneal administration	30 min before irradiation	Adult C57BL/6 male mice	γ-ray (7.5 Gy)	548
TMDC-based	Cys-WSe_2 dots	Intravenous administration	30 min before irradiation	Adult C57BL/6 male mice	γ-ray (7.5 Gy)	687
TMDC-based	Au-MoS_2 clusters	Intraperitoneal administration	30 min before irradiation	Adult C57BL/6 male mice	γ-ray (5 Gy)	688
MXene-based	Nb_2C-PVP	Intravenous administration	1 d before irradiation	Adult BALB/c male mice	γ-ray (6.5 Gy)	549
Organic nanoradioprotectors	PHA-L	Intraperitoneal administration	Once per day for 3 days before and 7 days after irradiation	Adult C57BL/6 male mice	γ-ray (7.2 Gy)	683

as radioprotectors to scavenge ROS, including H_2O_2, $^{\bullet}OH$, hydroperoxy radicals (HO_2) and O_2^{-}.[559–564]

Fullerenol ($C_{60}(OH)_n$; n = 12–26, one type of C_{60} fullerene derivatives) was prepared by introducing hydroxyl groups into the structure of fullerene.[565,566] Fullerenol has attracted wide attention in the radioprotection field owing to its excellent free radical scavenging capability.[567] For example, Zhao *et al.* investigated the radioprotective effect of fullerenols on γ-ray-irradiated *Stylonychia mytilus* (*S. mytilus*) cells.[568] They found that fullerenols exhibited great anti-oxidative and ROS scavenging activities, thus increasing the survival fraction of γ-ray-irradiated *S. mytilus*. In addition, the radioprotective efficacy was associated with both the irradiation dose and fullerenol concentration. Trajković *et al.* revealed that intraperitoneal administration of fullerenol $C_{60}(OH)_{24}$ (100 mg kg^{-1}) into rats exposed to X-ray irradiation (8 Gy) could provide a 60% survival rate 30 days after treatment.[569] However, the irradiated rats in the control group died within 30 days.

Radiodermatitis, one of the most common side effects of cancer RT, not only reduces the life quality of patients, but also increases the risk of infection.[570] Zhao *et al.* systematically evaluated the radioprotective effect of fullerenols on radiodermatitis.[571] They proposed an environmentally friendly and gram-scale (>20 g) synthesis method for mass production of fullerenols (Fig. 31a). Then the evaluation of free radical scavenging capabilities showed that fullerenols presented much higher 2,2′-azinobis(3-ethylbenzthiazoline-6-sulfonate) (ABTS) and 1,1-diphenyl-2-picrylhydrazyl (DPPH) scavenging performances than those of superoxide dismutase (SOD) at the same concentrations. Besides the two model radicals, fullerenols also exhibited great scavenging effects on $^{\bullet}OH$ and O_2^{-}. Furthermore, fullerenols (25 μg per Ml) could provide a survival fraction (56.34%) of human keratinocyte (HaCaT) cells under 8 Gy of X-ray irradiation, much higher than 33.95% in the X-ray alone group. Moreover, the further mechanism exploration indicated that fullerenols were able to decrease lipid peroxidation and reduce mitochondrial dysfunction and DNA damage (Fig. 31b). For *in vivo* protective effect evaluation, fullerenols were utilized to construct fullerenol-sodium hyaluronate (F-NaHA) hydrogels that could form a thin film on the skin surface

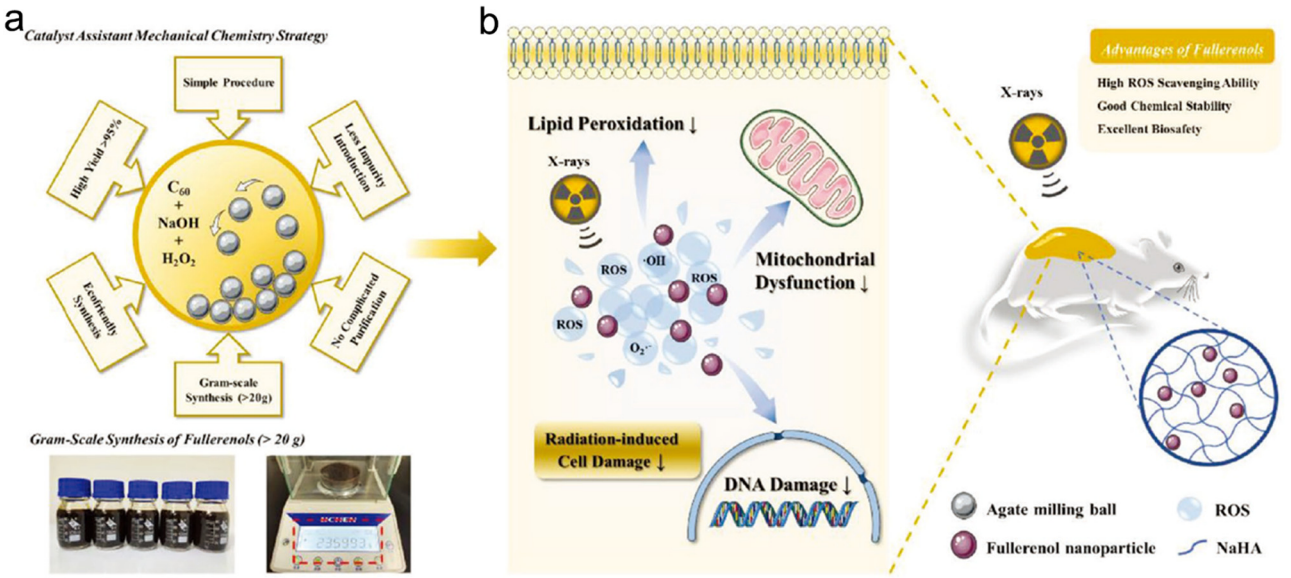

Fig. 31 Fullerene/graphene-based nanoradioprotectors. (a) Gram-scale synthesis of fullerenes using an ecofriendly method. (b) Fullerenes with excellent free radical scavenging properties for skin radioprotection. Reproduced with permission from ref. 571. Copyright 2021, Wiley.

for radiation protection. The commercial SOD salves were used as a positive control. The back skin of healthy BALB/c mice was irradiated with X-rays to induce radiodermatitis. Compared to X-ray alone and X-ray + SOD salve groups, the irradiated skin pre-smeared with F-NaHA hydrogels presented an obviously less inflammatory infiltration area at 4, 9, 16, and 25 d after irradiation, suggesting that F-NaHA hydrogels possess excellent radioprotective capacity for radiodermatitis *in vivo*.

6.1.1.2 Graphene-based nanoradioprotectors. Graphene and its derivatives have been previously reported to scavenge free ROS owing to their unique chemical structures, such as pristine sp^2 carbon domains.[572–577] For example, Nilewski *et al.* previously reported that graphene quantum dots (GQDs) possessed the capability of SOD enzyme and could scavenge O_2^- and $^{\bullet}OH$ to protect bEnd.3 murine endothelioma cells against H_2O_2.[578] Song *et al.* reported that carboxyl-decorated GO (GO-COOH) possessed peroxidase-like nature and could catalyze the oxidization of peroxidase substrate 3,3,5,5-tetramethylbenzidine (TMB) in the presence of H_2O_2.[579]

Graphene-encapsulated metal nanohybrids have been reported to possess excellent catalytic activities of oxygen evolution reaction (OER) and oxygen reduction reaction (ORR) processes, indicating that these nanohybrids are able to scavenge oxygen free radicals.[580–584] Wang *et al.* evaluated the *in vivo* radioprotective efficiency of a series of single-layer graphene-encapsulated metal nanoshields (M@Cs), including graphene-encapsulated Fe and CoNi (denoted as Fe@C and CoNi@C).[585] The TEM images showed that the metal cores were coated with a single layer of graphene (about 3.4 Å). Next, density functional theory (DFT) calculations were utilized to interpret the ROS scavenging processes. Specifically, graphene could adsorb $^{\bullet}OH$ and then react with a proton to generate H_2O during process 1. The O_2^- could transfer an electron to the surface of CoNi@C and be converted into O_2 during process 2. The O_2^- on the surface of Fe@C could be converted into H_2O during process 3. Moreover, the $^{\bullet}O$, $^{\bullet}OOH$, as well as the formed *O and *OOH adsorbed on the surface could be converted into H_2O_2. The pretreatment of Fe@C or CoNi@C nanoshields at 30 min before irradiation could remarkably rescue the ROS level and DNA damage, leading to a higher cell survival proportion (over 70%). However, the survival fraction of CHO cells in the RT alone group was about 50%. Additionally, to evaluate the *in vivo* radioprotective effect, healthy male C57BL/6 mice were intravenously administered with amifostine, Fe@C or CoNi@C 30 min before receiving whole-body γ-ray (7.5 Gy). Pretreatment with CoNi@C or Fe@C could significantly reduce the ROS level in irradiated organs and further increase 3,4-methylenedioxyamphetamine (MDA)/SOD contents in the lungs and liver. Therefore, the irradiated mice in the control group showed a 10% survival rate for 30 days; however, the mice pretreated with CoNi@C and Fe@C exhibited great radioprotective efficacy with 80% and 90% survival rates, respectively, which was even better than that in irradiated mice treated with amifostine (80% survival rate).

6.1.1.3 Graphdiyne-based nanoradioprotectors. Graphdiyne, a type of carbon network material, is composed of acetylenic and benzene moieties. Due to its unique chemical and electronic properties, graphdiyne has been widely applied in various fields, including photocatalysis,[586,587] solar cells,[588–591] energy storage,[592,593] *etc.*

Owing to its π-conjugated structure and diacetylenic linkages, graphdiyne has also been reported to possess ROS scavenging capability. Xie *et al.* fabricated bovine serum albumin (BSA)-decorated graphdiyne NPs (graphdiyne-BSA NPs) to investigate their radiation protection effect.[594] The graphdiyne-BSA NPs could effectively scavenge two model free radicals

(DPPH and ABTS) in a dose-dependent manner. To investigate the *in vivo* radioprotective effect, healthy BALB/c male mice irradiated with X-rays (6.5 Gy) after intravenous injection of graphdiyne-BSA NPs (200 μg each mouse) were collected for SOD, MDA, and bone marrow DNA measurements. The DNA content in bone marrow is an important indicator of ionizing radiation damage. The bone marrow DNA detection assays indicated that graphdiyne-BSA NPs were able to reduce the severe DNA damage induced by X-ray irradiation at day 1, 3, and 7. Furthermore, MDA, lipoxidation products induced by ROS, could be elevated in irradiated liver and lungs. Pretreatment with graphdiyne-BSA NPs could significantly decrease the MDA content to around normal levels. SOD, an antioxidant enzyme, was able to convert O_2^- into H_2O_2 or O_2. X-ray irradiation on mice could remarkably reduce the SOD contents in liver and lungs, while graphdiyne-BSA NPs were able to obviously rescue the SOD levels. These results suggested that graphdiyne-BSA NPs could act as a promising nanoradioprotector with excellent biocompatibility.

6.1.1.4 CNSI-based nanoradioprotectors. CNSI is the first China Food and Drug Administration (CFDA)-approved carbon NP for clinical application in lymph node mapping.[595] Recently, CNSI is found to possess free radical scavenging activity due to its delocalized π-conjugated structure. Moreover, CNSI shows great chemical tolerance toward intestinal conditions, making it possible for oral administration.

Wang *et al.* investigated the intestinal radioprotection performance of CNSI *via* oral administration.[545] CNSI is a graphene analog with 12 benzene rings conjugated and carbonylated. The CNSI was decorated with polyvinylpyrrolidone (PVP) to improve its biocompatibility and water solubility. The CNSI showed broad-spectrum free radical scavenging performance and great chemical stability. Specifically, the CNSI presented better $^{\bullet}OH$ and O_2^- scavenging abilities than amifostine at the same concentration. The UV absorption of CNSI showed no change under simulated gastric juice (pH = 1 acid conditions), which further confirmed its potential for oral administration.[596] The *in vitro* and *in vivo* radioprotection investigation indicated that CNSI could obviously remove intracellular ROS induced by X-ray irradiation and thereby suppress the apoptosis of crypt stem cells and small intestinal epithelial cells. In addition, CNSI could keep the balance of intestinal flora. CNSI could decrease the damage of ROS to the intestinal flora. Besides, CNSI was able to protect the intestinal mechanical barrier from ROS damage to suppress proliferation of pathogenic bacteria. Thus, CNSI as a CFDA-approved carbon material could be a potential intestinal nanoradioprotector to improve the quality of life of cancer patients.

6.1.2 Noble metal-based nanoradioprotectors. Recently, several noble metal-based nanomaterials, including silver (Ag),[597] Pt,[598–600] Au,[601,602] Ir,[603–605] and Pd NPs,[606,607] have been reported to possess free ROS scavenging properties, endowing them with the potential as nanoradioprotectors.

For example, Xu *et al.* utilized ultrasmall Pt clusters to scavenge free radicals induced by γ-ray exposure. The Pt clusters could rescue the SOD and bone marrow DNA levels as well as effectively improve the survival time of mice receiving γ-ray irradiation.[608] Long *et al.* found that hollow PtPd bimetal nanocubes could reduce the free radical levels and recover the SOD/MDA levels in γ-ray-irradiated mice.[609] Besides, Long *et al.* further introduced Mo into the PtPd nanocubes to improve their ROS scavenging ability.[610] The prepared ternary alloy PtPdMo nanocubes could effectively protect healthy cells from γ-ray irradiation and improve the survival rate of irradiated mice by 50%, which was higher than those pre-treated with Pt (30%) and PtPd (40%) counterparts. In addition, Wang *et al.* incorporated rhodium (Rh) into PtPd nanocubes to prepare ternary PtPdRh nanocubes for investigation of their free radical scavenging capability (Fig. 32a).[546] The energy dispersive spectroscopy (EDS) mapping confirmed the distribution of Pd, Pt, and Rh elements in the nanocubes. The atomic ratio of Pd : Pt : Rh in PtPdRh nanocubes was 4 : 2 : 1. In this work, the ternary PtPdRh nanocubes could not only clear excessive $^{\bullet}OH$, but also serve as catalase and peroxidase to scavenge H_2O_2 and O_2^-, respectively. Moreover, the free radical scavenging ability of PtPdRh nanotubes was better than that of Pt or PtPd nanotubes at the same concentration. The CHO cells pre-treated with PtPdRh nanotubes (1.2 μg mL^{-1}) followed by γ-ray irradiation (4 Gy) showed significantly improved cell viability (94%), much higher than that in the radiation alone group (Fig. 32b). To investigate the *in vivo* radioprotection, healthy C57BL/6 mice were intraperitoneally injected with Pt, PtPd, or PtPdRh nanocubes (1 mg each mouse) 30 min before γ-ray irradiation (7.3 Gy). The results showed that pretreatment of PtPdRh nanocubes remarkably improved the survival rate of irradiated mice to 50% on the 30th day, compared to 30% and 40% in the Pt and PtPd groups, respectively (Fig. 32c).

Furthermore, Ag-based nanomaterials have also been shown as one type of nanoradioprotectors. Chandrasekharan *et al.* complexed silver NPs (SN) with glycyrrhizic acid (GLY) to form the SN-GLY complex.[611] Oral administration of SN-GLY at 60 min before γ-ray irradiation (8 Gy) could improve the survival rate of irradiated mice to 40% on the 30th day. However, all the irradiated mice in the control group died within 9 days.

6.1.3 Metal oxide-based nanoradioprotectors. Recently, metal oxide-based nanomaterials, including cerium oxide (CeO_2),[612–614] manganese oxide,[615–618] and iron oxide,[619,620] have gained a lot of attention in the treatment of inflammatory diseases due to their ROS scavenging abilities.

CeO_2 is the most commonly used antioxidant metal oxide since its ability to reversibly shift between the two oxidation states (Ce^{3+} and Ce^{4+}) endows it with CAT and SOD mimetic activities. CeO_2 can catalytically scavenge diverse free radicals, including H_2O_2, O_2^-, and $^{\bullet}OH$.[434,621] Therefore, several studies have utilized CeO_2 NPs to protect radiation injury.[622–626]

To further strengthen the ROS scavenging capability, Han *et al.* grew manganese ions onto CeO_2 nanocrystals to form heterostructured CeO_2/Mn_3O_4 nanocrystals for enhanced radioprotection (Fig. 33a).[547] The UV Raman spectroscopy results revealed that the CeO_2/Mn_3O_4 nanocrystals had a higher oxygen

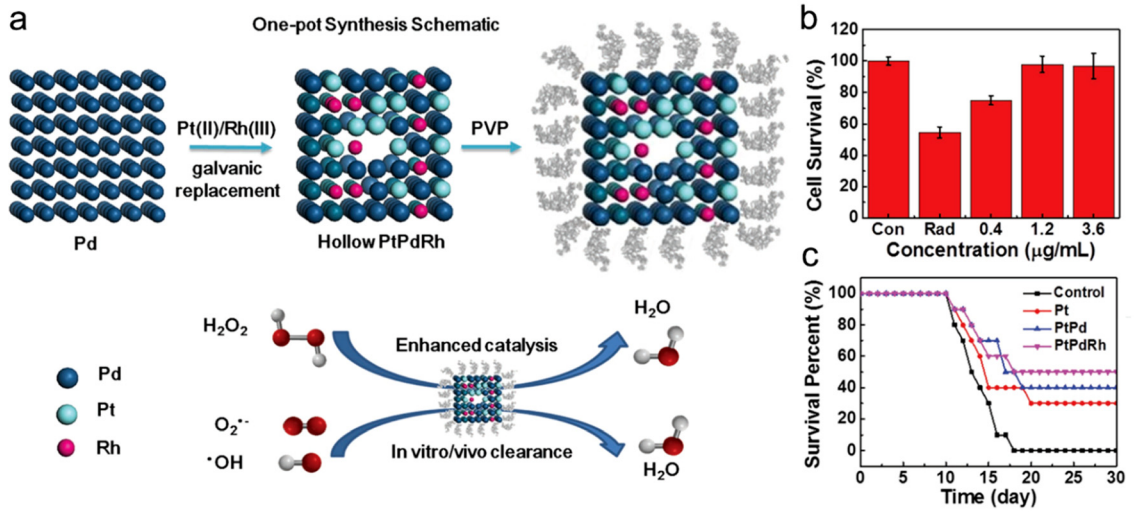

Fig. 32 Noble metal-based nanoradioprotectors. (a) A scheme showing the synthesis and catalysis of hollow PtPdRh nancubes. (b) Survival proportion of CHO-K1 cells under γ-ray radiation with or without the treatment of hollow PtPdRh nancubes at various concentrations. (c) Survival rates of mice receiving different treatments before γ-ray irradiation (7.3 Gy). Pt, PtPd, and PtPdRh nancubes: 1 mg each mouse. Reproduced with permission from ref. 546, 2018, Wiley.

vacancy level and stronger free radical scavenging ability than CeO_2 nanocrystals. To further improve the biocompatibility and dispersibility, the CeO_2/Mn_3O_4 nanocrystals were modified with PEG. Next, a mouse intestinal organoid (mIO) model constructed from leucine-rich repeat-containing G-protein coupled receptor 5-green fluorescence protein (LGR5-GFP) transgenic mice was used to evaluate the radioprotective effects of CeO_2/Mn_3O_4 nanocrystals. The irradiated mIOs (8 Gy) pre-treated with CeO_2/Mn_3O_4 nanocrystals showed more crypt buds and Ki67 positive cells than those pretreated with CeO_2 or Mn_3O_4 alone (Fig. 33b). LGR5-positive intestinal stem cells could recover the irradiation-induced intestinal structure damage and thus were regarded as an indicator of radioprotection.[627] The fluorescence-activated cell sorting (FACS) results showed around 14% LGR5 + mIOs under normal conditions while the proportion dropped sharply to 0.17% post-irradiation. Pretreatment with CeO_2/Mn_3O_4 nanocrystals could recover the proportion of LGR5 + mIOs by 9.78%, much higher than that in the CeO_2 (4.82%) or Mn_3O_4 group (2.54%). To investigate the *in vivo* radioprotective effect, healthy mice were intraperitoneally administered with various radioprotectors at 1 h before receiving a lethal dose of total body irradiation (TBI, 13 Gy). All the mice in the radiation alone group died within 13 days. The mice pre-treated with amifostine at a dose of 250 mg kg^{-1} showed an increased survival rate by 20% after 30 days post-TBI. However, 60% mice treated with a higher dose of amifostine (400 mg kg^{-1}) died instantly due to relatively high systemic toxicity. In addition, pretreatment with CeO_2/Mn_3O_4 nanocrystals (0.55 mg kg^{-1}) could significantly improve the survival rate by 67% even at 150 days post-TBI compared to the survival rate in the CeO_2 (20%) or Mn_3O_4 (30%) group (Fig. 33c).

6.1.4 TMDC-based nanoradioprotectors. TMDCs are semiconductors of the type MX_2, where M represents a transition metal from group 4–10 (W, Mo, Ti, or Ta) and X refers to a chalcogen atom (Se, S, or Te).[628–631] Linus Pauling first defined the structure of TMDCs, dating back to 1923.[632] Due to their unique chemical, physical, and structural properties, TMDCs have been utilized in many fields, including electronics,[633] optoelectronics,[634] energy storage,[635,636] catalysis,[637–639] gas sensors,[640–642] transistors,[643,644] and biomedicine.[645,646]

Recently, several TMDCs were reported to exhibit high catalytic activities, endowing them with potential radioprotective function. For instance, Zhang *et al.* found that Bi_2Se_3 NPs could be oxidized easily in air, PBS solution, and even blood.[647] Inspired by this, they employed PVP-modified Bi_2Se_3 NPs to clear the ROS induced by γ-ray radiation.[648] Healthy C57BL/6 mice were intraperitoneally administered with Bi_2Se_3 NPs at 30 min after γ-ray (a lethal dose of 7.5 Gy) irradiation. All the mice in the radiation alone group died within two weeks. Treatment with Bi_2Se_3 NPs (0.2 and 1 mg each mouse) could obviously improve the 30 day survival rate by 46% and 71%, respectively. Moreover, administration of Bi_2Se_3 NPs could also recover the radiation-induced changes in the blood cell levels, such as red blood cells, platelets, white blood cells, *etc.*

Ultrasmall nanoradioprotectors show rapid clearance through urine excretion and lead to low systemic toxicity. For example, Zhang's group developed ultrasmall MoS_2 dots and then modified the dots with a cysteine protection layer to improve their water-solubility and biocompatibility.[548] The prepared cysteine-protected MoS_2 dots at the concentration of 140 μg mL^{-1} showed no obvious cytotoxicity to 3T3/A31 cells. The *in vitro* experiments revealed that the cysteine-protected MoS_2 dots could effectively scavenge intracellular H_2O_2 and O_2^{-}. Moreover, the *in vivo* radioprotection was evaluated on high-dose (7.5 Gy) γ-ray irradiated C57BL/6 mice. The cysteine-protected MoS_2 dots could remarkably rescue radiation-induced DNA damage as well as the SOD and MDA contents in liver and lungs. All the mice receiving radiation alone died

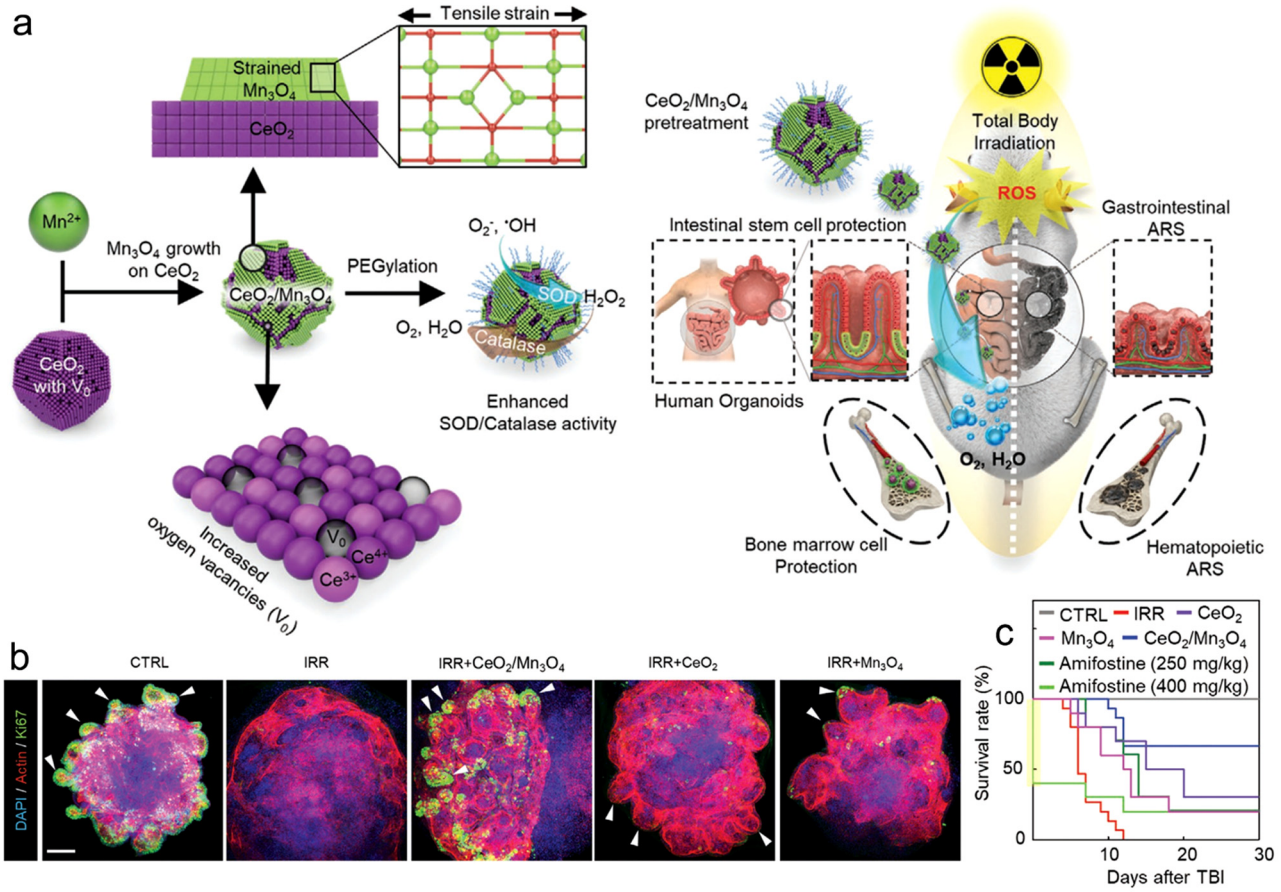

Fig. 33 Metal oxide-based nanoradioprotectors (a) A scheme of CeO_2/Mn_3O_4 nanocrystals for radioprotection. (b) Immunofluorescence staining images (DAPI, Actin, and Ki67) of cells after different treatments. The white arrow heads indicate representative crypt buds. Scale bar = 200 μm. (c) Survival rates of irradiated mice (13 Gy) treated with CeO_2, Mn_3O_4 and CeO_2/Mn_3O_4 nanocrystals (0.55 mg kg^{-1}), and amifostine (250 and 400 mg kg^{-1}). Reproduced with permission from ref. 547, 2020, Wiley.

within 14 days. However, pretreatment with various concentrations (10, 20, and 50 mg kg^{-1}) of cysteine-protected MoS_2 dots *via* intraperitoneal injection at 30 min before radiation could significantly improve the 30 day survival rates to 7.1%, 42.9%, and 78.6%, respectively. In addition, the *in vivo* pharmacokinetics results indicated that the cysteine-protected MoS_2 dots with a blood circulation half-time of 2.1 h could be removed around 80% *via* renal clearance within 1 day owing to the ultrasmall hydrodynamic size of 3.1 nm. The biodistribution analysis showed almost no accumulation of MoS_2 dots in various organs at 30 d post-injection. The rapid renal clearance and great radioprotective effect make the ultrasmall MoS_2 dots potential for clinical translation.

6.1.5 MXene-based nanoradioprotectors. First described in 2011, transition-metal nitrides and carbonitrides (MXenes, a class of two-dimensional inorganic nanomaterials composed of transition metal carbides, nitrides, or carbonitrides) have been explored for application in various fields such as energy storage,[649,650] energy conversion,[651] water purification,[652,653] electrochromic devices,[654] and gas sensors,[655,656] *etc.*[657,658] Owing to their unique physiochemical properties, MXenes have also been applied in biomedical fields, such as PTT,[659,660] antibacterial,[661] antiviral,[662] bioimaging,[663] biosensors,[664] tissue engineering,[665] *etc.*

Ren *et al.* designed ultrathin two-dimensional (2D) niobium carbide (Nb_2C) MXenes for radioprotection.[549] The prepared Nb_2C MXenes were decorated with PVP (denoted as Nb_2C-PVP) to improve their dispersibility and biocompatibility (Fig. 34a). The DFT calculations suggested that the ROS scavenging capability of Nb_2C-PVP nanosheets (NSs) was due to the continuous •OH attack. The •OH attack resulted in the dehydration of hydroxyl groups on the surface and formation of an oxygenic layer above Nb nanosheets (NbO_x species) (Fig. 34b and c). The Nb_2C-PVP NSs exhibited great antioxidant activities to scavenge O_2^-, H_2O_2, and •OH in a concentration-dependent manner. The *in vitro* experiments revealed that Nb_2C-PVP NSs showed no cytotoxicity to the 3T3/A31 cells even at a concentration of 200 μg mL^{-1}, and that pretreatment with Nb_2C-PVP NSs at different concentrations (50 and 100 μg mL^{-1}) could remarkably reduce 3T3/A31 cell death induced by X-ray irradiation at various doses (Fig. 34d). To evaluate the *in vivo* radioprotective effect, healthy BALB/C mice were intravenously administered with Nb_2C-PVP NSs at 1 d before receiving γ-ray TBI at a lethal dose of 6.5 Gy. Pretreatment with 5, 10, and 20 mg kg^{-1} of

Nb_2C-PVP NSs significantly improved the survival rate by 30%, 50%, and 81% at day 30. However, the mice in the TBI alone group all died within 20 days. The bone marrow mononuclear cell (BM-MNC) count was utilized to investigate the radioprotective effect on the hematopoietic system. The results showed that the BM-MNC count in irradiated mice pre-treated with Nb_2C-PVP NSs was obviously higher than that in the TBI only group (Fig. 34e). Moreover, the BM-MNC count in the Nb_2C-PVP NS-treated mice was totally rescued to the normal level at 30 d after irradiation, suggesting the great radioprotective effect of Nb_2C-PVP NSs on the hematopoietic system. In addition, the biodistribution analysis showed that Nb_2C-PVP NSs could be effectively metabolized through kidneys and liver with almost no accumulation in the organs at 14 d after intravenous injection (Fig. 34f).

6.1.6 Organic nanoradioprotectors. Increasing studies have utilized organic NPs for radioprotection due to their excellent biodegradability and ease of modification. For example, the melanin NPs have been shown to possess free radical scavenging properties.[666–668] Several studies revealed that melanin NPs could effectively clear the ROS induced by X-ray or γ-ray irradiation and rescue the bone marrow DNA damage, SOD/MDA contents in liver and lungs, various organ injuries, and survival rate of irradiated mice.[669–671]

Besides, protein NPs based on natural biomolecules have gained considerable interest owing to their intrinsic biocompatibility, biodegradability, and low toxicity.[672–674] The protein NPs can not only serve as drug carriers but also target the receptors on the cell membrane to activate intracellular signaling pathways.[675–679]

Previous studies have revealed that several certain proteins were able to function as protectors against radiation damage.[680–682] Long *et al.* designed phytohemagglutinin (PHA-L) protein NPs to activate toll-like receptor 5 (TLR5) for radioprotection.[683] Due to spontaneous biocompatibility, the PHA-L protein NPs showed no significant cytotoxicity to CHO-K1 cells at a concentration of 100 μg mL^{-1}. The PHA-L protein NPs could target the TLR5 receptor on the cell surface and then activate the TLR5/NF-kB pathway to inhibit radiation-induced CHO-K1 cell death. Moreover, the PHA-L protein NPs could also induce the expression of TLR5 receptor on innate immune cells to modulate immune responses. Then, to investigate the *in vivo* radioprotective efficacy, the healthy C57BL/6 mice were intraperitoneally administered with PHA-L protein NPs before γ-ray TBI (7.2 Gy). The treatment of 5 and 10 mg PHA-L protein NPs significantly improved the 30 day survival rate by 38% and 69%, respectively. However, all the mice in the TBI alone group died within 20 days. In addition, PHA-L protein NPs could obviously rescue various radiation-induced injury parameters, including bone marrow DNA content, hematopoietic system, gastrointestinal tract injury, *etc.* To further confirm the protective mechanisms, the $TLR5^{-/-}$ mice were used to evaluate the radioprotection of the PHA-L protein NPs. The results showed that the 30 day survival rate of irradiated $TLR5^{-/-}$ mice pre-treated with PHA-L protein NPs was 0%, suggesting that the

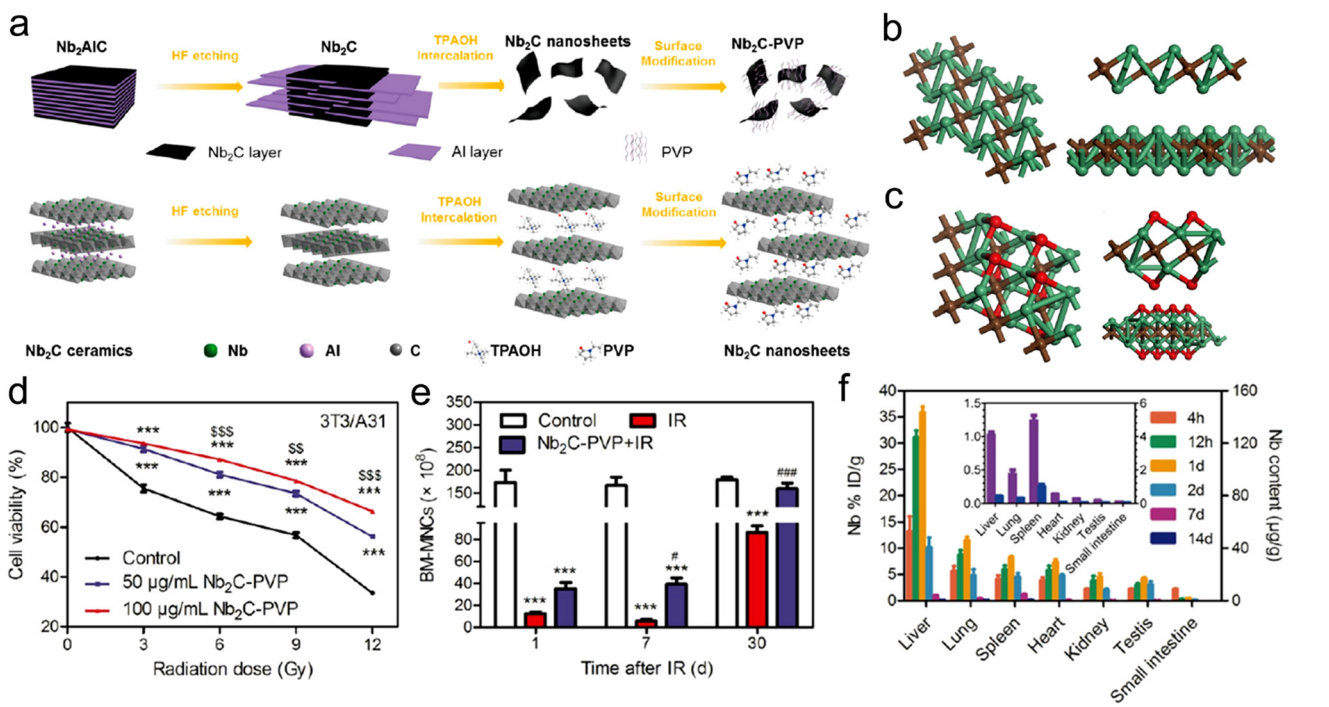

Fig. 34 MXene-based nanoradioprotectors. (a) A scheme of synthesis process and exfoliation process of ultrathin Nb_2C-PVP NSs. (b) Geometrically optimized single-layer Nb_2C nanostructure viewed from the orthogonal, front, and left sides. (c) Geometrically optimized full nanostructure of oxidized Nb_2C viewed from the orthogonal, front, and left sides. (d) Viability of 3T1/A31 cells treated with Nb_2C-PVP NSs (50 and 100 μg mL^{-1}) under various radiation doses. (e) BM-MNC counts of irradiated mice (5 Gy) at 1, 7, and 30 days after treatment with Nb_2C-PVP NSs (20 mg kg^{-1}). (f) Biodistribution of Nb in various organs at 4 h, 12 h, 1, 2, 7, and 14 days after intravenous injection of Nb_2C-PVP NSs (20 mg kg^{-1}). Reproduced with permission from ref. 549, 2019, American Chemical Society.

TLR5 receptor was necessary for the radioprotection of PHA-L protein NPs. Furthermore, about 70% of PHA-L protein NPs could be rapidly excreted from the organs *via* kidneys within 48 h of injection. Overall, compared to those inorganic nanoradioprotectors, the organic nanoradioprotectors with superior biocompatibility and rapid renal-clearance exhibit more potential for clinical translation.

6.2 Nanocarriers to deliver small molecular radioprotectors

So far, numerous small molecular radioprotectors of both natural and synthetic origin have been developed to protect normal tissues from radiation, such as amifostine, curcumin, glycyrrhizic acid, melanin, caffeic acid, baicalein, dihydropyridines, MnTnBuOE-2-PyP^{5+}, *etc.*[689–695] However, these small molecular radioprotectors exhibit poor bioavailability and short blood circulation half-life, resulting in limited protective efficacy.[696] Advanced nanotechnology promises to overcome these challenges. Besides acting as nanoradioprotectors to scavenge free ROS, the nanomaterials have also been utilized as carriers to improve the protective efficacy of small molecular radioprotectors. These nanocarriers are divided into the following four categories: (1) inorganic nanocarriers; (2) organic nanocarriers; (3) organic–inorganic hybrid nanocarriers; and (4) assembled nanoradioprotectors.

6.2.1 Inorganic nanocarriers to deliver small molecular radioprotectors. Inorganic nanocarriers, especially mesoporous nanomaterials, have attracted wide interest for delivery of small molecular radioprotectors owing to several advantages, such as controllable shape and size, high surface area, potential imaging capability, and facile surface modification.[697–701]

For example, Dadachova's group utilized silica NPs as carriers to deliver melanin into the bone marrow for radioprotection of the hematopoietic system.[702] The intravenous injection of MNs (50 mg kg^{-1}) at 3 h before TBI with ^{137}Cs radiation (125 cGy) could effectively rescue the hematopoietic damage caused by TBI. Chandrasekharan *et al.* complexed silver NPs (SN, $<$50 nm) with glycyrrhizic acid (SN-GLY, a radioprotective molecule) to reduce radiation-induced injuries. The *in vivo* experiments revealed that oral administration of SN-GLY before γ-ray TBI was able to rescue bone marrow DNA damage and decrease peripheral blood cells.[703–705]

Curcumin, a hydrophobic polyphenol drug derived from turmeric, has gained considerable interest in biomedicine, including tumor therapy, antibacterial, antiviral, antioxidant, *etc.*[706–713] Besides, curcumin is able to serve as both a radiosensitizer for various tumors and a radioprotector for healthy tissues.[714] However, the poor water solubility and biocompatibility of curcumin result in short blood circulation half-time and low tissue accumulation, thus limiting its biomedical application.[715,716] Various nanocarriers have been utilized to load curcumin for longer blood circulation half-life and better tissue distribution.[717–721] For example, Xie *et al.* modified bamboo charcoal NPs (BCNPs) with D-α-tocopherol polyethylene glycol succinate (TPGS) and then loaded curcumin into the NPs (TPGS-BCNPs@curcumin) for both radiosensitization and radioprotection.[550] The TPGS-BCNPs exhibited good biocompatibility and high tumor accumulation. With a large surface area of 259.31 m^2 g^{-1}, curcumin could be efficiently loaded into TPGS-BCNPs with a loading ratio of 36.15%. Moreover, the TPGS-BCNPs@curcumin possessed high photothermal conversion efficiency, and the curcumin could be released on demand upon NIR laser stimulation. In addition, the TGPS, a P-glycoprotein (P-gp) inhibitor, could suppress the efflux of curcumin and further enhance chemotherapy efficacy. Besides, the TPGS-BCNPs@curcumin could deliver considerable curcumin into normal cells. The curcumin exhibited radioprotective effect by effectively clearing intracellular ROS content and reducing radiation-generated DNA damage.

6.2.2 Organic nanocarriers to deliver small molecular radioprotectors. Organic nanocarriers, including liposomes, polymeric NPs, micelles, dendrimers, protein nanocarriers, solid lipid NPs, and virus-like particles (VLPs), possess a lot of advantages, such as low toxicity, drug loading capacity, and easy modification of targeting moieties.[722–724] Various organic nanocarriers have been used to deliver small molecular radioprotectors, such as WR-1065, curcumin, γ-tocotrienol and baicalein, to specific organs or tissues for higher accumulation and longer retention time.[725–739]

Gastrointestinal tract, one of the organs most vulnerable to radiation, can progress to severe gastrointestinal syndrome under radiation at a dose higher than 8–10 Gy.[740,741] Thus, radioprotection of the gastrointestinal tract is urgent and important. However, systemic administration of radioprotectors causes poor distribution in the gastrointestinal tract. Besides, conventional molecular radioprotectors administered orally may fail in the specific environment of gastrointestinal tract, especially the gastric acid.[742] In addition, the radioprotective agents would be rapidly removed by the mucus layer even if they reach to the gastrointestinal tract.[743] To overcome these challenges, Zhang *et al.* loaded molecular radioprotectors into organic nanocarriers for small intestine radioprotection.[737] Since a previous study revealed that deficiency in Absent-In-Melanoma 2 (AIM2) protein could reduce the radiation-induced gastrointestinal injury,[744] in this work, the arginine-chitosan (Arg-CS) polymer was loaded with thalidomide (THA, an AIM2 inhibitor) and then coated with the polydopamine layer (PDA@Arg-CS(THA) NPs) for water-resistant adhesion in small intestine (Fig. 35a).[745] *Ex vivo* intestinal crypt 3D model was used to evaluate biocompatibility and radioprotection efficacy. The results indicated that PDA@Arg-CS(THA) showed no significant toxicity to the intestinal crypts and PDA@Arg-CS(THA) could effectively protect the intestinal crypts from radiation. Next, the SEM, FT-IR, and DLS analyses revealed that the morphology, chemical structure, and hydrodynamic size of PDA@Arg-CS(THA) were stable in simulated gastric acid and intestinal medium due to the acid-resistance of the PDA layer (Fig. 35b). Moreover, the zeta potential of PDA@Arg-CS(THA) was neutral in a simulated intestinal medium, which could reduce the electrostatic interactions with mucus and further enhance the diffusion of NPs (Fig. 35c). Interestingly, PDA@Arg-CS(THA) exhibited a pH-switchable release profile. The THA release was inhibited in

the simulated gastric acid (pH 1.2) for the first 2 h, whereas the THA was rapidly released in the next 48 h an a simulated intestinal medium (pH 6.0) owing to the neutral surface charge of PDA@Arg-CS(THA) in an intestinal environment (Fig. 35d). Furthermore, the PDA@Arg-CS(THA) was labeled with Cy5.5 to investigate the *in vivo* biodistribution, which showed that Cy5.5-PDA@Arg-CS(THA) was mainly distributed in the small intestine after oral administration (Fig. 35e). In addition, the Cy5.5-PDA@Arg-CS(THA) showed a longer retention time than Cy5.5-Arg-CS(THA) due to PDA coating (Fig. 35f). To evaluate the *in vivo* radioprotective effect, the mice were orally administered with vehicle, PDA@Arg-CS, free THA, and PDA@Arg-CS(THA) 12 h before receiving whole abdominal irradiation at a lethal dose. The results showed that PDA@Arg-CS(THA) could effectively improve the survival rate by 45% compared to 15% in the free THA group (Fig. 35g).

6.2.3 Organic–inorganic hybrid nanocarriers to deliver small molecular radioprotectors. Organic–inorganic hybrid nanocarriers contain two or more organic and inorganic components.[746–749] The hybrid nanocarriers not only reserve the physical and chemical properties of each component, but also show advantages over each component.

MOFs, one type of hybrid materials composed of metal centers and organic linkers, have gained considerable interest in biomedical application due to their large surface areas, tunable pore sizes, and great biodegradability.[750–752] For example, Cao *et al.* used PEGylated MIL-101(Cr) MOFs to load WR-1065 (the major active metabolite of amifostine) (WR@PEG-MIL-101(Cr)) for hematopoietic radioprotection.[552] With a large surface area of over 1300 $m^2 g^{-1}$, the MOF NPs were loaded with WR-1065 (47.2 wt%) to improve blood circulation and tissue distribution. To investigate the *in vivo* radioprotective efficacy, healthy C57/BL male mice were orally administered with radioprotective agents at 1 h before γ-ray TBI at a lethal dose of 8.0 Gy. Administration of 150 and 265 mg kg^{-1} of WR@PEG-MIL-101(Cr) significantly improved the 30 day survival rate by 50% and 80%, respectively, compared to 30% in the free WR-1065 group (125 mg kg^{-1}) and 0% in the control group.

6.2.4 Assembled nanoradioprotectors by small molecular radioprotectors. Most of small molecular radioprotectors need to be administered intravenously in a relatively narrow time window before radiation due to their rapid renal-clearance and short circulation half-time. Several studies assembled these molecular radioprotectors into nano-sized agents and thereby improved the circulation and retention times.

4-Amino-2,2,6,6-tetramethylpiperidine 1-oxyl (TEMPO), one type of low-molecular-weight (LMW) nitroxide compound, is able to serve as an antioxidant to scavenge oxidants. Previous studies have reported that 4-amino-TEMPO could function as a radioprotector *in vitro*. However, free TEMPO could lead to severe off-target effects and disrupt the redox balance in normal cells.[753–755] In addition, free TEMPO could be rapidly removed from the body due to its extremely poor bioavailability.[756] Nagasaki's group conjugated 4-amino-TEMPO to PEG-*b*-poly(chloromethylstyrene) (PEG-*b*-PCMS, a diblock copolymer) to form PEG-*b*-PMNT. Then, the PEG-*b*-PMNT could self-assemble into redox NPs (RNPs) (Fig. 36a).[553] The self-assembly of RNPs could not only avoid leakage of TEMPO

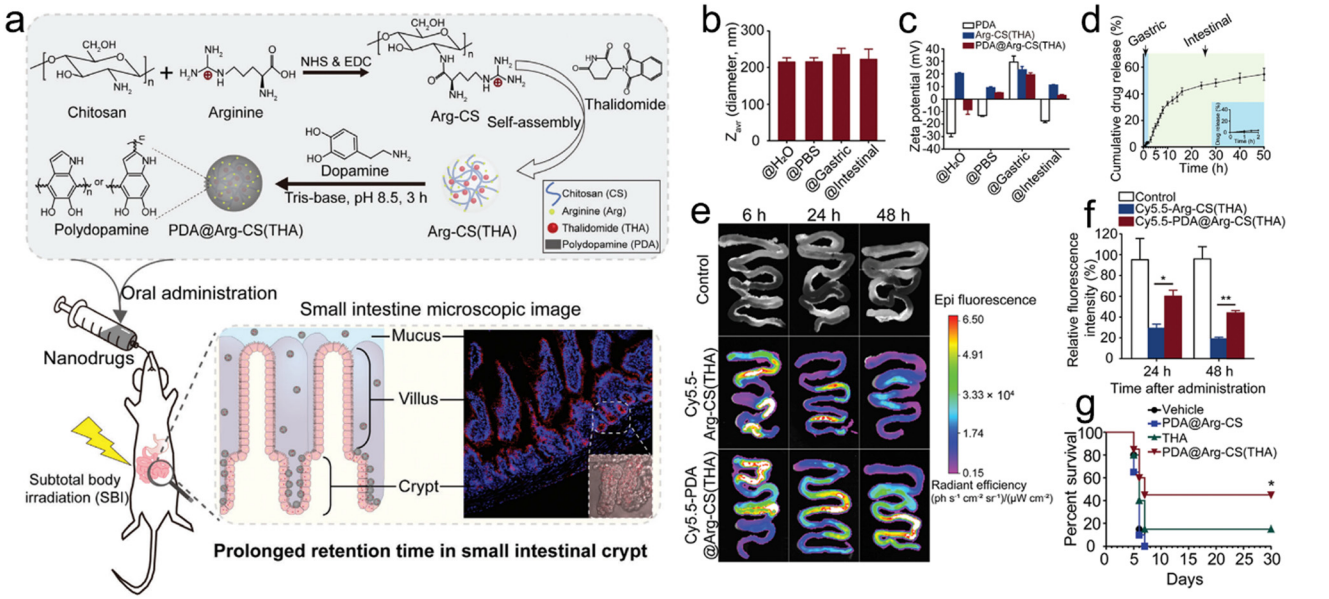

Fig. 35 Organic nanocarriers to deliver small molecular radioprotectors. (a) A scheme showing the synthetic process of PDA@Arg-CS(THA) and its radioprotective effect on small intestine. (b) Hydrodynamic sizes of PDA@Arg-CS(THA)in H_2O, PBS, and simulated gastric and intestinal media. (c) Zeta potentials of self-polymerized PDA, Arg-CS(THA), and PDA@Arg-CS(THA) in different media. (d) Drug release profile of PDA@Arg-CS(THA) in simulated gastric and intestinal media. Inset: THA release profile of PDA@Arg-CS(THA) in a simulated gastric medium in the first 2 h. (e) *Ex vivo* FL images of small intestine at 6, 24, and 48 h after oral administration of PDA@Arg-CS(THA), Cy5.5-Arg-CS(THA), or Cy5.5-PDA@Arg-CS(THA). (f) Relative FL intensity of the small intestine at 24 and 48 h after oral administration. (g) Survival rate of irradiated mice (14 Gy) treated with free THA, Arg-CS(THA), or PDA@Arg-CS(THA). Reproduced with permission from ref. 737, 2020, Wiley.

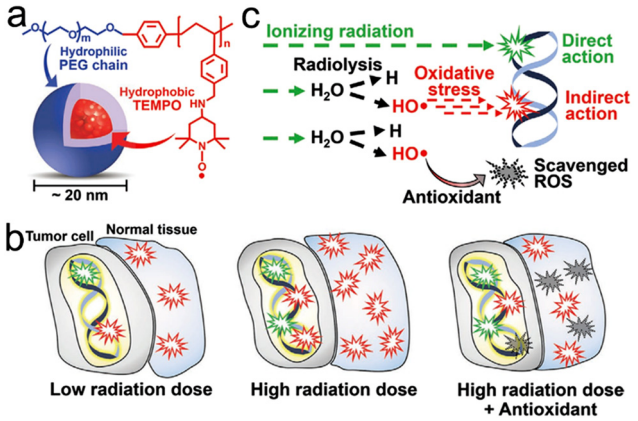

Fig. 36 Assembled nanoradioprotectors by small molecular radioprotectors. (a) Chemical structure of the RNP. (b) Antioxidant clears most of radiation-induced ROS in normal tissues. (c) Antioxidant removes ROS produced by the indirect action of ionizing radiation. Reproduced with permission from ref. 553, 2020, Royal Society of Chemistry.

molecules but also increase blood circulation half-life and tissue retention time. The RNPs were prepared to alleviate excessive ROS in healthy tissues induced by indirect damage of radiation (Fig. 36b and c). To evaluate the *in vivo* radioprotective effect of RNPs, the tumor-bearing mice were subcutaneously injected with RNPs (TEMPO = 200 mg kg^{-1}) at 1 d before X-ray irradiation at various doses (10, 20, 25, and 30 Gy). The tumor-bearing mice subcutaneously injected with amifostine (500 mg kg^{-1}) at 2 h before radiation were used as a positive control. The results showed that pre-administration of RNPs could significantly prolong the median survival time of mice receiving 10, 20, and 25 Gy of X-ray irradiation compared to the amifostine group. Moreover, the treatment of RNPs could also remarkably rescue the decline of body weight in X-ray-irradiated tumor mice compared to the PBS or amifostine group. In addition, both RNPs and amifostine could rescue the abnormal changes of various hematological and biochemical indicators, including RBC, white blood cells, PLT, creatinine (CRE), blood urea nitrogen (BUN), alanine aminotransferase (ALT), aspartate transaminase (AST), and total bilirubin (TBIL), indicating that the RNPs were able to reduce off-target damage of radiation to the hematopoietic system, kidneys, and liver. Overall, both nanocarriers and self-assembled nanoradioprotectors can effectively improve blood circulation and tissue retention of small molecular radioprotectors, thus enhancing radioprotective efficacy.

7. Prospects and challenges

In this review, we systematically summarized the strategies for maximizing RT efficacy of tumors, including tumor-targeted delivery, exo/endogenous stimuli-responsive strategies, and imaging-guided precision RT. Besides, we also reviewed two representative featured applications of precision RT: the nanomaterial-mediated RT-induced abscopal effect against distant metastasis, and nanomaterial-mediated radioprotection of the healthy tissues. However, there are a lot of challenges that still require to be overcome.

Various tumor-targeted strategies, including EPR effect-based passive targeting, ligand-based targeting, biomimetic targeting, magnetic targeting, and subcellular organelle targeting, were utilized to enhance the tumor accumulation of nanoradiosensitizers. For the EPR effect, several studies have revealed that the particle sizes and shapes are quite important for tumor accumulation and retention. However, the specific mechanism for this phenomenon has not been deeply discussed. Biological ligand-based modification is one of the most common active targeting strategies for nanoradiosensitizers. The density of targeting ligands on the surfaces of NPs needs to be adjusted to balance targeting efficiency and potential instability of NPs, especially in a complex biological environment. Due to the highly specific recognition, bioorthogonal ligand-based targeting has been a promising strategy for targeted theranostics. However, there are still some issues that need to be considered in the future research. For example, the antibodies cannot be completely eliminated from the body even with administration of the clearing agents. Biomimetic targeting as an emerging strategy utilizes cells or cell membrane to load or coat nanoradiosensitizers for targeted delivery. However, these biomimetic nanoradiosensitizers cannot be stored for a long time, which may affect their potential for clinical translation. Moreover, the efficiency of magnetic targeting is mainly limited by the distance between the magnets and the target sits. Future research needs to take the geometry of the magnetic field into account. In addition, most current nanoradiosensitizers act on traditional physical enhancement, such as X-ray energy deposition by high-*Z* elements. However, the toxicity of these heavy metals is unavoidable. Bu's group systematically reviewed the development of catalytic radiosensitization on the basis of radio–nano interactions and catalysis–biological interactions.[757] Catalytic radiosensitization refers to the development of nanocatalysts to enhance X-ray radiation-induced chemical reactions to produce active species or molecules for treatment, thus improving RT efficacy. The catalytic radiosensitization might provide more opportunities for biological applications of different nanocatalysts.

Exogenous and/or endogenous stimuli-responsive strategies are able to induce size/shape change, structural degradation, and drug release, for precision RT. However, there are still several challenges. First, the exogeneous stimuli, such as X-rays, light, and US, can achieve spatiotemporally precise control of responsive nanoradiosensitizers. However, the efficiency of responsiveness may be limited. The endogenous stimuli-based responsiveness may be more efficient but less controllable. Therefore, combining exogenous and endogenous stimuli is able to realize spatiotemporally controllable and efficient responsiveness for precision RT. Second, endogenous stimuli-responsive nanoradiosensitizers can respond to tumor tissues based on the differences in biomarker levels (*e.g.*, pH, GSH, ROS, hypoxia, and enzymes, *etc.*), between tumors and normal tissues. However, these nanoradiosensitizers will still

exhibit a certain degree of off-target side effects owing to the prevalence of these biomarkers in normal tissues. Third, there are also several shortcomings of exogeneous stimuli in clinical applications. For example, light stimuli do not work in deep tumors due to poor tissue penetration. The US stimuli are more suitable to superficial tumors rather than deep tissues. Thus, considering the advantages and disadvantages of different exogenous and/or endogenous stimuli, responsive strategies will be proposed according to various clinical applications to achieve precision RT in future studies. In addition, other exogenous (*e.g.*, magnetic field, hyperthermia, *etc.*) and endogenous stimuli (*e.g.*, glucose, nucleic acids, ATP, *etc.*) can be considered to develop responsive nanoradiosensitizers in future research.

In clinical practice of RT, the imaging techniques, such as MRI and CT, were commonly used for precise organ/tumor delineation and thereby minimize the radiation dose to normal tissues. For example, magnetic resonance-guided radiotherapy (MRgRT) has become clinically available, which offers excellent soft-tissue contrast for precise observation of interfractional changes in tumor anatomy.[758,759] The MRgRT allows for on-table treatment adaptation that enables dose escalation and reducing toxicity. So far, many types of imaging techniques, including FLI, PAI, MRI, CT, US, PET, and SPECT, have been applied to guide precision RT. However, these studies mainly utilized imaging methods to monitor the biodistribution and tumor accumulation of nanoradiosensitizers, which could help select the optimal time point for RT. In addition, the imaging methods could provide ample information of tumors, such as TME, and tumor response to therapy. The functional imaging techniques, including functional CT, fMRI, and PET, allow visualizing various pathophysiological characteristics of tumors, including perfusion, hypoxia, proliferation, and metabolism.[760] Thus, functional imaging-based guidance can provide more opportunities for individualized RT treatment. For example, dynamic contrast enhanced CT (DCE-CT) as a functional CT technique can be utilized to monitor tissue perfusion.[761] The BOLD/DWI fMRI was used to monitor tumor radiosensitivity and oxygen concentration.[36] Liu *et al.* developed a quantitative MRI-based diagnostic system to predict tumors' responses to RT. The system could stratify pancreatic patients into resistant and sensitive groups.[335] Moreover, the PA and US imaging could also be applied for monitoring tumor oxygenation. Therefore, more future efforts are required to extend various imaging techniques to provide information on tumor location, boundary, response to therapy, and TME (*e.g.*, hypoxia, GSH, *etc.*).

The antitumor immune responses induced by RT alone are inefficient to inhibit distant and metastatic tumors. However, nanomaterial-based RT is able to induce potent ICD and thereby elicit systemic antitumor immunity against metastasis. The anti-metastasis efficacy could be further improved in combination with ICB therapy, immunoadjuvant, or other treatment modalities, such as PTT, PDT, CDT, gas therapy, chemotherapy, *etc.* Besides, nanoimmunotherapeutics could be designed to exert immunotherapeutic action only in response to external stimuli, such as X-ray irradiation, resulting in more precise anti-tumor immune activation and less incidence of immune-related adverse events.[762] Animal models are crucial for investigation of RT-mediated antitumor immune responses. First, the tumors established with cancer cell lines are generally homogenous, which makes it difficult to stimulate heterogenous tumors of clinical patients. Second, most subcutaneous tumors used in these studies, although easy to monitor and operate, do not represent appropriate sites for human tumors. Thus, the subcutaneous tumor model is less predictive when used to test response to RT and immunotherapy. Third, the human cancer cell lines or patient-derived xenograft can only be inoculated into immunodeficiency animals, which makes it difficult to measure systemic immune responses. Moreover, immunocompetent tumor-bearing mice based on mouse cancer cell lines cannot stimulate human tumors well, since the immune system in mice is quite different from that in human. Therefore, more suitable animal models used for immunotherapy evaluation need to developed in the future. In addition, lung metastasis is the most common metastatic model in most previous studies. However, the metastasis in clinical practice can appear in various organs, such as liver, bones, lungs, brain, and peritoneal cavity. The response of different organ metastases to immunotherapy varies greatly. Therefore, various metastatic models need to be considered in future studies.

Amifostine as a phosphorothioate is able to diffuse into cells after being dephosphorylated by alkaline phosphatase and then function as a free radical scavenger.[763] Previous studies have revealed that amifostine could rapidly accumulate in normal tissues rather than tumors, which is believed to result from intratumoral blood flow, acidic tumor microenvironment, and the low level of alkaline phosphatase in tumors.[538,764] Likewise, the nanoradioprotectors can be designed to exert radioprotective effect only in response to specific intratumoral stimuli, such as acidosis, hypoxia, high GSH, H_2O_2 levels, *etc.*, so that the nanoradioprotectors can more concentrate in and protect normal tissues rather than tumor tissues. In addition, targeting strategies, such as ligand-based targeting and magnetic targeting, can also be used to enhance accumulation of normal tissues. Moreover, the nanoradioprotectors are mainly administered intraperitoneally or intravenously to protect healthy tissues from whole body radiation, which might, however, induce systemic toxicity. Typically, the RT only irradiates surrounding tissues or organs when treating local tumors. Thus, more future efforts need to be focused on other routes of nanoradioprotector administration that are easier to be translated to the clinic. For example, the oral or rectal route can be used for radioprotection of gastrointestinal tracts. Inhalation (intratracheal) route is more suitable to protect lung from RILI. External route may be suitable for radioprotection of skin. Moreover, the intrathecal or topical route can be applied for radioprotection of specific tissues, such as brain, spinal, eyes, *etc.* In addition, most studies have been focused on the evaluation of *in vitro* and *in vivo* radioprotective performance of nanoradioprotectors. However, the specific radioprotective mechanisms have not been explored in depth, which requires

further investigation in future studies. Furthermore, the choice of animal models to investigate the radioprotective performance is important for clinical translation. Most studies utilized mouse models to evaluate the radioprotective effect of nanomaterials. Large animals can be considered as models for *in vivo* investigation of protective efficacy of nanoradioprotectors.

Besides, a lot of challenges still remain before the clinical translation of these nanoradiosensitizers. Nanoradiosensitizers that can be produced in a large-scale have more potential for clinical translation. Moreover, most studies have performed *in vivo* biosafety evaluations of nanoradiosensitizers. However, most evaluations were short-term rather than long-term. Moreover, these biosafety evaluations were focused on major organs without considering that these nanoradiosensitizers could also accumulate in other tissues, such as eyes, brain, and muscle. Thus, more comprehensive and long-term biosafety evaluations of the nanoradiosensitizers are required before clinical translation. In addition, the choice of nanomaterials directly affects the time required for clinical translation. The nanoradiosensitizers composed of FDA-approved drugs or materials could be applied in clinical practice faster.

Conflicts of interest

There are no conflicts to declare.

Acknowledgements

This work was supported by the National Nature Science Foundation of China (82071287, 81870916), the MOE Frontier Science Center for Brain Science & Brain-Machine Integration, Zhejiang University, the Funding of Double First-Rate Discipline Innovation Team of China Pharmaceutical University (CPUQNJC22_04), the National University of Singapore Start-up Grant (NUHSRO/2020/133/Startup/08), the NUS School of Medicine Nanomedicine Translational Research Programme (NUHSRO/2021/034/TRP/09/Nanomedicine), National University of Singapore (NUS Startup Fund: A-0008499-00-00 and A-0008505-00-00 to W. T.), the Singapore Ministry of Education (MOE Tier 1 grant: A-0008503-00-00 to W. T.), and the Singapore National Medical Research Council (NMRC OF-YIRG grant: A-8000675-00-00 to W. T.). Y. P. thanks China Scholarship Council (CSC) for a scholarship allowing him to study in Singapore.

Notes and references

1 H. Sung, J. Ferlay, R. L. Siegel, M. Laversanne, I. Soerjomataram, A. Jemal and F. Bray, *CA Cancer J. Clin.*, 2021, **71**, 209–249.
2 G. Petroni, L. C. Cantley, L. Santambrogio, S. C. Formenti and L. Galluzzi, *Nat. Rev. Clin. Oncol.*, 2022, **19**, 114–131.
3 R. A. Chandra, F. K. Keane, F. E. M. Voncken and C. R. Thomas Jr., *Lancet*, 2021, **398**, 171–184.
4 C. F. Dunne-Daly, *Cancer Nurs.*, 1994, **17**, 355–366.
5 H. Westerveld, N. Nesvacil, L. Fokdal, C. Chargari, M. P. Schmid, M. Milosevic, U. M. Mahantshetty and R. A. Nout, *Lancet Oncol.*, 2020, **21**, e157–e167.
6 P. Pei, T. Liu, W. Shen, Z. Liu and K. Yang, *Mater. Horiz.*, 2021, **8**, 1348–1366.
7 A. M. Chinnaiyan, U. Prasad, S. Shankar, D. A. Hamstra, M. Shanaiah, T. L. Chenevert, B. D. Ross and A. Rehemtulla, *Proc. Natl. Acad. Sci. U. S. A.*, 2000, **97**, 1754–1759.
8 R. Imai, T. Kamada, N. Araki, S. Abe, Y. Iwamoto, T. Ozaki, C. Kanehira, M. Kaya, K. Takahashi, H. Chuman, H. Tsujii, M. Tsuneyoshi, Y. Nishida, H. Hiraga, T. Hiruma, R. Machinami, A. Matsumine, S. Matsumoto, H. Morioka, T. Yamaguchi and T. Yonemoto, *Int. J. Radiat. Oncol. Biol. Phys.*, 2016, **95**, 322–327.
9 S. Hall, S. Rudrawar, M. Zunk, N. Bernaitis, D. Arora, C. M. McDermott and S. Anoopkumar-Dukie, *Antioxidants*, 2016, **5**, 22.
10 T. Kusumoto, R. Ogawara, K. Igawa, K. Baba, T. Konishi, Y. Furusawa and S. Kodaira, *J. Radiat. Res.*, 2020, **62**, 86–93.
11 H. Liew, S. Mein, J. Debus, I. Dokic and A. Mairani, *Int. J. Mol. Sci.*, 2020, **21**, 3471.
12 C. Borek, *J. Nutr.*, 2004, **134**, 3207S–3209S.
13 H. Wang, X. Mu, H. He and X.-D. Zhang, *Trends Pharmacol. Sci.*, 2018, **39**, 24–48.
14 R. Hodson, *Nature*, 2016, **537**, S49–S49.
15 Y.-B. Pan, S. Wang, B. Yang, Z. Jiang, C. Lenahan, J. Wang, J. Zhang and A. Shao, *J. Cell. Mol. Med.*, 2020, **24**, 3901–3916.
16 S. H. Abid, V. Malhotra and M. C. Perry, *Curr. Opin. Oncol.*, 2001, **13**, 242–248.
17 R. A. Rosiello and W. W. Merrill, *Clin. Chest Med.*, 1990, **11**, 65–71.
18 D. G. Kirsch, P. M. Santiago, E. d Tomaso, J. M. Sullivan, W.-S. Hou, T. Dayton, L. B. Jeffords, P. Sodha, K. L. Mercer, R. Cohen, O. Takeuchi, S. J. Korsmeyer, R. T. Bronson, C. F. Kim, K. M. Haigis, R. K. Jain and T. Jacks, *Science*, 2010, **327**, 593–596.
19 P. B. Romesser, A. S. Kim, J. Jeong, A. Mayle, L. E. Dow and S. W. Lowe, *Proc. Natl. Acad. Sci. U. S. A.*, 2019, **116**, 20672–20678.
20 R. G. Bristow, B. Alexander, M. Baumann, S. V. Bratman, J. M. Brown, K. Camphausen, P. Choyke, D. Citrin, J. N. Contessa, A. Dicker, D. G. Kirsch, M. Krause, Q. T. Le, M. Milosevic, Z. S. Morris, J. N. Sarkaria, P. M. Sondel, P. T. Tran, G. D. Wilson, H. Willers, R. K. S. Wong and P. M. Harari, *Lancet Oncol.*, 2018, **19**, e240–e251.
21 G. Song, L. Cheng, Y. Chao, K. Yang and Z. Liu, *Adv. Mater.*, 2017, **29**, 1700996.
22 B. J. Choi, K. O. Jung, E. E. Graves and G. Pratx, *Nanotechnology*, 2018, **29**, 504001.
23 T. Hasegawa, J. Takahashi, S. Nagasawa, M. Doi, A. Moriyama and H. Iwahashi, *Int. J. Mol. Sci.*, 2020, **21**, 2302.
24 A. Moriyama, T. Hasegawa, L. Jiang, H. Iwahashi, T. Mori and J. Takahashi, *Sci. Rep.*, 2019, **9**, 18163.

25 J. Takahashi, M. Murakami, T. Mori and H. Iwahashi, *Sci. Rep.*, 2018, **8**, 2728.
26 J. Xie, L. Gong, S. Zhu, Y. Yong, Z. Gu and Y. Zhao, *Adv. Mater.*, 2019, **31**, e1802244.
27 X. Song, C. Liang, L. Feng, K. Yang and Z. Liu, *Biomater. Sci.*, 2017, **5**, 1828–1835.
28 J. Zang, Q. Liu, H. Sui, R. Wang, O. Jacobson, X. Fan, Z. Zhu and X. Chen, *J. Nucl. Med.*, 2020, **61**, 1772–1778.
29 M. Gao, C. Liang, X. Song, Q. Chen, Q. Jin, C. Wang and Z. Liu, *Adv. Mater.*, 2017, **29**, 1701429.
30 X. Qin, C. Yang, H. Xu, R. Zhang, D. Zhang, J. Tu, Y. Guo, B. Niu, L. Kong and Z. Zhang, *Small*, 2021, **17**, e2103984.
31 M. Lyu, D. Zhu, X. Kong, Y. Yang, S. Ding, Y. Zhou, H. Quan, Y. Duo and Z. Bao, *Adv. Healthcare Mater.*, 2020, **9**, e1901819.
32 C. Y. Y. Yu, H. Xu, S. Ji, R. T. K. Kwok, J. W. Y. Lam, X. Li, S. Krishnan, D. Ding and B. Z. Tang, *Adv. Mater.*, 2017, **29**, 1606167.
33 G. Le Duc, I. Miladi, C. Alric, P. Mowat, E. Bräuer-Krisch, A. Bouchet, E. Khalil, C. Billotey, M. Janier, F. Lux, T. Epicier, P. Perriat, S. Roux and O. Tillement, *ACS Nano*, 2011, **5**, 9566–9574.
34 Z. Zhang, L. Wang, Y. Ding, J. Wu, Y. Hu and A. Yuan, *Biomater. Sci.*, 2020, **8**, 4739–4749.
35 M. Wang, H. Li, B. Huang, S. Chen, R. Cui, Z. J. Sun, M. Zhang and T. Sun, *Adv. Healthcare Mater.*, 2021, **10**, e2100090.
36 Y. Dou, F. Zhao, X. Li and Y. Guo, *ACS Biomater. Sci. Eng.*, 2021, **7**, 5242–5254.
37 H. Huang, C. Zhang, X. Wang, J. Shao, C. Chen, H. Li, C. Ju, J. He, H. Gu and D. Xia, *Nano Lett.*, 2020, **20**, 4211–4219.
38 W. Sun, L. Luo, Y. Feng, Y. Cai, Y. Zhuang, R. J. Xie, X. Chen and H. Chen, *Angew. Chem., Int. Ed.*, 2020, **59**, 9914–9921.
39 X. Li, L. Yu, C. Zhang, X. Niu, M. Sun, Z. Yan, W. Wang and Z. Yuan, *Bioact. Mater.*, 2022, **7**, 377–388.
40 X. Hu, J. Sun, F. Li, R. Li, J. Wu, J. He, N. Wang, J. Liu, S. Wang, F. Zhou, X. Sun, D. Kim, T. Hyeon and D. Ling, *Nano Lett.*, 2018, **18**, 1196–1204.
41 Z. Huang, Y. Wang, D. Yao, J. Wu, Y. Hu and A. Yuan, *Nat. Commun.*, 2021, **12**, 145.
42 Y. Chao, L. Xu, C. Liang, L. Feng, J. Xu, Z. Dong, L. Tian, X. Yi, K. Yang and Z. Liu, *Nat. Biomed. Eng.*, 2018, **2**, 611–621.
43 T. I. Liu, T. Y. Lu, Y. C. Yang, S. H. Chang, H. H. Chen, I. L. Lu, A. Sabu and H. C. Chiu, *Biomaterials*, 2020, **257**, 120229.
44 J. Xie, M. Zhao, C. Wang, S. Zhu, W. Niu, Y. Yong, L. Zhao and Z. Gu, *Chem. Eng. J.*, 2022, **430**, 132866.
45 J. Du, Z. Gu, L. Yan, Y. Yong, X. Yi, X. Zhang, J. Liu, R. Wu, C. Ge, C. Chen and Y. Zhao, *Adv. Mater.*, 2017, **29**, 1701268.
46 A. P. Brown, E. J. Chung, M. E. Urick, W. P. Shield, A. L. Sowers, A. Thetford, U. T. Shankavaram, J. B. Mitchell and D. E. Citrin, *Radiat. Oncol.*, 2010, **5**, 34.
47 J. Colon, S. Seal, S. Konduri, A. Limaye, M. Abdelrahim and C. Baker, *Cancer Res.*, 2007, **67**, 754.
48 R. W. Tarnuzzer, J. Colon, S. Patil and S. Seal, *Nano Lett.*, 2005, **5**, 2573–2577.
49 C. A. Theriot, R. C. Casey, V. C. Moore, L. Mitchell, J. O. Reynolds, M. Burgoyne, R. Partha, J. L. Huff, J. L. Conyers, A. Jeevarajan and H. Wu, *Radiat. Environ. Biophys.*, 2010, **49**, 437–445.
50 K. C. Black, Y. Wang, H. P. Luehmann, X. Cai, W. Xing, B. Pang, Y. Zhao, C. S. Cutler, L. V. Wang, Y. Liu and Y. Xia, *ACS Nano*, 2014, **8**, 4385–4394.
51 Y. Yang, L. Zhang, J. Cai, X. Li, D. Cheng, H. Su, J. Zhang, S. Liu, H. Shi, Y. Zhang and C. Zhang, *ACS Appl. Mater. Interfaces*, 2016, **8**, 1718–1732.
52 Y. Wang, L. Zou, Z. Qiang, J. Jiang, Z. Zhu and J. Ren, *ACS Biomater. Sci. Eng.*, 2020, **6**, 3550–3562.
53 J. Liu, F. Hu, M. Wu, L. Tian, F. Gong, X. Zhong, M. Chen, Z. Liu and B. Liu, *Adv. Mater.*, 2021, **33**, e2007888.
54 W. Pan, B. Cui, P. Gao, Y. Ge, N. Li and B. Tang, *Chem. Commun.*, 2020, **56**, 547–550.
55 W. Fan, B. Shen, W. Bu, X. Zheng, Q. He, Z. Cui, D. Ni, K. Zhao, S. Zhang and J. Shi, *Biomaterials*, 2015, **69**, 89–98.
56 X. Fang, Y. Wang, X. Ma, Y. Li, Z. Zhang, Z. Xiao, L. Liu, X. Gao and J. Liu, *J. Mater. Chem. B*, 2017, **5**, 4190–4197.
57 H. Kobayashi and M. W. Brechbiel, *Adv. Drug Delivery Rev.*, 2005, **57**, 2271–2286.
58 H. Maeda, *Bioconjugate Chem.*, 2010, **21**, 797–802.
59 H. Kobayashi, R. Watanabe and P. L. Choyke, *Theranostics*, 2013, **4**, 81–89.
60 Z. He, H. Yan, W. Zeng, K. Yang and P. Rong, *J. Mater. Chem. B*, 2021, **9**, 1625–1637.
61 K. Kim, K. S. Oh, D. Y. Park, J. Y. Lee, B. S. Lee, I. S. Kim, K. Kim, I. C. Kwon, Y. K. Sang and S. H. Yuk, *J. Controlled Release*, 2016, **228**, 141–149.
62 C. H. Chang, M. G. Stabin, Y. J. Chang, L. C. Chen, M. H. Chen, T. J. Chang, T. W. Lee and G. Ting, *Cancer Biother. Radiopharm.*, 2008, **23**, 749–758.
63 J. Goos, A. Cho, L. M. Carter, T. R. Dilling, M. Davydova, K. Mandleywala, S. Puttick, A. Gupta, W. S. Price, J. F. Quinn, M. R. Whittaker, J. S. Lewis and T. P. Davis, *Theranostics*, 2020, **10**, 567–584.
64 Y. Dou, Y. Liu, F. Zhao, Y. Guo, X. Li, M. Wu, J. Chang and C. Yu, *Theranostics*, 2018, **8**, 5870–5889.
65 Q. Zhang, J. Chen, J. Shen, S. Chen, K. Liang, H. Wang and H. Chen, *Theranostics*, 2019, **9**, 2779–2790.
66 S. Gao, W. Zhang, R. Wang, S. P. Hopkins, J. C. Spagnoli, M. Racin, L. Bai, L. Li, W. Jiang, X. Yang, C. Lee, K. Nagata, E. W. Howerth, H. Handa, J. Xie, Q. Ma and A. Kumar, *ACS Nano*, 2020, **14**, 1468–1481.
67 R. Duncan, Y.-N. Sat-Klopsch, A. M. Burger, M. C. Bibby, H. H. Fiebig and E. A. Sausville, *Cancer Chemother. Pharmacol.*, 2013, **72**, 417–427.
68 D. Huang, L. Sun, L. Huang and Y. Chen, *J. Pers. Med.*, 2021, **11**, 124.
69 A. K. Iyer, G. Khaled, J. Fang and H. Maeda, *Drug Discovery Today*, 2006, **11**, 812–818.
70 A. Nel, E. Ruoslahti and H. Meng, *ACS Nano*, 2017, **11**, 9567–9569.

71 U. Prabhakar, H. Maeda, R. K. Jain, E. M. Sevick-Muraca, W. Zamboni, O. C. Farokhzad, S. T. Barry, A. Gabizon, P. Grodzinski and D. C. Blakey, *Cancer Res.*, 2013, **73**, 2412–2417.
72 G. Song, H. Wu, K. Yoshino and W. C. Zamboni, *J. Liposome Res.*, 2012, **22**, 177–192.
73 A. Dimou, K. N. Syrigos and M. W. Saif, *Ther. Adv. Med. Oncol.*, 2012, **4**, 271–279.
74 E. Blanco, H. Shen and M. Ferrari, *Nat. Biotechnol.*, 2015, **33**, 941–951.
75 Y. Liu, P. Bhattarai, Z. Dai and X. Chen, *Chem. Soc. Rev.*, 2019, **48**, 2053–2108.
76 C. Kinnear, T. L. Moore, L. Rodriguez-Lorenzo, B. Rothen-Rutishauser and A. Petri-Fink, *Chem. Rev.*, 2017, **117**, 11476–11521.
77 M. J. Ernsting, M. Murakami, A. Roy and S.-D. Li, *J. Controlled Release*, 2013, **172**, 782–794.
78 Y. Geng, P. Dalhaimer, S. Cai, R. Tsai, M. Tewari, T. Minko and D. E. Discher, *Nat. Nanotechnol.*, 2007, **2**, 249–255.
79 Y. Wang, K. C. L. Black, H. Luehmann, W. Li, Y. Zhang, X. Cai, D. Wan, S.-Y. Liu, M. Li, P. Kim, Z.-Y. Li, L. V. Wang, Y. Liu and Y. Xia, *ACS Nano*, 2013, **7**, 2068–2077.
80 N. Ma, F. G. Wu, X. Zhang, Y. W. Jiang, H. R. Jia, H. Y. Wang, Y. H. Li, P. Liu, N. Gu and Z. Chen, *ACS Appl. Mater. Interfaces*, 2017, **9**, 13037–13048.
81 L. Zhang, H. Su, H. Wang, Q. Li, X. Li, C. Zhou, J. Xu, Y. Chai, X. Liang, L. Xiong and C. Zhang, *Theranostics*, 2019, **9**, 1893–1908.
82 A. Wilhelm and Q. D. Tavares, *Nat. Rev. Mater.*, 2016, **1**, 16014.
83 D. B. Chithrani, S. Jelveh, F. Jalali, M. van Prooijen, C. Allen, R. G. Bristow, R. P. Hill and D. A. Jaffray, *Radiat. Res.*, 2010, **173**, 719–728.
84 X.-D. Zhang, D. Wu, X. Shen, J. Chen, Y.-M. Sun, P.-X. Liu and X.-J. Liang, *Biomaterials*, 2012, **33**, 6408–6419.
85 P. S. Low and A. C. Antony, *Adv. Drug Delivery Rev.*, 2004, **56**, 1055–1058.
86 H. Nosrati, Y. Baghdadchi, R. Abbasi, M. Barsbay, M. Ghaffarlou, F. Abhari, A. Mohammadi, T. Kavetskyy, S. Bochani, H. Rezaeejam, S. Davaran and H. Danafar, *J. Mater. Chem. B*, 2021, **9**, 4510–4522.
87 Y. Huang, Y. Luo, W. Zheng and T. Chen, *ACS Appl. Mater. Interfaces*, 2014, **6**, 19217–19228.
88 M. E. Werner, S. Karve, R. Sukumar, N. D. Cummings, J. A. Copp, R. C. Chen, T. Zhang and A. Z. Wang, *Biomaterials*, 2011, **32**, 8548–8554.
89 M. E. Werner, J. A. Copp, S. Karve, N. D. Cummings, R. Sukumar, C. Li, M. E. Napier, R. C. Chen, A. D. Cox and A. Z. Wang, *ACS Nano*, 2011, **5**, 8990–8998.
90 X. Liu, Z. Yuan, Z. Tang, Q. Chen, J. Huang, L. He and T. Chen, *Biomater. Sci.*, 2021, **9**, 4691–4700.
91 G. C. Zhang, J. Liu, X. N. Yu, Y. Deng, Y. Sun, T. T. Liu, L. Dong, C. F. Zhu, X. Z. Shen, J. M. Zhu, S. Q. Weng and Y. Li, *Adv. Healthcare Mater.*, 2020, **9**, e2000650.
92 L. Lapcık Jr, L. Lapcık, S. De Smedt, J. Demeester and P. Chabrecek, *Chem. Rev.*, 1998, **98**, 2663–2684.
93 B. P. Toole, *Nat. Rev. Cancer*, 2004, **4**, 528–539.
94 K. Y. Choi, K. H. Min, H. Y. Yoon, K. Kim, J. H. Park, I. C. Kwon, K. Choi and S. Y. Jeong, *Biomaterials*, 2011, **32**, 1880–1889.
95 Y. Chong, J. Huang, X. Xu, C. Yu, X. Ning, S. Fan and Z. Zhang, *Bioconjugate Chem.*, 2020, **31**, 1756–1765.
96 C. S. Chiang, I. J. Shih, P. W. Shueng, M. Kao, L. W. Zhang, S. F. Chen, M. H. Chen and T. Y. Liu, *Acta Biomater.*, 2021, **125**, 300–311.
97 C. Du, M. Zhou, F. Jia, L. Ruan, H. Lu, J. Zhang, B. Zhu, X. Liu, J. Chen, Z. Chai and Y. Hu, *Biomaterials*, 2021, **269**, 120642.
98 M. A. Askar, N. M. Thabet, G. S. El-Sayyad, A. I. El-Batal, M. Abd Elkodous, O. E. El Shawi, H. Helal and M. K. Abdel-Rafei, *Cancers*, 2021, **13**, 5571.
99 Y. Sun, C. Kang, F. Liu, Y. Zhou, L. Luo and H. Qiao, *Drug Delivery Res.*, 2017, **78**, 283–291.
100 Y. Ding, X. Xiao, L. Zeng, Q. Shang, W. Jiang, S. Xiong, X. Duan, J. Shen, R. Wang, J. Guo and Y. Pan, *Bioact. Mater.*, 2021, **6**, 4707–4716.
101 P. Li, Y. W. Shi, B. X. Li, W. C. Xu, Z. L. Shi, C. Zhou and S. Fu, *J. Nanobiotechnol.*, 2015, **13**, 52.
102 L. Zhao, H. Chen, Z. Guo, K. Fu, L. Yao, L. Fu, W. Guo, X. Wen, O. Jacobson, X. Zhang, L. Sun, H. Wu, Q. Lin and X. Chen, *Mol. Cancer Ther.*, 2020, **19**, 2034–2043.
103 L. Chan, P. Gao, W. Zhou, C. Mei, Y. Huang, X. F. Yu, P. K. Chu and T. Chen, *ACS Nano*, 2018, **12**, 12401–12415.
104 L. Chan, X. Chen, P. Gao, J. Xie, Z. Zhang, J. Zhao and T. Chen, *ACS Nano*, 2021, **15**, 3047–3060.
105 D. Luo, X. Wang, S. Zeng, G. Ramamurthy, C. Burda and J. P. Basilion, *Small*, 2019, **15**, e1900968.
106 S. J. DeNardo, G. L. DeNardo, L. A. Miers, A. Natarajan, A. R. Foreman, C. Gruettner, G. N. Adamson and R. Ivkov, *Clin. Cancer Res.*, 2005, **11**, 7087s–7092s.
107 E. Thomas, J. U. Menon, J. Owen, I. Skaripa-Koukelli, S. Wallington, M. Gray, C. Mannaris, V. Kersemans, D. Allen, P. Kinchesh, S. Smart, R. Carlisle and K. A. Vallis, *Theranostics*, 2019, **9**, 5595–5609.
108 K. J. Lee, E. J. Ko, Y. Y. Park, S. S. Park, E. J. Ju, J. Park, S. H. Shin, Y. A. Suh, S. M. Hong, I. J. Park, K. P. Kim, J. J. Hwang, S. J. Jang, J. S. Lee, S. Y. Song, S. Y. Jeong and E. K. Choi, *Biomaterials*, 2020, **255**, 120151.
109 W. Sun, Q. Hu, W. Ji, G. Wright and Z. Gu, *Physiol. Rev.*, 2017, **97**, 189–225.
110 L. Brannon-Peppas and J. O. Blanchette, *Adv. Drug Delivery Rev.*, 2012, **64**, 206–212.
111 S. N. Ekdawi, D. A. Jaffray and C. Allen, *Nano Today*, 2016, **11**, 402–414.
112 H. C. Hang, C. Yu, D. L. Kato and C. R. Bertozzi, *Proc. Natl. Acad. Sci. U. S. A.*, 2003, **100**, 14846–14851.
113 L. Du, H. Qin, T. Ma, T. Zhang and D. Xing, *ACS Nano*, 2017, **11**, 8930–8943.
114 Y. Han, H. Pan, W. Li, Z. Chen, A. Ma, T. Yin, R. Liang, F. Chen, Y. Ma, Y. Jin, M. Zheng, B. Li and L. Cai, *Adv. Sci.*, 2019, **6**, 1900251.

115 S. Hou, J.-S. Choi, M. A. Garcia, Y. Xing, K.-J. Chen, Y.-M. Chen, Z. K. Jiang, T. Ro, L. Wu, D. B. Stout, J. S. Tomlinson, H. Wang, K. Chen, H.-R. Tseng and W.-Y. Lin, *ACS Nano*, 2016, **10**, 1417–1424.
116 L.-L. Huang, W. Nie, J. Zhang and H.-Y. Xie, *Acc. Chem. Res.*, 2020, **53**, 276–287.
117 B. Li, P. Liu, H. Wu, X. Xie, Z. Chen, F. Zeng and S. Wu, *Biomaterials*, 2017, **138**, 57–68.
118 Q. Wang, Y. Wang, J. Ding, C. Wang, X. Zhou, W. Gao, H. Huang, F. Shao and Z. Liu, *Nature*, 2020, **579**, 421–426.
119 H. Y. Yoon, M. L. Shin, M. K. Shim, S. Lee, J. H. Na, H. Koo, H. Lee, J.-H. Kim, K. Y. Lee, K. Kim and I. C. Kwon, *Mol. Pharm.*, 2017, **14**, 1558–1570.
120 F. Hu, D. Mao, Kenry, X. Cai, W. Wu, D. Kong and B. Liu, *Angew. Chem., Int. Ed.*, 2018, **57**, 10182–10186.
121 J.-S. Ni, P. Zhang, T. Jiang, Y. Chen, H. Su, D. Wang, Z.-Q. Yu, R. T. K. Kwok, Z. Zhao, J. W. Y. Lam and B. Z. Tang, *Adv. Mater.*, 2018, **30**, 1805220.
122 Y. Tu, Y. Dong, K. Wang, S. Shen, Y. Yuan and J. Wang, *Biomaterials*, 2020, **259**, 120298.
123 R. Membreno, B. E. Cook, K. Fung, J. S. Lewis and B. M. Zeglis, *Mol. Pharm.*, 2018, **15**, 1729–1734.
124 J. L. Houghton, R. Membreno, D. Abdel-Atti, K. M. Cunanan, S. Carlin, W. W. Scholz, P. B. Zanzonico, J. S. Lewis and B. M. Zeglis, *Mol. Cancer Ther.*, 2017, **16**, 124–133.
125 S. Poty, L. M. Carter, K. Mandleywala, R. Membreno, D. Abdel-Atti, A. Ragupathi, W. W. Scholz, B. M. Zeglis and J. S. Lewis, *Clin. Cancer Res.*, 2019, **25**, 868–880.
126 A. Rondon, S. Schmitt, A. Briat, N. Ty, L. Maigne, M. Quintana, R. Membreno, B. M. Zeglis, I. Navarro-Teulon, J.-P. Pouget, J.-M. Chezal, E. Miot-Noirault, E. Moreau and F. Degoul, *Theranostics*, 2019, **9**, 6706–6718.
127 C.-M. J. Hu, L. Zhang, S. Aryal, C. Cheung, R. H. Fang and L. Zhang, *Proc. Natl. Acad. Sci. U. S. A.*, 2011, **108**, 10980–10985.
128 C.-M. J. Hu, R. H. Fang, K.-C. Wang, B. T. Luk, S. Thamphiwatana, D. Dehaini, P. Nguyen, P. Angsantikul, C. H. Wen, A. V. Kroll, C. Carpenter, M. Ramesh, V. Qu, S. H. Patel, J. Zhu, W. Shi, F. M. Hofman, T. C. Chen, W. Gao, K. Zhang, S. Chien and L. Zhang, *Nature*, 2015, **526**, 118–121.
129 Y. Pan, C. Xu, H. Deng, Q. You, C. Zhao, Y. Li, Q. Gao, O. U. Akakuru, J. Li, J. Zhang, A. Wu and X. Chen, *Nano Today*, 2022, **43**, 101435.
130 D. Zhu, M. Lyu, W. Jiang, M. Suo, Q. Huang and K. Li, *J. Mater. Chem. B*, 2020, **8**, 5312–5319.
131 Q. Sun, J. Wu, L. Jin, L. Hong, F. Wang, Z. Mao and M. Wu, *J. Mater. Chem. B*, 2020, **8**, 7253–7263.
132 S. Gou, W. Liu, S. Wang, G. Chen, Z. Chen, L. Qiu, X. Zhou, Y. Wu, Y. Qi and Y. Gao, *Nano Lett.*, 2021, **21**, 9939–9950.
133 C. Huang, T. Chen, D. Zhu and Q. Huang, *Front. Chem.*, 2020, **8**, 225.
134 M. Sun, Y. Duan, Y. Ma and Q. Zhang, *Int. J. Nanomed.*, 2020, **15**, 6749–6760.
135 J. Deng, S. Xu, W. Hu, X. Xun, L. Zheng and M. Su, *Biomaterials*, 2018, **154**, 24–33.
136 Y. Chen, G. Zhao, S. Wang, Y. He, S. Han, C. Du, S. Li, Z. Fan, C. Wang and J. Wang, *Biomater. Sci.*, 2019, **7**, 3450–3459.
137 M. Lyu, M. Chen, L. Liu, D. Zhu, X. Wu, Y. Li, L. Rao and Z. Bao, *Theranostics*, 2021, **11**, 7589–7599.
138 Y. Yin, Y. Li, S. Wang, Z. Dong, C. Liang, J. Sun, C. Wang, R. Chai, W. Fei, J. Zhang, M. Qi, L. Feng and Q. Zhang, *J. Nanobiotechnol.*, 2021, **19**, 80.
139 W. Zai, L. Kang, T. Dong, H. Wang, L. Yin, S. Gan, W. Lai, Y. Ding, Y. Hu and J. Wu, *ACS Nano*, 2021, **15**, 15381–15394.
140 M. H. Chen, T. Y. Liu, Y. C. Chen and M. H. Chen, *Nanomaterials*, 2021, **11**, 1661.
141 C. Huang, F. B. Wang, L. Liu, W. Jiang, W. Liu, W. Ma and H. Zhao, *Adv. Healthcare Mater.*, 2021, **10**, e2002207.
142 R. J. C. Bose, R. Paulmurugan, J. Moon, S.-H. Lee and H. Park, *Drug Discovery Today*, 2018, **23**, 891–899.
143 R. H. Fang, A. V. Kroll, W. Gao and L. Zhang, *Adv. Mater.*, 2018, **30**, e1706759.
144 E. Zocchi, M. Tonetti, C. Polvani, L. Guida, U. Benatti and A. D. Flora, *Proc. Natl. Acad. Sci. U. S. A.*, 1989, **86**, 2040–2044.
145 N. Talwar and N. K. Jain, *Drug Dev. Ind. Pharm.*, 1992, **18**, 1799–1812.
146 G. V. Shavi, R. C. Doijad, P. B. Deshpande, F. Manvi, S. R. Meka, N. Udupa, R. Omprakash and K. Dhirendra, *Pak. J. Pharm. Sci.*, 2010, **23**, 194–200.
147 M. J. Mitchell and M. R. King, *Expert Opin. Drug Delivery*, 2015, **12**, 375–392.
148 C. G. Millán, M. a L. S. Marinero, A. Z. Castañeda and J. M. Lanao, *J. Controlled Release*, 2004, **95**, 27–49.
149 Y. Lu, Q. Hu, C. Jiang and Z. Gu, *Curr. Opin. Biotechnol.*, 2019, **58**, 81–91.
150 D. Xia, D. Hang, Y. Li, W. Jiang, J. Zhu, Y. Ding, H. Gu and Y. Hu, *ACS Nano*, 2020, **14**, 15654–15668.
151 D. Zhu, M. Lyu, Q. Huang, M. Suo, Y. Liu, W. Jiang, Y. Duo and K. Fan, *ACS Appl. Mater. Interfaces*, 2020, **12**, 36928–36937.
152 A. Kumar, P. K. Jena, S. Behera, R. F. Lockey, S. Mohapatra and S. Mohapatra, *Nanomedicine*, 2010, **6**, 64–69.
153 A. Amirfazli, *Nat. Nanotechnol.*, 2007, **2**, 467–468.
154 J. Dobson, *Drug Delivery Res.*, 2006, **67**, 55–60.
155 U. Häfeli, G. Pauer, S. Failing and G. Tapolsky, *J. Magn. Magn. Mater.*, 2001, **225**, 73–78.
156 U. O. Häfeli, S. M. Sweeney, B. A. Beresford, J. L. Humm and R. M. Macklis, *Nucl. Med. Biol.*, 1995, **22**, 147–155.
157 S. Liang, Y. Wang, J. Yu, C. Zhang, J. Xia and D. Yin, *J. Mater. Sci.: Mater. Med.*, 2007, **18**, 2297–2302.
158 J. Cao, Y. Wang, J. Yu, J. Xia, C. Zhang, D. Yin and U. O. Häfeli, *J. Magn. Magn. Mater.*, 2004, **277**, 165–174.
159 Z. Chunfu, C. Jinquan, Y. Duanzhi, W. Yongxian, F. Yanlin and T. Jiajü, *Appl. Radiat. Isot.*, 2004, **61**, 1255–1259.
160 J. G. Huang, T. Leshuk and F. X. Gu, *Nano Today*, 2011, **6**, 478–492.

161 G. Wan, Y. Cheng, J. Song, Q. Chen, B. Chen, Y. Liu, S. Ji, H. Chen and Y. Wang, *Chem. Eng. J.*, 2020, **380**, 122458.
162 B. Hoang, R. M. Reilly and C. Allen, *Biomacromolecules*, 2012, **13**, 455–465.
163 L. Wang, T. Zhang, M. Huo, J. Guo, Y. Chen and H. Xu, *Small*, 2019, **15**, 1903254.
164 W. Pan, S. Gong, J. Wang, L. Yu, Y. Chen, N. Li and B. Tang, *Chem. Commun.*, 2019, **55**, 8182–8185.
165 X.-H. Wang, H.-S. Peng, L. Yang, F.-T. You, F. Teng, A.-W. Tang, F.-J. Zhang and X.-H. Li, *J. Mater. Chem. B*, 2013, **1**, 5143–5152.
166 Y. Wang, G. Wei, X. Zhang, X. Huang, J. Zhao, X. Guo and S. Zhou, *Small*, 2018, **14**, 1702994.
167 H. Yu, J.-M. Li, K. Deng, W. Zhou, C.-X. Wang, Q. Wang, K.-H. Li, H.-Y. Zhao and S.-W. Huang, *Theranostics*, 2019, **9**, 7033–7050.
168 P. Yuan, X. Mao, X. Wu, S. S. Liew, L. Li and S. Q. Yao, *Angew. Chem., Int. Ed.*, 2019, **58**, 7657–7661.
169 W. Deng, K. J. McKelvey, A. Guller, A. Fayzullin, J. M. Campbell, S. Clement, A. Habibalahi, Z. Wargocka, L. Liang, C. Shen, V. M. Howell, A. F. Engel and E. M. Goldys, *ACS Cent. Sci.*, 2020, **6**, 715–726.
170 Y. Chen, N. Li, J. Wang, X. Zhang, W. Pan, L. Yu and B. Tang, *Theranostics*, 2019, **9**, 167–178.
171 Z. Zhang, L. Zhou, Y. Zhou, J. Liu, X. Xing, J. Zhong, G. Xu, Z. Kang and J. Liu, *Biomaterials*, 2015, **65**, 56–65.
172 Z. Zhou, J. Liu, T. W. Rees, H. Wang, X. Li, H. Chao and P. J. Stang, *Proc. Natl. Acad. Sci. U. S. A.*, 2018, **115**, 5664–5669.
173 V. Pierroz, T. Joshi, A. Leonidova, C. Mari, J. Schur, I. Ott, L. Spiccia, S. Ferrari and G. Gasser, *J. Am. Chem. Soc.*, 2012, **134**, 20376–20387.
174 K. Ni, G. Lan, S. S. Veroneau, X. Duan, Y. Song and W. Lin, *Nat. Commun.*, 2018, **9**, 4321.
175 M. Michalak, J. M. Robert Parker and M. Opas, *Cell Calcium*, 2002, **32**, 269–278.
176 K. F. Ferri and G. Kroemer, *Nat. Cell Biol.*, 2001, **3**, E255–E263.
177 S. C. Chiu, S. P. Chen, S. Y. Huang, M. J. Wang, S. Z. Lin, H. J. Harn and C. Y. Pang, *PLoS One*, 2012, **7**, e33742.
178 S. Chen, Y. Zhang and D. Zhang, *Sci. Rep.*, 2015, **5**, 14723.
179 X.-L. Pang, G. He, Y.-B. Liu, Y. Wang and B. Zhang, *World J. Gastroenterol.*, 2013, **19**, 1736–1748.
180 S. Klein, M. L. Dell'Arciprete, M. Wegmann, L. V. Distel, W. Neuhuber, M. C. Gonzalez and C. Kryschi, *Biochem. Biophys. Res. Commun.*, 2013, **434**, 217–222.
181 H. Deng, Z. Zhou, W. Yang, L.-S. Lin, S. Wang, G. Niu, J. Song and X. Chen, *Nano Lett.*, 2020, **20**, 1928–1933.
182 Z. Zhang, P. Yue, T. Lu, Y. Wang, Y. Wei and X. Wei, *J. Hematol. Oncol.*, 2021, **14**, 79.
183 H. Appelqvist, P. Wäster, K. Kågedal and K. Öllinger, *J. Mol. Cell Biol.*, 2013, **5**, 214–226.
184 X. Zhang, J. Wang, X. Li and D. Wang, *Cancer Lett.*, 2018, **439**, 39–46.
185 S. Simonet, C. Rodriguez-Lafrasse, D. Beal, S. Gerbaud, C. Malesys, O. Tillement, F. Lux, H. Fayyad-Kazan, W. Rachidi and D. Ardail, *J. Biomed. Nanotechnol.*, 2020, **16**, 111–124.
186 M. Hullo, R. Grall, Y. Perrot, C. Mathé, V. Ménard, X. Yang, S. Lacombe, E. Porcel, C. Villagrasa, S. Chevillard and E. Bourneuf, *Int. J. Mol. Sci.*, 2021, **22**, 4436.
187 L. Štefančíková, E. Porcel, P. Eustache, S. Li, D. Salado, S. Marco, J.-L. Guerquin-Kern, M. Réfrégiers, O. Tillement, F. Lux and S. Lacombe, *Cancer Nanotechnol.*, 2014, **5**, 6.
188 E. S. Lee, K. Na and Y. H. Bae, *Nano Lett.*, 2005, **5**, 325–329.
189 D. Rotin, P. Wan, S. Grinstein and I. Tannock, *Cancer Res.*, 1987, **47**, 1497–1504.
190 H. Lee, W. Akers, K. Bhushan, S. Bloch, G. Sudlow, R. Tang and S. Achilefu, *Bioconjugate Chem.*, 2011, **22**, 777–784.
191 Z. Tian, C. Yang, W. Wang and Z. Yuan, *ACS Appl. Mater. Interfaces*, 2014, **6**, 17865–17876.
192 Z. Hu, J. Ma, F. Fu, C. Cui, X. Li, X. Wang, W. Wang, Y. Wan and Z. Yuan, *J. Controlled Release*, 2017, **268**, 1–9.
193 L. Yu, X. Zhang, X. Li, Z. Zhang, X. Niu, X. Wang, W. Wang and Z. Yuan, *Nanoscale*, 2021, **13**, 13735–13745.
194 Y. Li, T. Gong, H. Gao, Y. Chen, H. Li, P. Zhao, Y. Jiang, K. Wang, Y. Wu, X. Zheng and W. Bu, *Angew. Chem., Int. Ed.*, 2021, **60**, 15472–15481.
195 B. A. Arrick and C. F. Nathan, *Cancer Res.*, 1984, **44**, 4224–4232.
196 X. Guo, Y. Cheng, X. Zhao, Y. Luo, J. Chen and W.-E. Yuan, *J. Nanobiotechnol.*, 2018, **16**, 74.
197 R. Li and Y. Xie, *J. Controlled Release*, 2017, **251**, 49–67.
198 F. Meng, W. E. Hennink and Z. Zhong, *Biomaterials*, 2009, **30**, 2180–2198.
199 M. Diehn, R. W. Cho, N. A. Lobo, T. Kalisky, M. J. Dorie, A. N. Kulp, D. Qian, J. S. Lam, L. E. Ailles, M. Wong, B. Joshua, M. J. Kaplan, I. Wapnir, F. M. Dirbas, G. Somlo, C. Garberoglio, B. Paz, J. Shen, S. K. Lau, S. R. Quake, J. M. Brown, I. L. Weissman and M. F. Clarke, *Nature*, 2009, **458**, 780–783.
200 D. Siemann and K. Beyers, *Br. J. Radiol.*, 1993, **68**, 1071–1079.
201 Y. Ding, Z. Tong, L. Jin, B. Ye, J. Zhou, Z. Sun, H. Yang, L. Hong, F. Huang, W. Wang and Z. Mao, *Adv. Mater.*, 2021, **34**, e2106388.
202 Y. Song, Y. Wang, Y. Zhu, Y. Cheng, Y. Wang, S. Wang, F. Tan, F. Lian and N. Li, *Adv. Healthcare Mater.*, 2019, **8**, e1900250.
203 W. Fan, P. Huang and X. Chen, *Chem. Soc. Rev.*, 2016, **45**, 6488–6519.
204 Z. Zhou, J. Song, L. Nie and X. Chen, *Chem. Soc. Rev.*, 2016, **45**, 6597–6626.
205 C. Zhang, K. Zhao, W. Bu, D. Ni, Y. Liu, J. Feng and J. Shi, *Angew. Chem., Int. Ed.*, 2015, **54**, 1770–1774.
206 H. Pelicano, W. Lu, Y. Zhou, W. Zhang, Z. Chen, Y. Hu and P. Huang, *Cancer Res.*, 2009, **69**, 2375–2383.
207 X. Chen, M. Song, B. Zhang and Y. Zhang, *Oxid. Med. Cell. Longev.*, 2016, **2016**, 1580967.
208 C. Xu, H. Hong, Y. Lee, K. S. Park, M. Sun, T. Wang, M. E. Aikins, Y. Xu and J. J. Moon, *ACS Nano*, 2020, **14**, 13268–13278.

209 Y. He, S. Guo, L. Wu, P. Chen, L. Wang, Y. Liu and H. Ju, *Biomaterials*, 2019, **225**, 119501.
210 C. Yue, Y. Yang, C. Zhang, G. Alfranca, S. Cheng, L. Ma, Y. Liu, X. Zhi, J. Ni, W. Jiang, J. Song, J. M. de la Fuente and D. Cui, *Theranostics*, 2016, **6**, 2352–2366.
211 J. Wang, Y. Zhang, E. Archibong, F. S. Ligler and Z. Gu, *Adv. Biosyst.*, 2017, **1**, 1700084.
212 S. J. Lee, T. B. Neugut, K. L. Rosenblum, R. M. Tolman, W. J. Travis and M. H. Walker, *Child. Youth Serv. Rev.*, 2013, **35**, 908–915.
213 C.-C. Song, F.-S. Du and Z.-C. Li, *J. Mater. Chem. B*, 2014, **2**, 3413–3426.
214 Q. Xu, C. He, C. Xiao and X. Chen, *Macromol. Biosci.*, 2016, **16**, 635–646.
215 Y. Yu, Z. Feng, J. Liu, X. Hou, X. Zhou, J. Gao, W. Wang, Y. Zhang, G. Li and J. Liu, *ACS Omega*, 2021, **6**, 19445–19457.
216 L. Meng, Y. Cheng, X. Tong, S. Gan, Y. Ding, Y. Zhang, C. Wang, L. Xu, Y. Zhu, J. Wu, Y. Hu and A. Yuan, *ACS Nano*, 2018, **12**, 8308–8322.
217 X. Wang, X. Niu, W. Sha, X. Feng, L. Yu, Z. Zhang, W. Wang and Z. Yuan, *Biomater. Sci.*, 2021, **9**, 6308–6324.
218 R. Chandrawati, *Exp. Biol. Med.*, 2016, **241**, 972–979.
219 M. Egeblad and Z. Werb, *Nat. Rev. Cancer*, 2002, **2**, 161–174.
220 J. R. Graff, B. W. Konicek, J. A. Deddens, M. Chedid, B. M. Hurst, B. Colligan, B. L. Neubauer, H. W. Carter and J. H. Carter, *Clin. Cancer Res.*, 2001, **7**, 3857–3861.
221 J. Ge, D. Lu, C. Yang and Z. Liu, *Macromol. Rapid Commun.*, 2011, **32**, 546–550.
222 R. Huang, W. Qi, L. Feng, R. Su and Z. He, *Soft Matter*, 2011, **7**, 6222–6230.
223 Z.-H. Peng and J. Kopeček, *J. Am. Chem. Soc.*, 2015, **137**, 6726–6729.
224 R. Zou, Q. Gong, Z. Shi, J. Zheng, J. Xing, C. Liu, Z. Jiang and A. Wu, *Nanoscale*, 2020, **12**, 14870–14881.
225 J. Mu, J. Lin, P. Huang and X. Chen, *Chem. Soc. Rev.*, 2018, **47**, 5554–5573.
226 Z. Zhang, Q. Zhang, J. Xie, Z. Zhong and C. Deng, *Biomater. Sci.*, 2021, **9**, 6915–6926.
227 Y. Ding, Z. Sun, Z. Tong, S. Zhang, J. Min, Q. Xu, L. Zhou, Z. Mao, H. Xia and W. Wang, *Theranostics*, 2020, **10**, 5195–5208.
228 P. Pan, X. Dong, Y. Chen, X. Zeng and X. Z. Zhang, *ACS Nano*, 2022, **16**, 801–812.
229 L. Wu, B. Lin, H. Yang, J. Chen, Z. Mao, W. Wang and C. Gao, *Acta Biomater.*, 2019, **86**, 363–372.
230 L. Wang, T. Zhang, M. Huo, J. Guo, Y. Chen and H. Xu, *Small*, 2019, **15**, e1903254.
231 E. S. Olson, T. Jiang, T. A. Aguilera, Q. T. Nguyen, L. G. Ellies, M. Scadeng and R. Y. Tsien, *Proc. Natl. Acad. Sci. U. S. A.*, 2010, **107**, 4311–4316.
232 S. Yu, Y. Duan, X. Zuo, X. Chen, Z. Mao and C. Gao, *Biomaterials*, 2018, **180**, 193–205.
233 Y. Yuan, C. J. Zhang, M. Gao, R. Zhang, B. Z. Tang and B. Liu, *Angew. Chem., Int. Ed.*, 2015, **54**, 1780–1786.
234 T. Ren, S. Yu, Z. Mao and C. Gao, *Biomaterials*, 2015, **56**, 58–67.
235 S. Chen, Z. Cao and S. Jiang, *Biomaterials*, 2009, **30**, 5892–5896.
236 C. S. Gondi and J. S. Rao, *Expert Opin. Ther. Targets*, 2013, **17**, 281–291.
237 S. Roshy, B. F. Sloane and K. Moin, *Cancer Metastasis Rev.*, 2003, **22**, 271–286.
238 L. Yin, H. Sun, H. Zhang, L. He, L. Qiu, J. Lin, H. Xia, Y. Zhang, S. Ji, H. Shi and M. Gao, *J. Am. Chem. Soc.*, 2019, **141**, 3265–3273.
239 V. K. Garripelli, J. K. Kim, S. Son, W. J. Kim, M. A. Repka and S. Jo, *Acta Biomater.*, 2011, **7**, 1984–1992.
240 L. Blavier, A. Lazaryev, F. Dorey, G. M. Shackleford and Y. A. DeClerck, *Cancer Res.*, 2006, **66**, 2691–2699.
241 L. E. Samuelson, R. L. Scherer, L. M. Matrisian, J. O. McIntyre and D. J. Bornhop, *Mol. Pharm.*, 2013, **10**, 3164–3174.
242 M. Shahriari, M. Zahiri, K. Abnous, S. M. Taghdisi, M. Ramezani and M. Alibolandi, *J. Controlled Release*, 2019, **308**, 172–189.
243 W.-X. Qiu, L.-H. Liu, S.-Y. Li, Q. Lei, G.-F. Luo and X.-Z. Zhang, *Small*, 2017, **13**, 1603956.
244 G. Wei, Y. Wang, X. Huang, H. Hou and S. Zhou, *Small Methods*, 2018, **2**, 1700358.
245 J. M. Brown and W. R. Wilson, *Nat. Rev. Cancer*, 2004, **4**, 437–447.
246 W. R. Wilson and M. P. Hay, *Nat. Rev. Cancer*, 2011, **11**, 393–410.
247 C. Chu, H. Lin, H. Liu, X. Wang, J. Wang, P. Zhang, H. Gao, C. Huang, Y. Zeng, Y. Tan, G. Liu and X. Chen, *Adv. Mater.*, 2017, **29**, 1605928.
248 X. Zhang, S. Wang, G. Cheng, P. Yu, J. Chang and X. Chen, *Matter*, 2021, **4**, 26–53.
249 K. Kiyose, K. Hanaoka, D. Oushiki, T. Nakamura, M. Kajimura, M. Suematsu, H. Nishimatsu, T. Yamane, T. Terai, Y. Hirata and T. Nagano, *J. Am. Chem. Soc.*, 2010, **132**, 15846–15848.
250 L. Cui, Y. Zhong, W. Zhu, Y. Xu, Q. Du, X. Wang, X. Qian and Y. Xiao, *Org. Lett.*, 2011, **13**, 928–931.
251 S. Im, J. Lee, D. Park, A. Park, Y. M. Kim and W. J. Kim, *ACS Nano*, 2019, **13**, 476–488.
252 Z. Yuan, C. Lin, Y. He, B. Tao, M. Chen, J. Zhang, P. Liu and K. Cai, *ACS Nano*, 2020, **14**, 3546–3562.
253 G. Yang, S. Z. F. Phua, W. Q. Lim, R. Zhang, L. Feng, G. Liu, H. Wu, A. K. Bindra, D. Jana, Z. Liu and Y. Zhao, *Adv. Mater.*, 2019, **31**, e1901513.
254 K. Zhang, X. Meng, Z. Yang, H. Dong and X. Zhang, *Biomaterials*, 2020, **258**, 120278.
255 L. Hua, Z. Wang, L. Zhao, H. Mao, G. Wang, K. Zhang, X. Liu, D. Wu, Y. Zheng, J. Lu, R. Yu and H. Liu, *Theranostics*, 2018, **8**, 5088–5105.
256 H. Mao, Y. Xie, H. Ju, H. Mao, L. Zhao, Z. Wang, L. Hua, C. Zhao, Y. Li, R. Yu and H. Liu, *ACS Appl. Mater. Interfaces*, 2018, **10**, 33923–33935.

257 A. Wang, J. Fang, S. Ye, Q. Mao, Y. Zhao, C. Cui, Y. Zhang, Y. Feng, J. Li, L. He, L. Qiu and H. Shi, *ACS Appl. Mater. Interfaces*, 2021, **13**, 59787–59802.
258 Z. Zhang, X. Niu, X. Feng, X. Wang, L. Yu, W. Wang and Z. Yuan, *ACS Biomater. Sci. Eng.*, 2021, **7**, 3434–3445.
259 J. Weng, Z. Huang, X. Pu, X. Chen, G. Yin, Y. Tian and Y. Song, *Colloids Surf., B*, 2020, **191**, 110943.
260 J. Liu, J. Zhang, K. Song, J. Du, X. Wang, J. Liu, B. Li, R. Ouyang, Y. Miao, Y. Sun and Y. Li, *Small*, 2021, **17**, e2101015.
261 Y. Chang, K. Yang, P. Wei, S. Huang, Y. Pei, W. Zhao and Z. Pei, *Angew. Chem., Int. Ed.*, 2014, **53**, 13126–13130.
262 C. Qian, J. Yu, Y. Chen, Q. Hu, X. Xiao, W. Sun, C. Wang, P. Feng, Q.-D. Shen and Z. Gu, *Adv. Mater.*, 2016, **28**, 3313–3320.
263 J. Yu, Y. Zhang, Y. Ye, R. Di Santo, W. Sun, D. Ranson, F. S. Ligler, J. B. Buse and Z. Gu, *Proc. Natl. Acad. Sci. U. S. A.*, 2015, **112**, 8260–8265.
264 X. Yi, H. Zhou, Z. Zhang, S. Xiong and K. Yang, *Biomaterials*, 2020, **233**, 119764.
265 C. Ju, Y. Wen, L. Zhang, Q. Wang, L. Xue, J. Shen and C. Zhang, *Small*, 2019, **15**, e1804191.
266 X. Yi, L. Chen, J. Chen, D. Maiti, Z. Chai, Z. Liu and K. Yang, *Adv. Funct. Mater.*, 2018, **28**, 1705161.
267 M. Pucci, V. Bravatà, G. I. Forte, F. P. Cammarata, C. Messa, M. C. Gilardi and L. Minafra, *Cancer Genomics Proteomics*, 2015, **12**, 143–152.
268 M. Chatterjee, E. Ben-Josef, R. Robb, M. Vedaie, S. Seum, K. Thirumoorthy, K. Palanichamy, M. Harbrecht, A. Chakravarti and T. M. Williams, *Cancer Res.*, 2017, **77**, 5925–5937.
269 M. Bouché, Y. C. Dong, S. Sheikh, K. Taing, D. Saxena, J. C. Hsu, M. H. Chen, R. D. Salinas, H. Song, J. A. Burdick, J. Dorsey and D. P. Cormode, *ACS Biomater. Sci. Eng.*, 2021, **7**, 3209–3220.
270 S. Gao, T. Li, Y. Guo, C. Sun, B. Xianyu and H. Xu, *Adv. Mater.*, 2020, **32**, e1907568.
271 B. Choi, H. Choi, B. Yu and D. H. Kim, *ACS Nano*, 2020, **14**, 13115–13126.
272 Z. Du, X. Zhang, Z. Guo, J. Xie, X. Dong, S. Zhu, J. Du, Z. Gu and Y. Zhao, *Adv. Mater.*, 2018, **30**, e1804046.
273 L. Zhang, S. Zhang, J. Xu, Y. Li, J. He, Y. Yang, T. Huynh, P. Ni, G. Duan, Z. Yang and R. Zhou, *ACS Appl. Mater. Interfaces*, 2020, **12**, 43398–43407.
274 D. Shao, F. Zhang, F. Chen, X. Zheng, H. Hu, C. Yang, Z. Tu, Z. Wang, Z. Chang, J. Lu, T. Li, Y. Zhang, L. Chen, K. W. Leong and W. F. Dong, *Adv. Mater.*, 2020, **32**, e2004385.
275 X. Chen, J. Song, X. Chen and H. Yang, *Chem. Soc. Rev.*, 2019, **48**, 3073–3101.
276 K. Tanabe, T. Asada, T. Ito and S.-i Nishimoto, *Bioconjugate Chem.*, 2012, **23**, 1909–1914.
277 J. Wang, W. Xu, N. Zhang, C. Yang, H. Xu, Z. Wang, B. Li, J. Ding and X. Chen, *J. Controlled Release*, 2021, **332**, 1–9.
278 B. Tao, C. Lin, Z. Yuan, Y. He, M. Chen, K. Li, J. Hu, Y. Yang, Z. Xia and K. Cai, *Chem. Eng. J.*, 2021, **403**, 126182.
279 H. P. Lee, G. Lokhande, K. A. Singh, M. K. Jaiswal, S. Rajput and A. K. Gaharwar, *Adv. Mater.*, 2021, **33**, 2101238.
280 Y. Wang, L. Shi, W. Wu, G. Qi, X. Zhu and B. Liu, *Adv. Funct. Mater.*, 2021, **31**, 2010241.
281 T. He, Y. Yuan, C. Jiang, N. T. Blum, J. He, P. Huang and J. Lin, *Angew. Chem., Int. Ed.*, 2021, **133**, 6112–6119.
282 X. Zhou, Y. Li, Y. Xing, J. Li and X. Jiang, *Dalton Trans.*, 2019, **48**, 15068–15073.
283 S. Li, B. A. Moosa, J. G. Croissant and N. M. Khashab, *Angew. Chem., Int. Ed.*, 2015, **127**, 6908–6912.
284 L. Feng, Z. Dong, C. Liang, M. Chen, D. Tao, L. Cheng, K. Yang and Z. Liu, *Biomaterials*, 2018, **181**, 81–91.
285 Z. Meng, Y. Chao, X. Zhou, C. Liang, J. Liu, R. Zhang, L. Cheng, K. Yang, W. Pan, M. Zhu and Z. Liu, *ACS Nano*, 2018, **12**, 9412–9422.
286 G. Song, L. Cheng, Y. Chao, K. Yang and Z. Liu, *Adv. Mater.*, 2017, **29**, 1700996.
287 G. Song, C. Liang, X. Yi, Q. Zhao, L. Cheng, K. Yang and Z. Liu, *Adv. Mater.*, 2016, **28**, 2716–2723.
288 H.-J. Kim, H. Matsuda, H. Zhou and I. Honma, *Adv. Mater.*, 2006, **18**, 3083–3088.
289 N. Y. Rapoport, A. M. Kennedy, J. E. Shea, C. L. Scaife and K. H. Nam, *J. Controlled Release*, 2009, **138**, 268–276.
290 T. Porter, D. Kricsfeld, S. Cheatham and S. Li, *J. Am. Soc. Echocardiogr.*, 1998, **11**, 421–425.
291 X. Song, L. Feng, C. Liang, K. Yang and Z. Liu, *Nano Lett.*, 2016, **16**, 6145–6153.
292 S. Hua, J. He, F. Zhang, J. Yu, W. Zhang, L. Gao, Y. Li and M. Zhou, *Biomaterials*, 2021, **268**, 120590.
293 W. Fu, X. Zhang, L. Mei, R. Zhou, W. Yin, Q. Wang, Z. Gu and Y. Zhao, *ACS Nano*, 2020, **14**, 10001–10017.
294 C. Zhang, L. Yan, X. Wang, X. Dong, R. Zhou, Z. Gu and Y. Zhao, *Nano Lett.*, 2019, **19**, 1749–1757.
295 X. Zhou, Y. Zhang, C. Wang, X. Wu, Y. Yang, B. Zheng, H. Wu, S. Guo and J. Zhang, *ACS Nano*, 2012, **6**, 6592–6599.
296 P. Hu, T. Wu, W. Fan, L. Chen, Y. Liu, D. Ni, W. Bu and J. Shi, *Biomaterials*, 2017, **141**, 86–95.
297 Y. Cui, J. Zhang, H. He and G. Qian, *Chem. Soc. Rev.*, 2018, **47**, 5740–5785.
298 L. Ju, Z. Chen, L. Fang, W. Dong, F. Zheng and M. Shen, *J. Am. Ceram. Soc.*, 2011, **94**, 3418–3424.
299 S. Mura, J. Nicolas and P. Couvreur, *Nat. Mater.*, 2013, **12**, 991–1003.
300 N. Zheng, Q. Wang, C. Li, X. Wang, X. Liu, X. Wang, G. Deng, J. Wang, L. Zhao and J. Lu, *Adv. Healthcare Mater.*, 2021, **10**, e2002024.
301 Y. Chen, G. Song, Z. Dong, X. Yi, Y. Chao, C. Liang, K. Yang, L. Cheng and Z. Liu, *Small*, 2017, **13**, 1602869.
302 Y. Yong, C. Zhang, Z. Gu, J. Du, Z. Guo, X. Dong, J. Xie, G. Zhang, X. Liu and Y. Zhao, *ACS Nano*, 2017, **11**, 7164–7176.
303 X. Cheng, R. Sun, H. Xia, J. Ding, L. Yin, Z. Chai, H. Shi and M. Gao, *Nanomedicine*, 2019, **14**, 2941–2955.
304 F. Ding, J. Feng, X. Zhang, J. Sun, C. Fan and Z. Ge, *Adv. Drug Delivery Rev.*, 2021, **173**, 141–163.

305 G. Hong, A. L. Antaris and H. Dai, *Nat. Biomed. Eng.*, 2017, **1**, 0010.
306 V. Ntziachristos, J. Ripoll, L. V. Wang and R. Weissleder, *Nat. Biotechnol.*, 2005, **23**, 313–320.
307 Z. Duan, Q. Luo, L. Gu, X. Li, H. Zhu, Z. Gu, Q. Gong, H. Zhang and K. Luo, *Nanoscale*, 2021, **13**, 13681–13692.
308 C. Yao, J. Li, X. Cao, J. R. Gunn, M. Wu, S. Jiang and B. W. Pogue, *ACS Appl. Mater. Interfaces*, 2020, **12**, 44383–44392.
309 S. Chen, S. Yu, Z. Du, X. Huang, M. He, S. Long, J. Liu, Y. Lan, D. Yang, H. Wang, S. Li, A. Chen, Y. Hao, Y. Su, C. Wang and S. Luo, *J. Med. Chem.*, 2021, **64**, 3381–3391.
310 Y. Li, M. H. Cho, S. S. Lee, D. E. Lee, H. Cheong and Y. Choi, *J. Controlled Release*, 2020, **325**, 100–110.
311 A. Mizrachi, Y. Shamay, J. Shah, S. Brook, J. Soong, V. K. Rajasekhar, J. L. Humm, J. H. Healey, S. N. Powell, J. Baselga, D. A. Heller, A. Haimovitz-Friedman and M. Scaltriti, *Nat. Commun.*, 2017, **8**, 14292.
312 C. He, Z. Zhang, Y. Ding, K. Xue, X. Wang, R. Yang, Y. An, D. Liu, C. Hu and Q. Tang, *J. Nanobiotechnol.*, 2021, **19**, 29.
313 Z. Yang, Y. Dai, C. Yin, Q. Fan, W. Zhang, J. Song, G. Yu, W. Tang, W. Fan, B. C. Yung, J. Li, X. Li, X. Li, Y. Tang, W. Huang, J. Song and X. Chen, *Adv. Mater.*, 2018, **30**, 1707509.
314 F. Feng, L. Liu, Q. Yang and S. Wang, *Macromol. Rapid Commun.*, 2010, **31**, 1405–1421.
315 J. Li, R. Jiang, Q. Wang, X. Li, X. Hu, Y. Yuan, X. Lu, W. Wang, W. Huang and Q. Fan, *Biomaterials*, 2019, **217**, 119304.
316 K. Shou, Y. Tang, H. Chen, S. Chen, L. Zhang, A. Zhang, Q. Fan, A. Yu and Z. Cheng, *Chem. Sci.*, 2018, **9**, 3105–3110.
317 J. Li, W. Li, L. Xie, W. Sang, G. Wang, Z. Zhang, B. Li, H. Tian, J. Yan, Y. Tian, Z. Li, Q. Fan, L. Yu and Y. Dai, *Chem. Commun.*, 2021, **57**, 11473–11476.
318 Y. B. Pan, S. Wang, X. He, W. Tang, J. Wang, A. Shao and J. Zhang, *J. Mater. Chem. B*, 2019, **7**, 7683–7689.
319 H. Wang, D. Jia, D. Yuan, X. Yin, F. Yuan, F. Wang, W. Shi, H. Li, L. M. Zhu and Q. Fan, *J. Nanobiotechnol.*, 2021, **19**, 138.
320 W. Liu, J. Deacon, H. Yan, B. Sun, Y. Liu, D. Hegan, Q. Li, D. Coman, M. Parent, F. Hyder, K. Roberts, R. Nath, O. Tillement, D. Engelman and P. Glazer, *Transl. Oncol.*, 2020, **13**, 100839.
321 Y. Fan, J. Zhang, M. Shi, D. Li, C. Lu, X. Cao, C. Peng, S. Mignani, J. P. Majoral and X. Shi, *Nano Lett.*, 2019, **19**, 1216–1226.
322 F. Du, L. Zhang, L. Zhang, M. Zhang, A. Gong, Y. Tan, J. Miao, Y. Gong, M. Sun, H. Ju, C. Wu and S. Zou, *Biomaterials*, 2017, **121**, 109–120.
323 C. Wu, R. Cai, T. Zhao, L. Wu, L. Zhang, J. Jin, L. Xu, P. Li, T. Li, M. Zhang and F. Du, *Nanoscale Res. Lett.*, 2020, **15**, 94.
324 S. Dufort, G. Le Duc, M. Salomé, V. Bentivegna, L. Sancey, E. Bräuer-Krisch, H. Requardt, F. Lux, J.-L. Coll, P. Perriat, S. Roux and O. Tillement, *Sci. Rep.*, 2016, **6**, 29678.
325 R. M. Martens, D. P. Noij, M. Ali, T. Koopman, J. T. Marcus, M. R. Vergeer, H. de Vet, M. C. de Jong, C. R. Leemans, O. S. Hoekstra, R. de Bree, P. de Graaf, R. Boellaard and J. A. Castelijns, *Oral Oncol.*, 2019, **88**, 75–83.
326 A. Hillebrand, K. D. Singh, I. E. Holliday, P. L. Furlong and G. R. Barnes, *Hum. Brain Mapp.*, 2005, **25**, 199–211.
327 P. Rolfe, *Annu. Rev. Biomed. Eng.*, 2000, **2**, 715–754.
328 J. W. Wheless, E. Castillo, V. Maggio, H. L. Kim, J. I. Breier, P. G. Simos and A. C. Papanicolaou, *Neurologist*, 2004, **10**, 138–153.
329 A. Shen, X. Meng, X. Gao, X. Xu, C. Shao, Z. Tang, Y. Liu, W. Bu and P. Wang, *Adv. Funct. Mater.*, 2019, **29**, 1803832.
330 J. M. Lupo and S. J. Nelson, *Semin. Radiat. Oncol.*, 2014, **24**, 248–258.
331 D. M. Lambregts, M. Maas, M. P. Stokkel and R. G. Beets-Tan, *Semin. Radiat. Oncol.*, 2016, **26**, 193–198.
332 J. Ye, G. Fu, X. Yan, J. Liu, X. Wang, L. Cheng, F. Zhang, P. Z. Sun and G. Liu, *Nanoscale*, 2018, **10**, 5864–5868.
333 M. Liu, X. Guo, S. Wang, M. Jin, Y. Wang, J. Li and J. Liu, *Eur. Radiol.*, 2013, **23**, 3221–3227.
334 R. Fusco, V. Granata, P. Pariante, V. Cerciello, C. Siani, M. Di Bonito, M. Valentino, M. Sansone, G. Botti and A. Petrillo, *Magn. Reson. Imaging*, 2021, **75**, 51–59.
335 J. Liu, H. Cabral, B. Song, I. Aoki, Z. Chen, N. Nishiyama, Y. Huang, K. Kataoka and P. Mi, *ACS Nano*, 2021, **15**, 13526–13538.
336 P. Mi, D. Kokuryo, H. Cabral, H. Wu, Y. Terada, T. Saga, I. Aoki, N. Nishiyama and K. Kataoka, *Nat. Nanotechnol.*, 2016, **11**, 724–730.
337 J. Hörner-Rieber, S. Klüter, J. Debus, G. Adema, M. Ansems and M. Verheij, *Front. Oncol.*, 2020, **10**, 615697.
338 W. Jiang, Q. Li, L. Xiao, J. Dou, Y. Liu, W. Yu, Y. Ma, X. Li, Y. Z. You, Z. Tong, H. Liu, H. Liang, L. Lu, X. Xu, Y. Yao, G. Zhang, Y. Wang and J. Wang, *ACS Nano*, 2018, **12**, 5684–5698.
339 M. Xu and L. V. Wang, *Rev. Sci. Instrum.*, 2006, **77**, 041101.
340 J. Weber, P. C. Beard and S. E. Bohndiek, *Nat. Methods*, 2016, **13**, 639–650.
341 D. Jiao, K. Wu, K. Xu, Y. Liu, D. Zhao, X. Han and R. Fan, *Front. Bioeng. Biotechnol.*, 2021, **9**, 764531.
342 Y. Wu, L. Su, M. Yuan, T. Chen, J. Ye, Y. Jiang, J. Song and H. Yang, *Angew. Chem., Int. Ed.*, 2021, **60**, 12868–12875.
343 X. Zhou, H. Liu, Y. Zheng, Y. Han, T. Wang, H. Zhang, Q. Sun and Z. Li, *ACS Appl. Mater. Interfaces*, 2020, **12**, 4231–4240.
344 R. Zhou, X. Liu, Y. Wu, H. Xiang, J. Cao, Y. Li, W. Yin, Y. Zu, J. Li, R. Liu, F. Zhao, Z. Liu, C. Chen, Z. Gu, L. Yan and Y. Zhao, *ACS Nano*, 2020, **14**, 13016–13029.
345 H. F. Zhang, K. Maslov, G. Stoica and L. V. Wang, *Nat. Biotechnol.*, 2006, **24**, 848–851.
346 F. Hyafil, J.-C. Cornily, J. E. Feig, R. Gordon, E. Vucic, V. Amirbekian, E. A. Fisher, V. Fuster, L. J. Feldman and Z. A. Fayad, *Nat. Med.*, 2007, **13**, 636–641.
347 C. Haller and I. Hizoh, *Investig. Radiol.*, 2004, **39**, 149–154.
348 O. Rabin, J. Manuel Perez, J. Grimm, G. Wojtkiewicz and R. Weissleder, *Nat. Mater.*, 2006, **5**, 118–122.
349 L. Zhang, X.-Q. Yang, J.-S. Wei, X. Li, H. Wang and Y.-D. Zhao, *Theranostics*, 2019, **9**, 5424–5442.

350 Y. Dai, H. Xiao, J. Liu, Q. Yuan, P. a Ma, D. Yang, C. Li, Z. Cheng, Z. Hou, P. Yang and J. Lin, *J. Am. Chem. Soc.*, 2013, **135**, 18920–18929.
351 M. H. Oh, N. Lee, H. Kim, S. P. Park, Y. Piao, J. Lee, S. W. Jun, W. K. Moon, S. H. Choi and T. Hyeon, *J. Am. Chem. Soc.*, 2011, **133**, 5508–5515.
352 J. Ding, Q. Mao, M. Zhao, Y. Gao, A. Wang, S. Ye, X. Wang, W. Xie and H. Shi, *Nanoscale*, 2020, **12**, 22963–22969.
353 F. Zhang, S. Liu, N. Zhang, Y. Kuang, W. Li, S. Gai, F. He, A. Gulzar and P. Yang, *Nanoscale*, 2020, **12**, 19293–19307.
354 J. Liu, J. Chen, H. Liu, K. Zhang, Q. Zeng, S. Yang, Z. Jiang, X. Zhang, T. Chen, D. Li and H. Shan, *ACS Appl. Mater. Interfaces*, 2021, **13**, 42473–42485.
355 D. Huo, S. Liu, C. Zhang, J. He, Z. Zhou, H. Zhang and Y. Hu, *ACS Nano*, 2017, **11**, 10159–10174.
356 E. B. Ehlerding, F. Chen and W. Cai, *Adv. Sci.*, 2016, **3**, 1500223.
357 J. Pellico, P. J. Gawne and R. T. M. de Rosales, *Chem. Soc. Rev.*, 2021, **50**, 3355–3423.
358 J. Ge, Q. Zhang, J. Zeng, Z. Gu and M. Gao, *Biomaterials*, 2020, **228**, 119553.
359 M. Plotkin, U. Gneveckow, K. Meier-Hauff, H. Amthauer, A. Feußner, T. Denecke, M. Gutberlet, A. Jordan, R. Felix and P. Wust, *Int. J. Hyperthermia*, 2006, **22**, 319–325.
360 P. Garrigue, J. Tang, L. Ding, A. Bouhlel, A. Tintaru, E. Laurini, Y. Huang, Z. Lyu, M. Zhang, S. Fernandez, L. Balasse, W. Lan, E. Mas, D. Marson, Y. Weng, X. Liu, S. Giorgio, J. Iovanna, S. Pricl, B. Guillet and L. Peng, *Proc. Natl. Acad. Sci. U. S. A.*, 2018, **115**, 11454–11459.
361 N. Song, L. Zhao, X. Xu, M. Zhu, C. Liu, N. Sun, J. Yang, X. Shi and J. Zhao, *ACS Appl. Mater. Interfaces*, 2020, **12**, 12395–12406.
362 X. Yi, M. Xu, H. Zhou, S. Xiong, R. Qian, Z. Chai, L. Zhao and K. Yang, *ACS Nano*, 2018, **12**, 9142–9151.
363 X. Shi, Q. Li, C. Zhang, H. Pei, G. Wang, H. Zhou, L. Fan, K. Yang, B. Jiang, F. Wang and R. Zhu, *J. Nanobiotechnol.*, 2021, **19**, 337.
364 D. Cheng, J. Gong, P. Wang, J. Zhu, N. Yu, J. Zhao, Q. Zhang and J. Li, *J. Mater. Chem. B*, 2021, **9**, 9316–9323.
365 L. Luo, W. Sun, Y. Feng, R. Qin, J. Zhang, D. Ding, T. Shi, X. Liu, X. Chen and H. Chen, *ACS Appl. Mater. Interfaces*, 2020, **12**, 12591–12599.
366 S. Wang, R. Tian, X. Zhang, G. Cheng, P. Yu, J. Chang and X. Chen, *Adv. Mater.*, 2021, **33**, e2007488.
367 F. Ahmad, X. Wang, Z. Jiang, X. Yu, X. Liu, R. Mao, X. Chen and W. Li, *ACS Nano*, 2019, **13**, 10419–10433.
368 B. Cline, I. Delahunty and J. Xie, *Wiley Interdiscip. Rev.: Nanomed. Nanobiotechnol.*, 2019, **11**, e1541.
369 D. Ni, C. A. Ferreira, T. E. Barnhart, V. Quach, B. Yu, D. Jiang, W. Wei, H. Liu, J. W. Engle, P. Hu and W. Cai, *J. Am. Chem. Soc.*, 2018, **140**, 14971–14979.
370 W. Lee, M. Jeon, J. Choi, C. Oh, G. Kim, S. Jung, C. Kim, S. J. Ye and H. J. Im, *ACS Nano*, 2020, **14**, 13004–13015.
371 Z. Wang, O. Jacobson, R. Tian, R. C. Mease, D. O. Kiesewetter, G. Niu, M. G. Pomper and X. Chen, *Bioconjugate Chem.*, 2018, **29**, 2309–2315.
372 C. A. Ferreira, S. Goel, E. B. Ehlerding, Z. T. Rosenkrans, D. Jiang, T. Sun, E. Aluicio-Sarduy, J. W. Engle, D. Ni and W. Cai, *Nano Lett.*, 2021, **21**, 4692–4699.
373 D. Chen, D. Yang, C. A. Dougherty, W. Lu, H. Wu, X. He, T. Cai, M. E. Van Dort, B. D. Ross and H. Hong, *ACS Nano*, 2017, **11**, 4315–4327.
374 Z. He, X. Huang, C. Wang, X. Li, Y. Liu, Z. Zhou, S. Wang, F. Zhang, Z. Wang, O. Jacobson, J. J. Zhu, G. Yu, Y. Dai and X. Chen, *Angew. Chem., Int. Ed.*, 2019, **58**, 8752–8756.
375 D. W. Townsend, J. P. J. Carney, J. T. Yap and N. C. Hall, *J. Nucl. Med.*, 2004, **45**, 4S–14S.
376 G. Delso, S. Fürst, B. Jakoby, R. Ladebeck, C. Ganter, S. G. Nekolla, M. Schwaiger and S. I. Ziegler, *J. Nucl. Med.*, 2011, **52**, 1914–1922.
377 Z. Dong, L. Feng, Y. Chao, Y. Hao, M. Chen, F. Gong, X. Han, R. Zhang, L. Cheng and Z. Liu, *Nano Lett.*, 2019, **19**, 805–815.
378 E. Bindini, M. L. A. Ramirez, X. Rios, U. Cossío, C. Simó, V. Gomez-Vallejo, G. Soler-Illia, J. Llop and S. E. Moya, *Small*, 2021, **17**, e2101519.
379 Y. Shi, Q. Fu, J. Li, H. Liu, Z. Zhang, T. Liu and Z. Liu, *ACS Appl. Mater. Interfaces*, 2020, **12**, 55564–55573.
380 R. Tang, A. Zheleznyak, M. Mixdorf, A. Ghai, J. Prior, K. C. L. Black, M. Shokeen, N. Reed, P. Biswas and S. Achilefu, *ACS Nano*, 2020, **14**, 4255–4264.
381 A. R. Muslimov, D. O. Antuganov, Y. V. Tarakanchikova, M. V. Zhukov, M. A. Nadporojskii, M. V. Zyuzin and A. S. Timin, *ACS Appl. Mater. Interfaces*, 2021, **13**, 25599–25610.
382 Y. Yong, X. Cheng, T. Bao, M. Zu, L. Yan, W. Yin, C. Ge, D. Wang, Z. Gu and Y. Zhao, *ACS Nano*, 2015, **9**, 12451–12463.
383 Z. Zhang, J. Yang, Q. Min, C. Ling, D. Maiti, J. Xu, L. Qin and K. Yang, *Small*, 2019, **15**, e1803703.
384 D. Zhong, W. Li, S. Hua, Y. Qi, T. Xie, Y. Qiao and M. Zhou, *Theranostics*, 2021, **11**, 3580–3594.
385 W. Li, D. Zhong, S. Hua, Z. Du and M. Zhou, *ACS Appl. Mater. Interfaces*, 2020, **12**, 44541–44553.
386 M. Lyu, D. Zhu, Y. Duo, Y. Li and H. Quan, *Biomaterials*, 2020, **233**, 119656.
387 Z. Wang, G. Wang, T. Kang, S. Liu, L. Wang, H. Zou, Y. Chong and Y. Liu, *J. Nanobiotechnol.*, 2021, **19**, 90.
388 Q. Dan, D. Hu, Y. Ge, S. Zhang, S. Li, D. Gao, W. Luo, T. Ma, X. Liu, H. Zheng, Y. Li and Z. Sheng, *Biomater. Sci.*, 2020, **8**, 973–987.
389 L. Xia, X. Meng, L. Wen, N. Zhou, T. Liu, X. Xu, F. Wang, Z. Cheng, Z. Yang and H. Zhu, *Small*, 2021, **17**, e2100378.
390 Z. Guo, M. Chen, C. Peng, S. Mo, C. Shi, G. Fu, X. Wen, R. Zhuang, X. Su, T. Liu, N. Zheng and X. Zhang, *Biomaterials*, 2018, **179**, 134–143.
391 N. Lu, W. Fan, X. Yi, S. Wang, Z. Wang, R. Tian, O. Jacobson, Y. Liu, B. C. Yung, G. Zhang, Z. Teng, K. Yang, M. Zhang, G. Niu, G. Lu and X. Chen, *ACS Nano*, 2018, **12**, 1580–1591.
392 Q. Huang, S. Zhang, H. Zhang, Y. Han, H. Liu, F. Ren, Q. Sun, Z. Li and M. Gao, *ACS Nano*, 2019, **13**, 1342–1353.

393 F. Mao, L. Wen, C. Sun, S. Zhang, G. Wang, J. Zeng, Y. Wang, J. Ma, M. Gao and Z. Li, *ACS Nano*, 2016, **10**, 11145–11155.
394 X. Li, J. Li, C. Li, Q. Guo, M. Wu, L. Su, Y. Dou, X. Wu, Z. Xiao and X. Zhang, *J. Mater. Chem. B*, 2021, **9**, 7530–7543.
395 Y. Kang, X. Yu, X. Fan, Aodenggerile, S. Zhao, C. Tu, Z. Yan, R. Wang, W. Li and H. Qiu, *ACS Nano*, 2020, **14**, 4336–4351.
396 C. Zhu, X. Guo, L. Luo, Z. Wu, Z. Luo, M. Jiang, J. Zhang, B. Qin, Y. Shi, Y. Lou, Y. Qiu and J. You, *ACS Appl. Mater. Interfaces*, 2019, **11**, 46536–46547.
397 W. Tang, Z. Dong, R. Zhang, X. Yi, K. Yang, M. Jin, C. Yuan, Z. Xiao, Z. Liu and L. Cheng, *ACS Nano*, 2019, **13**, 284–294.
398 S. C. Formenti and S. Demaria, *Lancet Oncol.*, 2009, **10**, 718–726.
399 J. Antoniades, L. W. Brady and D. A. Lightfoot, *Int. J. Radiat. Oncol. Biol. Phys.*, 1977, **2**, 141–147.
400 G. Ehlers and M. Fridman, *Br. J. Radiol.*, 1973, **46**, 220–222.
401 K. Ohba, K. Omagari, T. Nakamura, N. Ikuno, S. Saeki, I. Matsuo, H. Kinoshita, J. Masuda, H. Hazama, I. Sakamoto and S. Kohno, *Gut*, 1998, **43**, 575–577.
402 G. J. Rees and C. M. Ross, *Br. J. Radiol.*, 1983, **56**, 63–66.
403 S. Demaria, B. Ng, M. L. Devitt, J. S. Babb, N. Kawashima, L. Liebes and S. C. Formenti, *Int. J. Radiat. Oncol. Biol. Phys.*, 2004, **58**, 862–870.
404 S. Demaria, N. Kawashima, A. M. Yang, M. L. Devitt, J. S. Babb, J. P. Allison and S. C. Formenti, *Clin. Cancer Res.*, 2005, **11**, 728–734.
405 M. Z. Dewan, A. E. Galloway, N. Kawashima, J. K. Dewyngaert, J. S. Babb, S. C. Formenti and S. Demaria, *Clin. Cancer Res.*, 2009, **15**, 5379–5388.
406 W. Ngwa, O. C. Irabor, J. D. Schoenfeld, J. Hesser, S. Demaria and S. C. Formenti, *Nat. Rev. Cancer*, 2018, **18**, 313–322.
407 R. R. Weichselbaum, H. Liang, L. Deng and Y.-X. Fu, *Nat. Rev. Clin. Oncol.*, 2017, **14**, 365–379.
408 E. Deutsch, C. Chargari, L. Galluzzi and G. Kroemer, *Lancet Oncol.*, 2019, **20**, e452–e463.
409 J. Li, Y. Luo and K. Pu, *Angew. Chem., Int. Ed.*, 2021, **60**, 12682–12705.
410 E. E. Sweeney, J. Cano-Mejia and R. Fernandes, *Small*, 2018, **14**, 1800678.
411 W. Yang, F. Zhang, H. Deng, L. Lin, S. Wang, F. Kang, G. Yu, J. Lau, R. Tian, M. Zhang, Z. Wang, L. He, Y. Ma, G. Niu, S. Hu and X. Chen, *ACS Nano*, 2020, **14**, 620–631.
412 Y. Yin, X. Jiang, L. Sun, H. Li, C. Su, Y. Zhang, G. Xu, X. Li, C. Zhao, Y. Chen, H. Xu and K. Zhang, *Nano Today*, 2021, **36**, 101009.
413 G. Zhan, Q. Xu, Z. Zhang, Z. Wei, T. Yong, N. Bie, X. Zhang, X. Li, J. Li, L. Gan and X. Yang, *Nano Today*, 2021, **38**, 101195.
414 E. Golden, I. Pellicciotta, S. Demaria, M. H. Barcellos-Hoff and S. Formenti, *Front. Oncol.*, 2012, **2**, 404–408.
415 E. B. Golden and L. Apetoh, *Semin. Radiat. Oncol.*, 2015, **25**, 11–17.
416 S. Chen, D. Li, X. Du, X. He, M. Huang, Y. Wang, X. Yang and J. Wang, *Nano Today*, 2020, **35**, 100924.
417 W. Wu, Y. Pu, H. Yao, H. Lin and J. Shi, *Nano Today*, 2022, **42**, 101377.
418 X. Xiong, J. Zhao, R. Su, C. Liu, X. Guo and S. Zhou, *Nano Today*, 2021, **39**, 101225.
419 F. Zhou, J. Gao, Z. Xu, T. Li, A. Gao, F. Sun, F. Wang, W. Wang, Y. Geng, F. Zhang, Z. P. Xu and H. Yu, *Nano Today*, 2021, **36**, 101025.
420 W. Chen, S. Wang, Y. Wu, X. Shen, Z. Guo, Q. Li and D. Xing, *Microb. Pathog.*, 2020, **141**, 103983.
421 L. Galluzzi, A. Buqué, O. Kepp, L. Zitvogel and G. Kroemer, *Nat. Rev. Immunol.*, 2017, **17**, 97–111.
422 A. Takasu, A. Masui, M. Hamada, T. Imai, S. Iwai and Y. Yura, *Cancer Gene Ther.*, 2016, **23**, 107–113.
423 P.-J. Tian, B.-L. Li, Y.-J. Shan, J.-N. Zhang, J.-Y. Chen, M. Yu and L.-W. Zhang, *Int. J. Mol. Sci.*, 2015, **16**, 20033–20049.
424 M. Obeid, A. Tesniere, F. Ghiringhelli, G. M. Fimia, L. Apetoh, J. L. Perfettini, M. Castedo, G. Mignot, T. Panaretakis, N. Casares, D. Métivier, N. Larochette, P. van Endert, F. Ciccosanti, M. Piacentini, L. Zitvogel and G. Kroemer, *Nat. Med.*, 2007, **13**, 54–61.
425 P. Scaffidi, T. Misteli and M. E. Bianchi, *Nature*, 2002, **418**, 191–195.
426 R. Spisek, A. Charalambous, A. Mazumder, D. H. Vesole, S. Jagannath and M. V. Dhodapkar, *Blood*, 2007, **109**, 4839–4845.
427 J. Fucikova, P. Kralikova, A. Fialova, T. Brtnicky, L. Rob, J. Bartunkova and R. Spísek, *Cancer Res.*, 2011, **71**, 4821–4833.
428 A. D. Garg, D. V. Krysko, P. Vandenabeele and P. Agostinis, *Cancer Immunol. Immunother.*, 2012, **61**, 215–221.
429 A. D. Garg, D. V. Krysko, T. Verfaillie, A. Kaczmarek, G. B. Ferreira, T. Marysael, N. Rubio, M. Firczuk, C. Mathieu, A. J. Roebroek, W. Annaert, J. Golab, P. de Witte, P. Vandenabeele and P. Agostinis, *EMBO J.*, 2012, **31**, 1062–1079.
430 G. Kroemer, L. Galluzzi, O. Kepp and L. Zitvogel, *Annu. Rev. Immunol.*, 2013, **31**, 51–72.
431 D. V. Krysko, A. D. Garg, A. Kaczmarek, O. Krysko, P. Agostinis and P. Vandenabeele, *Nat. Rev. Cancer*, 2012, **12**, 860–875.
432 Q. Chen, J. Chen, Z. Yang, J. Xu, L. Xu, C. Liang, X. Han and Z. Liu, *Adv. Mater.*, 2019, **31**, e1802228.
433 A. Bansal and M. C. Simon, *J. Cell Biol.*, 2018, **217**, 2291–2298.
434 B. Yang, Y. Chen and J. Shi, *Chem. Rev.*, 2019, **119**, 4881–4985.
435 Y. Wang, J. Chen, R. Duan, R. Gu, W. Wang, J. Wu, H. Lian, Y. Hu and A. Yuan, *Adv. Mater.*, 2022, **34**, 2109726.
436 C. Cosentino, D. Grieco and V. Costanzo, *EMBO J.*, 2011, **30**, 546–555.
437 Q. Li, T. Qin, Z. Bi, H. Hong, L. Ding, J. Chen, W. Wu, X. Lin, W. Fu, F. Zheng, Y. Yao, M.-L. Luo, P. E. Saw, G. M. Wulf, X. Xu, E. Song, H. Yao and H. Hu, *Nat. Commun.*, 2020, **11**, 1456.
438 S. J. Moon, W. Dong, G. N. Stephanopoulos and H. D. Sikes, *Bioeng. Transl. Med.*, 2020, **5**, e10184.

439 K. C. Patra and N. Hay, *Trends Biochem. Sci.*, 2014, **39**, 347–354.
440 C. Mills, *Crit. Rev. Immunol.*, 2012, **32**, 463–488.
441 A. Sica, P. Larghi, A. Mancino, L. Rubino, C. Porta, M. G. Totaro, M. Rimoldi, S. K. Biswas, P. Allavena and A. Mantovani, *Semin. Cancer Biol.*, 2008, **18**(5), 349–355.
442 A. Gulzar, J. Xu, C. Wang, F. He, D. Yang, S. Gai, P. Yang, J. Lin, D. Jin and B. Xing, *Nano Today*, 2019, **26**, 16–56.
443 D. G. DeNardo and B. Ruffell, *Nat. Rev. Immunol.*, 2019, **19**, 369–382.
444 A. Zhang, Y. Xu, H. Xu, J. Ren, T. Meng, Y. Ni, Q. Zhu, W.-B. Zhang, Y.-B. Pan, J. Jin, Y. Bi, Z. B. Wu, S. Lin and M. Lou, *Theranostics*, 2021, **11**, 3839–3852.
445 B. Ruffell and Lisa M. Coussens, *Cancer Cell*, 2015, **27**, 462–472.
446 A. Oweida, M. K. Hararah, A. Phan, D. Binder, S. Bhatia, S. Lennon, S. Bukkapatnam, B. Van Court, N. Uyanga, L. Darragh, H. M. Kim, D. Raben, A. C. Tan, L. Heasley, E. Clambey, R. Nemenoff and S. D. Karam, *Clin. Cancer Res.*, 2018, **24**, 5368–5380.
447 E. Persa, A. Balogh, G. Sáfrány and K. Lumniczky, *Cancer Lett.*, 2015, **368**, 252–261.
448 G. Genard, S. Lucas and C. Michiels, *Front. Immunol.*, 2017, **8**, 828.
449 L. Seifert, G. Werba, S. Tiwari, N. N. Giao Ly, S. Nguy, S. Alothman, D. Alqunaibit, A. Avanzi, D. Daley, R. Barilla, D. Tippens, A. Torres-Hernandez, M. Hundeyin, V. R. Mani, C. Hajdu, I. Pellicciotta, P. Oh, K. Du and G. Miller, *Gastroenterology*, 2016, **150**, 1659–1672.e5.
450 Y. Meng, M. A. Beckett, H. Liang, H. J. Mauceri, N. van Rooijen, K. S. Cohen and R. R. Weichselbaum, *Cancer Res.*, 2010, **70**, 1534–1543.
451 T. Inoue, S. Fujishima, E. Ikeda, O. Yoshie, N. Tsukamoto, S. Aiso, N. Aikawa, A. Kubo, K. Matsushima and K. Yamaguchi, *Eur. Respir. J.*, 2004, **24**, 49–56.
452 J. Ma, R. Liu, X. Wang, Q. Liu, Y. Chen, R. P. Valle, Y. Y. Zuo, T. Xia and S. Liu, *ACS Nano*, 2015, **9**, 10498–10515.
453 S. Zanganeh, G. Hutter, R. Spitler, O. Lenkov, M. Mahmoudi, A. Shaw, J. S. Pajarinen, H. Nejadnik, S. Goodman, M. Moseley, L. M. Coussens and H. E. Daldrup-Link, *Nat. Nanotechnol.*, 2016, **11**, 986–994.
454 Y. W. Choo, M. Kang, H. Y. Kim, J. Han, S. Kang, J.-R. Lee, G.-J. Jeong, S. P. Kwon, S. Y. Song, S. Go, M. Jung, J. Hong and B.-S. Kim, *ACS Nano*, 2018, **12**, 8977–8993.
455 C. Shi, T. Liu, Z. Guo, R. Zhuang, X. Zhang and X. Chen, *Nano Lett.*, 2018, **18**, 7330–7342.
456 L. Tian, X. Yi, Z. Dong, J. Xu, C. Liang, Y. Chao, Y. Wang, K. Yang and Z. Liu, *ACS Nano*, 2018, **12**, 11541–11551.
457 X. Song, J. Xu, C. Liang, Y. Chao, Q. Jin, C. Wang, M. Chen and Z. Liu, *Nano Lett.*, 2018, **18**, 6360–6368.
458 Y. Cao, S. Ding, L. Zeng, J. Miao, K. Wang, G. Chen, C. Li, J. Zhou, X. W. Bian and G. Tian, *ACS Appl. Mater. Interfaces*, 2021, **13**, 53504–53518.
459 Z. Huang, D. Yao, Q. Ye, H. Jiang, R. Gu, C. Ji, J. Wu, Y. Hu and A. Yuan, *ACS Nano*, 2021, **15**, 8450–8465.
460 S. P. Luckman, D. E. Hughes, F. P. Coxon, R. G. G. Russell and M. J. Rogers, *J. Bone Miner. Res.*, 1998, **13**, 581–589.
461 M. A. Caligiuri, *Blood*, 2008, **112**, 461–469.
462 L. E. Lowry and W. A. Zehring, *Front. Immunol.*, 2017, **8**, 1061.
463 C. J. Chan, M. J. Smyth and L. Martinet, *Cell Death Differ.*, 2014, **21**, 5–14.
464 S. Paul and G. Lal, *Front. Immunol.*, 2017, **8**, 1124.
465 E. Vivier, E. Tomasello, M. Baratin, T. Walzer and S. Ugolini, *Nat. Immunol.*, 2008, **9**, 503–510.
466 J. Bi and Z. Tian, *Front. Immunol.*, 2017, **8**, 760.
467 E. L. Monaco, E. Tremante, C. Cerboni, E. Melucci, L. Sibilio, A. Zingoni, M. R. Nicotra, P. G. Natali and P. Giacomini, *Neoplasia*, 2011, **13**, 822-IN814.
468 C. Sun, J. Xu, Q. Huang, M. Huang, H. Wen, C. Zhang, J. Wang, J. Song, M. Zheng, H. Sun, H. Wei, W. Xiao, R. Sun and Z. Tian, *Oncoimmunology*, 2017, **6**, e1264562.
469 J.-Y. Kim, Y.-O. Son, S.-W. Park, J.-H. Bae, J. S. Chung, H. H. Kim, B.-S. Chung, S.-H. Kim and C.-D. Kang, *Exp. Mol. Med.*, 2006, **38**, 474–484.
470 K. M. Au, S. I. Park and A. Z. Wang, *Sci. Adv.*, 2020, **6**, eaba8564.
471 M. Enqvist, G. Nilsonne, O. Hammarfjord, R. P. A. Wallin, N. K. Björkström, M. Björnstedt, A. Hjerpe, H.-G. Ljunggren, K. Dobra, K.-J. Malmberg and M. Carlsten, *J. Immunol.*, 2011, **187**, 3546–3554.
472 T. Li, S. Pan, S. Gao, W. Xiang, C. Sun, W. Cao and H. Xu, *Angew. Chem., Int. Ed.*, 2020, **59**, 2700–2704.
473 W. Cao, X. Zhang, X. Miao, Z. Yang and H. Xu, *Angew. Chem., Int. Ed.*, 2013, **52**, 6233–6237.
474 N. Ma, H. Xu, L. An, J. Li, Z. Sun and X. Zhang, *Langmuir*, 2011, **27**, 5874–5878.
475 J. Xia, T. Li, C. Lu and H. Xu, *Macromolecules*, 2018, **51**, 7435–7455.
476 J. K. Chan, J. Roth, J. J. Oppenheim, K. J. Tracey, T. Vogl, M. Feldmann, N. Horwood and J. Nanchahal, *J. Clin. Invest.*, 2012, **122**, 2711–2719.
477 J. F. Curtin, N. Liu, M. Candolfi, W. Xiong, H. Assi, K. Yagiz, M. R. Edwards, K. S. Michelsen, K. M. Kroeger, C. Liu, A. K. M. G. Muhammad, M. C. Clark, M. Arditi, B. Comin-Anduix, A. Ribas, P. R. Lowenstein and M. G. Castro, *PLoS Med.*, 2009, **6**, e1000010.
478 A. B. Sharabi, M. Lim, T. L. DeWeese and C. G. Drake, *Lancet Oncol.*, 2015, **16**, e498–e509.
479 L. Apetoh, F. Ghiringhelli, A. Tesniere, M. Obeid, C. Ortiz, A. Criollo, G. Mignot, M. C. Maiuri, E. Ullrich, P. Saulnier, H. Yang, S. Amigorena, B. Ryffel, F. J. Barrat, P. Saftig, F. Levi, R. Lidereau, C. Nogues, J.-P. Mira, A. Chompret, V. Joulin, F. Clavel-Chapelon, J. Bourhis, F. André, S. Delaloge, T. Tursz, G. Kroemer and L. Zitvogel, *Nat. Med.*, 2007, **13**, 1050–1059.
480 R. H. Fang, A. V. Kroll and L. Zhang, *Small*, 2015, **11**, 5483–5496.
481 M. S. Goldberg, *Cell*, 2015, **161**, 201–204.
482 D. J. Irvine, M. C. Hanson, K. Rakhra and T. Tokatlian, *Chem. Rev.*, 2015, **115**, 11109–11146.

483 J. Kim, W. A. Li, Y. Choi, S. A. Lewin, C. S. Verbeke, G. Dranoff and D. J. Mooney, *Nat. Biotechnol.*, 2015, **33**, 64–72.
484 K. Shao, S. Singha, X. Clemente-Casares, S. Tsai, Y. Yang and P. Santamaria, *ACS Nano*, 2015, **9**, 16–30.
485 D. M. Smith, J. K. Simon and J. R. Baker Jr, *Nat. Rev. Immunol.*, 2013, **13**, 592–605.
486 Y. Min, K. C. Roche, S. Tian, M. J. Eblan, K. P. McKinnon, J. M. Caster, S. Chai, L. E. Herring, L. Zhang, T. Zhang, J. M. DeSimone, J. E. Tepper, B. G. Vincent, J. S. Serody and A. Z. Wang, *Nat. Nanotechnol.*, 2017, **12**, 877–882.
487 M. L. Broz, M. Binnewies, B. Boldajipour, A. E. Nelson, J. L. Pollack, D. J. Erle, A. Barczak, M. D. Rosenblum, A. Daud, D. L. Barber, S. Amigorena, L. J. van't Veer, A. I. Sperling, D. M. Wolf and M. F. Krummel, *Cancer Cell*, 2014, **26**, 638–652.
488 S. LeibundGut-Landmann, J.-M. Waldburger, C. R. e Sousa, H. Acha-Orbea and W. Reith, *Nat. Immunol.*, 2004, **5**, 899–908.
489 R. A. Franklin, W. Liao, A. Sarkar, M. V. Kim, M. R. Bivona, K. Liu, E. G. Pamer and M. O. Li, *Science*, 2014, **344**, 921–925.
490 K. D. Moynihan and D. J. Irvine, *Cancer Res.*, 2017, **77**, 5215–5221.
491 F. Veglia, M. Perego and D. Gabrilovich, *Nat. Immunol.*, 2018, **19**, 108–119.
492 V. Cortez-Retamozo, M. Etzrodt, A. Newton, P. J. Rauch, A. Chudnovskiy, C. Berger, R. J. H. Ryan, Y. Iwamoto, B. Marinelli, R. Gorbatov, R. Forghani, T. I. Novobrantseva, V. Koteliansky, J.-L. Figueiredo, J. W. Chen, D. G. Anderson, M. Nahrendorf, F. K. Swirski, R. Weissleder and M. J. Pittet, *Proc. Natl. Acad. Sci. U. S. A.*, 2012, **109**, 2491–2496.
493 T. N. Mayadas, X. Cullere and C. A. Lowell, *Annu. Rev. Pathol.: Mech. Dis.*, 2014, **9**, 181–218.
494 C. Nathan, *Nat. Rev. Immunol.*, 2006, **6**, 173–182.
495 T. Engeman, A. V. Gorbachev, D. D. Kish and R. L. Fairchild, *J. Leukoc. Biol.*, 2004, **76**, 941–949.
496 A. Mantovani, M. A. Cassatella, C. Costantini and S. Jaillon, *Nat. Rev. Immunol.*, 2011, **11**, 519–531.
497 M. Vono, A. Lin, A. Norrby-Teglund, R. A. Koup, F. Liang and K. Loré, *Blood*, 2017, **129**, 1991–2001.
498 N. Guo, K. Ni, T. Luo, G. Lan, A. Arina, Z. Xu, J. Mao, R. R. Weichselbaum, M. Spiotto and W. Lin, *ACS Nano*, 2021, **15**, 17515–17527.
499 L. Deng, H. Liang, B. Burnette, M. Beckett, T. Darga, R. R. Weichselbaum and Y. X. Fu, *J. Clin. Invest.*, 2014, **124**, 687–695.
500 E. Lauret Marie Joseph, A. Kirilovsky, B. Lecoester, C. El Sissy, L. Boullerot, L. Rangan, A. Marguier, F. Tochet, M. Dosset, J. Boustani, P. Ravel, R. Boidot, L. Spehner, N. Haicheur-Adjouri, F. Marliot, J. R. Pallandre, F. Bonnefoy, V. Scripcariu, M. Van den Eynde, E. Cornillot, C. Mirjolet, F. Pages and O. Adotevi, *J. Immunother. Cancer*, 2021, **9**, 687–695.
501 S. J. Dovedi, A. L. Adlard, G. Lipowska-Bhalla, C. McKenna, S. Jones, E. J. Cheadle, I. J. Stratford, E. Poon, M. Morrow, R. Stewart, H. Jones, R. W. Wilkinson, J. Honeychurch and T. M. Illidge, *Cancer Res.*, 2014, **74**, 5458–5468.
502 C. Twyman-Saint Victor, A. J. Rech, A. Maity, R. Rengan, K. E. Pauken, E. Stelekati, J. L. Benci, B. Xu, H. Dada, P. M. Odorizzi, R. S. Herati, K. D. Mansfield, D. Patsch, R. K. Amaravadi, L. M. Schuchter, H. Ishwaran, R. Mick, D. A. Pryma, X. Xu, M. D. Feldman, T. C. Gangadhar, S. M. Hahn, E. J. Wherry, R. H. Vonderheide and A. J. Minn, *Nature*, 2015, **520**, 373–377.
503 D. Chen, H. B. Barsoumian, G. Fischer, L. Yang, V. Verma, A. I. Younes, Y. Hu, F. Masropour, K. Klein, C. Vellano, J. Marszalek, M. Davies, M. A. Cortez and J. Welsh, *J. Immunother. Cancer*, 2020, **8**, e000289.
504 J. Zeng, A. P. See, J. Phallen, C. M. Jackson, Z. Belcaid, J. Ruzevick, N. Durham, C. Meyer, T. J. Harris, E. Albesiano, G. Pradilla, E. Ford, J. Wong, H. J. Hammers, D. Mathios, B. Tyler, H. Brem, P. T. Tran, D. Pardoll, C. G. Drake and M. Lim, *Int. J. Radiat. Oncol., Biol., Phys.*, 2013, **86**, 343–349.
505 W. Sang, L. Xie, G. Wang, J. Li, Z. Zhang, B. Li, S. Guo, C. X. Deng and Y. Dai, *Adv. Sci.*, 2021, **8**, 2003338.
506 Y. Wang, N. Shen, Y. Wang, M. Li, W. Zhang, L. Fan, L. Liu, Z. Tang and X. Chen, *Biomater. Sci.*, 2021, **9**, 3019–3027.
507 K. Lu, C. He, N. Guo, C. Chan, K. Ni, G. Lan, H. Tang, C. Pelizzari, Y. X. Fu, M. T. Spiotto, R. R. Weichselbaum and W. Lin, *Nat. Biomed. Eng.*, 2018, **2**, 600–610.
508 T. Seremet, F. Brasseur and P. G. Coulie, *Cancer J.*, 2011, **17**, 325–330.
509 F. R. Vogel, *Ann. N. Y. Acad. Sci.*, 1995, **754**, 153–160.
510 P. Aiyer-Harini, H. Ashok-Kumar, G. P. Kumar and N. Shivakumar, *J. Vaccines Vaccination*, 2013, **4**, 1000167.
511 R. L. Coffman, A. Sher and R. A. Seder, *Immunity*, 2010, **33**, 492–503.
512 Y. Yoshizaki, E. Yuba, N. Sakaguchi, K. Koiwai, A. Harada and K. Kono, *Biomaterials*, 2017, **141**, 272–283.
513 A. Banstola, J.-H. Jeong and S. Yook, *Acta Biomater.*, 2020, **114**, 16–30.
514 M. Li, Z. Wang, X. Liu, N. Song, Y. Song, X. Shi, J. Liu, J. Liu and Z. Yu, *J. Controlled Release*, 2021, **340**, 35–47.
515 F. Castro, M. L. Pinto, C. L. Pereira, K. Serre, M. A. Barbosa, K. Vermaelen, F. Gärtner, R. M. Gonçalves, O. De Wever and M. J. Oliveira, *Biomaterials*, 2020, **257**, 120218.
516 J. Wei, D. Wu, S. Zhao, Y. Shao, Y. Xia, D. Ni, X. Qiu, J. Zhang, J. Chen, F. Meng and Z. Zhong, *Adv. Sci.*, 2022, **9**, 2103689.
517 L. Sun, F. Shen, L. Tian, H. Tao, Z. Xiong, J. Xu and Z. Liu, *Adv. Mater.*, 2021, **33**, e2007910.
518 R. B. Patel, M. Ye, P. M. Carlson, A. Jaquish, L. Zangl, B. Ma, Y. Wang, I. Arthur, R. Xie, R. J. Brown, X. Wang, R. Sriramaneni, K. Kim, S. Gong and Z. S. Morris, *Adv. Mater.*, 2019, **31**, 1902626.
519 M. Luo, Z. Liu, X. Zhang, C. Han, L. Z. Samandi, C. Dong, B. D. Sumer, J. Lea, Y.-X. Fu and J. Gao, *J. Controlled Release*, 2019, **300**, 154–160.
520 M. Luo, H. Wang, Z. Wang, H. Cai, Z. Lu, Y. Li, M. Du, G. Huang, C. Wang, X. Chen, M. R. Porembka, J. Lea,

A. E. Frankel, Y.-X. Fu, Z. J. Chen and J. Gao, *Nat. Nanotechnol.*, 2017, **12**, 648–654.
521 E. Albini, A. Coletti, F. Greco, M. T. Pallotta, G. Mondanelli, M. Gargaro, M. L. Belladonna, C. Volpi, R. Bianchi, U. Grohmann, A. Macchiarulo and C. Orabona, *Biochem. Pharmacol.*, 2018, **158**, 286–297.
522 J. B. Katz, A. J. Muller and G. C. Prendergast, *Immunol. Rev.*, 2008, **222**, 206–221.
523 A. L. Mellor and D. H. Munn, *Nat. Rev. Immunol.*, 2004, **4**, 762–774.
524 D. H. Munn, M. Zhou, J. T. Attwood, I. Bondarev, S. J. Conway, B. Marshall, C. Brown and A. L. Mellor, *Science*, 1998, **281**, 1191–1193.
525 G. C. Prendergast, A. Mondal, S. Dey, L. D. Laury-Kleintop and A. J. Muller, *Trends Cancer*, 2018, **4**, 38–58.
526 T. Miyazaki, K. Moritake, K. Yamada, N. Hara, H. Osago, T. Shibata, Y. Akiyama and M. Tsuchiya, *J. Neurosurg.*, 2009, **111**, 230–237.
527 T. Singh and R. K. Goel, *Eur. J. Pharmacol.*, 2016, **784**, 111–120.
528 X. Dong, R. Cheng, S. Zhu, H. Liu, R. Zhou, C. Zhang, K. Chen, L. Mei, C. Wang, C. Su, X. Liu, Z. Gu and Y. Zhao, *ACS Nano*, 2020, **14**, 5400–5416.
529 W. Huang, L. He, Z. Zhang, S. Shi and T. Chen, *ACS Nano*, 2021, **15**, 20225–20241.
530 X. Zhou, Z. Meng, J. She, Y. Zhang, X. Yi, H. Zhou, J. Zhong, Z. Dong, X. Han, M. Chen, Q. Fan, K. Yang and C. Wang, *Nano-Micro Lett.*, 2020, **12**, 100.
531 Q. Zhang, X. Guo, Y. Cheng, L. Chudal, N. K. Pandey, J. Zhang, L. Ma, Q. Xi, G. Yang, Y. Chen, X. Ran, C. Wang, J. Zhao, Y. Li, L. Liu, Z. Yao, W. Chen, Y. Ran and R. Zhang, *Signal Transduction Targeted Ther.*, 2020, **5**, 58.
532 Y. Wang, Y. Ding, D. Yao, H. Dong, C. Ji, J. Wu, Y. Hu and A. Yuan, *Small*, 2021, **17**, e2006231.
533 C. Wang, Z. Dong, Y. Hao, Y. Zhu, J. Ni, Q. Li, B. Liu, Y. Han, Z. Yang, J. Wan, K. Yang, Z. Liu and L. Feng, *Adv. Mater.*, 2021, **34**, 2106520.
534 A. Shirazi, G. Ghobadi and M. Ghazi-Khansari, *J. Radiat. Res.*, 2007, **48**, 263–272.
535 E. J. Moding, M. B. Kastan and D. G. Kirsch, *Nat. Rev. Drug Discovery*, 2013, **12**, 526–542.
536 G.-I. Mun, S. Kim, E. Choi, C. S. Kim and Y.-S. Lee, *Arch. Pharm. Res.*, 2018, **41**, 1033–1050.
537 C. K. K. Nair, D. K. Parida and T. Nomura, *J. Radiat. Res.*, 2001, **42**, 21–37.
538 D. Citrin, A. P. Cotrim, F. Hyodo, B. J. Baum, M. C. Krishna and J. B. Mitchell, *Oncologist*, 2010, **15**, 360–371.
539 E. González, M. P. Cruces, E. Pimentel and P. Sánchez, *Environ. Toxicol. Pharmacol.*, 2018, **62**, 210–214.
540 F. Tabeie, S. M. Tabatabaei, A. Mahmoud-Pashazadeh and M. Assadi, *J. Clin. Diagn. Res.*, 2017, **11**, TC08.
541 T. K. Mandal, L. A. Bostanian, R. A. Graves, S. R. Chapman and I. Womack, *Drug Dev. Ind. Pharm.*, 2002, **28**, 339–344.
542 I. Ahmad, M. Anwar, S. Akhter, P. Thakur, R. Chawla, R. K. Sharma, A. Ali and F. J. Ahmad, *J. Pharm. Innov.*, 2016, **11**, 308–322.
543 S. J. Hosseinimehr, *Drug Discovery Today*, 2007, **12**, 794–805.
544 M. Cheki, E. Mihandoost, A. Shirazi and A. Mahmoudzadeh, *J. Cancer Res. Ther.*, 2016, **12**, 1234–1242.
545 C. Wang, J. Xie, X. Dong, L. Mei, M. Zhao, Z. Leng, H. Hu, L. Li, Z. Gu and Y. Zhao, *Small*, 2020, **16**, e1906915.
546 J.-Y. Wang, X. Mu, Y. Li, F. Xu, W. Long, J. Yang, P. Bian, J. Chen, L. Ouyang, H. Liu, Y. Jing, J. Wang, L. Liu, H. Dai, Y. Sun, C. Liu and X.-D. Zhang, *Small*, 2018, **14**, 1703736.
547 S. I. Han, S. W. Lee, M. G. Cho, J. M. Yoo, M. H. Oh, B. Jeong, D. Kim, O. K. Park, J. Kim, E. Namkoong, J. Jo, N. Lee, C. Lim, M. Soh, Y. E. Sung, J. Yoo, K. Park and T. Hyeon, *Adv. Mater.*, 2020, **32**, e2001566.
548 X. D. Zhang, J. Zhang, J. Wang, J. Yang, J. Chen, X. Shen, J. Deng, D. Deng, W. Long, Y. M. Sun, C. Liu and M. Li, *ACS Nano*, 2016, **10**, 4511–4519.
549 X. Ren, M. Huo, M. Wang, H. Lin, X. Zhang, J. Yin, Y. Chen and H. Chen, *ACS Nano*, 2019, **13**, 6438–6454.
550 J. Xie, Y. Yong, X. Dong, J. Du, Z. Guo, L. Gong, S. Zhu, G. Tian, S. Yu, Z. Gu and Y. Zhao, *ACS Appl. Mater. Interfaces*, 2017, **9**, 14281–14291.
551 T. Liu, Q. Yang, H. Zheng, H. Jia, Y. He, X. Zhang, J. Zheng, Y. Xi, H. Zhang, R. Sun, X. Chen and W. Shan, *Biomaterials*, 2021, **277**, 121103.
552 J. Cao, X. Peng, H. Li, L. Ren, T. Xu, K. Sun, Y. Zhang and D. Li, *Mater. Sci. Eng., C*, 2021, **129**, 112369.
553 A. Kim, C. Yonemoto, C. P. Feliciano, B. Shashni and Y. Nagasaki, *Small*, 2021, **17**, e2008210.
554 N. M. Molino and S.-W. Wang, *Curr. Opin. Biotechnol.*, 2014, **28**, 75–82.
555 C. F. Richardson, D. I. Schuster and S. R. Wilson, *Org. Lett.*, 2000, **2**, 1011–1014.
556 G. Seifert, K. Vietze and R. Schmidt, *J. Phys. B: At., Mol. Opt. Phys.*, 1996, **29**, 5183–5192.
557 Y. Ueno and S. Saito, *Phys. Rev. B: Condens. Matter Mater. Phys.*, 2008, **77**, 085403.
558 J. Grebowski, A. Krokosz, A. Konarska, M. Wolszczak and M. Puchala, *Radiat. Phys. Chem.*, 2014, **103**, 146–152.
559 S. S. Ali, J. I. Hardt, K. L. Quick, J. Sook Kim-Han, B. F. Erlanger, T.-t Huang, C. J. Epstein and L. L. Dugan, *Free Radical Biol. Med.*, 2004, **37**, 1191–1202.
560 P. J. Krusic, E. Wasserman, P. N. Keizer, J. R. Morton and K. F. Preston, *Science*, 1991, **254**, 1183–1185.
561 X. Cheng, X. Ni, R. Wu, Y. Chong, X. Gao, C. Ge and J. J. Yin, *Nanomedicine*, 2018, **13**, 733–747.
562 H. Ma, J. Zhao, H. Meng, D. Hu, Y. Zhou, X. Zhang, C. Wang, J. Li, J. Yuan and Y. Wei, *ACS Appl. Mater. Interfaces*, 2020, **12**, 16104–16113.
563 J. Tong, M. C. Zimmerman, S. Li, X. Yi, R. Luxenhofer, R. Jordan and A. V. Kabanov, *Biomaterials*, 2011, **32**, 3654–3665.
564 J.-J. Yin, F. Lao, P. P. Fu, W. G. Wamer, Y. Zhao, P. C. Wang, Y. Qiu, B. Sun, G. Xing, J. Dong, X.-J. Liang and C. Chen, *Biomaterials*, 2009, **30**, 611–621.
565 A. Djordjevic, B. Srdjenovic, M. Seke, D. Petrovic, R. Injac and J. Mrdjanovic, *J. Nanomater.*, 2015, **2015**, 567073.

566 S.-E. Zhu, F. Li and G.-W. Wang, *Chem. Soc. Rev.*, 2013, **42**, 7535–7570.
567 J. Vesna, J. Danica, K. Kamil, D.-S. Viktorija, D. Silva, T. Sanja, B. Ivana, S. Zoran, M. Zoran, B. Dubravko and D. Aleksandar, *J. Appl. Biomed.*, 2016, **14**, 285–297.
568 Q. Zhao, Y. Li, J. Xu, R. Liu and W. Li, *Int. J. Radiat. Biol.*, 2005, **81**, 169–175.
569 S. Trajković, S. Dobrić, V. Jaćević, V. Dragojević-Simić, Z. Milovanović and A. Dordević, *Colloids Surf., B*, 2007, **58**, 39–43.
570 M. Singh, A. Alavi, R. Wong and S. Akita, *Am. J. Clin. Dermatol.*, 2016, **17**, 277–292.
571 M. Zhao, C. Wang, J. Xie, C. Ji and Z. Gu, *Small*, 2021, **17**, e2102035.
572 L. Zhao, Y. Wang and Y. Li, *Nanomaterials*, 2019, **9**, 1708.
573 W. Xia, H. Xue, J. Wang, T. Wang, L. Song, H. Guo, X. Fan, H. Gong and J. He, *Carbon*, 2016, **101**, 315–323.
574 E. Kolanthai, S. Bose, K. S. Bhagyashree, S. V. Bhat, K. Asokan, D. Kanjilal and K. Chatterjee, *Phys. Chem. Chem. Phys.*, 2015, **17**, 22900–22910.
575 M. Mahmudzadeh, H. Yari, B. Ramezanzadeh and M. Mahdavian, *J. Hazard. Mater.*, 2019, **371**, 609–624.
576 H. Cho, M. R. Jones, S. C. Nguyen, M. R. Hauwiller, A. Zettl and A. P. Alivisatos, *Nano Lett.*, 2017, **17**, 414–420.
577 C. Zhang, S. Chen, P. J. J. Alvarez and W. Chen, *Carbon*, 2015, **94**, 531–538.
578 L. Nilewski, K. Mendoza, A. S. Jalilov, V. Berka, G. Wu, W. K. A. Sikkema, A. Metzger, R. Ye, R. Zhang, D. X. Luong, T. Wang, E. McHugh, P. J. Derry, E. L. Samuel, T. A. Kent, A.-L. Tsai and J. M. Tour, *ACS Appl. Mater. Interfaces*, 2019, **11**, 16815–16821.
579 Y. Song, K. Qu, C. Zhao, J. Ren and X. Qu, *Adv. Mater.*, 2010, **22**, 2206–2210.
580 X. Cui, P. Ren, D. Deng, J. Deng and X. Bao, *Energy Environ. Sci.*, 2016, **9**, 123–129.
581 D. Deng, K. S. Novoselov, Q. Fu, N. Zheng, Z. Tian and X. Bao, *Nat. Nanotechnol.*, 2016, **11**, 218–230.
582 D. Deng, L. Yu, X. Chen, G. Wang, L. Jin, X. Pan, J. Deng, G. Sun and X. Bao, *Angew. Chem., Int. Ed.*, 2013, **52**, 371–375.
583 M. Gong and H. Dai, *Nano Res.*, 2015, **8**, 23–39.
584 M. Gong, D.-Y. Wang, C.-C. Chen, B.-J. Hwang and H. Dai, *Nano Res.*, 2016, **9**, 28–46.
585 J. Wang, X. Cui, H. Li, J. Xiao, J. Yang, X. Mu, H. Liu, Y.-M. Sun, X. Xue, C. Liu, X.-D. Zhang, D. Deng and X. Bao, *Nano Res.*, 2018, **11**, 2821–2835.
586 S. Wang, L. Yi, J. E. Halpert, X. Lai, Y. Liu, H. Cao, R. Yu, D. Wang and Y. Li, *Small*, 2012, **8**, 265–271.
587 J. Li, J. Xu, Z. Xie, X. Gao, J. Zhou, Y. Xiong, C. Chen, J. Zhang and Z. Liu, *Adv. Mater.*, 2018, **30**, 1800548.
588 Z. Jin, M. Yuan, H. Li, H. Yang, Q. Zhou, H. Liu, X. Lan, M. Liu, J. Wang, E. H. Sargent and Y. Li, *Adv. Funct. Mater.*, 2016, **26**, 5284–5289.
589 C. Kuang, G. Tang, T. Jiu, H. Yang, H. Liu, B. Li, W. Luo, X. Li, W. Zhang, F. Lu, J. Fang and Y. Li, *Nano Lett.*, 2015, **15**, 2756–2762.
590 H. Ren, H. Shao, L. Zhang, D. Guo, Q. Jin, R. Yu, L. Wang, Y. Li, Y. Wang, H. Zhao and D. Wang, *Adv. Energy Mater.*, 2015, **5**, 1500296.
591 J. Xiao, J. Shi, H. Liu, Y. Xu, S. Lv, Y. Luo, D. Li, Q. Meng and Y. Li, *Adv. Energy Mater.*, 2015, **5**, 1401943.
592 H. Du, H. Yang, C. Huang, J. He, H. Liu and Y. Li, *Nano Energy*, 2016, **22**, 615–622.
593 C. Huang, S. Zhang, H. Liu, Y. Li, G. Cui and Y. Li, *Nano Energy*, 2015, **11**, 481–489.
594 J. Xie, N. Wang, X. Dong, C. Wang, Z. Du, L. Mei, Y. Yong, C. Huang, Y. Li, Z. Gu and Y. Zhao, *ACS Appl. Mater. Interfaces*, 2019, **11**, 2579–2590.
595 P. Xie, S.-T. Yang, T. He, S. Yang and X.-H. Tang, *Int. J. Mol. Sci.*, 2017, **18**, 2562.
596 E. M. Pridgen, F. Alexis and O. C. Farokhzad, *Expert Opin. Drug Delivery*, 2015, **12**, 1459–1473.
597 Y. Yang, L. Guo, Z. Wang, P. Liu, X. Liu, J. Ding and W. Zhou, *Biomaterials*, 2021, **264**, 120390.
598 A. Watanabe, M. Kajita, J. Kim, A. Kanayama, K. Takahashi, T. Mashino and Y. Miyamoto, *Nanotechnology*, 2009, **20**, 455105.
599 T. Hamasaki, T. Kashiwagi, T. Imada, N. Nakamichi, S. Aramaki, K. Toh, S. Morisawa, H. Shimakoshi, Y. Hisaeda and S. Shirahata, *Langmuir*, 2008, **24**, 7354–7364.
600 M. Kajita, K. Hikosaka, M. Iitsuka, A. Kanayama, N. Toshima and Y. Miyamoto, *Free Radical Res.*, 2007, **41**, 615–626.
601 W. Luo, C. Zhu, S. Su, D. Li, Y. He, Q. Huang and C. Fan, *ACS Nano*, 2010, **4**, 7451–7458.
602 Y. Hu, H. Cheng, X. Zhao, J. Wu, F. Muhammad, S. Lin, J. He, L. Zhou, C. Zhang, Y. Deng, P. Wang, Z. Zhou, S. Nie and H. Wei, *ACS Nano*, 2017, **11**, 5558–5566.
603 M. Cui, Y. Zhao, C. Wang and Q. Song, *Mikrochim. Acta*, 2017, **184**, 3113–3119.
604 M. Cui, J. Zhou, Y. Zhao and Q. Song, *Sens. Actuators, B*, 2017, **243**, 203–210.
605 D.-Y. Zhang, M. R. Younis, H. Liu, S. Lei, Y. Wan, J. Qu, J. Lin and P. Huang, *Biomaterials*, 2021, **271**, 120706.
606 T. Wen, W. He, Y. Chong, Y. Liu, J.-J. Yin and X. Wu, *Phys. Chem. Chem. Phys.*, 2015, **17**, 24937–24943.
607 Z. Jia, X. Yuan, J.-a Wei, X. Guo, Y. Gong, J. Li, H. Zhou, L. Zhang and J. Liu, *ACS Appl. Mater. Interfaces*, 2021, **13**, 49602–49613.
608 F. Xu, X. Mu, J. Wang, P. Bian, L. Liu, H. Liu, Y. Jing, W. Long, C. Liu and X. D. Zhang, *J. Biomed. Nanotechnol.*, 2017, **13**, 1512–1521.
609 W. Long, J. Wang, F. Xu, H. Wu, X. Mu, J. Wang, Y. Sun and X.-D. Zhang, *Chin. Chem. Lett.*, 2020, **31**, 269–274.
610 W. Long, X. Mu, J.-Y. Wang, F. Xu, J. Yang, J. Wang, S. Sun, J. Chen, Y.-M. Sun, H. Wang and X.-D. Zhang, *Front. Chem.*, 2019, **7**, 784.
611 D. K. Chandrasekharan and C. K. Nair, *Cancer Biother. Radiopharm.*, 2012, **27**, 642–651.
612 L. He, G. Huang, H. Liu, C. Sang, X. Liu and T. Chen, *Sci. Adv.*, 2020, **6**, eaay9751.
613 Q. Bao, P. Hu, Y. Xu, T. Cheng, C. Wei, L. Pan and J. Shi, *ACS Nano*, 2018, **12**, 6794–6805.

614 K. E. Peloi, B. A. Ratti, C. V. Nakamura, C. J. Neal, T. S. Sakthivel, S. Singh, S. Seal and S. de Oliveira Silva Lautenschlager, *J. Biomed. Mater. Res.*, 2021, **109**, 2570–2579.
615 S. Wang, H. Zheng, L. Zhou, F. Cheng, Z. Liu, H. Zhang and Q. Zhang, *Biomaterials*, 2020, **260**, 120314.
616 W. Sun, Y. Xu, Y. Yao, J. Yue, Z. Wu, H. Li, G. Shen, Y. Liao, H. Wang and W. Zhou, *J. Nanobiotechnol.*, 2022, **20**, 88.
617 C. Li, Z. Zhao, Y. Luo, T. Ning, P. Liu, Q. Chen, Y. Chu, Q. Guo, Y. Zhang, W. Zhou, H. Chen, Z. Zhou, Y. Wang, B. Su, H. You, T. Zhang, X. Li, H. Song, C. Li, T. Sun and C. Jiang, *Adv. Sci.*, 2021, **8**, e2101526.
618 W. Hou, Y. Jiang, G. Xie, L. Zhao, F. Zhao, X. Zhang, S. K. Sun, C. Yu and J. Pan, *Nanoscale*, 2021, **13**, 8531–8542.
619 L. Gao, J. Zhuang, L. Nie, J. Zhang, Y. Zhang, N. Gu, T. Wang, J. Feng, D. Yang, S. Perrett and X. Yan, *Nat. Nanotechnol.*, 2007, **2**, 577–583.
620 Z. Chen, J.-J. Yin, Y.-T. Zhou, Y. Zhang, L. Song, M. Song, S. Hu and N. Gu, *ACS Nano*, 2012, **6**, 4001–4012.
621 M. Soh, D. W. Kang, H. G. Jeong, D. Kim, D. Y. Kim, W. Yang, C. Song, S. Baik, I. Y. Choi, S. K. Ki, H. J. Kwon, T. Kim, C. K. Kim, S. H. Lee and T. Hyeon, *Angew. Chem., Int. Ed.*, 2017, **56**, 11399–11403.
622 A. Briggs, S. Corde, S. Oktaria, R. Brown, A. Rosenfeld, M. Lerch, K. Konstantinov and M. Tehei, *Nanomedicine*, 2013, **9**, 1098–1105.
623 S. Das, C. J. Neal, J. Ortiz and S. Seal, *Nanoscale*, 2018, **10**, 21069–21075.
624 N. Abdi Goushbolagh, R. Abedi Firouzjah, K. Ebrahimnejad Gorji, M. Khosravanipour, S. Moradi, A. Banaei, A. Astani, M. Najafi, M. H. Zare and B. Farhood, *Artif. Cells, Nanomed., Biotechnol.*, 2018, **46**, S1215–S1225.
625 A. Salvetti, G. Gambino, L. Rossi, D. De Pasquale, C. Pucci, S. Linsalata, A. Degl'Innocenti, S. Nitti, M. Prato, C. Ippolito and G. Ciofani, *Mater. Sci. Eng., C*, 2020, **115**, 111113.
626 Z. Zal, A. Ghasemi, S. Azizi, H. Asgarian-Omran, A. Montazeri and S. J. Hosseinimehr, *Curr. Radiopharm.*, 2018, **11**, 109–115.
627 C. Metcalfe, Noelyn M. Kljavin, R. Ybarra and Frederic J. de Sauvage, *Cell Stem Cell*, 2014, **14**, 149–159.
628 S. Manzeli, D. Ovchinnikov, D. Pasquier, O. V. Yazyev and A. Kis, *Nat. Rev. Mater.*, 2017, **2**, 17033.
629 D. Voiry, A. Mohite and M. Chhowalla, *Chem. Soc. Rev.*, 2015, **44**, 2702–2712.
630 R. Lv, H. Terrones, A. L. Elías, N. Perea-López, H. R. Gutiérrez, E. Cruz-Silva, L. P. Rajukumar, M. S. Dresselhaus and M. Terrones, *Nano Today*, 2015, **10**, 559–592.
631 H. Zhang, M. Chhowalla and Z. Liu, *Chem. Soc. Rev.*, 2018, **47**, 3015–3017.
632 R. G. Dickinson and L. Pauling, *J. Am. Chem. Soc.*, 1923, **45**, 1466–1471.
633 Q. H. Wang, K. Kalantar-Zadeh, A. Kis, J. N. Coleman and M. S. Strano, *Nat. Nanotechnol.*, 2012, **7**, 699–712.
634 K. F. Mak and J. Shan, *Nat. Photonics*, 2016, **10**, 216–226.
635 J. Xu, J. Zhang, W. Zhang and C.-S. Lee, *Adv. Energy Mater.*, 2017, **7**, 1700571.
636 Q. Yun, L. Li, Z. Hu, Q. Lu, B. Chen and H. Zhang, *Adv. Mater.*, 2020, **32**, 1903826.
637 D. Er, H. Ye, N. C. Frey, H. Kumar, J. Lou and V. B. Shenoy, *Nano Lett.*, 2018, **18**, 3943–3949.
638 L. Lin, P. Sherrell, Y. Liu, W. Lei, S. Zhang, H. Zhang, G. G. Wallace and J. Chen, *Adv. Energy Mater.*, 2020, **10**, 1903870.
639 R. J. Toh, Z. Sofer and M. Pumera, *J. Mater. Chem. A*, 2016, **4**, 18322–18334.
640 R. Kumar, N. Goel, M. Hojamberdiev and M. Kumar, *Sens. Actuators, A*, 2020, **303**, 111875.
641 E. Lee, Y. S. Yoon and D.-J. Kim, *ACS Sens.*, 2018, **3**, 2045–2060.
642 D. Sarkar, X. Xie, J. Kang, H. Zhang, W. Liu, J. Navarrete, M. Moskovits and K. Banerjee, *Nano Lett.*, 2015, **15**, 2852–2862.
643 A. Daus, S. Vaziri, V. Chen, Ç. Köroğlu, R. W. Grady, C. S. Bailey, H. R. Lee, K. Schauble, K. Brenner and E. Pop, *Nat. Electron.*, 2021, **4**, 495–501.
644 C. Gong, H. Zhang, W. Wang, L. Colombo, R. M. Wallace and K. Cho, *Appl. Phys. Lett.*, 2013, **103**, 053513.
645 Y. Chen, Y. He, H. Xu, C. Du, X. Wu and G. Yang, *Nano Today*, 2022, **43**, 101421.
646 S. Zhu, L. Gong, J. Xie, Z. Gu and Y. Zhao, *Small Methods*, 2017, **1**, 1700220.
647 X.-D. Zhang, J. Chen, Y. Min, G. B. Park, X. Shen, S.-S. Song, Y.-M. Sun, H. Wang, W. Long, J. Xie, K. Gao, L. Zhang, S. Fan, F. Fan and U. Jeong, *Adv. Funct. Mater.*, 2014, **24**, 1718–1729.
648 X. D. Zhang, Y. Jing, S. Song, J. Yang, J. Y. Wang, X. Xue, Y. Min, G. Park, X. Shen, Y. M. Sun and U. Jeong, *Nanomedicine*, 2017, **13**, 1597–1605.
649 B. Anasori, M. R. Lukatskaya and Y. Gogotsi, *Nat. Rev. Mater.*, 2017, **2**, 16098.
650 W. Meng, X. Liu, H. Song, Y. Xie, X. Shi, M. Dargusch, Z.-G. Chen, Z. Tang and S. Lu, *Nano Today*, 2021, **40**, 101273.
651 J. Pang, R. G. Mendes, A. Bachmatiuk, L. Zhao, H. Q. Ta, T. Gemming, H. Liu, Z. Liu and M. H. Rummeli, *Chem. Soc. Rev.*, 2019, **48**, 72–133.
652 Y. A. J. Al-Hamadani, B.-M. Jun, M. Yoon, N. Taheri-Qazvini, S. A. Snyder, M. Jang, J. Heo and Y. Yoon, *Chemosphere*, 2020, **254**, 126821.
653 X. Xie, C. Chen, N. Zhang, Z.-R. Tang, J. Jiang and Y.-J. Xu, *Nat. Sustain*, 2019, **2**, 856–862.
654 P. Salles, D. Pinto, K. Hantanasirisakul, K. Maleski, C. E. Shuck and Y. Gogotsi, *Adv. Funct. Mater.*, 2019, **29**, 1809223.
655 S. J. Kim, H.-J. Koh, C. E. Ren, O. Kwon, K. Maleski, S.-Y. Cho, B. Anasori, C.-K. Kim, Y.-K. Choi, J. Kim, Y. Gogotsi and H.-T. Jung, *ACS Nano*, 2018, **12**, 986–993.
656 S. Sun, M. Wang, X. Chang, Y. Jiang, D. Zhang, D. Wang, Y. Zhang and Y. Lei, *Sens. Actuators, B*, 2020, **304**, 127274.
657 Y. Gogotsi and B. Anasori, *ACS Nano*, 2019, **13**, 8491–8494.
658 M. Naguib, M. Kurtoglu, V. Presser, J. Lu, J. Niu, M. Heon, L. Hultman, Y. Gogotsi and M. W. Barsoum, *Adv. Mater.*, 2011, **23**, 4248–4253.

659 B. Zhou, Y. Pu, H. Lin, W. Yue, H. Yin, Y. Yin, W. Ren, C. Zhao, Y. Chen and H. Xu, *J. Mater. Chem. B*, 2020, **8**, 5257–5266.
660 B. Zhou, H. Yin, C. Dong, L. Sun, W. Feng, Y. Pu, X. Han, X. Li, D. Du, H. Xu and Y. Chen, *Adv. Sci.*, 2021, **8**, 2101043.
661 K. Rasool, M. Helal, A. Ali, C. E. Ren, Y. Gogotsi and K. A. Mahmoud, *ACS Nano*, 2016, **10**, 3674–3684.
662 M. A. Unal, F. Bayrakdar, L. Fusco, O. Besbinar, C. E. Shuck, S. Yalcin, M. T. Erken, A. Ozkul, C. Gurcan, O. Panatli, G. Y. Summak, C. Gokce, M. Orecchioni, A. Gazzi, F. Vitale, J. Somers, E. Demir, S. S. Yildiz, H. Nazir, J.-C. Grivel, D. Bedognetti, A. Crisanti, K. C. Akcali, Y. Gogotsi, L. G. Delogu and A. Yilmazer, *Nano Today*, 2021, **38**, 101136.
663 F. Bu, M. M. Zagho, Y. Ibrahim, B. Ma, A. Elzatahry and D. Zhao, *Nano Today*, 2020, **30**, 100803.
664 R. B. Rakhi, P. Nayak, C. Xia and H. N. Alshareef, *Sci. Rep.*, 2016, **6**, 36422.
665 S. Iravani and R. S. Varma, *Mater. Adv.*, 2021, **2**, 2906–2917.
666 M. Caldas, A. C. Santos, F. Veiga, R. Rebelo, R. L. Reis and V. M. Correlo, *Acta Biomater.*, 2020, **105**, 26–43.
667 Y. Liu, K. Ai, X. Ji, D. Askhatova, R. Du, L. Lu and J. Shi, *J. Am. Chem. Soc.*, 2017, **139**, 856–862.
668 G. Zhong, X. Yang, X. Jiang, A. Kumar, H. Long, J. Xie, L. Zheng and J. Zhao, *Nanoscale*, 2019, **11**, 11605–11616.
669 M. M. Rageh, R. H. El-Gebaly, H. Abou-Shady and D. G. Amin, *Mol. Cell. Biochem.*, 2015, **399**, 59–69.
670 N. T. Le Na, S. Duc Loc, N. L. Minh Tri, N. T. Bich Loan, H. Anh Son, N. Linh Toan, H. Phuong Thu, H. T. My Nhung, N. Lai Thanh, N. T. Van Anh and N. Dinh Thang, *Materials*, 2019, **12**, 1725.
671 M. M. Rageh and R. H. El-Gebaly, *Mutat. Res., Genet. Toxicol. Environ. Mutagen.*, 2018, **828**, 15–22.
672 W. Lohcharoenkal, L. Wang, Y. C. Chen and Y. Rojanasakul, *Biomed Res. Int.*, 2014, **2014**, 180549.
673 L. P. Herrera Estrada and J. A. Champion, *Biomater. Sci.*, 2015, **3**, 787–799.
674 M. J. Hawkins, P. Soon-Shiong and N. Desai, *Adv. Drug Delivery Rev.*, 2008, **60**, 876–885.
675 M. Bellini, B. Riva, V. Tinelli, M. A. Rizzuto, L. Salvioni, M. Colombo, F. Mingozzi, A. Visioli, L. Marongiu, G. Frascotti, M. S. Christodoulou, D. Passarella, D. Prosperi and L. Fiandra, *Small*, 2020, **16**, e2001450.
676 K. Fan, X. Jia, M. Zhou, K. Wang, J. Conde, J. He, J. Tian and X. Yan, *ACS Nano*, 2018, **12**, 4105–4115.
677 L. He, X. Lin, Y. Wang, C. Abraham, C. Sou, T. Ngo, Y. Zhang, I. A. Wilson and J. Zhu, *Sci. Adv.*, 2021, **7**, eabf1591.
678 W. Wang, B. Huang, Y. Zhu, W. Tan and M. Zhu, *Cell. Mol. Immunol.*, 2021, **18**, 749–751.
679 J. Zhang, D. Cheng, J. He, J. Hong, C. Yuan and M. Liang, *Nat. Protoc.*, 2021, **16**, 4878–4896.
680 A. Haimovitz-Friedman, N. Balaban, M. McLoughlin, D. Ehleiter, J. Michaeli, I. Vlodavsky and Z. Fuks, *Cancer Res.*, 1994, **54**, 2591–2597.
681 M. Li, A. Du, J. Xu, Y. Ma, H. Cao, C. Yang, X.-D. Yang, C.-G. Xing, M. Chen, W. Zhu, S. Zhang and J. Cao, *Sci. Rep.*, 2016, **6**, 30180.
682 Y. Shi, W. Wu, H. Qiao, L. Yue, L. Ren, S. Zhang, W. Yang and Z. Yang, *Sci. Rep.*, 2016, **6**, 26664.
683 W. Long, J. Wang, J. Yang, H. Wu, J. Wang, X. Mu, H. He, Q. Liu, Y. M. Sun, H. Wang and X. D. Zhang, *J. Biomed. Nanotechnol.*, 2019, **15**, 62–76.
684 B. Daroczi, G. Kari, M. F. McAleer, J. C. Wolf, U. Rodeck and A. P. Dicker, *Clin. Cancer Res.*, 2006, **12**, 7086–7091.
685 J. Guo, H. Yang, Y. Liu, W. Liu, R. Zhao, H. Li, W. Long, W. Xu, M. Guo and X. Zhang, *J. Nanobiotechnol.*, 2021, **19**, 377.
686 S. Lv, W. Long, J. Chen, Q. Ren, J. Wang, X. Mu, H. Liu, X. D. Zhang and R. Zhang, *Nanoscale*, 2020, **12**, 548–557.
687 H. Liu, J. Wang, Y. Jing, J. Yang, X. Bai, X. Mu, F. Xu, X. Xue, L. Liu, Y.-M. Sun, Q. Liu, H. Dai, C. Liu and X.-D. Zhang, *Part. Part. Syst. Charact.*, 2017, **34**, 1700035.
688 P. Bian, J. Zhang, J. Wang, J. Yang, J. Wang, H. Liu, Y. Sun, M. Li and X.-D. Zhang, *Sci. Bull.*, 2018, **63**, 925–934.
689 R. S. Patwardhan, D. Sharma, R. Checker and S. K. Sandur, *Free Radicals Biol. Med.*, 2014, **68**, 52–64.
690 S. L. Schlichte, S. Romanova, K. Katsurada, E. A. Kosmacek, T. K. Bronich, K. P. Patel, R. E. Oberley-Deegan and M. C. Zimmerman, *Redox. Biol.*, 2020, **36**, 101610.
691 Y. Zhang, J. Wang, Y. Li, F. Wang, F. Yang and W. Xu, *Int. J. Mol. Sci.*, 2017, **18**, 2233.
692 U. Anand, P. Biswas, V. Kumar, D. Ray, P. Ray, V. I. P. Loake, R. Kandimalla, A. Chaudhary, B. Singh, N. K. Routhu, Z.-S. Chen, J. Proćków and A. Dey, *Biomed. Pharmacother.*, 2022, **146**, 112555.
693 C. N. Andreassen, C. Grau and J. C. Lindegaard, *Semin. Radiat. Oncol.*, 2003, **13**, 62–72.
694 N. M. Gandhi, D. K. Maurya, V. Salvi, S. Kapoor, T. Mukherjee and C. K. K. Nair, *J. Radiat. Res.*, 2004, **45**, 461–468.
695 H.-J. Sim, G. Bhattarai, J. Lee, J.-C. Lee and S.-H. Kook, *Aging Dis.*, 2019, **10**, 1320–1327.
696 J. Yi, J. Zhu, C. Zhao, Q. Kang, X. Zhang, K. Suo, N. Cao, L. Hao and J. Lu, *Food Funct.*, 2021, **12**, 5204–5218.
697 S. Klein, L. V. R. Distel, W. Neuhuber and C. Kryschi, *Nanomaterials*, 2021, **11**, 1167.
698 C. C. Perry, S. M. Urata, M. Lee, J. A. Aguilera and J. R. Milligan, *Radiat. Environ. Biophys.*, 2012, **51**, 457–468.
699 S. Klein, M. Smuda, C. Harreiß, C. Menter, L. V. R. Distel and C. Kryschi, *ACS Appl. Mater. Interfaces*, 2019, **11**, 39613–39623.
700 J. Lin, M. Wang, H. Hu, X. Yang, B. Wen, Z. Wang, O. Jacobson, J. Song, G. Zhang, G. Niu, P. Huang and X. Chen, *Adv. Mater.*, 2016, **28**, 3273–3279.
701 G. Lin, P. Mi, C. Chu, J. Zhang and G. Liu, *Adv. Sci.*, 2016, **3**, 1600134.
702 A. D. Schweitzer, E. Revskaya, P. Chu, V. Pazo, M. Friedman, J. D. Nosanchuk, S. Cahill, S. Frases, A. Casadevall and E. Dadachova, *Int. J. Radiat. Oncol. Biol. Phys.*, 2010, **78**, 1494–1502.

703 D. K. Chandrasekharan, P. K. Khanna and C. K. K. Nair, *Mutat. Res., Genet. Toxicol. Environ. Mutagen.*, 2011, **723**, 51–57.
704 D. K. Chandrasekharan and C. K. K. Nair, *Int. J. Low Radiat.*, 2010, **7**, 453–466.
705 D. K. Chandrasekharan and C. K. K. Nair, *Cancer Biother. Radiopharm.*, 2012, **27**, 642–651.
706 T. Ak and İ. Gülçin, *Chem.-Biol. Interact.*, 2008, **174**, 27–37.
707 Y. Cui, M. Zhang, F. Zeng, H. Jin, Q. Xu and Y. Huang, *ACS Appl. Mater. Interfaces*, 2016, **8**, 32159–32169.
708 W.-H. Lee, C.-Y. Loo, P. M. Young, D. Traini, R. S. Mason and R. Rohanizadeh, *Expert Opin. Drug Delivery*, 2014, **11**, 1183–1201.
709 K. Mansouri, S. Rasoulpoor, A. Daneshkhah, S. Abolfathi, N. Salari, M. Mohammadi, S. Rasoulpoor and S. Shabani, *BMC Cancer*, 2020, **20**, 1–11.
710 E. SchraufstÄTter and H. Bernt, *Nature*, 1949, **164**, 456–457.
711 M. M. Yallapu, M. Jaggi and S. C. Chauhan, *Drug Discovery Today*, 2012, **17**, 71–80.
712 S. Zorofchian Moghadamtousi, H. Abdul Kadir, P. Hassandarvish, H. Tajik, S. Abubakar and K. Zandi, *Biomed Res. Int.*, 2014, **2014**, 186864.
713 J. Trujillo, Y. I. Chirino, E. Molina-Jijón, A. C. Andérica-Romero, E. Tapia and J. Pedraza-Chaverrí, *Redox. Biol.*, 2013, **1**, 448–456.
714 V. Verma, *World J. Clin. Oncol.*, 2016, **7**, 275–283.
715 P. Anand, A. B. Kunnumakkara, R. A. Newman and B. B. Aggarwal, *Mol. Pharm.*, 2007, **4**, 807–818.
716 E. Babaei, M. Sadeghizadeh, Z. M. Hassan, M. A. H. Feizi, F. Najafi and S. M. Hashemi, *Int. Immunopharmacol.*, 2012, **12**, 226–234.
717 F. Akhtar, M. M. Rizvi and S. K. Kar, *Biotechnol. Adv.*, 2012, **30**, 310–320.
718 Y. Chen, C. Chen, X. Zhang, C. He, P. Zhao, M. Li, T. Fan, R. Yan, Y. Lu, R. J. Lee, M. W. Khan, M. Sarfraz, X. Ma, T. Yang and G. Xiang, *Acta Pharm. Sin. B*, 2020, **10**, 1106–1121.
719 F. D. S. Feltrin, T. Agner, C. Sayer and L. M. F. Lona, *Adv. Colloid Interface Sci.*, 2022, **300**, 102582.
720 G. Jia, Y. Han, Y. An, Y. Ding, C. He, X. Wang and Q. Tang, *Biomaterials*, 2018, **178**, 302–316.
721 M. M. Yallapu, S. Khan, D. M. Maher, M. C. Ebeling, V. Sundram, N. Chauhan, A. Ganju, S. Balakrishna, B. K. Gupta, N. Zafar, M. Jaggi and S. C. Chauhan, *Biomaterials*, 2014, **35**, 8635–8648.
722 H. Kang, J. Gravier, K. Bao, H. Wada, J. H. Lee, Y. Baek, G. El Fakhri, S. Gioux, B. P. Rubin, J.-L. Coll and H. S. Choi, *Adv. Mater.*, 2016, **28**, 8162–8168.
723 Y. Peng, J. Bariwal, V. Kumar, C. Tan and R. I. Mahato, *Adv. Ther.*, 2020, **3**, 1900136.
724 V. López-Dávila, A. M. Seifalian and M. Loizidou, *Curr. Opin. Pharmacol.*, 2012, **12**, 414–419.
725 H. A. Joshi, R. S. Patwardhan, D. Sharma, S. K. Sandur and P. V. Devarajan, *Int. J. Pharm.*, 2021, **595**, 120181.
726 S. H. Choi, D. Y. Lee, S. Kang, M. K. Lee, J. H. Lee, S. H. Lee, H. L. Lee, H. Y. Lee and Y. I. Jeong, *Int. J. Mol. Sci.*, 2021, **22**, 6347.
727 X. Lin, Y. Shi, S. Yu, S. Li, W. Li, M. Li, S. Chen, Y. Wang and M. Cong, *Front. Chem.*, 2020, **8**, 212.
728 M. H. Nguyen, N. D. Pham, B. Dong, T. H. Nguyen, C. B. Bui and K. Hadinoto, *Int. J. Radiat. Biol.*, 2017, **93**, 1267–1273.
729 H. Nosrati, H. Danafar, H. Rezaeejam, N. Gholipour and M. Rahimi-Nasrabadi, *Bioorg. Chem.*, 2020, **100**, 103891.
730 Y. Liu, L. Miao, Y. Guo, R. Yuan, X. Li, X. Wang, X. Lin and H. Tian, *ACS Biomater. Sci. Eng.*, 2021, **7**, 2496–2507.
731 Y. Zhou, S. Hua, J. Yu, P. Dong, F. Liu and D. Hua, *J. Mater. Chem. B*, 2015, **3**, 2931–2934.
732 J. Kinoda, M. Ishihara, S. Nakamura, M. Fujita, K. Fukuda, Y. Sato and H. Yokoe, *J. Radiat. Res.*, 2018, **59**, 27–34.
733 S. Y. Wu, V. Parasuraman, T. Hsieh Chih, V. Arunagiri, S. Gunaseelan, H. Y. Chou, R. Anbazhagan, J. Y. Lai and N. R. Prasad, *Int. J. Pharm.*, 2020, **579**, 119161.
734 R. H. El-Gebaly, M. M. Rageh and I. K. Maamoun, *J. X-Ray Sci. Technol.*, 2019, **27**, 83–96.
735 S. Arany, D. S. Benoit, S. Dewhurst and C. E. Ovitt, *Mol. Ther.*, 2013, **21**, 1182–1194.
736 S. Kumar, R. Meena and P. Rajamani, *J. Agric. Food Chem.*, 2016, **64**, 6024–6034.
737 Y. Zhang, L. Wang, M. Xu, T. Zhao, L. Kuang and D. Hua, *Adv. Healthcare Mater.*, 2020, **9**, e1901778.
738 S. Pamujula, V. Kishore, B. Rider, K. C. Agrawal and T. K. Mandal, *Int. J. Radiat. Biol.*, 2008, **84**, 900–908.
739 S. G. Lee, T. M. Kalidindi, H. Lou, K. Gangangari, B. Punzalan, A. Bitton, C. J. Lee, H. A. Vargas, S. Park, L. Bodei, M. G. Kharas, V. K. Singh, N. V. Kishore Pillarsetty and S. M. Larson, *J. Nucl. Med.*, 2021, **62**, 584–590.
740 A. Dubois and R. I. Walker, *Gastroenterology*, 1988, **95**, 500–507.
741 S. Saha, P. Bhanja, L. Liu, A. A. Alfieri, D. Yu, E. R. Kandimalla, S. Agrawal and C. Guha, *PLoS One*, 2012, **7**, e29357.
742 Y. Lee, T. E. Deelman, K. Chen, D. S. Y. Lin, A. Tavakkoli and J. M. Karp, *Nat. Mater.*, 2018, **17**, 834–842.
743 F. Laffleur and A. Bernkop-Schnürch, *Nanomedicine*, 2013, **8**, 2061–2075.
744 B. Hu, C. Jin, H.-B. Li, J. Tong, X. Ouyang, N. M. Cetinbas, S. Zhu, T. Strowig, F. C. Lam, C. Zhao, J. Henao-Mejia, O. Yilmaz, K. A. Fitzgerald, S. C. Eisenbarth, E. Elinav and R. A. Flavell, *Science*, 2016, **354**, 765–768.
745 L. Zitvogel, O. Kepp, L. Galluzzi and G. Kroemer, *Nat. Immunol.*, 2012, **13**, 343–351.
746 W. Park, H. Shin, B. Choi, W.-K. Rhim, K. Na and D. Keun Han, *Prog. Mater. Sci.*, 2020, **114**, 100686.
747 L. Wang and Y. Yan, *Macromol. Biosci.*, 2021, **21**, 2100183.
748 Y.-Y. Wang, Y.-C. Liu, H. Sun and D.-S. Guo, *Coord. Chem. Rev.*, 2019, **395**, 46–62.
749 G. Chen, Y. Qian, H. Zhang, A. Ullah, X. He, Z. Zhou, H. Fenniri and J. Shen, *Appl. Mater. Today*, 2021, **23**, 101003.
750 P. Horcajada, R. Gref, T. Baati, P. K. Allan, G. Maurin, P. Couvreur, G. Férey, R. E. Morris and C. Serre, *Chem. Rev.*, 2012, **112**, 1232–1268.

751 X. Liu, T. Liang, R. Zhang, Q. Ding, S. Wu, C. Li, Y. Lin, Y. Ye, Z. Zhong and M. Zhou, *ACS Appl. Mater. Interfaces*, 2021, **13**, 9643–9655.
752 R. F. Mendes, F. Figueira, J. P. Leite, L. Gales and F. A. Almeida Paz, *Chem. Soc. Rev.*, 2020, **49**, 9121–9153.
753 L. B. Vong, T. Yoshitomi, H. Matsui and Y. Nagasaki, *Biomaterials*, 2015, **55**, 54–63.
754 L. B. Vong, M. Kobayashi and Y. Nagasaki, *Mol. Pharm.*, 2016, **13**, 3091–3097.
755 C. P. Feliciano and Y. Nagasaki, *ACS Biomater. Sci. Eng.*, 2019, **5**, 5631–5636.
756 C. P. Feliciano, K. Tsuboi, K. Suzuki, H. Kimura and Y. Nagasaki, *Biomaterials*, 2017, **129**, 68–82.
757 Y. Wang, H. Zhang, Y. Liu, M. H. Younis, W. Cai and W. Bu, *Mater. Today*, 2022, **57**, 262–278.
758 S. Chin, C. L. Eccles, A. McWilliam, R. Chuter, E. Walker, P. Whitehurst, J. Berresford, M. Van Herk, P. J. Hoskin and A. Choudhury, *J. Med. Imaging Radiat. Oncol.*, 2020, **64**, 163–177.
759 S. Corradini, F. Alongi, N. Andratschke, C. Belka, L. Boldrini, F. Cellini, J. Debus, M. Guckenberger, J. Hörner-Rieber, F. J. Lagerwaard, R. Mazzola, M. A. Palacios, M. E. P. Philippens, C. P. J. Raaijmakers, C. H. J. Terhaard, V. Valentini and M. Niyazi, *Radiat. Oncol.*, 2019, **14**, 92.
760 S. M. Bentzen and V. Gregoire, *Semin. Radiat. Oncol.*, 2011, **21**, 101–110.
761 D. Thorwarth, *Br. J. Radiol.*, 2015, **88**, 20150056.
762 C. Zhang and K. Pu, *Chem. Soc. Rev.*, 2020, **49**, 4234–4253.
763 P. M. Calabro-Jones, R. C. Fahey, G. D. Smoluk and J. F. Ward, *Int. J. Radiat. Biol. Relat. Stud. Phys., Chem. Med.*, 1985, **47**, 23–27.
764 J. M. Yuhas, *Cancer Res.*, 1980, **40**, 1519–1524.

